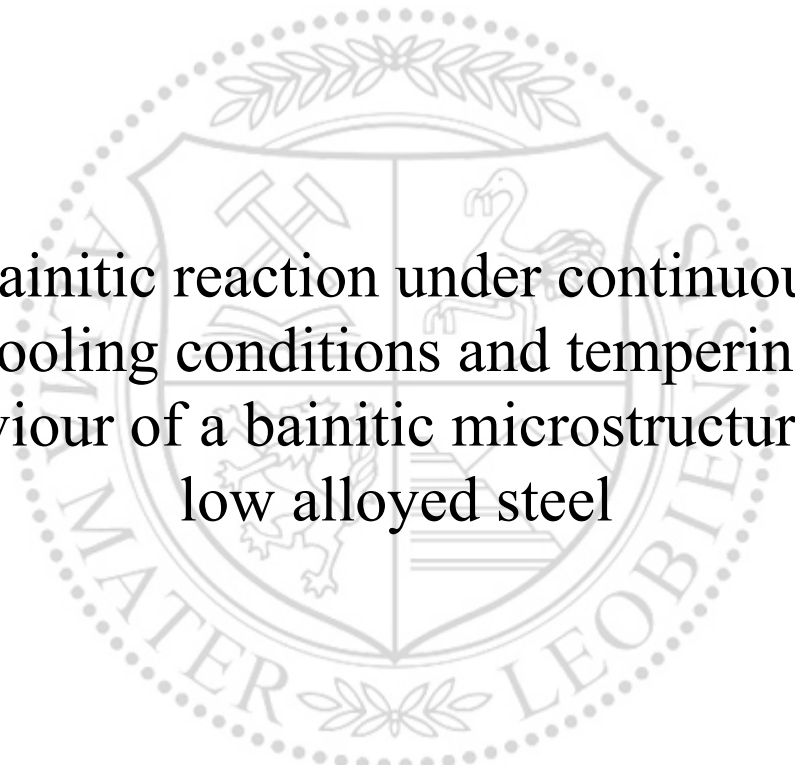




Chair of Physical Metallurgy and Metallic Materials

Doctoral Thesis



Bainitic reaction under continuous  
cooling conditions and tempering  
behaviour of a bainitic microstructure in a  
low alloyed steel

Dipl.-Ing. Stephan Reisinger

August 2019

## EIDESSTÄTTLICHE ERKLÄRUNG

Ich erkläre an Eides statt, dass ich diese Arbeit selbständig verfasst, andere als die angegebenen Quellen und Hilfsmittel nicht benutzt, und mich auch sonst keiner unerlaubten Hilfsmittel bedient habe.

Ich erkläre, dass ich die Richtlinien des Senats der Montanuniversität Leoben zu "Gute wissenschaftliche Praxis" gelesen, verstanden und befolgt habe.

Weiters erkläre ich, dass die elektronische und gedruckte Version der eingereichten wissenschaftlichen Abschlussarbeit formal und inhaltlich identisch sind.

Datum 11.08.2019



Unterschrift Verfasser/in  
Stephan, Reisinger  
Matrikelnummer: 01035016

# Preface

The present work is submitted for the attainment of a doctorate “Doktor der montanistischen Wissenschaften” at the “Montanuniversität Leoben” and was supervised by ao. Univ. Prof. DI Dr. mont Reinhold Ebner. The present thesis was carried out within the framework of the COMET project kp1.21 (“carbide hardening bainite”). The project was realized in the time between March 2014 and December 2017 with industrial partners Robert BOSCH GmbH and Deutsche Edelstahlwerke GmbH as well as scientific partners Department of Physical Metallurgy and Materials Testing and Institute of Materials Science and Technology Vienna.

The project was financially supported by the Austrian Federal Government (in particular from Bundesministerium für Verkehr, Innovation und Technologie and Bundesministerium für Wissenschaft, Forschung und Wirtschaft) represented by Österreichische Forschungsförderungsgesellschaft mbH and the Styrian and the Tyrolean Provincial Government, represented by Steirische Wirtschaftsförderungsgesellschaft mbH and Standortagentur Tirol, within the framework of the COMET Funding Programme.

---

## Acknowledgement

I am very grateful to ao. Univ. Prof. DI Dr. mont. Reinhold Ebner for enabling and supervising the present PhD thesis as well as for numerous interesting discussions.

I also would like to acknowledge DI Dr. Stefan Marsoner for the possibility to work at the Materials Center Leoben Forschung GmbH. Without his support, it would not have been possible to complete this work.

In addition, I would like to thank my second supervisor, Assoc. Prof. Dr. Daniel Kiener for giving me the basic insights in the wonderful world of material physics.

I am also very grateful to Prof. Ernst Kozeschnik for the many interesting discussions while enjoying some beers together. You taught me a lot in the last years, also beside thermodynamics and precipitation kinetics.

I would also like to express my gratitude to Dr. Francisca Mendez-Martin for their huge support during difficult data evaluations and to draw out the right conclusions from these data.

I also would like to extend thanks to my industrial partners DI Kathrin Eger, Dr. Hans-Günther Krull and Dr. Matthias Kuntz.

Furthermore, I would like to thank all colleagues from the Materials Center Leoben Forschung GmbH, especially Dr. Annika Eggbauer, DI Josef Pörnbacher, Dr. Sven Eck and Dr. Gerald Ressel for their support during my time as a PhD student.

Special thanks go to my college and good friend DI Dominik Brandl. I will never forget the daily morning discussion about our “challenges” with material science.

Last, but not least I would like to thank my girlfriend Birgit, my family and my friends for their huge support during my time in Leoben.



---

## Abstract

The use of bainitic steels in the automotive industry constantly increases, because of the excellent combination of toughness and strength. However, due to economic reasons, it is not possible to realize long isothermal holding times to achieve a bainitic microstructure. Therefore, the aim of the present work is to analyse the bainitic reaction during continuous cooling conditions and to describe the microstructural changes that occur during a subsequent tempering treatment in a low alloyed steel.

It was found that the decomposition of austenite to bainite occurs between cooling rates higher than  $0.3^{\circ}\text{C s}^{-1}$  and lower than  $6^{\circ}\text{C s}^{-1}$ . The transformation kinetics of the bainitic reaction can be described on the basis of an adopted T0' concept, which incorporates elastic strain energy values between 950 and 1100  $\text{J mol}^{-1}$ . However, the phase transformation remains incomplete and amounts of 10 to 17 vol.-% of retained austenite in the form of blocks and films are present in the final bainitic microstructure. A further reheating leads to the decomposition of retained austenite, whereas the block morphology is thermally more stable than the films of austenite. An isothermal tempering treatment at  $620^{\circ}\text{C}$  for 4 hours lead to the precipitation of  $\text{M}_2\text{C}$  type secondary hardening carbides, which increases the hardness around 100HV1.

---

*Für meine Eltern in Liebe und Dankbarkeit!*

*Denke lieber an das, was du hast, als an das, was dir fehlt! Suche von den Dingen, die du hast, die besten aus und bedenke dann, wie eifrig du nach ihnen gesucht haben würdest, wenn du sie nicht hättest.*

*-Marc Aurel (römischer Kaiser 181n. Chr.)-*

---

## Table of contents

1	Motivation and scope of this work.....	- 1 -
2	Phase transformations in steels.....	- 3 -
2.1	Reconstructive decomposition of austenite.....	- 6 -
2.1.1.	Allotriomorphic and idiomorphic ferrite.....	- 6 -
2.1.2.	Massive Ferrite.....	- 7 -
2.1.3.	Pearlite.....	- 8 -
2.2	Displacive decomposition of austenite.....	- 10 -
2.2.1.	General aspects.....	- 10 -
2.2.2.	Widmanstätten ferrite.....	- 12 -
2.2.3.	Bainite.....	- 14 -
2.2.3.1.	Bainitic ferrite.....	- 14 -
2.2.3.2.	Incomplete transformation phenomenon.....	- 16 -
2.2.3.3.	Stability of retained austenite.....	- 20 -
2.2.3.4.	Upper & lower bainite.....	- 21 -
2.2.3.5.	Granular bainite.....	- 23 -
2.2.4.	Martensite.....	- 24 -
3	Tempering and precipitation hardening in steels containing a bainitic microstructure.....	- 26 -
3.1	General Aspects on tempering.....	- 26 -
3.2	Precipitation hardening.....	- 28 -
3.3	Carbide precipitation in Fe-C-Mo steels.....	- 29 -
3.4	Numerical Simulation of precipitation kinetics using MatCalc.....	- 31 -
4	Investigated material and setup of experiments.....	- 32 -
4.1	Investigated Material.....	- 32 -
4.2	Heat treatment experiments using dilatometry.....	- 33 -
4.2.1.	Time-temperature cycles for high-energy X-ray diffraction.....	- 34 -
4.2.2.	Time-temperature cycles for microstructure observations.....	- 34 -
4.3	Microstructure characterization methods.....	- 35 -
4.3.1.	Quantitative metallography.....	- 35 -
4.3.2.	Optical light microscopy.....	- 36 -

---

4.3.3.	Scanning electron microscopy .....	36 -
4.3.4.	Electron back scatter diffraction.....	37 -
4.3.5.	Transmission electron microscopy .....	38 -
4.3.6.	Atom probe tomography.....	40 -
4.4	Phase analysis using lab scale X-ray diffraction.....	41 -
4.5	Studying in-situ phase transformation using high energy X-ray diffraction...-	42 -
4.5.1.	Calculation of phase fractions and lattice parameter .....	42 -
4.5.2.	Determination of overall carbon content in austenite and bainitic ferrite .....	43 -
4.6	Hardness measurements.....	44 -
5	Characterization of the initial microstructure and the continuous cooling transformation diagram .....	45 -
5.1	Carbide type and volume fraction in the soft annealed microstructure .....	45 -
5.2	Comparison to the equilibrium phase diagram.....	50 -
5.3	Reheating of the soft annealed microstructure and austenite grain size .....	53 -
5.4	Continuous cooling transformation diagram.....	56 -
5.5	Summary.....	58 -
6	Bainitic reaction during continuous cooling.....	59 -
6.1	Bainite phase evolution during continuous cooling .....	59 -
6.1.1.	Dilatometry.....	59 -
6.1.2.	High energy X-ray diffraction.....	61 -
6.1.3.	Comparison of transformation kinetics obtained by dilatometry and high energy X-ray diffraction .....	62 -
6.2	Characterization of the bainitic microstructure.....	64 -
6.2.1.	Early stages of bainitic transformation during continuous cooling .....	64 -
6.2.2.	Microstructure after phase transformation.....	67 -
6.3	Carbon in bainitic ferrite and retained austenite .....	71 -
6.3.1.	Overall carbon distribution during transformation .....	71 -
6.3.2.	Local carbon distribution on bainitic ferrite/austenite interface.....	73 -
6.3.3.	Carbon trapped at defects .....	76 -
6.4	Discussion on the bainitic reaction during continuous cooling.....	78 -
6.4.1.	The incomplete transformation phenomenon .....	78 -
6.4.2.	Excess carbon in bainitic ferrite .....	81 -

---

7	Tempering of continuous cooled bainite .....	- 85 -
7.1	Tempering effects during continuous reheating .....	- 87 -
7.1.1.	Phase evolution during continuous reheating .....	- 87 -
7.1.2.	Microstructural development during continuous reheating .....	- 91 -
7.2	Tempering effects during isothermal tempering .....	- 97 -
7.2.1.	Phase evolution during isothermal tempering .....	- 97 -
7.2.2.	Precipitation of secondary hardening carbides .....	- 99 -
7.3	Discussion on the observed tempering effects.....	- 102 -
8	General summary .....	- 108 -
9	References .....	- 111 -
10	Appendix.....	- 124 -
A.	Publications .....	- 124 -
A.1.	Differentiation of grain orientation with corrosive and colour etching on a granular bainitic steel.....	- 125 -
A.2.	Strain energy contributions on the bainitic reaction in a CrMoV steel.....	- 133 -
B.	MatCalc scripts.....	- 144 -
B.1.	Thermodynamic equilibrium calculation .....	- 144 -
B.2.	Decomposition of retained austenite during reheating .....	- 146 -

# 1 Motivation and scope of this work

Diesel engines are one of the most effective combustion engines. The high efficiency of such diesel engines primarily depends on the diesel injection system and the associated high-pressure components, e.g. injection nozzle. Nowadays, the requirements for such high-pressure components constantly increase, especially the need for higher injection pressures. However, higher injection pressures also require an improvement of the strength and especially fatigue strength of the used materials for injection nozzles.

An injection nozzle is an element with a complex internal 3D structure where the highest level of precision during manufacturing is necessary. Therefore, the use of higher alloyed steels and a much more complicated production route is limited by economic reasons. Due to this fact, a new alloying concept was developed by the Materials Center Leoben Forschung GmbH (MCL) and tested with respect to its suitability for full-scale production in cooperation with the Robert BOSCH GmbH (BOSCH) and the Deutsche Edelstahlwerke GmbH (DEW). This alloying concept is based on the idea to achieve a well machine-able soft granular bainitic microstructure (35-38 HRC) after continuous cooling. After machining the specimens are hardened by means of a tempering process that is based on precipitation secondary hardening precipitates to achieve the necessary hardness (45-48 HRC). With respect to current steel concepts containing a martensitic microstructure, the new concept promises a much lower macroscopic deformation during the “precipitation hardening” process, i.e. no or minor need for further geometry corrections (machining) of the product after the hardening.

The first step to achieve these goals is to understand the complex bainitic reaction during continuous cooling. A key role in this context plays the carbon and its possibility to build precipitates or to stabilize austenite during the bainitic reaction [1–3].

The second step is the understanding of the tempering process starting from a bainitic microstructure with secondary constituents like retained austenite or precipitates. Tempering of steel includes several complex processes, such as the decomposition of retained austenite, segregation of carbon on lattice defects and the precipitation of coarse (~100-500 nm) and fine (~10-50 nm) carbides. The precipitation of carbides influences the material properties, e.g. hardness and yield strength essentially. To correlate e.g. the increase in yield strength with the precipitation of carbides, a detailed knowledge about the carbide distribution is necessary. However, due to the

small dimensions of these precipitates it is a challenging task to characterize them. Thus, a correlative microstructure characterization by using high resolution techniques, such as transmission electron microscopy (TEM) and atom probe tomography (APT) is necessary. A disadvantage of the mentioned methods, however, is the substantial experimental effort.

A possibility to reduce the experimental effort are numerical simulation, which enables a faster materials design and also process optimization [4]. Therefore, the thermo-kinetic software package MatCalc [5] is used in this thesis to understand and model the complex precipitation sequences during tempering.

## 2 Phase transformations in steels

Iron based alloys are well-known for their special characteristics, such as magnetism, allotropic phase changes and the different solubility and diffusion behaviour of interstitial as well as substitutional alloying elements [6]. According, [6,7] these phase transformations could be classified based upon microstructure, thermodynamics or transformation mechanisms. In the following, the phase transformations are classified according to their mechanism. In this scheme the phase transformations in steels are usually divided into two major groups named according to whether long-range diffusion of atoms occurs or not.

If long-range diffusion of atoms occurs the phase transformations is called reconstructive phase transformation or diffusional phase transformation. The diffusion of substitutional as well as interstitial elements leads to the formation of the new crystal structure. Therefore, diffusional phase transformations are only accompanied by a change in the volume because the flow of matter is sufficient to prevent any shear components [7]. The diffusion process also leads to a redistribution of the alloying elements between the phases which further lead to a reduction in the overall free energy [8].

If no diffusion of atoms occurs the phase transformations are called displacive or diffusionless phase transformation. During a displacive phase transformation, the change in crystal structure also causes a macroscopic shape change of the sample when the latter is not constrained [8]. The shape deformation during constrained transformation is accommodated by a combination of elastic and plastic strains in the surrounding matrix [8–11]. The product phase grows in the form of thin plates to minimize these strains [1,12]. The atoms are displaced into their new positions in a coordinated motion. Displacive transformations can therefore occur at temperatures where diffusion is inconceivable within the time scale of the experiment [13–15].

To illustrate the reconstructive and displacive phase transformation the mechanisms are summarized in the following sketch. Imagine, as illustrated in **Figure 2.1**, that the austenite ( $\gamma$ ) consists of a mixture of blue atoms (circle) and red atoms (square), and has the unit cell outlined in red.

A possibility to change the crystal structure without disrupting the relative order of the atoms is to form the ferrite unit cell by a homogenous deformation of the parent austenite [16]. In such a case, the overall shape of the sample must change in the same way as the crystal structure. Subsequently, this shape deformation leads to an accumulation of elastic strain energy which can be minimised if the ferrite ( $\alpha$ ) adopts a thin-plate shape [1,12].



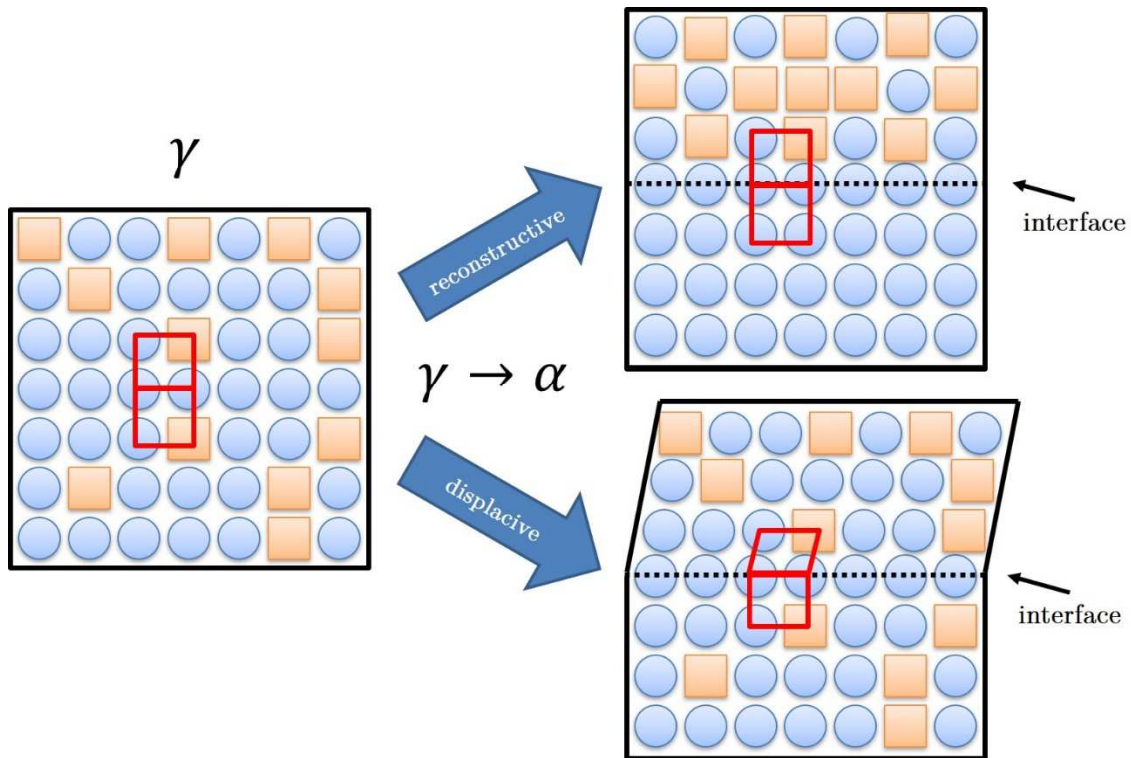


Figure 2.1: Schematic illustration of reconstructive and displacive phase transformation of austenite ( $\gamma$ ) to ferrite ( $\alpha$ ).

A further consequence of the deformation is that the atoms maintain in their position as in the parent phase. Therefore, there is no change in the chemical composition and there is a one-to-one atomic correspondence between ferrite and austenite.

The change in crystal structure can also be achieved in effect by breaking the atomic bonds in the austenite and rearranging the atoms into the structure of ferrite whilst maintaining the overall shape [7]. In that case atoms have to diffuse over distances which are comparable to the new phase. Thus, although the accumulated strain energy which is associated with displacive transformations is avoided. However, reconstructive phase transformations can only occur at temperatures where the atoms exhibit a sufficiently mobility. Given the premise that atoms are mobile enough, certain species will diffuse in that phase ( $\alpha$  or  $\gamma$ ) where the solubility limit is highest. This partitioning process leads to a change in the chemical composition between ferrite and austenite. Therefore, no atomic correspondence exists between the parent and product phase after a diffusional transformation.

The shape of the newly formed phase is controlled by the growth conditions or as an equilibrium is reached where the overall interfacial energy per unit volume is minimised [16]. Another feature which is characteristic for reconstructive transformation is that the newly formed phase can grow across grain boundaries.

The reconstructive and displacive phase transformations in steels can be summarized as illustrated in **Figure 2.2**.

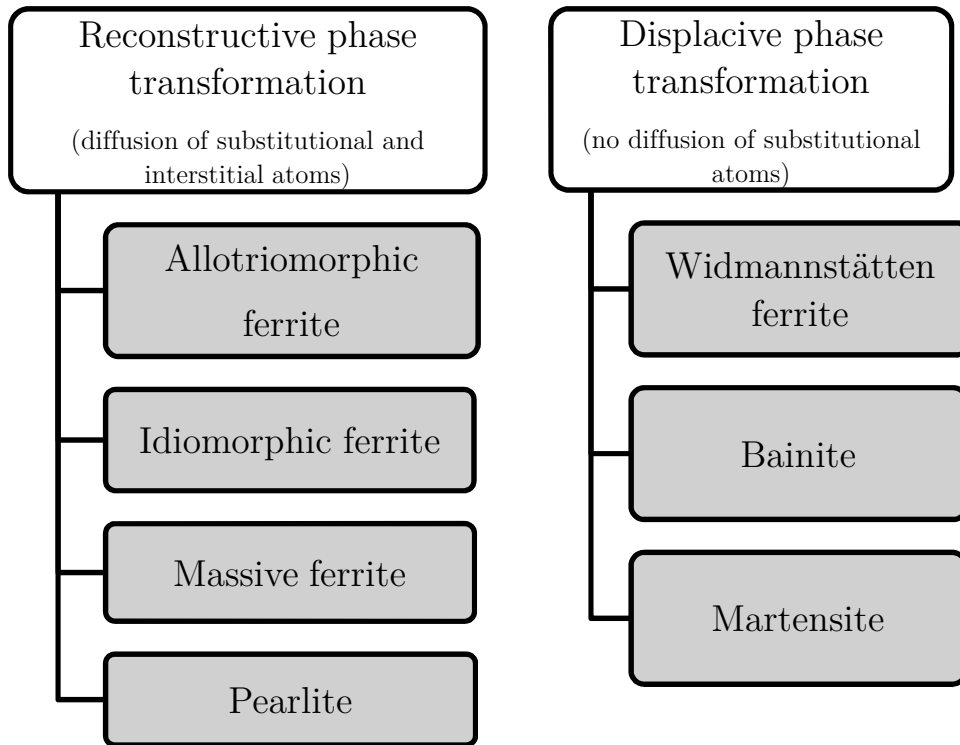


Figure 2.2: Possible reconstructive and displacive phase transformation in steels.

## 2.1 Reconstructive decomposition of austenite

As already described above a reconstructive phase transformation leads to diffusion of atoms. This includes substitutional atoms (e.g. Fe, Cr, Mo, ...) as well as interstitial atoms (e.g. C, N, ...). During a reconstructive phase transformation, both nucleation and growth of the new phase are determined by diffusion of substitutional and interstitial atoms. In the following subsections, the most important reconstructive phase transformations will be explained in detail.

### 2.1.1. Allotriomorphic and idiomorphic ferrite

In 1955, Aaronson [17] classified ferrite, which grows by a diffusional process into two forms: allotriomorphic and idiomorphic ferrite. The term “allotriomorphic” means that the ferrite is crystalline in internal structure but does not reflect the symmetry of the parent austenite.

This allotriomorphic ferrite ( $\alpha_a$ ) nucleates at prior austenite grain boundaries at temperatures, i.e. just below  $A_{e3}$  (upper temperature limit of the  $\alpha + \gamma$  phase field at equilibrium conditions).

The growth of allotriomorphic ferrite can be treated in terms of normal migration of planar  $\gamma/\alpha$  interfaces along austenite grain boundaries. Aaronson and Domain [18] observed that the growth of allotriomorphic ferrite in low alloyed steels occurs without bulk partitioning of substitutional alloying elements. Under these circumstances, ferrite growth is controlled by the diffusion of carbon in the surrounding austenite ahead of the interface. These growth condition is also well known as paraequilibrium ( $A_{e3}'$ ) [19]. Therefore, the growth rate of  $\alpha_a$  is much faster along austenite grain boundaries than in the direction normal to the boundary. Consequently, the shape of allotriomorphic ferrite is strongly influenced by austenite grain boundaries, **Figure 2.3**.

In contrast, idiomorphic ferrite usually nucleates intragranularly at inclusions or other heterogeneous nucleation sites and is therefore not influenced by the austenite grain boundary [19].

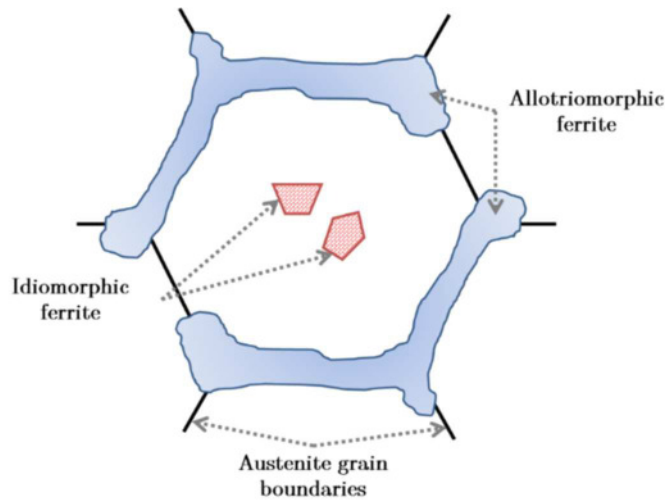


Figure 2.3: Schematic illustration of allotropic ferrite and idiomorphic ferrite in steels.

### 2.1.2. Massive Ferrite

Massive ferrite, which also grows by a reconstructive transformation mechanism in very-low carbon steels ( $<0.05\text{wt.}\% \text{ C}$ ), has the distinction that it inherits the composition of the parent austenite [20]. This is only possible by rapid cooling from the single-phase field of austenite to the single-phase field of ferrite without partitioning of atoms in the intervening two-phase ferrite/austenite field [21,22]. As a consequence of the absent change in chemical composition, the transformation proceeds until all of the austenite has been transformed. The resulting microstructure consists of larger ferrite grains which have an approximately equiaxed morphology [19], **Figure 2.4**.

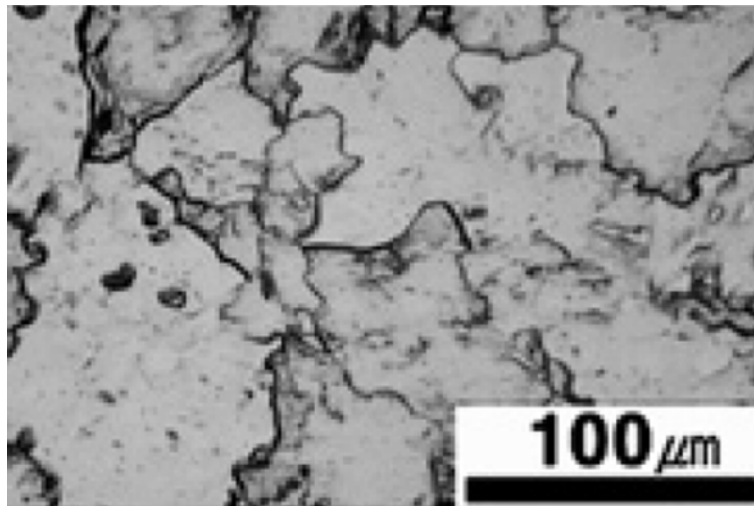


Figure 2.4: Massive ferrite in a Fe-0.0031C-0.53Mn-0.02Ni interstitial free steel, austenitized at  $980^\circ\text{C}$  for 10 min and subsequent quenching in a salt bath (60%  $\text{CaCl}_2$  + 40%  $\text{NaCl}$ ) to  $600^\circ\text{C}$  and held for 30 min, taken from [22].

### 2.1.3. Pearlite

Pearlite occupies a special position in the scheme of reconstructive transformations since this is not a direct decomposition of austenite into ferrite. Pearlite is in fact a mixture of two phases, eutectoid ferrite ( $\alpha_e$ ) and cementite ( $\text{Fe}_3\text{C}$ ).

In eutectoid steels, i.e. Fe-0.8C-0.5Mn-0.25Si, the nucleation of pearlite starts at austenite grain boundaries involving the nucleation of eutectoid ferrite and cementite [23–25]. In steels which have a lower or higher carbon content than the eutectoid composition (0.8wt.-%), the pearlite transformation occurs after the formation of proeutectoid ferrite or cementite. Proeutectoid ferrite forms in hypoeutectoid steels ( $C < 0.8\text{wt.-%}$ ), whereas proeutectoid cementite forms in hypereutectoid steels ( $C > 0.8\text{wt.-%}$ ) [23].

Generally it is proposed in literature [26], that the pearlite formation begins with the nucleation of a cementite nucleus, followed rapidly by the formation of eutectoid ferrite at the cementite-austenite interface. The conclusion that cementite is the first phase to form during the process of pearlite nucleation is based on selected area diffraction (SAD) experiments [27–29]. The experiments showed that proeutectoid cementite has the same orientation relationship with the pearlitic cementite, whereas the orientation relationship between proeutectoid ferrite and austenite is not the same as that between eutectoid ferrite and austenite.

Therefore, the formation of pearlite can be divided according to the C-content in steel (**Figure 2.5**):

**a) Hypoeutectoid steel  $0.02\text{wt.-%} < C < 0.8\text{wt.-%}$**

Nucleation of a cementite nucleus at a proeutectoid ferrite/austenite interface, followed by cooperative growth of cementite and eutectoid ferrite

**b) Eutectoid steel  $C = 0.8\text{wt.-%}$**

Nucleation of a cementite nucleus at austenite grain boundaries, followed by cooperative growth of cementite and eutectoid ferrite

**c) Hypereutectoid steel  $0.8\text{wt.-%} < C < 2.06\text{wt.-%}$**

Nucleation of a ferrite nucleus at a proeutectoid cementite/austenite interface, followed by cooperative growth of cementite and eutectoid ferrite

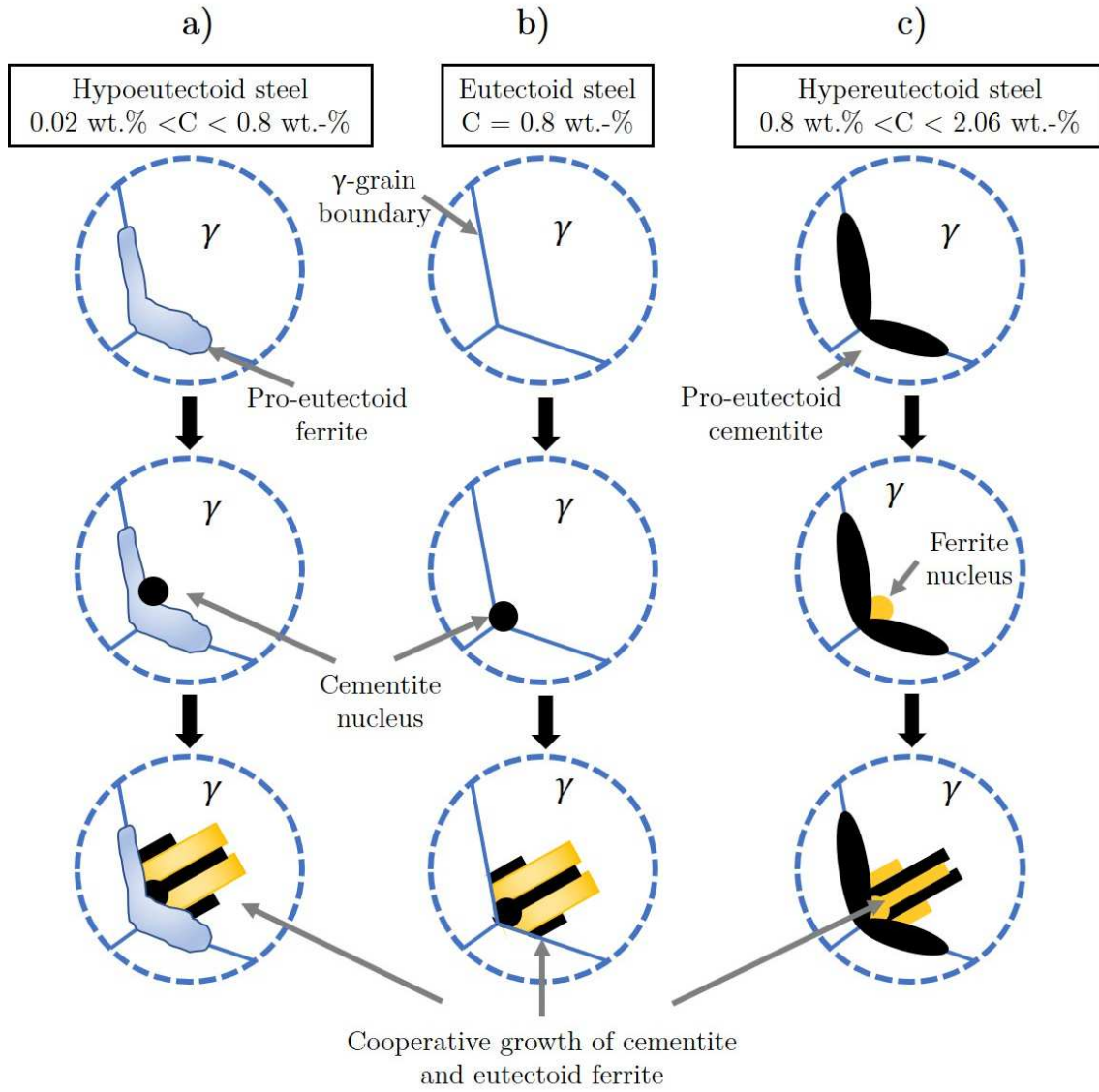


Figure 2.5: Pearlite formation in a) hypoeutectoid steel, b) eutectoid steel and c) hypereutectoid steel.

## 2.2 Displacive decomposition of austenite

### 2.2.1. General aspects

The phases resulting from a displacive decomposition of austenite can be Widmanstätten ferrite, bainite and martensite, depending on chemical composition and transformation temperature. A special feature of these phases is the thin-plate morphology, resulting from a shape deformation strain to minimize the strain energy per unit volume ( $E_s$ ). Eshelby's classic work [30], on the strain energy associated with a constrained transformation showed clearly that the strain energy per unit volume of a transformed particle in the form of an infinitely thin oblate spheroid, with semi-thickness  $c$  and an radius  $r$  ( $r \gg c$ ), could be reduced to zero, if the strains associated with the transformation leave one plane (habit plane) of the parent crystal unrotated and undistorted. Such a strain is known as invariant plane strain (IPS). The IPS involves a shear strain component ( $\mathbf{s}$ ) parallel to the habit plane, as well as, a dilatational strain component ( $\boldsymbol{\delta}$ ) normal to the habit plane which corresponds to the volume change ( $\Delta V$ ). An example for the displacive decomposition of austenite to martensite ( $\alpha'$ ) according an IPS is shown in **Figure 2.6**. Furthermore, the shear strain component of the IPS varies with the transformation product, **Table 2.1**.

**Table 2.1:** Approximate values of shear strain ( $\mathbf{s}$ ) and dilatational strain ( $\boldsymbol{\delta}$ ) for displacive transformation products according Bhadeshia [31].

Phase	$\mathbf{s}$	$\boldsymbol{\delta}$
Widmanstätten ferrite	0.36	0.03
Bainite	0.22-0.26	0.03
Martensite	0.24	0.03

In practise, the geometrical parameters  $c$  and  $r$  of such a spheroid cannot be reduced indefinitely and the strain energy cannot be minimized to a value of zero. Christian [12], therefore postulated an formula to determine the strain energy per unit volume as follows:

$$E_s = \frac{GV_m\pi}{4(1-\nu)} \frac{c}{r} [\delta^2 + 0.5(2-\nu)s^2] \quad (1)$$

, where  $\nu$  is the Poisson ratio,  $G$  represents the shear modulus of austenite and  $V_m$  is the molar volume of austenite. Under constrained transformation conditions, as they are present in a polycrystalline bulk material, the strain energy per unit volume can only be minimized by forming thin and long plates of ferrite during the displacive decomposition of austenite.

In the following sub-sections, the individual displacive decomposition products of austenite will be explained in detail.

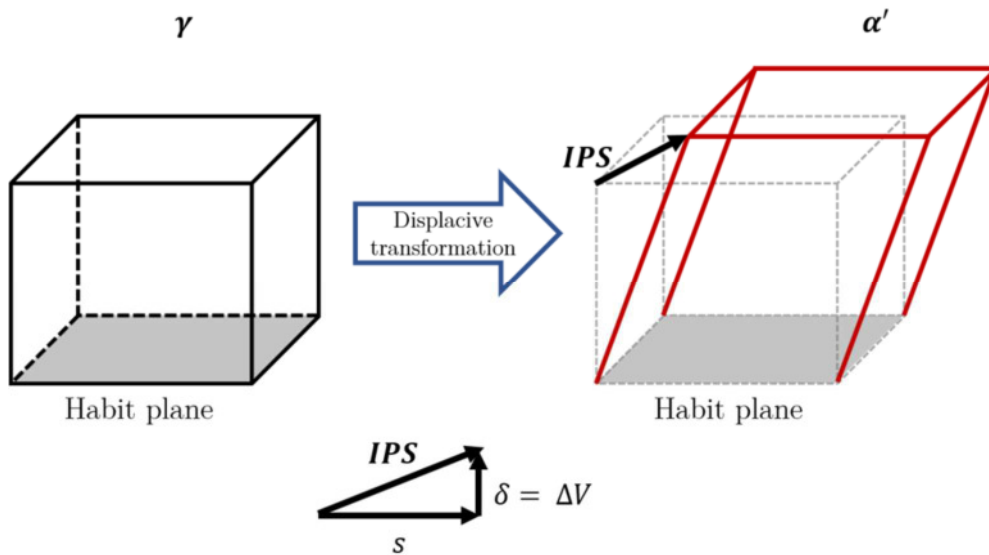


Figure 2.6: Displacive phase transformation of austenite ( $\gamma$ ) to, e.g. martensite ( $\alpha'$ ) via an invariant plane strain IPS, that consists of a shear strain  $s$  in a direction lying in the habit plane (shaded) and a dilatation strain  $\delta$  that is an expansion or contraction normal to the habit plane according [6]. The dilatation component is equal to the volume change  $\Delta V$  that results from the austenite to martensite transformation.



### 2.2.2. Widmanstätten ferrite

Widmanstätten ferrite is a phase formed by the decomposition of austenite close to  $A_{e3}$  and can be distinguished into a primary and a secondary form. Bhadeshia [32], pointed out that primary Widmanstätten ferrite nucleates at the austenite grain boundary, whereas secondary Widmanstätten ferrite grows from any allotriomorphic ferrite that may be present in the microstructure. On an optical scale Widmanstätten ferrite has the morphology of a thin wedge, **Figure 2.7a**.

The phase transformation from austenite to Widmanstätten ferrite proceeds at very low driving forces. Bhadeshia [33] determined that the change in free energy needed for the growth of Widmanstätten ferrite is approximately  $50 \text{ Jmol}^{-1}$ .

However, at the high temperatures at which Widmanstätten ferrite grows, the driving force is not sufficient to support the strain energy associated with a single plate, as is the case, e.g. martensite. To overcome this strain energy, Widmanstätten ferrite includes the simultaneous and adjacent cooperative growth of two ferritic plates ( $\alpha_{w1}$  and  $\alpha_{w2}$ ), which are crystallographic variants separated by a low-misorientation boundary [7,32,33], **Figure 2.7b**. Due to this cooperative growth, much of the strain energy is compensated. Widmanstätten ferrite has a habit plane which is close to the  $\{5\ 5\ 8\}$  plane of austenite, [7,32]. The two ferritic plates have different variants of this austenite habit plane and form together the thin-wedge shaped plate that is characteristic of Widmanstätten ferrite, **Figure 2.7c**.

As described before, the formation of Widmanstätten ferrite occurs at temperatures close to  $A_{e3}$  and low undercooling. At these conditions, it is thermodynamically necessary that the carbon is redistributed during growth in the surrounding austenite. Therefore, Widmanstätten ferrite inherits a paraequilibrium carbon content during growth and the growth rate is determined by the diffusion of carbon in the austenite ahead of the plate-tip [32]. Since the transformation is displacive, substitutional atoms do not partition during growth and an atomic correspondence between the parent and the product lattice occurs [32].

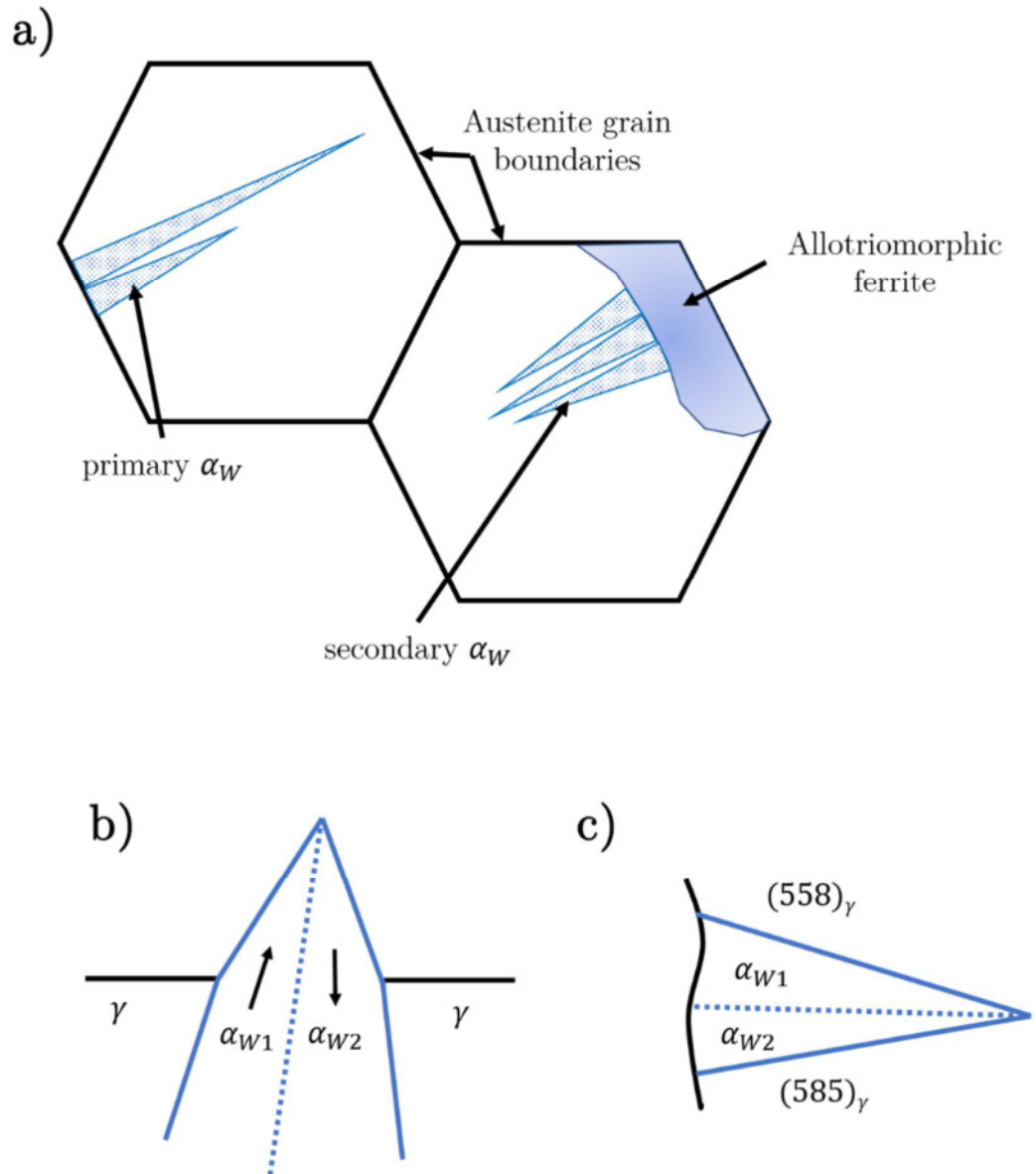


Figure 2.7: a) Possible forms of Widmanstätten ferrite ( $\alpha_W$ ): primary  $\alpha_W$  nucleate directly on austenite grain boundaries, whereas secondary  $\alpha_W$  nucleate on allotriomorphic ferrite if any is present in the microstructure, b) cooperative growth of two  $\alpha_W$  plates to minimize the strain energy associated with the phase transformation, c) the thin-wedge shaped morphology of  $\alpha_W$  is in fact a combination of different variants of the  $\{558\}$  habit plane [34].

## 2.2.3. Bainite

### 2.2.3.1. Bainitic ferrite

“**Bainite**”, named after E.C. Bain [35], is the generic term for fine aggregates of ferrite laths or plates separated by untransformed austenite, martensite or cementite.

Substantial research has been carried out regarding the mechanism of the bainitic transformation [1–3,33,36–38]. According to this literature, bainite grows in the form of wedge-shaped plates, so called **sheaves** [39–41], originating from austenite grain boundaries. A sheaf itself is built up of fine bainitic ferrite platelets, which are called **sub-units**. Within a sheaf, the sub-units are connected in three dimensions and they share the same crystallographic orientation. A representative transmission electron micrograph of a sheaf and the corresponding sub-units in a Fe-0.43C-2Si-3Mn (wt.-%) steel is shown in **Figure 2.8**.

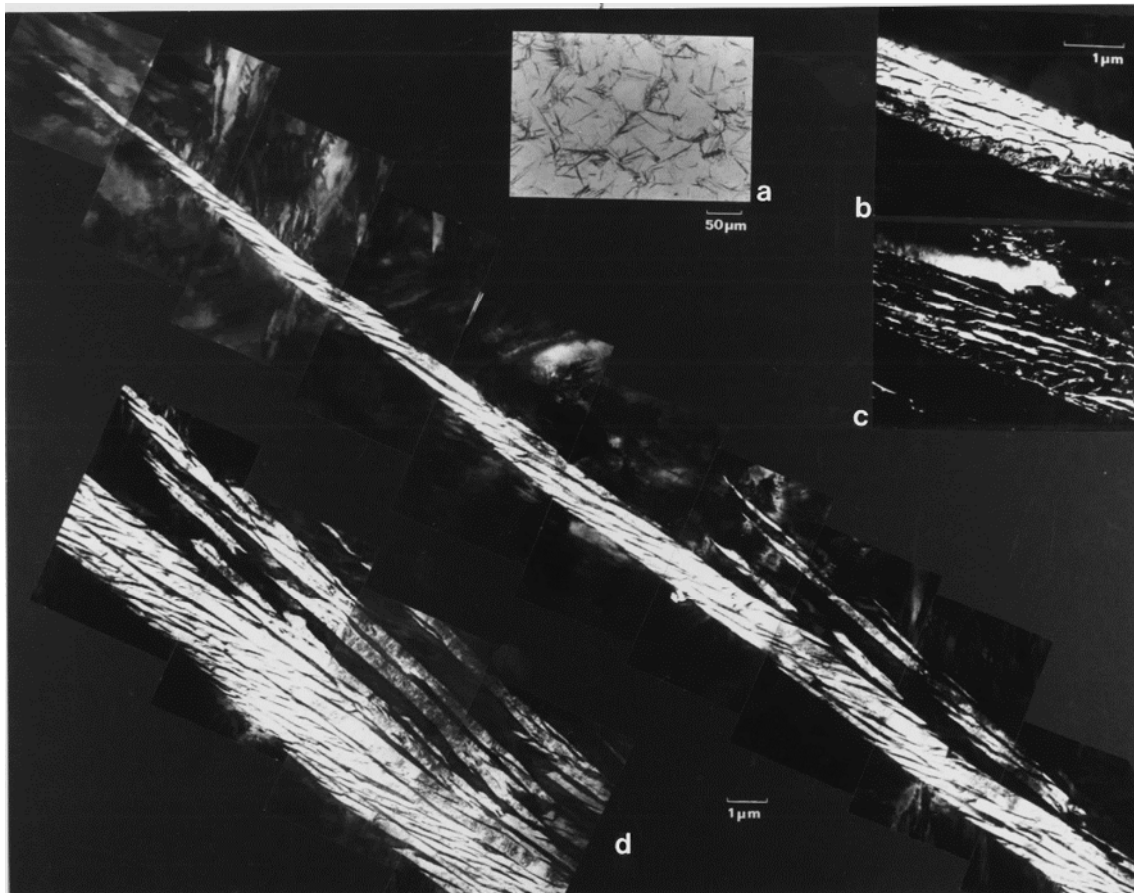


Figure 2.8: Transmission electron micrograph of a bainitic sheaf in a Fe-0.43C-2Si-3Mn (wt.-%) steel: a) corresponding optical light micrograph; b) bright field image of the bainitic ferrite sub-units with the corresponding retained austenite between sub-units in c); d) summary of bright field images showing the structure of a bainitic sheaf [42].

The dimensions of a sub-unit can be imagined as an oblate spheroid with semi-thickness  $c$  and radius  $r$ , where  $r \gg c$ , as described in section 2.2.1. The sub-unit size depends on the transformation temperature, austenite strength, chemical driving force and also on the impingement of adjacent sub-units [43–45]. The supposed effect of temperature could be indirect since the strength of austenite as well as the driving force strongly depend on temperature. Singh and Bhadeshia [45] investigated the bainite transformation on a series of silicon-rich alloys in the temperature range of 260–460°C. They found that the size of sub-units primarily depends on the strength of the austenite at the transformation temperature, whereas the temperature contribution is very small. This conclusion applies specifically when the shape deformation during the bainitic transformation causes plastic strain in the adjacent austenite. Direct observations of the austenite/bainite interface by means of atomic-force-microscopy (AFM) revealed the plastic deformation in the bainitic ferrite sub-unit as well as in the adjacent austenite [46], **Figure 2.8**. The adjacent austenite can accommodate the majority of the plastic strain by mechanical twinning or faulting, whereas the bainitic ferrite primarily builds dislocations [1,47]. Furthermore, the dislocation density in bainitic ferrite increases with decreasing transformation temperature [48].

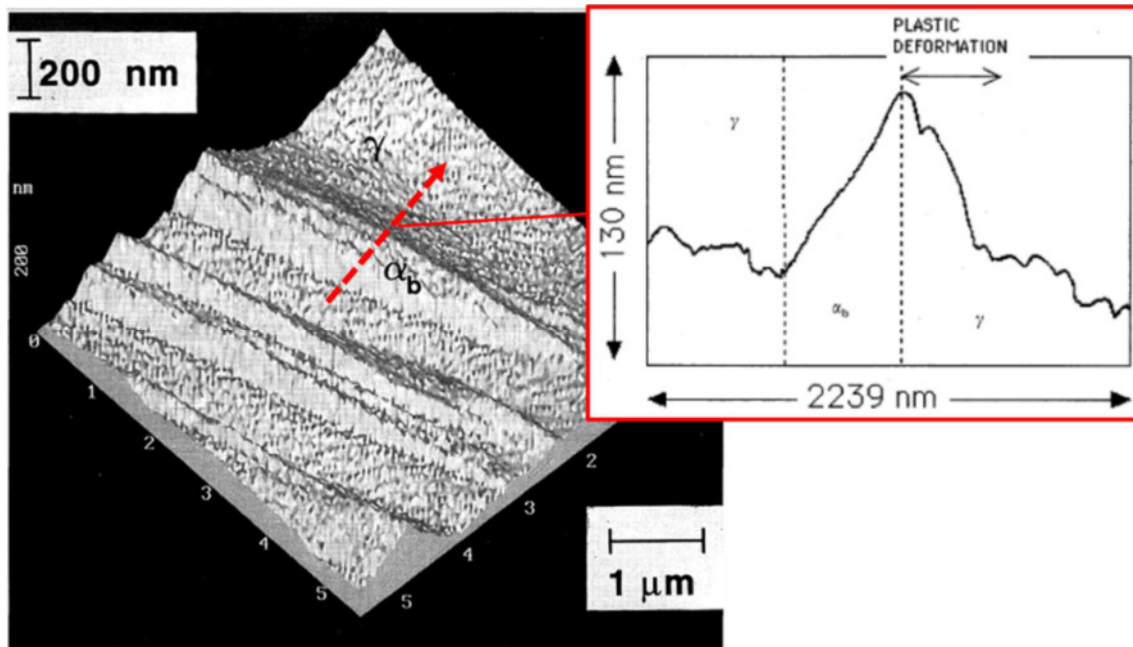


Figure 2.9: AFM image showing the surface relief of individual bainitic subunits in a Fe-0.24C-2.18Si-2.32Mn-1.05Ni during isothermal holding at 350°C with the corresponding linescan at the position marked with an red arrow; taken from Swallow and Bhadeshia [46].

The generated crystal defects (e.g. dislocations, stacking faults) during this plastic deformation resist the advance of an austenite/bainite interface and therefore the growth of a sub-unit stops. Consequently, the sheaf as a whole grows by the repeated nucleation of new sub-units, mostly near the tips of already existing sub-units [49].

The nucleation of a virgin sub-unit occurs under paraequilibrium conditions, whereas the growth proceeds totally diffusionless [33]. Therefore, the sub-unit inherits the chemical composition of the former austenite during growth, thus the bainitic ferrite is supersaturated with carbon. As a consequence of the high transformation temperatures (200-550°C), much of the excess carbon partitions in the remaining austenite after the phase transformation [37]. Some carbon still remains within the bainitic ferrite, either trapped at dislocations, defects or in solid solution [50,51]. Atomic scale observation of the bainite transformation by means of X-ray diffraction (XRD) and atom probe tomography (APT) in a Fe-1C-1.5Si-1.9Mn-0.3Mo-1.26Cr (wt.-%) alloy revealed that the carbon concentration in the bainitic ferrite is far away from equilibrium and paraequilibrium concentrations [51–54]. These investigations showed that the carbon concentration in bainitic ferrite increases with decreasing transformation temperature because of the lower diffusivity of the carbon at low temperatures.

In contrast to the remaining carbon in bainitic ferrite, the enrichment of austenite with carbon leads either to carbide precipitation or to the chemical stabilization of the austenite. The latter implies that the transformation from austenite to bainite does not proceed completely because of the carbon enrichment in austenite. This behaviour is known as “incomplete transformation phenomenon” and will be elucidated in the following section.

### **2.2.3.2. Incomplete transformation phenomenon**

During isothermal transformation below the bainite start temperature ( $B_s$ ), the austenite decomposes into bainitic ferrite whereas the maximum degree of reaction increases from zero at  $B_s$  to some other finite value below  $B_s$ , which is always a smaller amount than would be expected from an application of the lever rule to the equilibrium or paraequilibrium phase diagram [55]. This effect is termed the **incomplete transformation phenomenon (ICT)** [37,56]. The nature of the incomplete transformation phenomenon is still in dispute in literature [18,56–61].

Bradley and Aaronson [17] relate the ICT to a solute drag-like effect (SDLE), which states that the concentration of substitutional alloying elements, which have a strong interaction with carbon, increases at a migrating ferrite/austenite interface. This may

lead to a decrease of the carbon activity in austenite which is in direct contact with the interfaces, which in turn decrease the activity gradient of carbon in front of the interface and cause sluggish transformation kinetics [60]. This SDLE theory was adopted by Reynolds et al. [62] and Goldenstein and Aaronson [63] to explain the ICT phenomena observed in several high-purity ternary alloys, e.g. Fe–C–Mo, Fe–C–Mn and Fe–C–Cr.

Bhadeshia and Edmonds [37] explained the ICT by adapting the T<sub>0</sub>-concept firstly postulated by Zener [36]. The T<sub>0</sub>-temperature is defined as the temperature, where austenite and ferrite of the same composition have the same Gibbs free energy. The plot of temperature versus carbon concentration, where austenite and ferrite of the same chemical composition also have identical free energies represents the T<sub>0</sub> curve, as shown in **Figure 2.10**. Any austenite with a carbon concentration in excess of that defined by the T<sub>0</sub> curve, cannot transform without a change in composition between the parent and product phase. Thus, any diffusionless transformation involving a supersaturation of carbon can only occur below the appropriate T<sub>0</sub> temperature. The T<sub>0</sub> concept also accounts the fact that during the growth of bainite, untransformed austenite continuously absorbs carbon rejected from supersaturated bainitic ferrite [60]. Consequently, the actual T<sub>0</sub> temperature is decreasing, thus eventually a certain point would be reached where diffusionless formation of bainite is thermodynamically impossible.

Bhadeshia and Edmonds [1] inherited the diffusionless view of bainite formation and demonstrated Zener's theory in an Fe–C–Mn–Si alloy, showing that the carbon concentration limits in austenite, measured by X-ray diffraction, were in good agreement with T<sub>0</sub> line, although some data exceeded T<sub>0</sub> curve by 0.2–0.4wt.-%. In a subsequent article Bhadeshia [33] estimated that there is a strain energy of 400 Jmol<sup>-1</sup> associated with diffusionless growth of bainite, thus proposed a new limit T<sub>0</sub>' that is in essence similar to T<sub>0</sub> but takes into account the strain energy, **Figure 2.10**. Recently studies by Caballero et al. [61,64], regarding the ICT in Fe–C–Si–Mn alloys, also showed that the carbon concentrations in retained austenite also fits to the limits given by T<sub>0</sub> and T<sub>0</sub>'. This fact is taken as new experimental evidence that ICT is a manifestation of diffusionless formation of bainite.

Xia et al. [60] investigated the ICT in a series of low C (<0.15wt.-%), low Si (<0.1wt.-%) alloys with varying Mo content (0–1wt.-%). The addition of Mo (>0.3wt.-%) in these alloys leads to a stasis in the bainitic phase transformation during isothermal holding. Furthermore, they measured the carbon content in austenite in the stasis stage by means of electron probe microanalysis (EPMA) and found that the carbon concentration in austenite is 0.1–0.2wt.-%, lower than expected from

the T0' curve, by increasing the Mo content up to 1 wt.-%. This difference in the carbon concentration equals to an additional undercooling in a temperature range of 15-30°C which is necessary for further transformation.

A consequence of the ICT is the stabilization of austenite, hence retained austenite can be observed at room temperature in forms of blocks and films [2]. It has been observed that the thickness of austenite films can be estimated by assuming that the carbon diffusion field around an existing sub-unit prevents the close approach of another parallel plate [65]. This is because the regions of austenite with the highest carbon concentration are unable to transform to bainite. This theory predicts a dependence of film thickness on the bainite plate thickness since the net quantity of carbon partitioned into the austenite must increase with the thickness of the bainite plate. Conversely, retained austenite blocks are observed between sheaves of bainite.

Application of the lever rule allows the estimation of the maximum fraction of bainite ( $V_{\alpha_b}^{max}$ ) [66]:

$$V_{\alpha_b}^{max} = \frac{c_{T0} - \bar{c}}{c_{T0} - c_{\alpha_b}} \quad (2)$$

where  $c_{T0}$  is the carbon content given by the T0 curve,  $\bar{c}$  is the nominal carbon content of the alloy and  $c_{\alpha_b}$  is the carbon concentration of the bainitic ferrite after partitioning.

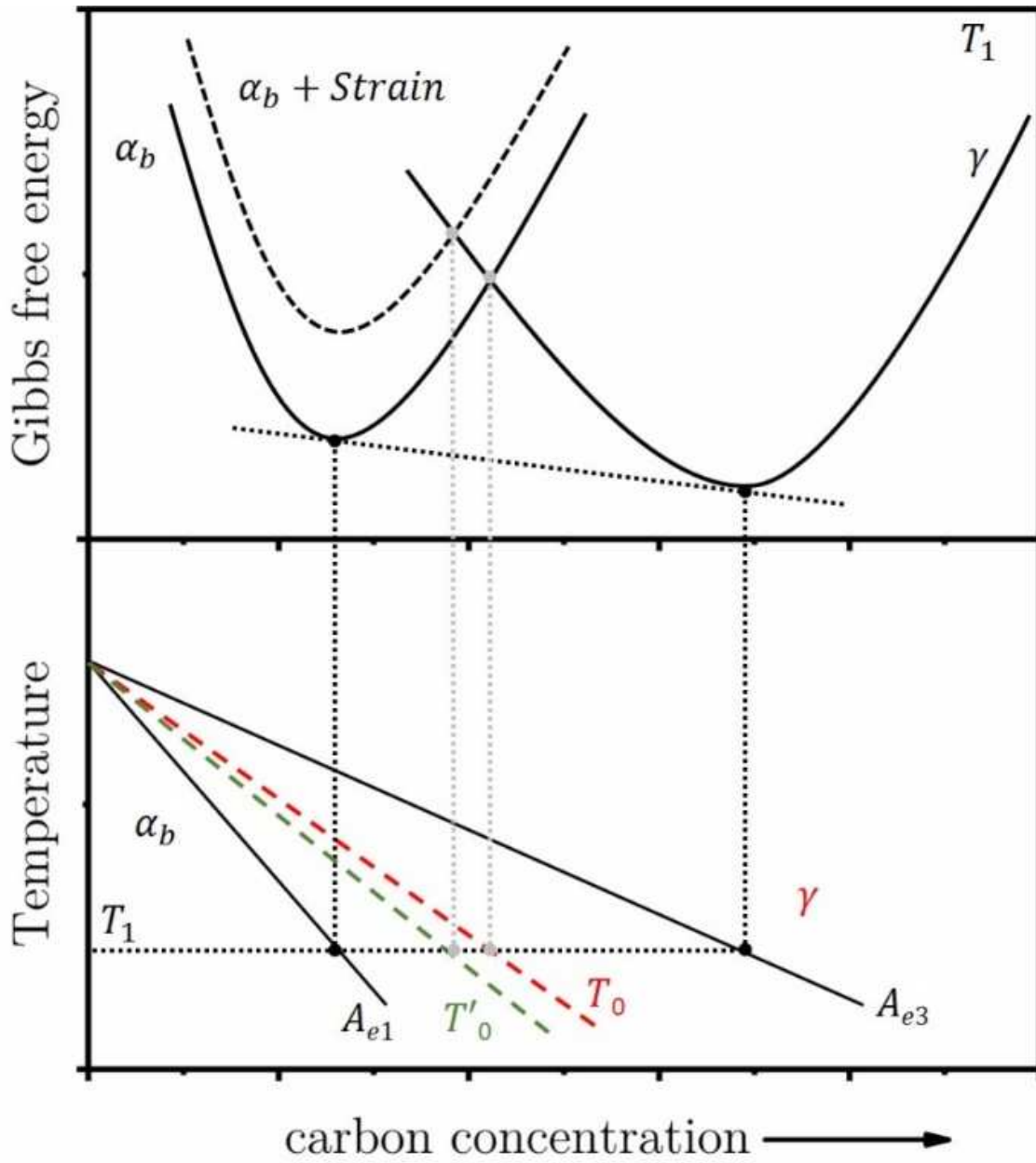


Figure 2.10: Schematic illustration of the  $T_0$  and  $T_0'$  at a certain temperature  $T_1$ . The  $T_0'$  curve also accounts the strain energy due to the displacive transformation of austenite ( $\gamma$ ) to bainitic ferrite ( $\alpha_b$ ).  $A_{e1}$  and  $A_{e3}$  denote the lower and upper limit of the  $\alpha_b + \gamma$  phase field at equilibrium conditions.



### 2.2.3.3. Stability of retained austenite

The previous chapter has shown that carbon enrichment of austenite leads to the chemical stabilization of austenite and no further bainitic transformation is observed. This phenomenon is very prominent in steels containing high amounts of silicon (>1.5wt.%). In these steel types, the precipitation of cementite is retarded due to the low solubility of silicon in cementite. Consequentially, it is possible to achieve a microstructure which is only built up of bainitic ferrite and retained austenite [2,3]. However, the stability of retained austenite can be considered in two different ways, the mechanical and thermal stability.

The mechanical stability of retained austenite depends on chemical composition (especially the carbon and manganese content) [67–69], retained austenite grain size and its crystallographic orientation with respect to the loading direction and the morphology [70–72]. As already mentioned in the previous chapter, retained austenite typically exhibits film or block morphologies. Both morphologies are enriched in carbon, but films are stronger enriched due to their geometrical isolation between bainitic ferrite sub-units [72]. The low carbon enriched blocky austenite tends to decompose in the early stages of plastic deformation into untempered martensite which is detrimental to the toughness of a steel. Contrary, austenite films which have a higher carbon content are much more stable and remain untransformed until the later stages of deformation [55]. Additionally, a composite microstructure of bainitic ferrite and film like retained austenite is beneficial to both strength and toughness. In such a microstructure, a possible crack has to traverse interphase interfaces as well as different crystal structures. Furthermore, the motion of the crack would be damped by the enhanced deformation in the softer austenite and perhaps by local phase transformation of the austenite which reduces local stress concentrations. Bhadeshia and Edmonds [3] have established that the ratio of films to blocky austenite should be large and exceed a value about 0.9 for optimum toughness properties:

$$\frac{V_{\gamma-f}}{V_{\gamma-B}} = \frac{V_{\gamma-f} V_{\alpha_b}}{V_{\gamma} - V_{\gamma-f} V_{\alpha_b}} > 0.9 \quad (3)$$

where  $V_{\alpha_b}$ ,  $V_{\gamma-f}$ ,  $V_{\gamma-B}$  and  $V_{\gamma}$  are the volume fractions of bainitic ferrite film type retained austenite, blocky retained austenite and the overall amount of retained austenite, respectively.

The overall carbon content of retained austenite  $c_\gamma$  can be estimated, as presented in [2]:

$$c_\gamma = \bar{c} + \frac{V_{\alpha_b}(\bar{c} - c_{\alpha_b})}{1 - V_{\alpha_b}} \quad (4)$$

The thermal stability of retained austenite is mainly related to the steel composition, especially to the carbon content [73,74]. The carbon content in retained austenite can have opposite effects on the thermal stability during reheating. Conversely, the driving force for cementite precipitation increases with the carbon content of austenite, which can result in a higher instability of retained austenite during reheating [67,69]. In general, retained austenite transforms into mixtures of ferrite and carbides in a temperature range of 200°C to 300°C [75]. The activation energy for this process is about 115 kJmol<sup>-1</sup> [76], which is consistent with the activation energy for the diffusion of carbon in austenite [77].

#### 2.2.3.4. Upper & lower bainite

It is reported in literature that the bainitic reaction can also be accompanied by the precipitation of carbides, as long as no alloying elements are present that retard carbide precipitation, e.g. silicon. The resulting microstructure consist of a non-lamellar mixture of bainitic ferrite plates and carbides and can be further classified into upper and lower bainite [31]. The essential difference between them is the nature of the carbide precipitation.

The bainitic ferrite sub-units in upper bainite are free of precipitates, and the precipitation of carbides occurs from carbon-enriched austenite. The most common carbide is cementite and the precipitation become possible when the carbon concentration in austenite exceeds the solubility limit given by the extrapolated  $\gamma/(\gamma + \theta)$  phase boundary, where  $\theta$  denotes cementite. This is schematically shown in **Figure 2.11**; the shaded area represents an expanded  $(\gamma + \theta)$  phase field where the precipitation of cementite from carbon enriched austenite is possible. Consequently, if there are no kinetic hindrances, carbide precipitation will accompany the growth of upper bainite if the transformation temperature is below  $T_C$  [31], see **Figure 2.11**.

Lower bainite is obtained by transformation at very low temperatures (200-350°C), whereas upper bainite is obtained at substantially higher temperatures (350-550°C). As a result of the lower transformation temperatures, the diffusion of solutes is reduced in lower bainite and therefore some of the carbon precipitates within the

bainitic ferrite sub-unit [64]. Further transformation also leads to diffusion of excess carbon from bainitic ferrite to austenite. Consequentially, carbide precipitation also occurs from carbon-enriched austenite. Therefore, Matas and Hehemann [78] proposed that the difference between upper and lower bainite comes from a competition between the rate at which carbides can precipitate from bainitic ferrite and the speed of carbon partitioning from supersaturated ferrite into austenite. This behaviour was quantitatively investigated by Takahashi and Bhadeshia [48], where they compared the time required to decarburize a supersaturated bainitic sub-unit against the cementite precipitation kinetics. **Figure 2.12** illustrates the transition from upper to lower bainite according the findings by Takahashi and Bhadeshia.

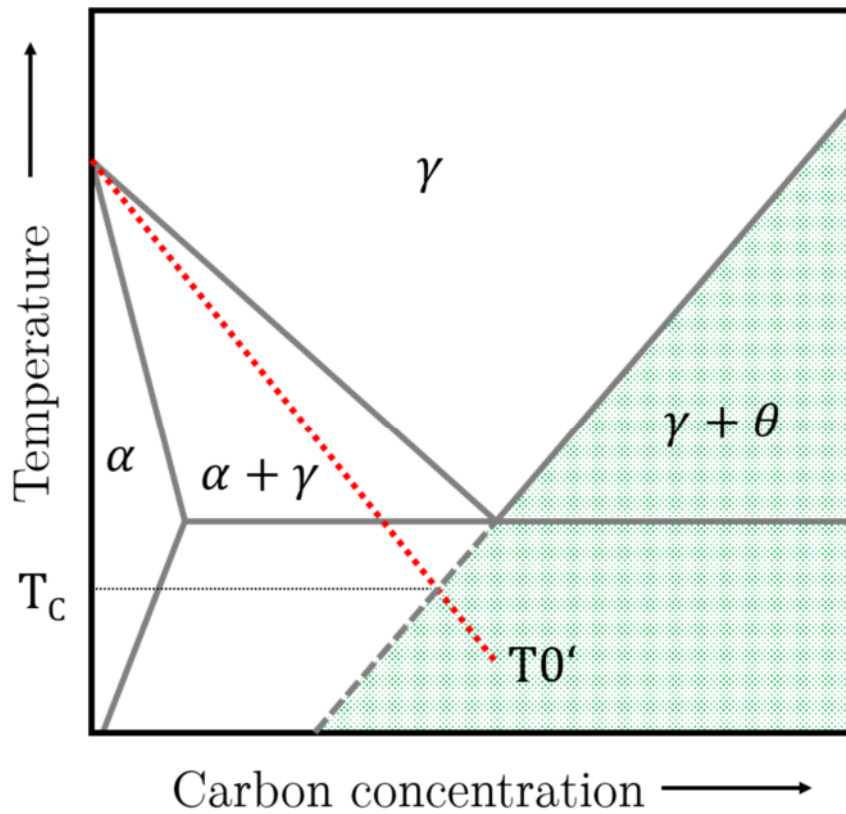


Figure 2.11: Schematic illustration of the thermodynamic condition that must be satisfied before cementite can precipitate from austenite.

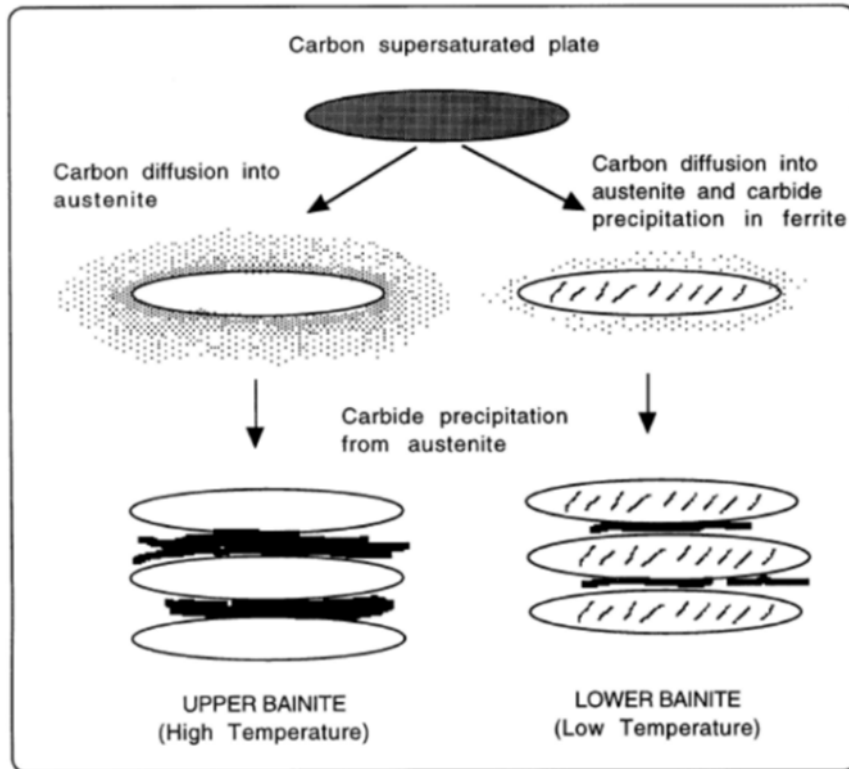


Figure 2.12: Schematic representation of the transition from upper to lower bainite, after Takashi and Bhadeshia [48].

### 2.2.3.5. Granular bainite

During the early 1950s, light microscopy investigations on continuously cooled low-carbon ( $<0.3\text{wt.}\%$ ) steels showed a microstructure which consists of coarse ferrite plates together with retained austenite and martensite on an optical scale [79,80], **Figure 2.13a**. This microstructure was called granular bainite. TEM examination of this microstructure revealed that the coarse ferrite plates referred to earlier do not exist. They are in fact sheaves of bainitic ferrite with films of retained austenite between the bainitic ferrite sub-units [81,82], **Figure 2.13b**. A characteristic feature of granular bainite is the lack of carbides in the microstructure [83]. Due to the slow cooling conditions carbon partitions from the supersaturated bainitic ferrite into the adjacent austenite and stabilises them, so that the final microstructure contains retained austenite and some regions of so-called martensite/austenite (M/A) constituents. Mazancova and Mazanec [84] pointed out that the formation of M/A constituents is typical for slow continuous cooling conditions ( $<10^\circ\text{C}\text{s}^{-1}$ ) and high transformation temperatures ( $\sim 500^\circ\text{C}$ ). Under these circumstances, carbon gradients in aus-

tenite can be reduced relatively quickly; carbon diffusion can occur over wider distances and the final mean carbon content of the retained austenite blocks ranges above the critical concentration given by the  $T_0'$ -line [33]. Consequently, these blocks do not transform into bainite but decompose partially into martensite during further cooling. The presence of retained austenite also reveals the incomplete transformation phenomenon in granular bainite. Additionally, the degree of transformation from austenite to granular bainite is found to depend on the undercooling below the bainite-start temperature [80,83]. This fact indicates that granular bainite is not different from isothermal formed bainite in its mechanism of transformation. The unusual morphology is only a consequence of the continuous cooling conditions and low carbon concentrations.

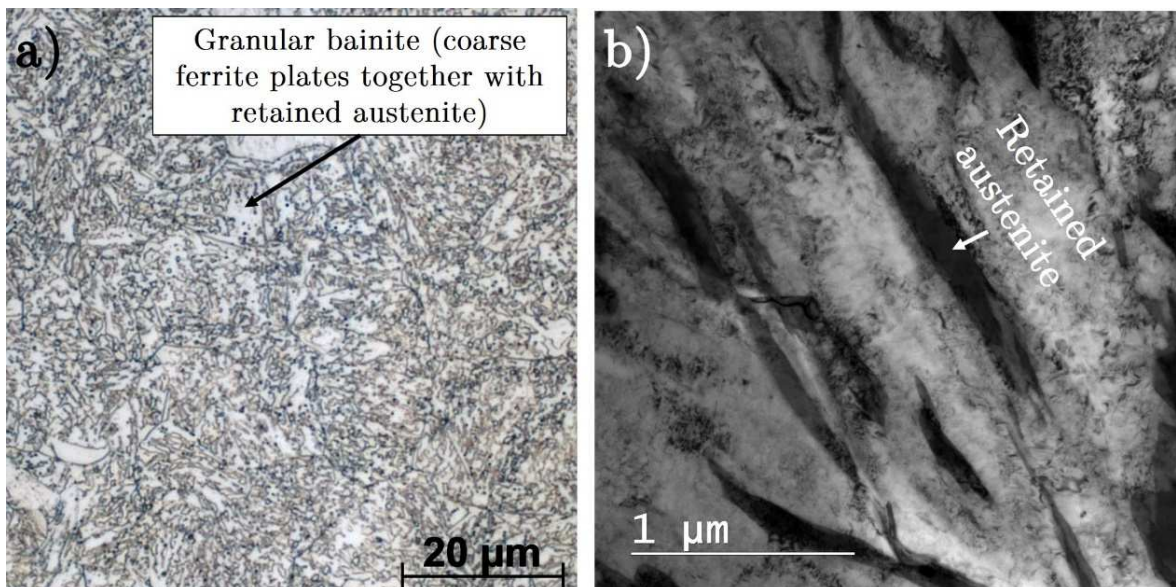


Figure 2.13: Representative images of granular bainite after cooling with 0.75K/s from the current thesis, a) light micrograph after etching with Nital for 3 seconds, b) TEM bright field image showing retained austenite (black) between bainitic ferrite subunits.

#### 2.2.4. Martensite

The quenching of austenite to room temperature can lead to the formation of martensite. As a consequence of the rapid cooling conditions, martensite inherits the chemical composition of the former austenite, where also the carbon remains in solid solution. Therefore, the transformation causes a shape change, consisting a large shear

and volume expansion, as already mentioned for displacive transformations in previous sections. The martensite reaction in steels normally occurs athermally, thus the degree of transformation depends on the undercooling below the martensite start temperature ( $M_s$ ), as expressed exemplarily by the Koistinen and Marburger equation [85]:

$$V_{\alpha'} = 1 - \exp[\beta(M_s - T_q)] \quad (5)$$

where  $V_{\alpha'}$  is the phase fraction of martensite,  $T_q$  denotes the quenching temperature below  $M_s$  and  $\beta$  is a dimensionless fitting constant and equals to -0.011. The nucleation of martensite in steels is believed to begin at structural imperfections in the parent austenite, such as arrays of dislocations [31]. Olsen and Cohen [86–88] assumed that these pre-existing dislocations dissociate into suitable partial dislocations during undercooling from  $M_s$  and that would lead to the nucleation of martensite. However, Khan and Bhadeshia [89] found that the initial number density of pre-existing defects typically found in austenite is not large enough to explain the kinetics of the martensitic transformation. The extra defects necessary to account for the fast transformation rates stem from autocatalysis of the martensite plates themselves, they induce new embryos which are then available for further transformation [90,91], **Figure 2.14**.



**Figure 2.14:** Martensitic microstructure of a Fe-1.8C (wt.-%) after solution annealing at 1200°C for 30 min and subsequent quenching in an iced brine to room temperature. The inset shows the autocatalysis of new martensitic side plates from a primary martensite plate [91].

## 3 Tempering and precipitation hardening in steels containing a bainitic microstructure

### 3.1 General Aspects on tempering

Tempering is a term historically associated with a heat treatment of martensite in steels. It describes how the microstructure and mechanical properties change as the metastable sample is reheated and held isothermally at a temperature lower than the austenitizing temperature ( $A_{c1}$ ) [73]. The extent and the rate of change of the microstructure and properties during tempering depend on how far the initial sample deviates from an equilibrium condition.

The mechanism associated with the structural changes produced by tempering a martensitic microstructure can be grouped into five stages [92–99]:

- Stage 0: (0-80°C) Redistribution of carbon atoms in the martensitic matrix leads to segregation of carbon to lattice defects or to the formation of randomly distributed carbon clusters
- Stage I: (80-250°C): Precipitation of non-stoichiometric  $\epsilon$  (steels containing <0.2 wt.-% carbon) or  $\eta$  (steels containing >0.2 wt.-% carbon) transition carbides.
- Stage II (250°C-420°C): Diffusion of carbon from martensite into retained austenite as well as decomposition of retained austenite into ferrite and cementite.
- Stage III (420°C-500°C): Replacement of transition carbides by cementite.
- Stage IV (500-700°C): Coarsening of cementite and secondary hardening due to precipitation of alloy carbides.

In fact, this classification is idealised. Some of these reactions ascribed before can occur simultaneously, especially when the martensite start temperature of a steel grade is relatively high. This phenomenon is known as auto-tempering. The bainitic transformation generally happens at even higher temperatures than the martensitic reaction. Consequentially, auto-tempering becomes an unavoidable part of the bainitic reaction. The redistribution of carbon from supersaturated bainitic ferrite into austenite and the precipitation of cementite during the bainitic reaction occur rapidly and are genuine auto-tempering effects [73]. **Figure 3.1** gives an overview of the different tempering phenomena that may occur in an alloyed bainitic microstructure.

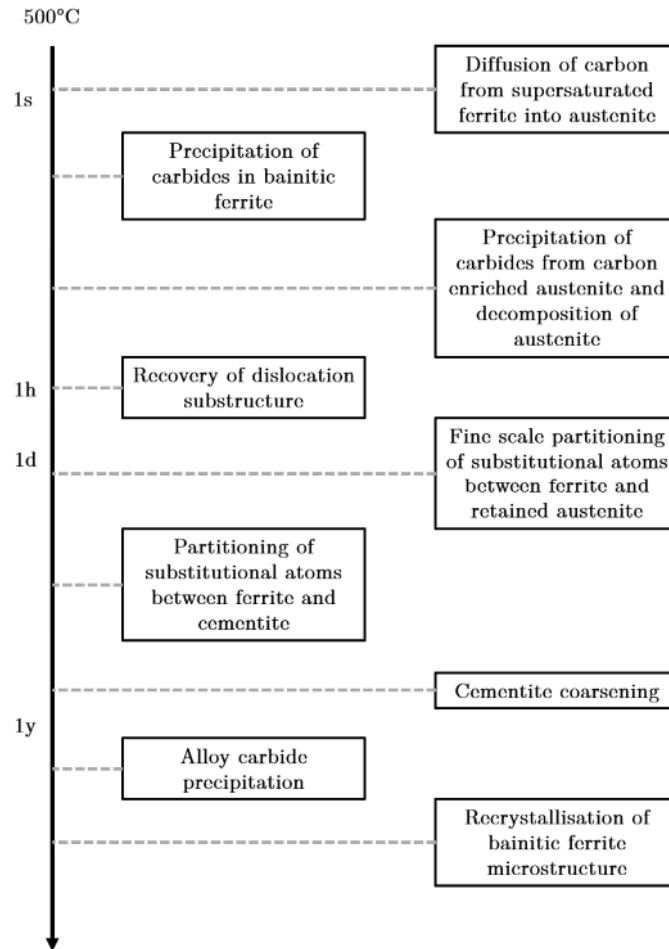


Figure 3.1: Time scale of the tempering phenomena that may occur in an alloyed bainite at an isothermal heat treatment of 500°C taken from ref. [73].

Unlike martensite, bainitic ferrite usually contains only low amounts of excess carbon in solid solution. The carbon in bainite is mostly trapped in coarse carbides or in retained austenite.

In the case of retained austenite, tempering only leads to further transformation when the carbon concentration in austenite is lower than given by the  $T_0'$  limit. If this condition is not satisfied, further transformation only occurs by a mechanism involving the diffusion of carbon in austenite. Subsequently, the austenite can decompose into a mixture of ferrite and cementite when the carbon concentration in austenite exceeds the extrapolated  $\gamma/(\gamma + \theta)$  phase boundary. The block-like austenite then tends to form colonies of pearlite with a fine interlamellar spacing, whereas the



films of austenite decompose into discrete particles of cementite in a matrix of ferrite [31,67,69], see **Figure 3.2**.

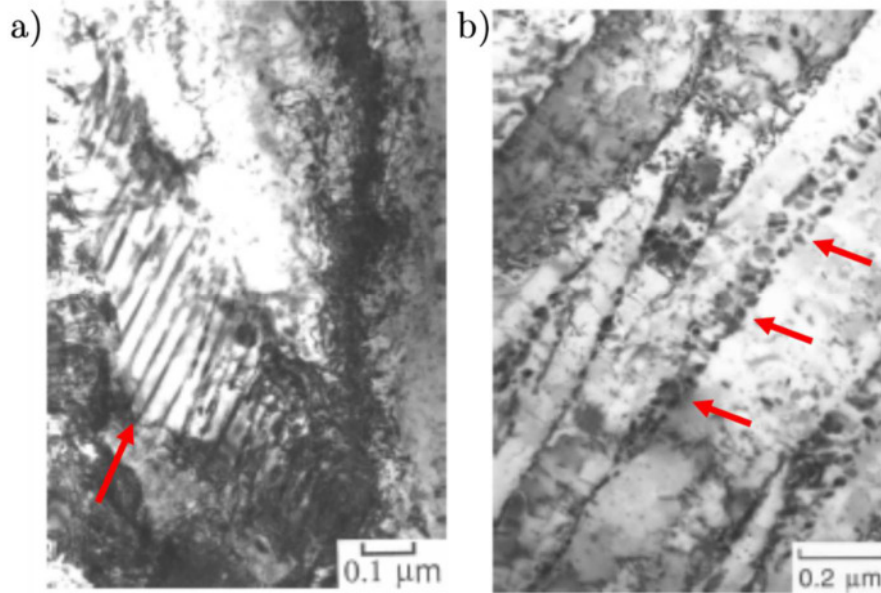


**Figure 3.2:** TEM micrograph illustration the tempering effect of a mixture of bainitic ferrite and retained austenite in a Fe-3Mn-2Si-0.4C (wt.-%) alloy after isothermal holding at 500°C for 60 min. a) former retained austenite blocks form colonies of pearlite, b) retained austenite film decomposes into arrays of discrete cementite particles between the bainitic sub-units. The red arrows indicate the cementite particles.

### 3.2 Precipitation hardening

The contributions to the yield strength ( $\sigma_y$ ) of bainite can be factorised into different factors [44,100]:

$$\sigma_y = \sigma_{Fe} + \sum_i \sigma_{ss,i} + \frac{K_L}{\bar{L}} + K_D \sqrt{\rho_D} + \frac{K_P}{\Delta l} \quad (6)$$

where  $K_L$ ,  $K_D$ , and  $K_P$  are constants,  $\sigma_{Fe}$  is the strength of pure annealed iron,  $\sigma_{ss,i}$  is the solid solution strengthening due to solute “ $i$ ”,  $\bar{L}$  is a measure of the bainitic ferrite plate size,  $\rho_D$  is the dislocation density and  $\Delta l$  represents the distance between oxide or carbide particles.

The strengthening effect due to carbide particles is also known as precipitation hardening or secondary hardening. Precipitation hardening occurs in steels containing

strong carbide forming elements like Cr, V, Mo, W and Nb. The formation of these alloy carbides involves the long range diffusion of substitutional atoms and their precipitation is consequently sluggish [73]. Therefore, precipitation hardening takes place at temperatures higher than 500°C. The formation of these more stable alloy carbides is accompanied by the dissolution of the existing metastable precipitates, such as cementite.

According [101], the nucleation mechanism of alloy carbides is classified into two categories: (1) in-situ transformation, and (2) separate nucleation. In the first case, alloy carbides nucleate at the same position as the existing metastable carbides e.g. cementite, and the hardening effect is reduced because the distribution of the nucleating carbides is dominated by that of the existing ones. In the second case, alloy carbides nucleate independently of the metastable carbides on lattice defects, such as dislocations and may produce a substantial hardening effect if the precipitates are coherent with the matrix [101].

The strengthening effect of alloy carbides results from a shear mechanism induced by a dislocation. The deformation of the carbide leads to an increase in the interfacial energy, whereas a passage of a dislocation through a particle may produce an anti-phase boundary with an associated disordering energy, or may produce a stacking fault energy [102]. The latter effect would naturally require the stacking fault energy in the particles to be significantly different from that of the matrix and must consider the changes in the width of the stacking fault from the matrix to the particle.

### 3.3 Carbide precipitation in Fe-C-Mo steels

Regarding the chemical composition of the investigated steel in this thesis, the current chapter will elucidate the essential carbides that occur in ternary Fe-C-Mo systems. In the following ‘M’ denotes the metallic components and ‘X’ denotes the interstitial element of the carbides.

#### I $M_3X$

The metastable carbide cementite forms first during or after the bainitic reaction by a paraequilibrium mechanism. Cementite has an orthorhombic  $M_3X$  crystal structure, with typical lattice parameters  $a=4.5241 \text{ \AA}$ ,  $b=5.0883 \text{ \AA}$  and  $c=6.7416 \text{ \AA}$ .

During the paraequilibrium precipitation, cementite inherits the chemical composition of the parent phase. Afterwards, cementite changes its chemical composition by exchanging solutes with the surrounding matrix to reach an orthoequilibrium concentration. Mn and Cr can dissolve into cementite in large quantities, whereas W, V,

and Mo have limited solubility in cementite [103]. The rate of enrichment will be fastest when the cementite particles are small and the ferrite is highly supersaturated in carbide-forming solute atoms [73]. Cementite, although kinetically favoured, is less stable than many alloy carbides [101]; consequently, while the cementite composition changes, alloy carbide precipitation starts and eventually leads to the dissolution of the cementite.

## II $M_2X$

In many cases,  $M_2X$  forms after the precipitation of cementite. It has a hexagonal crystal structure with lattice parameters of  $a=3.002 \text{ \AA}$  and  $c=4.724 \text{ \AA}$ . It is generally considered to nucleate on matrix dislocations or on an ferrite/cementite interface [104].

The composition of  $M_2X$  can vary with Mo, Cr, and V because of their high solubility. In steels containing Mo, with no N and low Cr contents,  $M_2X$  is often close to the equilibrium composition of  $Mo_2C$

In alloys containing a large amount ( $> 3 \text{ wt.-%}$ ) of Mo, precipitation of fine needle-shaped  $Mo_2C$  is observed just after the onset of secondary hardening [104]. On the other hand, in normal high-strength low-alloy (HSLA) steels, where the Mo content does not exceed  $1 \text{ wt.-%}$ , it was generally difficult to observe the precipitation of alloy carbides before or at the peak hardening stage [101]. When the steels were overaged, also needle-shaped  $Mo_2C$  was observed [105]. There is a well-defined orientation relationship between  $Mo_2C$  and the matrix according the findings by Pitsch and Schrader [106]:

$$\{0001\}_{M_2X} // \{011\}_\alpha \text{ and } \langle 11\bar{2}0 \rangle_{M_2X} // \langle 100 \rangle_\alpha$$

The spacing between Mo and Fe atoms in the preferred growth direction shows only a lattice mismatch of 4.5%.

## III $M_6X$

In steels containing Mo and relatively low levels of Cr,  $M_6X$  is thought to be the equilibrium carbide. It has a face-centred-cubic crystal structure with a lattice parameter  $a = 11.04 \text{ \AA}$ . In Mo-rich steels, the equilibrium composition lies between  $Fe_3Mo_3C$  and  $Fe_4Mo_2C$ .

$M_6C$  precipitates on the grain boundaries; therefore, it is thought that it nucleates separately from  $M_2X$ .

### 3.4 Numerical Simulation of precipitation kinetics using MatCalc

The term precipitation implies that a new phase grows on the expense of an existing one. These precipitates are very small particles (few nanometers to few micrometers) compared to the parent phase (matrix phase).

In general, precipitation occurs when the number of alloying elements exceeds the equilibrium solubility limit of elements in an alloying system. Beside the chemical composition of the matrix phase and the temperature where the precipitation process takes place, also the time for precipitation plays an important role. The precipitation process can be divided into three different stages, compare for instance [107]:

- **Nucleation:** The initial stages in precipitate life. Stochastic process controlled by local thermal and compositional fluctuations
- **Growth:** Controlled attachment of atoms to the precipitate. Deterministic process controlled by chemical and/or mechanical driving forces.
- **Coarsening** Dissolution of small precipitates in favour of larger ones. Driven by curvature-induced pressure, also called the Gibbs-Thomson effect.

MatCalc [108–110] is a thermo-kinetic software package developed by Ernst Kozeschnik for a various kinds of thermodynamic and kinetic simulations. An overview of the models embedded into the software package can be found within [111]. MatCalc is a simulation tool which can be summarized as a mean-field treatment of nucleation, growth and coarsening process of precipitates. It allows simulations in multi-component, multi-phase and multi particle systems. The concept behind is based on the Onsager thermodynamic extremal principle [112], assuming that a thermodynamic system selects the specific kinetic path, where maximum entropy is produced. Svoboda et al. [108] depicted the theory behind, whereas the numerical implementation in MatCalc was done by Kozeschnik et al. [109]. The basis for all thermodynamic calculations are chemical potentials and diffusivities of the involved alloying elements, which are taken from CALPHAD type databases [113]. All thermodynamic as well as thermo-kinetic simulations in the present thesis were performed with the software package MatCalc (V.6.01. rel. 0.003; <http://matcalc.at>) and the thermodynamic database ‘mc\_fe’ [114].

## 4 Investigated material and setup of experiments

In this chapter, the investigated material as well as the experimental approaches and devices will be presented.

### 4.1 Investigated Material

The chemical composition of the investigated alloy in the present thesis is given in **Table 4.1**. The raw material was prepared as a 7500kg vacuum induction melt by the Deutsche Edelstahlwerke GmbH (DEW). After melting, block casting of three ingots à 2500kg was performed. These ingots in form of 256x256x4000mm square bars were hot-rolled to rods with  $\varnothing 28$ mm, followed by a soft annealing heat treatment. A schematic time-temperature profile including the hot rolling and soft annealing process is shown in **Figure 4.1**. For the investigations presented in this thesis, all samples were taken from soft annealed rods with  $\varnothing 28$ mm.

**Table 4.1:** Chemical composition of the investigated bainitic steel in wt.-%.

C	Si	Mn	Cr	Ni	Mo	V	Fe
0.28	0.27	0.32	0.43	0.11	2.82	0.39	bal.

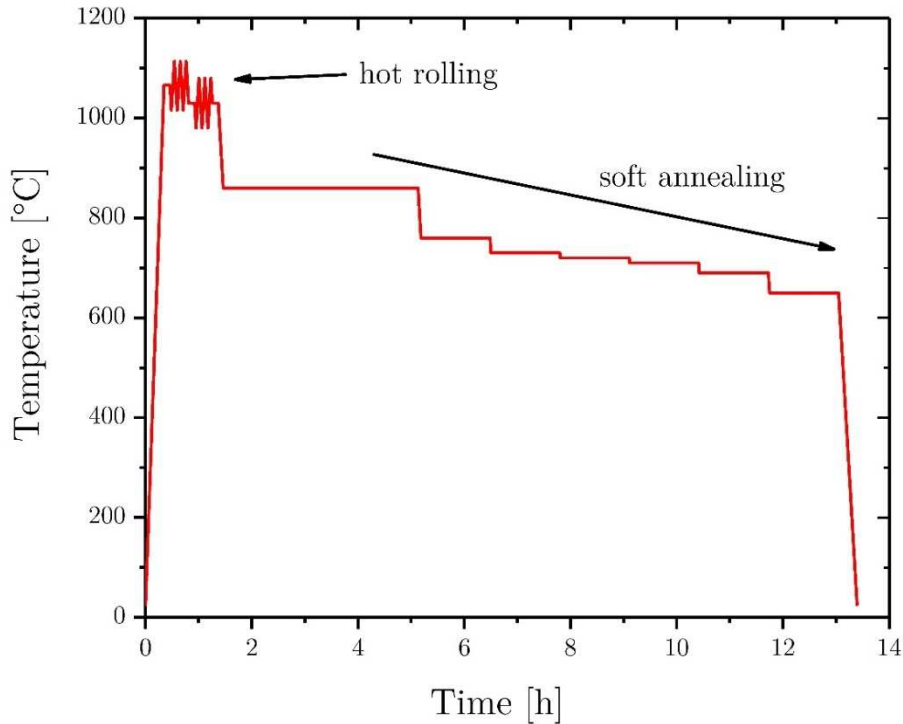


**Figure 4.1:** Schematic time-temperature profile of hot rolling and soft annealing for the investigated steel.

## 4.2 Heat treatment experiments using dilatometry

Dilatometry is a thermo-analytical measurement method for determining dimensional changes (expansion/contraction) of steel samples during a specific time-temperature cycle. The dimensional changes during heating or cooling allow insights on the phase transformation behaviour in steels. In the present study push-rod dilatometers are used where the samples were held between two quartz push-rods, one of the rods being fixed and the other connected to a linear voltage differential transducer. Samples were heated by an induction coil whereas cooling was done by gas (nitrogen) injection. During the measurements, the sample temperature was measured with a type S thermocouple. For all experiment's cylindrical samples with dimensions  $\text{Ø}4 \times 10 \text{ mm}$  were machined from the soft annealed rods. In order to make all results comparable and avoid material inhomogeneity's (e.g. segregation), all samples were taken from the half radius of the rod, as shown in **Figure 4.2**.

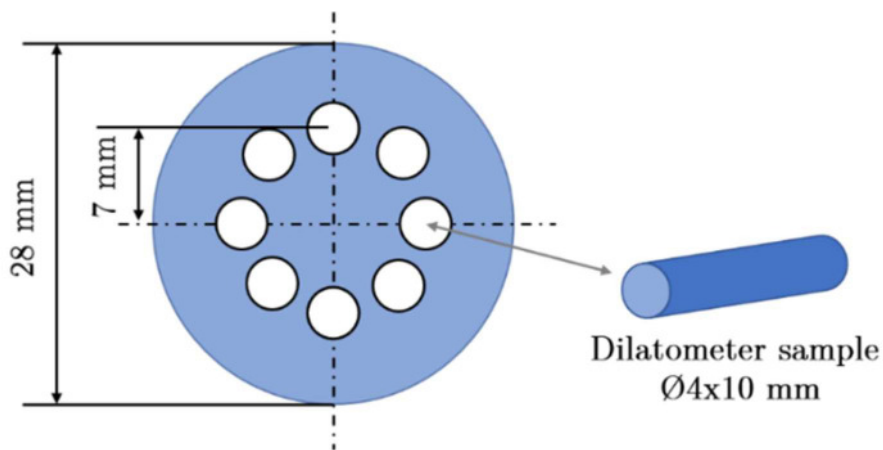


Figure 4.2: Samples for dilatometry experiments were taken from the half radius of the soft annealed rod.

#### 4.2.1. Time-temperature cycles for high-energy X-ray diffraction

To investigate the bainitic transformation during continuous cooling as well as the phase transformations during reheating of the bainitic matrix, time-temperature cycles according to **Figure 4.3** were carried out on a DIL805A/D dilatometer (TA-Instruments). To achieve a homogenous microstructure, samples were austenitized for 30min at 1020°C. To study the bainitic transformation kinetics, different cooling rates between 2°Cs<sup>-1</sup> and 0.43°Cs<sup>-1</sup> to room temperature were applied. After continuous cooling samples were reheated with 0.5°Cs<sup>-1</sup> at a tempering temperature of 620°C. After 30 min, isothermal holding the samples were quenched with approximately 100°Cs<sup>-1</sup> to room temperature.

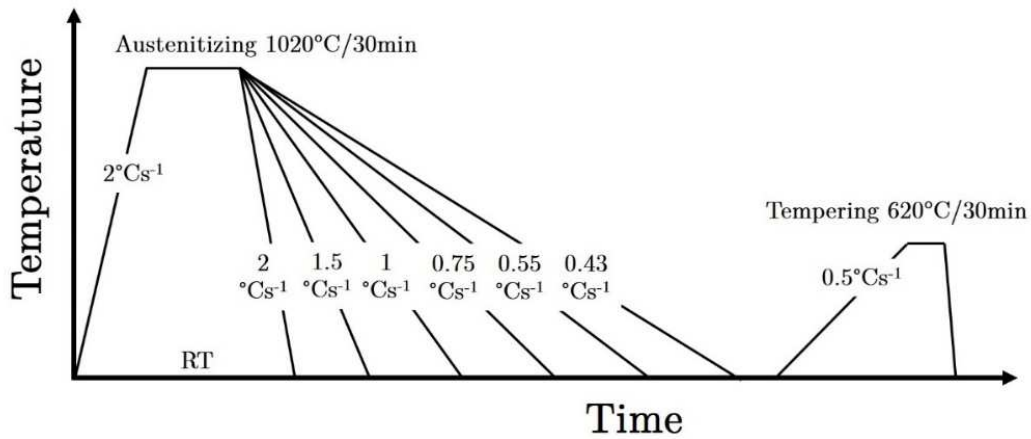


Figure 4.3: Time-temperature cycles for high-energy X-ray diffraction (HEXRD) experiments.

#### 4.2.2. Time-temperature cycles for microstructure observations

To investigate different stages in the bainitic phase transformation, heat treatments were carried out on a TA-instruments DIL805L lab dilatometer. The samples were austenitized for 30 min at 1020°C. After that, the samples were cooled at rates of 2, 0.75 and 0.43°Cs<sup>-1</sup>, to different quenching temperatures  $T_q$  (480, 470, 455, 430, 390°C) where the samples were subsequently quenched to room temperature, as schematically shown in **Figure 4.4a**. In order to investigate the microstructural changes during reheating and tempering, samples after continuous cooling with 2, 0.75 and 0.43°Cs<sup>-1</sup> were reheated to 620°C and tempered for 4h and subsequently cooled with 0.5°Cs<sup>-1</sup>, as shown in **Figure 4.4.b**. During this process, samples were quenched at each half hour to evaluate the evolution of hardness and microstructure.

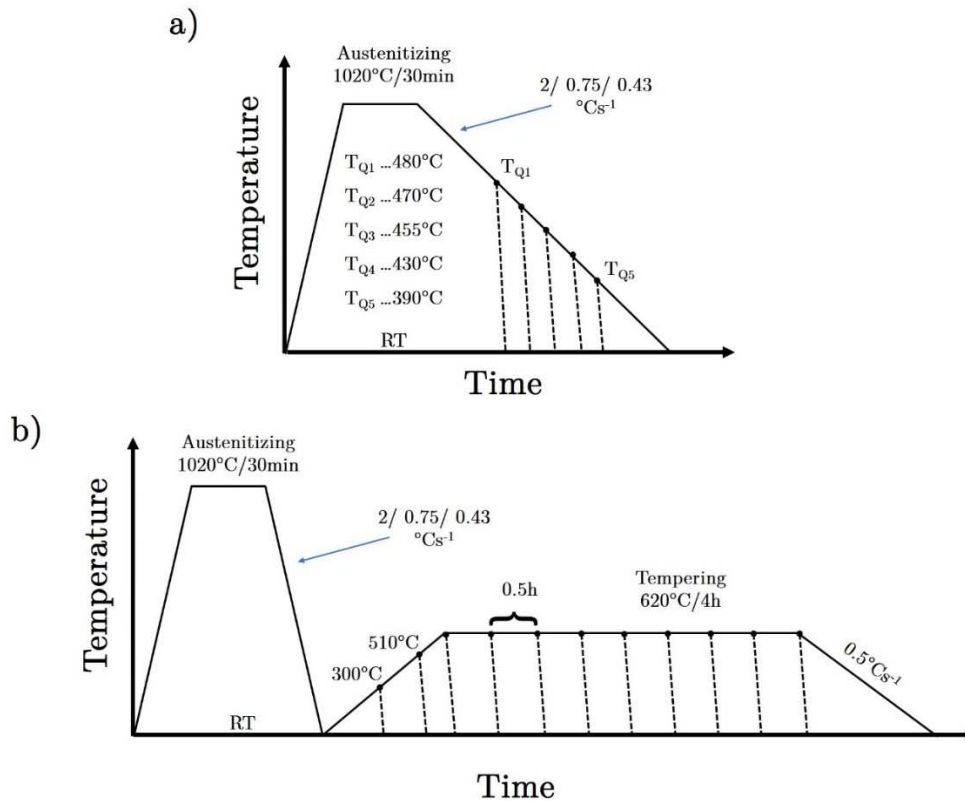


Figure 4.4: Time-temperature cycles for microstructure observations. Quenching experiments during a) the bainitic reaction and b) tempering.

### 4.3 Microstructure characterization methods

In physical metallurgy it is frequently necessary to obtain quantitative measurements of microstructural features to compare experimental observations with theoretical predictions. These may relate to the kinetics of processes such as grain growth, phase transformations or particle coarsening, or to the development of mechanical properties such as strength and toughness [115]. Therefore, a comprehensive set of high-resolution techniques as well as standard metallography techniques were applied on the heat-treated samples for a detailed study of the microstructure.

#### 4.3.1. Quantitative metallography

Quantitative metallography is concerned with the measurement of microstructural features such as grain size and the size and spatial distribution of second phase particles in optical as well as electron microscopy [115]. It should be noted that some systematic errors could arise depending on the specimen preparation (grinding and



etching). Due to the fact that observations are made on random sections of a sample, stereological corrections regarding the volume fraction or dimensions of particles are necessary. A detailed instruction of such stereological corrections are given within [65,115,116].

Nowadays, quantitative measurements are easily obtained using image analysis systems, where the measure of small increments of areas regarding their pixel size is possible. In the present thesis, all recorded images were analysed using the software package Stream Motion from Olympus<sup>TM</sup>.

### 4.3.2. Optical light microscopy

For microstructure observations by means of optical light microscopy, the tested dilatometer samples were sliced along the length axis and hot mounted ( $\sim 180^\circ\text{C}$ ) in a Struers<sup>TM</sup> Ctio-Press20 mounting press using a Struers DuroFast conductive thermo-plastic resin. Afterwards, the samples were grinded using silicon carbide grinding foils with different grits (800 and 1200) followed by polishing with a  $3\mu\text{m}$  and  $1\mu\text{m}$  diamond paste.

For standard microstructure observations, the samples were etched for 3 to 5s using Nital (3ml  $\text{HNO}_3$  in 97ml Ethanol). Additionally, the grain size was determined using the linear intercept method according ASTM E112-96 [117].

Colour etching offers an possibility to distinguish between different phases in steel according their chemical composition, especially on the carbon content [118,119]. Therefore, samples were colour etched using a Klemm1 (2g  $\text{K}_2\text{S}_2\text{O}_5$  in 100ml stock solution of 1000g  $\text{Na}_2\text{S}_2\text{O}_3 \cdot 5\text{H}_2\text{O}$ ) etchant after the polishing step. A detailed instruction for the colour etching procedure for the present alloy is given within **Paper A.1** in **Appendix A**. All microstructure investigations were carried out on an Olympus<sup>TM</sup> BX51 light microscope.

### 4.3.3. Scanning electron microscopy

In scanning electron microscopy (SEM) a high-energy electron beam, up to 25keV, is used for investigations. This high electron energy leads to a short wavelength of the electrons and therefore to a high spatial resolution of approximately 10nm. The examination can yield information about the topography (surface features of an object), morphology, composition and crystallographic information.

In the present thesis, SEM was used for a detailed examination of the bainitic microstructure after continuous cooling. To this end, the Nital etched samples as described above were transferred into a Zeiss<sup>TM</sup> AURIGA-CrossBeam-Workstation

equipped with a field emission gun. SEM micrographs were performed using 10kV accelerating voltage at a working distance of 10mm.

#### 4.3.4. Electron back scatter diffraction

Electron backscatter diffraction (EBSD) is a special enhancement of the SEM. The EBSD technique involves understanding the structure, crystal orientation and phase of materials observed via SEM. Typically it is used to explore microstructures, revealing texture, defects, grain orientation and morphology.

The operating principle of EBSD is comparable to conventional SEM. An incident electron beam (primary beam) is focused on a rotated sample ( $\sim 70^\circ$  normal to sample surface) and interacts with the electrons of the surface atoms. This interaction leads to a certain excitation volume, which depends on the accelerating voltage of the primary beam, the atomic number of elements and the density of the phases in the sample.

In general, the incident beam is elastically scattered on the sample surface. When the primary beam interacts with the crystal lattice, electrons with roughly the same energy as the primary beam are scattered. If these back scattered electrons fulfil Bragg's law (7), constructive interference follows and the electrons will be collected on a phosphorus screen (EBSD detector).

$$2d_{hkl} \sin \theta = n\lambda \quad (7)$$

In equation (7)  $d_{hkl}$  represents the spacing between two crystallographic planes (hkl),  $\theta$  stands for the diffraction angle (also called Bragg angle),  $\lambda$  is the wavelength and  $n$  is a natural multiple factor. A scheme of the experimental setup is shown in **Figure 4.5**.

It must be noted that every crystallographic orientation inherits two diffractions cones, the so-called Kossel-cones. The back scattered electrons build a hyperbolic cut across these cones on the EBSD detector. Due to the energy spread of the back scattered electrons, paired arrays of diffraction lines occur, also known as Kikuchi lines. For further analysis, these Kikuchi lines are recorded and analysed using the Hough transformation [120].

In the present thesis EBSD was used to differentiate between bainitic ferrite and retained austenite. Therefore, un-etched samples after continuous cooling to room temperature with cooling rates 2, 0.75 and  $0.43^\circ\text{Cs}^{-1}$  were analysed, using 20kV accelerating voltage and 50nm pixel size.

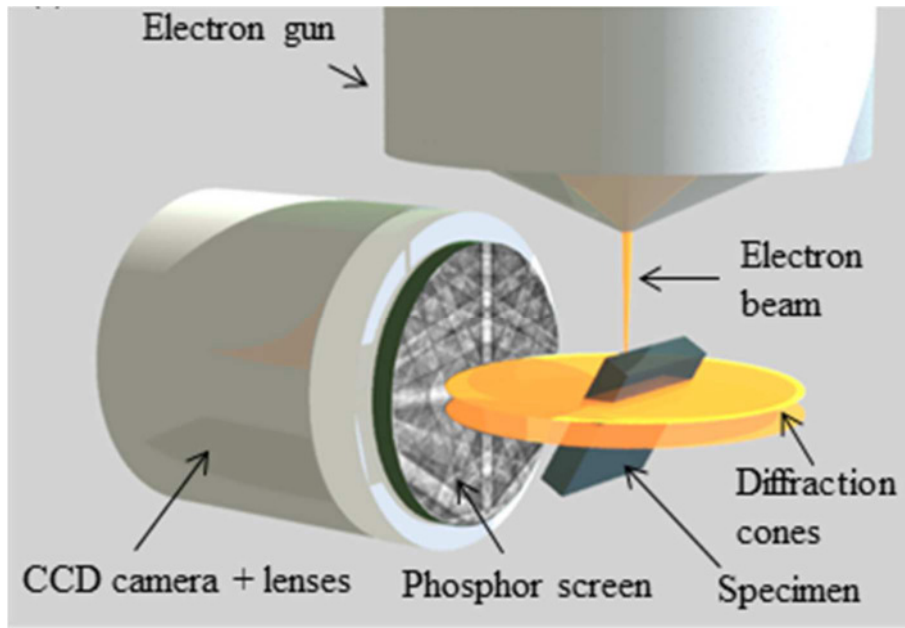


Figure 4.5: Schematic illustration of the EBSD setup, taken from [121].

#### 4.3.5. Transmission electron microscopy

In transmission electron microscopy (TEM) an electron beam with high energy up to 300keV transmits thin samples. This allows microstructure observations with a high spatial resolution of approximately  $\sim 2\text{\AA}$ . Due to the transmission of the sample, electrons are inelastically scattered, elastically scattered or un-scattered.

Incident electrons which interact in an inelastically manner with the sample lose energy during this scattering process. This loss in energy can be used for a detailed analysis regarding the chemical composition of an observed area. This type of analysis is also called electron energy loss spectroscopy (EELS). Since, EELS is not used in the present thesis the reader is referred to [122,123] for a detailed explanation.

In contrast, incident electrons that interact in an un-scattered or elastically scattered manner are used for imaging. In TEM, two main imaging modes are available, the bright field (BF) and dark field (DF) mode.

In the BF mode, the incident un-scattered beam is used for imaging. The transmission of un-scattered electrons is inversely proportional to the specimen thickness, which leads to a thickness contrast.

In the DF mode, the elastically scattered electrons are used for imaging. It must be noted, that the elastically scattered electrons fulfil Bragg's law. As a result of the thin

specimens a spot pattern is observed, where each spot corresponds to a specific crystallographic orientation of the sample. In the DF mode, only one of these spots is used for imaging.

The main advantage apart from high-resolution imaging, is the diffraction mode in TEM, which allows the identification of crystal structure and orientation of different phases as well as the determination of crystal defects (e.g. dislocations). **Figure 4.6** gives an overview about the imaging and diffraction mode in TEM. A detailed explanation is given within [122].

In the present thesis, TEM was used for identification of carbides and retained austenite. Measurements were carried out on a FEI Tecnai F20, equipped with a field emission gun at an accelerating voltage of 200kV. Thin foils were mechanically sliced from the tested dilatometer samples followed by mechanical polishing to a thickness of around 70 $\mu$ m. Finally, the polished foils were electrochemically etched on a Struers Tenupol5, using a 7% solution of perchloric acid at temperatures around -14°C. The recorded diffraction patterns were analysed using the software package JEMS™ (<http://www.jems-saas.ch/>).

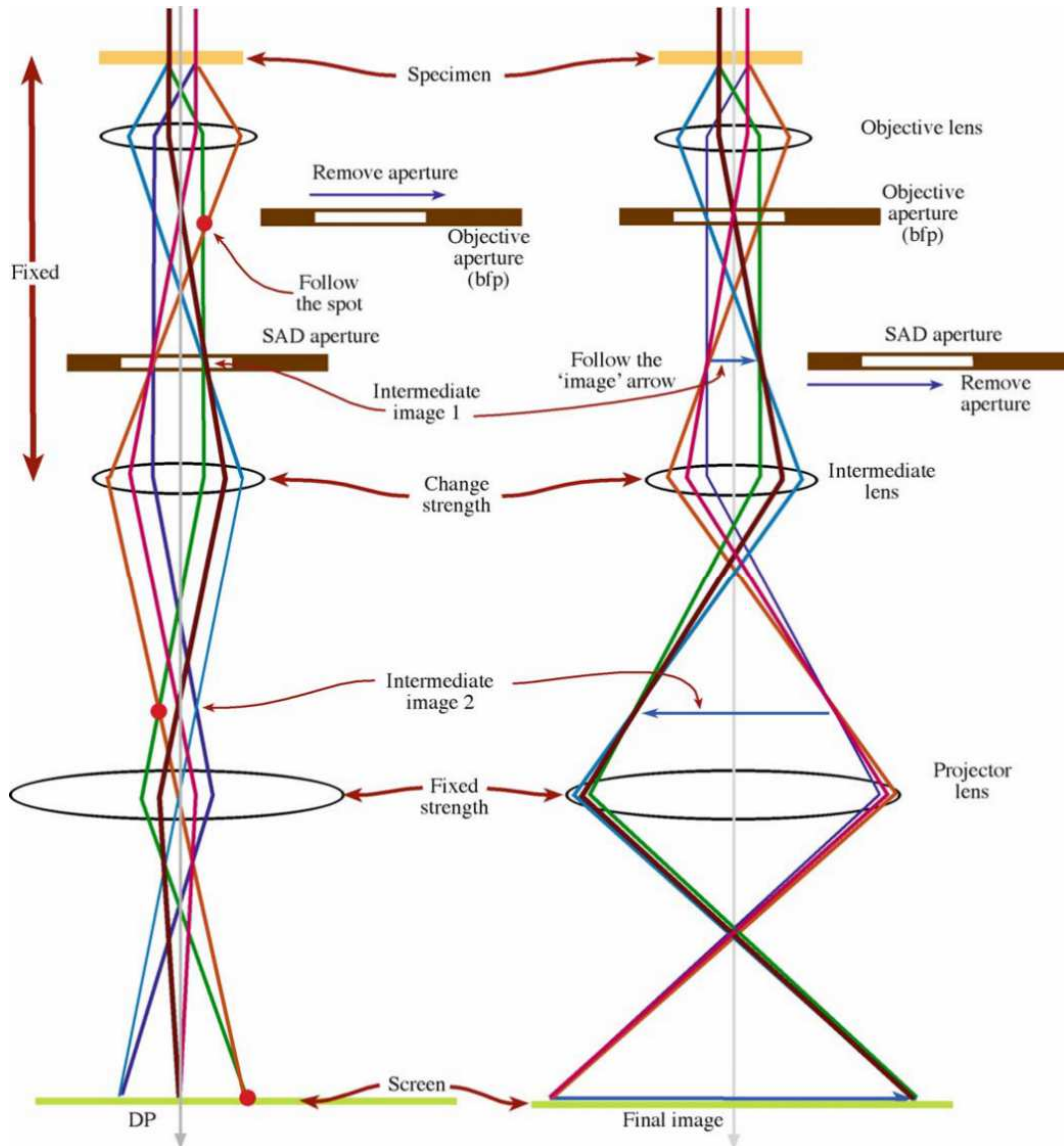


Figure 4.6: The basic operations in TEM: a) projecting the diffraction pattern (DP) on the viewing screen and b) projecting the image onto the screen [122].

#### 4.3.6. Atom probe tomography

Atom Probe Tomography (APT) is a powerful tool to visualize single atoms, precipitates, segregation and boundary surfaces. **Figure 4.7** briefly describes the working principle of an APT device, for detailed information it is referred to literature from Miller et al. [124].

Measurements were conducted at a LEAP<sup>TM</sup> System 3000XHR using the laser mode at 40K and with laser pulse energy of 0.2nJ. The reconstruction of the investigated volumes and the analysis of the data sets have been carried out with the software

package IVAS 3.4.14 from Cameca™. Specimens were prepared according standard electrolytic polishing as described within [125].

In the present thesis, APT was used for the differentiation between bainitic ferrite and carbon enriched austenite after the bainitic reaction, as well as the identification of carbides during the tempering process.

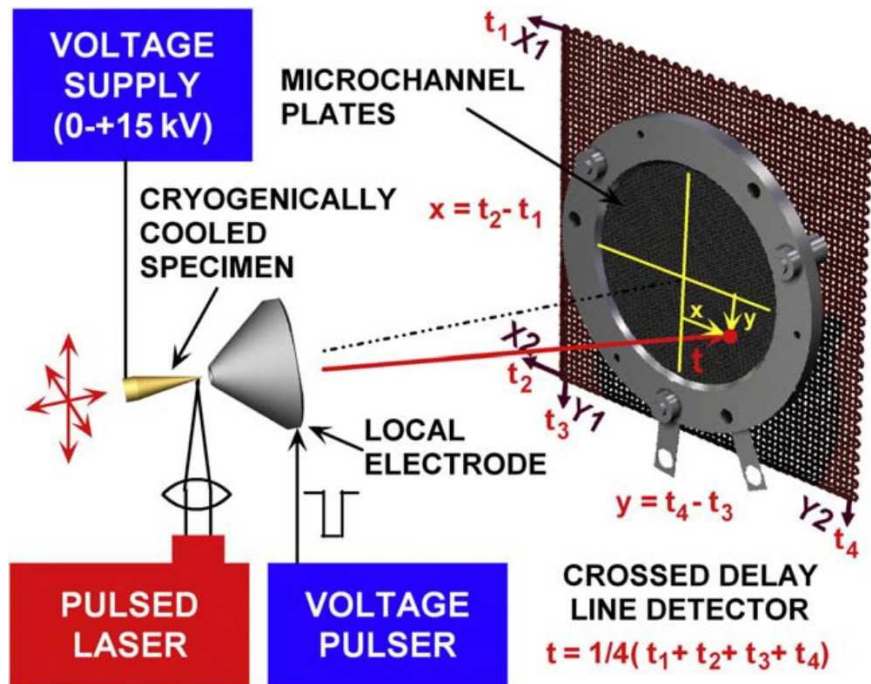


Figure 4.7: Illustration of the experimental setup during an APT measurement according [126].

#### 4.4 Phase analysis using lab scale X-ray diffraction

X-ray diffraction (XRD) is one of the most important non-destructive methods in material science to analyse a wide range of materials regarding their phases. Since steel contains crystalline phases such as ferrite, austenite or carbides, a unique X-ray diffraction pattern for each crystalline phase is produced when the steel sample is exposed with X-rays. For a randomly oriented sample, quantitative measurements of the relative volume fraction of a phase can be made from X-ray diffraction patterns because the total integrated intensity of all diffraction peaks for each phase is proportional to the volume fraction of that phase [127].

In the present thesis, X-ray diffraction experiments on a lab scale were used to determine the amount of retained austenite after the bainitic phase transformation at room temperature. Measurements were performed on a Bruker™ D8 Discover X-ray diffractometer using Mo - $K\alpha$  radiation with a corresponding wavelength of 0.7093Å.

The resulting X-ray diagrams spanned  $2\theta$ -angles from 10 to  $57^\circ$  with a step size of  $0.05^\circ$ . Phase fractions of bainitic ferrite and retained austenite were calculated from the integrated intensities of the (200), (220) and (311) austenite peaks and the ferrite (200), (211) and (220) reflections, according to ASTM-E975-13 [127].

## 4.5 Studying in-situ phase transformation using high energy X-ray diffraction

In order to get a better understanding of the bainitic transformation behaviour during continuous cooling, *in-situ* phase analysis using high energy X-ray diffraction (HEXRD) was used. HEXRD measurements were conducted at the Deutsches Elektronen-Synchrotron (DESY, Hamburg-Germany) on the beamline P07 at Petra III [128], where the dilatometer described in chapter 4.2.1 was placed within the beamline [129]. In order to penetrate the 4mm thick samples, high energy X-rays were used with a photon energy of 87.1keV, corresponding to a wavelength of  $0.14235\text{\AA}$ . The beam size was  $0.7\times 0.7\text{mm}$ , which corresponds to an examined volume of  $\sim 2\text{mm}^3$ . The resulting diffraction rings were recorded with a Perkin Elmer XRD1621 flat panel detector with “slow” mode acquisition. In this acquisition mode, 10 diffraction patterns at an exposure time of 0.2s per diffraction pattern were accumulated. The total recording time for one measurement, which includes shutter opening, data acquisition, subtracting the dark current image (that represents a thermal background of the detector), shutter closure and finally data erasing from the 2-D detector, requires 5 seconds per pattern. Due to this time lag between two measurements, the average temperature between two measurements was used for further analysis. The temperature difference between two measurements is accordingly  $10^\circ\text{C}$  for  $2^\circ\text{Cs}^{-1}$  and  $2^\circ\text{C}$  for  $0.43^\circ\text{Cs}^{-1}$ . To obtain sufficient diffraction peaks for quantitative phase analysis of ferrite and austenite, the distance between sample and detector was set to 1536 mm.

The raw data sets in form of Debye-Scherrer rings were integrated using the software package Fit2D from ESRF [130]. The distance and tilt of the detector and the wavelength were calibrated with patterns obtained by a  $\text{LaB}_6$  standard powder. The resulting corrected X-ray diagrams spanned  $2\theta$ -angles from 1 to  $10.8^\circ$  with a step size of  $0.0073076^\circ$ . For peak analysis, a Pseudo-Voigt fit function was used.

### 4.5.1. Calculation of phase fractions and lattice parameter

Phase fractions of bainitic ferrite and retained austenite were calculated from the integrated intensities of the (200), (220) and (311) austenite peaks and the ferrite

(200), (211) and (220) reflections, according to ASTM-E975-13 [127]. Additionally, the cementite phase fraction during tempering was calculated from the integrated intensities of the (231), (212) and (222) cementite reflections by using the theoretical integrated intensities determined by Faninger [131].

For each measured diffraction pattern, also the lattice parameters for ferrite ( $a_\alpha$ ) and austenite ( $a_\gamma$ ) were calculated with Cohen's method [132,133]. The calculated lattice parameters from individual ferrite or austenite peaks were plotted against  $\cos^2\{\theta\}/\sin\{\theta\}$  and the lattice parameters were obtained by extrapolating the diffraction angle to  $90^\circ$ . This method results in an average error of  $\pm 0.0002\text{\AA}$  for the lattice parameters of both, bainitic ferrite and austenite.

#### 4.5.2. Determination of overall carbon content in austenite and bainitic ferrite

It is well known that the lattice parameter is influenced by alloying elements [134–138]. In the case of a bainitic transformation, the lattice parameter of retained austenite should predominantly be affected by the carbon content, which is controlled by relatively rapid diffusion of carbon atoms from the supersaturated bainitic ferrite into the remaining austenite. In reference [139], Dyson and Holmes pointed out that the lattice parameter of austenite at room temperature varies by  $0.033\text{\AA}$  per weight percent carbon. In the present case, the lattice parameters of austenite and ferrite during phase transformation are also influenced by thermal expansion. It is possible to determine the carbon content of retained austenite ( $w_c^\gamma$ ) in weight percent at any temperature by a mass balance using the following equation [140]:

$$w_c^\gamma = \frac{f_\alpha * a_{\alpha,T}^3}{(1 - f_\alpha) * a_{\gamma,T}^3} (\bar{w} - w_c^\alpha) + \bar{w} \quad (8)$$

where  $f_\alpha$  represents the volume fraction of bainitic ferrite,  $a_{\alpha,T}$  denotes the lattice parameter of bainitic ferrite at given temperature,  $a_{\gamma,T}$  that of austenite,  $w_c^\alpha$  is the carbon content in bainitic ferrite at room temperature and  $\bar{w}$  stands for the overall carbon content in mass percent in the alloy. To estimate the carbon enrichment of austenite during transformation at any temperature, equation (8) must be solved iteratively. As a convergence criterion, a fractional change of  $1 \times 10^{-4}$  wt.-% C in austenite was defined.

The residual carbon content that is in solid solution in bainitic ferrite ( $x_{\alpha,C}$ ) in mole fraction was calculated from the bainitic ferrite lattice parameter at room temperature ( $a_\alpha$ ) using the following equation [140,141]:



$$\begin{aligned}
 a_{\alpha} = a_{\text{Fe}} + & \frac{(a_{\text{Fe}} - 0.279x_{\alpha,\text{C}})^2 (a_{\text{Fe}} + 2.496x_{\alpha,\text{C}}) - a_{\text{Fe}}^3}{3a_{\text{Fe}}^2} - 0.03x_{\alpha,\text{Si}} \\
 & + 0.06x_{\alpha,\text{Mn}} + 0.07x_{\alpha,\text{Ni}} + 0.31x_{\alpha,\text{Mo}} + 0.05x_{\alpha,\text{Cr}} \\
 & + 0.096x_{\alpha,\text{V}}
 \end{aligned} \tag{9}$$

where  $x_i$  represents the mole fraction of element “ $i$ ” in bainitic ferrite. Based on the assumption of low mobility of substitutional elements at transformation temperature and a homogenous distribution of alloying elements due to austenitization, their nominal concentration in the alloy is used. The lattice parameter of pure iron ( $a_{\text{Fe}}$ ) at room temperature is 2.8664Å [140].

## 4.6 Hardness measurements

In order to visualize the effect of secondary hardening during tempering, HV10 hardness measurements according EN ISO 6507-1 [142], were performed on a Qness™ Q10AQ+ Vickers hardness testing machine. Measurements were conducted from the as-hardened bainitic microstructure after continuous cooling as well as during the tempering process, according to **Figure 4.4b**.

## 5 Characterization of the initial microstructure and the continuous cooling transformation diagram

The present chapter deals with the characterization of the initial microstructure after the hot-rolling and soft annealing process according to the time-temperature cycle presented in **Figure 4.1**. A detailed knowledge of the microstructure constituents in the initial state is important to understand all further mechanisms that happen during heating, austenitization and subsequent cooling, e.g. phase transformations and grain growth. A special focus was set on the characterization of carbides that are present in the soft annealed microstructure, because they absorb high amounts of carbon and substitutional atoms from the surrounding matrix.

Therefore, a detailed microstructure examination by means of optical light microscopy (OLM) and scanning electron microscopy (SEM) was performed. A phase quantification via thresholding and area counting regarding the carbide amount is possible based on the assumption that the microstructure after the soft annealing process consists only of ferrite and carbides. It should be noted that a minimum of three micrographs were analysed in both cases. Additionally, transmission electron microscopy (TEM) coupled with selected area diffraction (SAD) was carried out to identify the different carbide types. Finally, three-dimensional atom probe tomography (3D-APT) was applied to determine the local chemical composition of the microstructure.

In order to investigate the influence of carbide dissolution during reheating, soft annealed samples were reheated with  $2^{\circ}\text{Cs}^{-1}$  to  $1020^{\circ}\text{C}$  and held there for 30 min. Subsequently, the sample was cooled with a cooling rate of approximately  $100^{\circ}\text{Cs}^{-1}$ . To observe the evolution of the individual phases during reheating, *in-situ* high energy X-ray diffraction (HEXRD) was carried out. Afterwards, the grain size was determined, using the linear intercept method according ASTM E112-96 [117].

Within the framework of the current research project, a continuous cooling transformation (CCT) diagram for the present alloy was evaluated in cooperation with DEW and will be presented in the end of this chapter. Therefore, the transformation kinetics during continuous cooling were measured by means of dilatometry. The analysis of the dilatometer data was performed according to SEP 1680 [143].

### 5.1 Carbide type and volume fraction in the soft annealed microstructure

The identification of carbides on basis of simply etched samples is very tough, as shown in **Figure 5.1a**. From this presentation, one can only suspect that carbides

are located at grain boundaries (marked with red arrows) as well as within the ferritic matrix. One can, however, deduce that the grain diameter of ferrite is approximately  $12\mu\text{m}$  using the linear intercept method according to ASTM E112-96 [117].

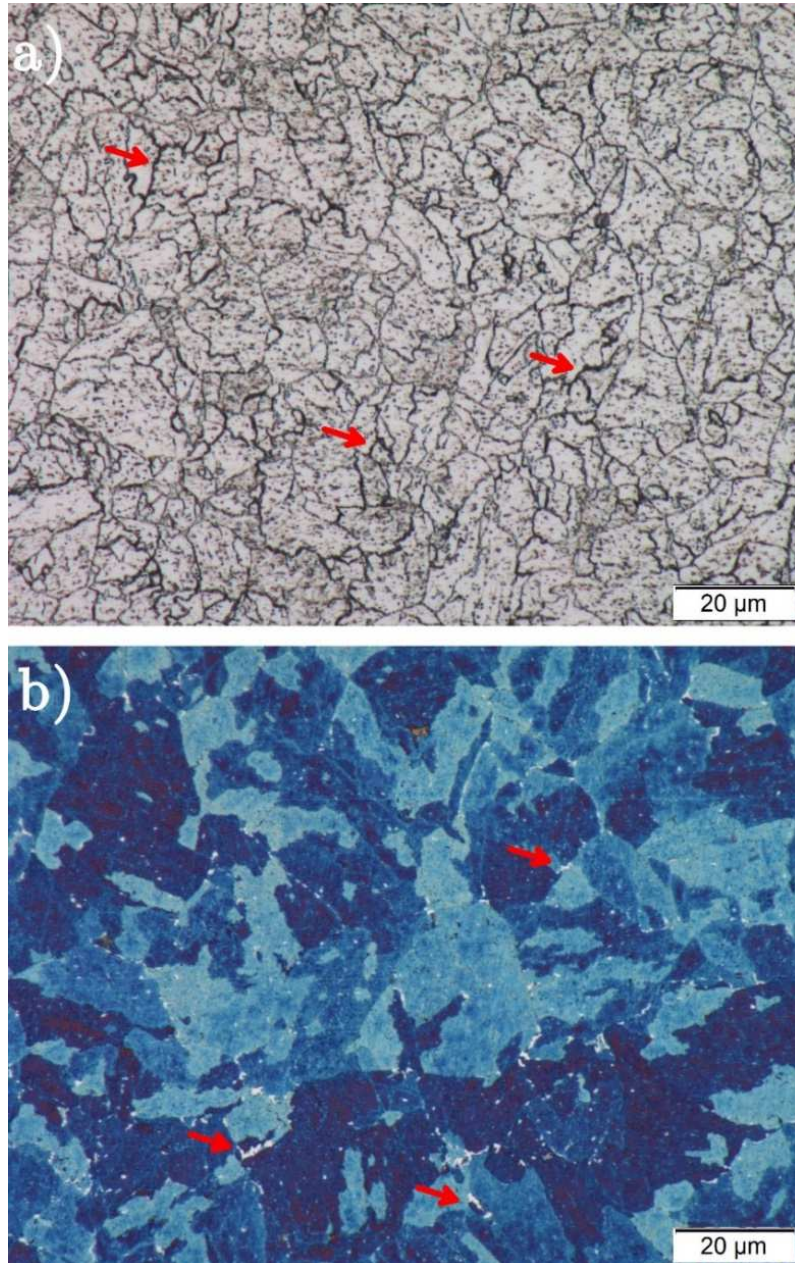


Figure 5.1: Representative OLM micrographs after etching with a) Nital for 3 seconds and b) Klemm 1 colour etchant for 180 seconds, showing precipitates (marked with red arrows) at grain boundaries.

In comparison, **Figure 5.1b** shows the microstructure after colour etching with a Klemm 1 etchant. The micrograph exhibits the blue coloured ferritic microstructure, whereas second phase particles remain bright and are mainly observed at grain boundaries (marked with red arrows). Analysis of these micrographs (image area  $14053\mu\text{m}^2$ ) revealed 711 particles with a total area fraction of  $0.77\pm 0.05\%$ . As reported in literature [115], the area fraction can be assimilated to the volume fraction.

Further microstructure examinations, using the backscatter contrast by means of SEM revealed three different carbide morphologies, see **Figure 5.2**:

- 1) irregular shaped carbides at grain boundaries,
- 2) oriented rod-shaped carbides and
- 3) nearly equiaxed carbides within the ferritic matrix

Evaluation of the SEM images (image area  $776\mu\text{m}^2$ ) with respect to the amount of carbides delivered a total fraction of  $4.4\pm 0.2\text{vol.}\%$ . In general, this value should be considered as a maximum value since etching may lead to an overestimation.

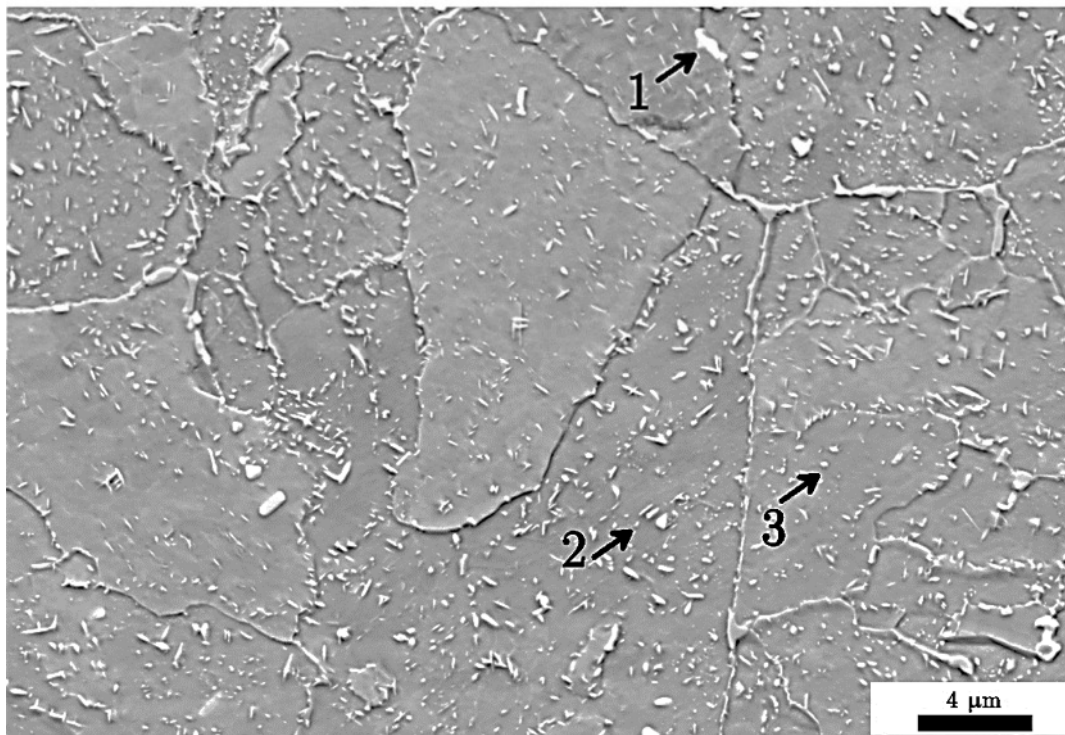


Figure 5.2: Representative SEM micrographs showing different carbide morphologies 1) irregular shaped carbides at grain boundaries, 2) oriented rod-shaped carbides, and 3) nearly equiaxed carbides within the ferritic matrix.

Based on these results, it is yet not possible to make a precise statement about the different carbide types and their individual phase fractions. Therefore, an intensive TEM study coupled with selected area diffraction (SAD) was carried out in order to identify and quantify the different carbide types.

The further recognized morphologies via SEM have been identified to  $M_2C$  (oriented rod-shaped),  $M_3C$  (near equiaxed) and  $M_6C$  (irregular shaped at grain boundaries), respectively shown in **Figure 5.3**. Additionally, the mean length ( $\bar{l}$ ), width ( $\bar{b}$ ) and aspect ratio ( $A_R = l/b$ ) of the identified carbide types were measured from at least three positions. For a better comparability, an equivalent circle radius ( $\bar{r}$ ) was determined based on the carbide area. The following **Table 5.1** summarizes the obtained results.

**Table 5.1:** Summary of the individual carbide dimensions observed via TEM;  $\bar{l}$ ...length,  $\bar{b}$ ...width,  $\bar{r}$ ...equivalent circle radius and  $A_R$ ...aspect ratio ( $l/b$ ).

Carbide	$(\bar{l})$ [nm]	$(\bar{b})$ [nm]	$(\bar{r})$ [nm]	$A_R$ [-]
$M_2C$	$468 \pm 186$	$80 \pm 22$	$108 \pm 32$	$6 \pm 2$
$M_3C$	$233 \pm 98$	$123 \pm 63$	$71 \pm 17$	$2 \pm 0.5$
$M_6C$	$617 \pm 184$	$350 \pm 118$	$257 \pm 64$	$1.9 \pm 0.5$

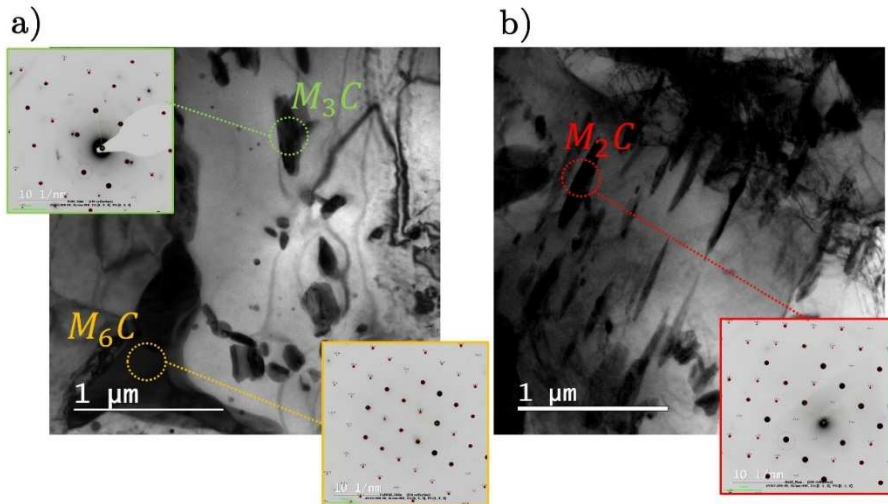


**Figure 5.3:** TEM micrographs with corresponding SAD pattern of the three different carbide types:  $M_2C$  (oriented rod-shaped),  $M_3C$  (near equiaxed) and  $M_6C$  (irregular shaped at grain boundaries).

Subsequently, these measured carbide dimensions can be utilized to differentiate between the carbide fractions observed by means of SEM. **Figure 5.4** illustrates the different carbide size distributions, i.e. plots of the occurrence frequency versus the determined equivalent circle radius. From the diagrams it can be seen that the most common carbide type is  $M_2C$  (2.9%), followed by  $M_3C$  (1%) and  $M_6C$  (0.5%).

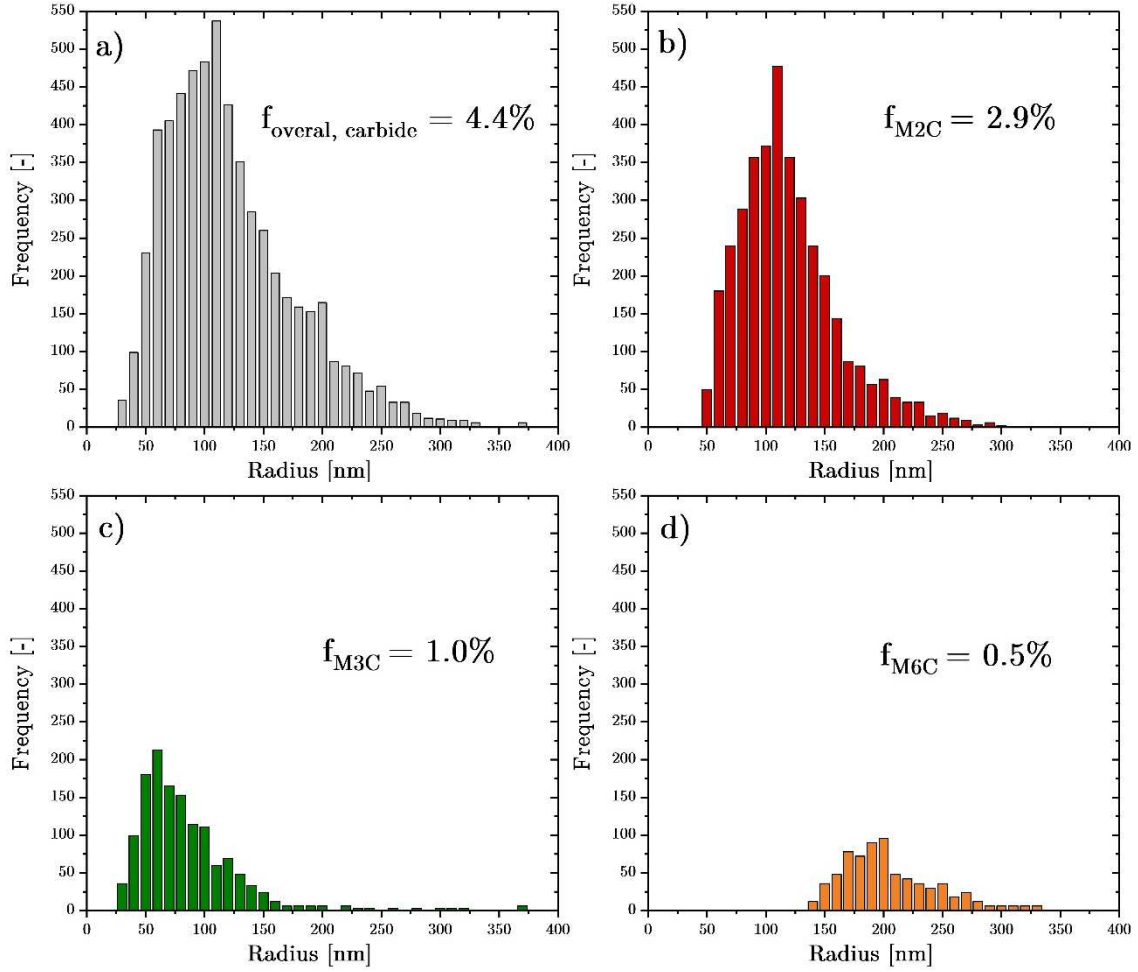


Figure 5.4: Size distribution of the determined equivalent radius as determined from SEM images; a) overall distribution, b)  $M_2C$ , c)  $M_3C$  and d)  $M_6C$ .

With the knowledge of the individual carbide phase fractions as determined from SEM images the overall carbon content in the alloy ( $\bar{x}_{c,\alpha}$ ) in mole fraction can be expressed as follows:

$$\bar{x}_{c,\alpha} = f_{M_2C} * x_{c,M_2C} + f_{M_3C} * x_{c,M_3C} + f_{M_6C} * x_{c,M_6C} + f_{\alpha} * x_{c,\alpha} \quad (10)$$



where  $f_i$  represents the phase fraction and  $x_i$  represents the corresponding mole fraction of carbon in the carbide phase “ $\gamma$ ” or in the residual ferritic matrix. By rearranging equation (10), the carbon content in the residual ferritic matrix ( $x_{c,\alpha}$ ) can be determined to 0.0002 or for a better comparability 0.02 at.-%. However, it should be noted that this calculated carbon content is idealized. In addition to statistical uncertainties, which arise from the determination of the volume fraction, also systematic uncertainties arise during the sample preparation, especially etching.

**Figure 5.5** shows representative atom maps of Fe, Mo, Cr, V and C of the ferritic matrix observed by means of APT. The APT analysis demonstrates clearly, that the elements are homogenously distributed in the matrix and no further nanocarbides are observed. Therefore, the average local chemical composition was determined from three different APT-measurements and is listed in **Table 5.2**. These measurements indicate that the matrix is strongly depleted in Mo, V and C. Furthermore, the measured carbon content in the ferritic matrix of  $0.012 \pm 0.01$  at. -% is in good accordance with the previous determined carbon content of 0.02 at. -%.

**Table 5.2:** Chemical composition of the ferritic matrix in at. -% measured by means of APT.

Element	C	Si	Mn	Cr	Ni	Mo	V	Fe
APT	0.012 $\pm 0.01$	0.5 $\pm 0.03$	0.29 $\pm 0.01$	0.4 $\pm 0.008$	0.1 $\pm 0.01$	0.15 $\pm 0.01$	0.011 $\pm 0.001$	bal.
nominal	1.3	0.54	0.33	0.46	0.1	1.64	0.43	bal.

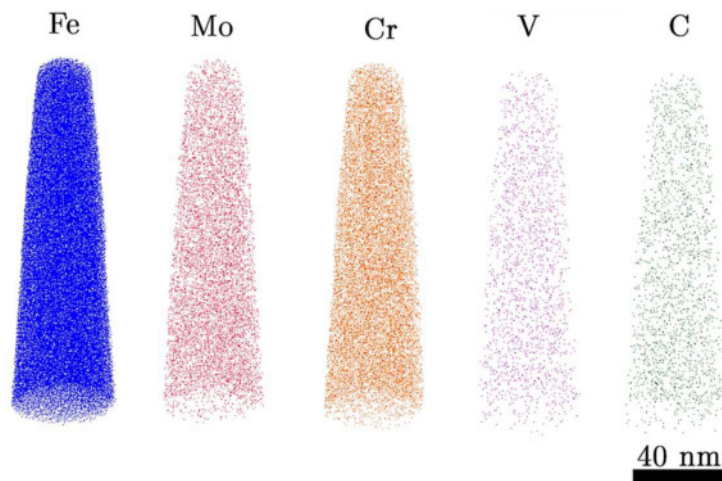


**Figure 5.5:** Representative atom maps of Fe, Mo, Cr, V and C in the ferritic matrix.

## 5.2 Comparison to the equilibrium phase diagram

Equilibrium phase diagrams are a basic and useful tool for metallurgists when analysing phase transformations or phase stability in multi-phase and multi-component alloys. In this context, the most stable phase is the phase with have the lowest Gibbs free energy at a certain temperature, chemical composition and pressure. If the pressure is constant, the Gibbs free energy of one mole of a phase can be expressed as follows:

$$G_m^\alpha = \sum_j x_j^\alpha G_j^\alpha + RT \sum_j x_j^\alpha \ln x_j^\alpha + G_m^{\alpha,E} \quad (11)$$

In this equation  $j$  denotes the number of components and  $x_j$  the mole fraction of the components. The first term indicates the sum of the Gibbs free energy of the pure components to the phase, the second term is the sum of entropy contributions on the Gibbs free energy, assuming ideal or random mixture of the various components and the third term is the excess free energy if the mixture is not ideal. The application of equation (11) to determine stable phase or phases in a system at a given temperature is then based on further assumptions, analytical expressions, and the availability of thermodynamic databases. Due to the increasing industrial interest, comprehensive thermodynamic databases are being developed in the framework of the CALPHAD technique, which in combination with commercial software for Gibbs energy minimization (e.g. MatCalc) can be used to predict phase stabilities and equilibrium phase diagrams in almost all alloy systems of technical relevance [144].

Thermodynamic and also thermo-kinetic calculations using MatCalc [5], begin with a choice of chemical elements and possible phases. In the present case, elements and composition according to the nominal alloy composition are used. Phases are chosen according to the findings in the previous section and are listed with their corresponding MatCalc declaration and lattice structure in **Table 5.3**. With these ingredients, it is possible to calculate a stepped equilibrium calculation in the temperature range between 1200°C and 400°C. The MatCalc scripts for this calculation can be found within **Appendix B**. Finally, the equilibrium phase diagram is presented in **Figure 5.5**.

Reading the diagram from the right high temperature side to the left low temperature side shows that in a temperature range of 1200-860°C, austenite and  $M_6C$  are in thermodynamic equilibrium. The stability of both phases decreases detrimentally in the temperature range between 860°C-760°C. In this temperature range, ferrite instead of austenite and  $M_2C$  instead of  $M_6C$  become the stable thermodynamic phases.



In the deepest temperature range of 760-400°C,  $M_3C$  becomes also stable but its stability decreases with decreasing temperature.

**Table 5.3:** Summary of the thermodynamic phases with their corresponding MatCalc declaration and lattice structure for thermodynamic calculations.

Thermodynamic phase	MatCalc declaration	Lattice structure
Austenite	FCC_A1	Face-centred-cubic
Ferrite	BCC_A2	Body-centred-cubic
$M_2C$	HCP_A3#01	Hexagonal close packed
$M_3C$	Cementite	Orthorhombic
$M_6C$	M6C	Face-centred-cubic

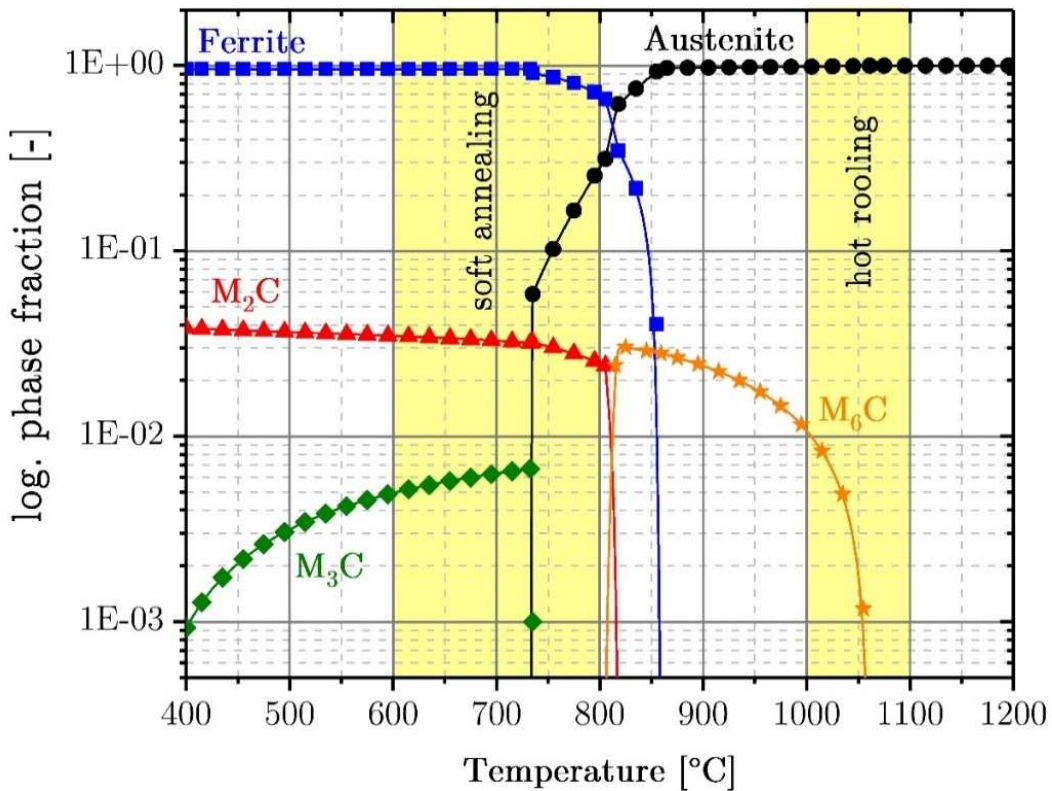


Figure 5.5: Thermodynamic phase fraction diagram calculated with MatCalc. Please note, the y-axis is set to a logarithmic scale for a better presentation.

Equilibrium phase diagrams do not represent phase transformation kinetics but they can give an idea of which phase transformation might occur when an alloy is

slowly cooled down from an austenitization temperature to a certain transformation temperature, as it is the case during the industrial production route. With the aid of this diagram, it is possible to deduce the different thermo-kinetic precipitation sequences during the hot-rolling and soft annealing process. The diagram shows that austenite and  $M_6C$  carbide are stable in the temperature range (1000-1080°C) where hot-rolling process is typically performed with this steel grade. The deformation during hot rolling leads to a tremendous increase in the dislocation density, which further leads to dynamic recovery and recrystallization of the austenite. Simultaneously, the possible nucleation sites (grain, subgrain boundaries) for  $M_6C$  carbides increase which also hinder further grain growth. However, during further cooling the  $M_6C$  coarsens, which the highest measured radius (see Table 5.1) also designates.

In a temperature range between 760-850°C, ferrite becomes thermodynamically more stable than austenite. Concurrently,  $M_2C$  precipitates from the fresh built ferrite and  $M_6C$  begin to dissolve. However, the thermodynamic simulation indicates that the entire  $M_6C$  dissolves, which contradicts with the microstructure observations. Finally, at approximately 740°C the austenite decomposes into a pearlitic mixture of ferrite and  $M_3C$  (cementite). In conclusion, the experimentally observed carbide fractions are in good accordance with a thermodynamic simulation.

### 5.3 Reheating of the soft annealed microstructure and austenite grain size

**Figure 5.6a** shows the room temperature diffractogram of the soft annealed microstructure, observed by means of HEXRD. At room temperature, ferrite ( $\alpha$ ) peaks can be seen together with several carbide peaks (for ease of reading not all carbide peaks are indexed). These carbide peaks can also be assigned to the previously identified carbide types of  $M_2C$ ,  $M_3C$  and  $M_6C$ . **Figure 5.6b** shows different diffractograms obtained in a temperature range between 700-1000°C during continuous heating with 2°Cs<sup>-1</sup>. A comparison of the different pattern reveals that the amount of carbides decreases with increasing temperature. Furthermore, the phase transformation from ferrite to austenite begins in a temperature range between 700-800°C. Due to the fact that the HEXRD setup was optimized for *in-situ* phase analysis of the bainitic reaction, it was not able to quantify the carbide evolution during these experiments.

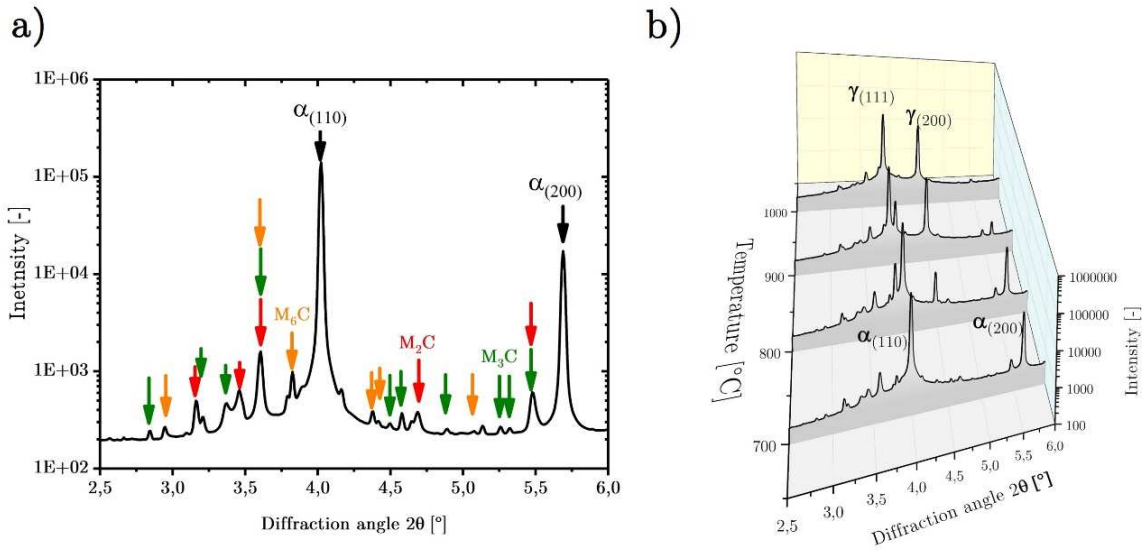


Figure 5.6: Observed X-ray diffraction pattern a) from the soft annealed microstructure and b) in a temperature range between 700-1100°C. (The intensity axis has a log scale to be able to observe low- intensity carbide peaks).

However, to simply visualize the carbide dissolution kinetics during reheating, the integrated intensity of the individual carbide peaks at room temperature were set to the distinct carbide fractions observed from microstructure observation in the previous chapter. **Figure 5.7a** illustrates the phase evolution of ferrite and austenite as well as that of the different carbide types during reheating of the soft annealed microstructure with 2°Cs<sup>-1</sup> to 1020°C. The dissolution of ferrite and M<sub>3</sub>C appears to start at the same temperature and continues simultaneously with austenite formation until cementite completely disappears. The dissolution of M<sub>2</sub>C begins with the end of the ferrite to austenite phase transformation at approximately 950°C and ends upon reaching the austenitization temperature of 1020°C. In contrast, the M<sub>6</sub>C carbide seems to be even stable at this temperature. Furthermore, no or minor change in the carbide fractions was observed during austenitization.

After austenitization for 30 min the sample was quenched to room temperature using a cooling rate of 100°Cs<sup>-1</sup>. **Figure 5.7b** shows an optical micrograph of the quenched martensitic microstructure. Measurements regarding the prior austenite grain size on such micrographs revealed an austenite grain size of 23±8 μm.

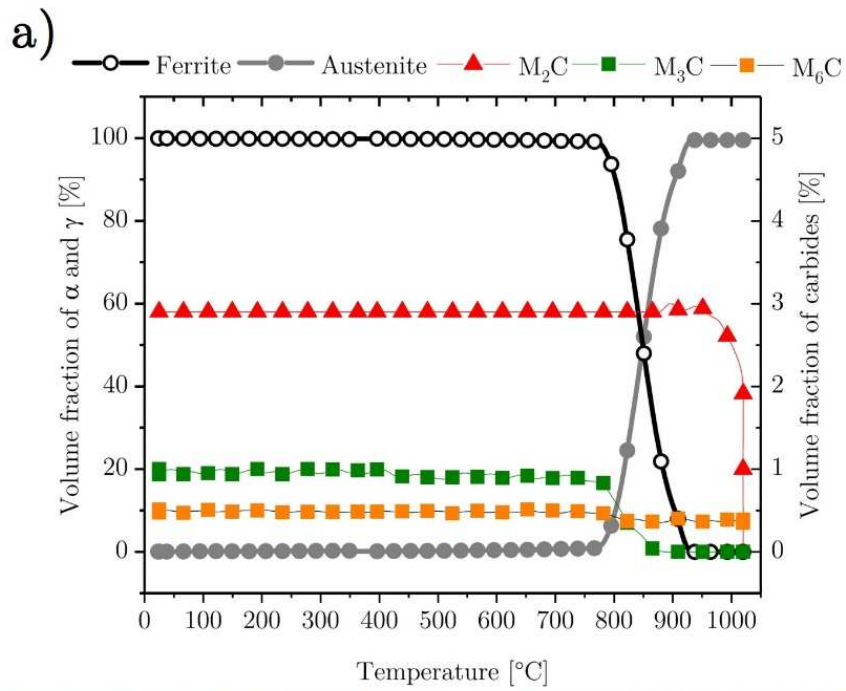
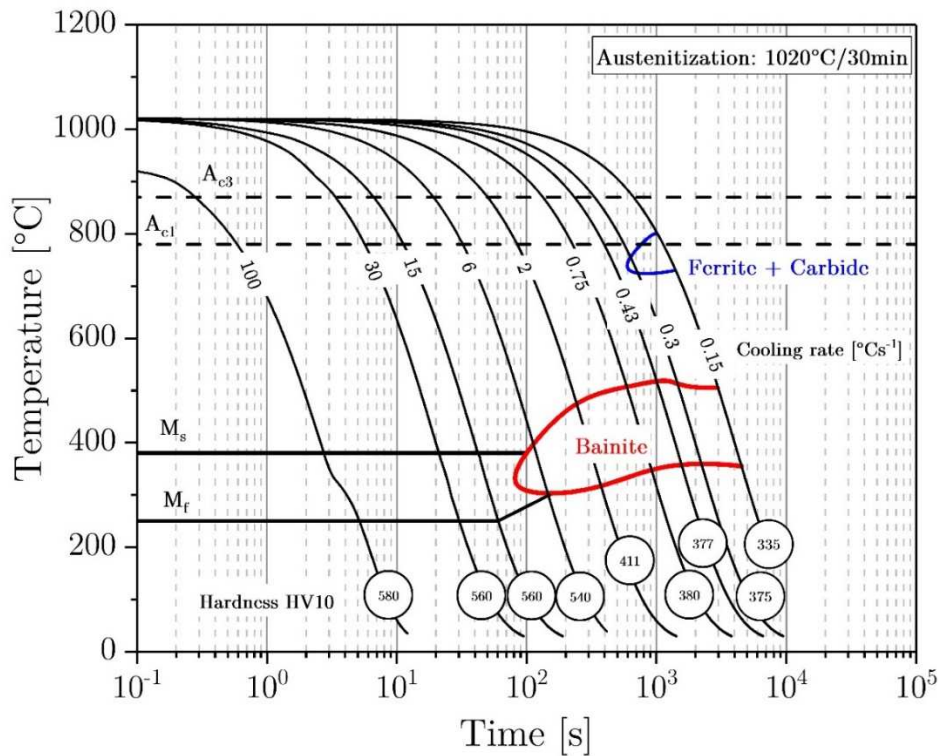


Figure 5.7: a) Evolution of volume fractions, obtained by HEXRD, of ferrite, austenite,  $M_2C$ ,  $M_3C$  and  $M_6C$  during reheating of the soft annealed microstructure with  $2^\circ\text{Cs}^{-1}$  to  $1020^\circ\text{C}$ . b) representative optical micrograph after quenching with  $100^\circ\text{Cs}^{-1}$  from austenitization temperature.

## 5.4 Continuous cooling transformation diagram

Continuous cooling transformation (CCT) diagrams are used to describe the decomposition of austenite as a function of the cooling rate after constant austenitization conditions. The applied time-temperature cycles for the CCT diagram shown in **Figure 5.8**, were as follows:

- i. Heating at the rate of  $2^{\circ}\text{Cs}^{-1}$  to austenitizing temperature of  $1020^{\circ}\text{C}$ ,
- ii. holding at  $1020^{\circ}\text{C}$  for 30 minutes, and
- iii. cooling down to ambient temperature with 15 different cooling rates between 100 to  $0.15^{\circ}\text{Cs}^{-1}$  (for a better presentation in the CCT diagram, not all cooling rates are drawn).



**Figure 5.8:** Continuous cooling transformation (CCT) diagram of the alloy under investigation for austenitization conditions of  $1020^{\circ}\text{C}/30\text{min}$ .

The CCT diagram reveals a martensitic phase transformation for cooling rates ranging from 100 to  $15^{\circ}\text{Cs}^{-1}$ . In these range, the martensite-start temperature ( $M_s$ ) can be determined to  $380^{\circ}\text{C}$  and the martensite-finish temperature ( $M_f$ ) to  $250^{\circ}\text{C}$ . The martensitic phase transformation obviously leads to the highest hardness of



580HV. A representative optical micrograph of the martensitic microstructure after cooling with  $15^{\circ}\text{C}\text{s}^{-1}$  is shown **Figure 5.9a**.

By lowering the cooling rate up to  $6^{\circ}\text{C}\text{s}^{-1}$ , the character of phase transformation gradually changes from martensitic to bainitic. A further decrease in the cooling rate (2 to  $0.43^{\circ}\text{C}\text{s}^{-1}$ ) leads to a region of sole bainitic phase transformation. The bainitic phase transformation starts in a temperature range between 480 to  $520^{\circ}\text{C}$  and stops at approximately 325 to  $350^{\circ}\text{C}$ . **Figure 5.9b-c** shows the bainitic microstructure after cooling with 2 and  $0.43^{\circ}\text{C}\text{s}^{-1}$ , respectively. As can be seen from these images that the microstructure slightly coarsens with decreasing cooling rate, which is also accompanied in a decrease in the hardness. Depending on the cooling rate, the hardness decreases from 411HV at  $2^{\circ}\text{C}\text{s}^{-1}$  to 377HV at  $0.43^{\circ}\text{C}\text{s}^{-1}$ . These hardness values are in good accordance with the required values of 35-38HRC ( $\sim 350$ -380HV) in the new alloying concept.

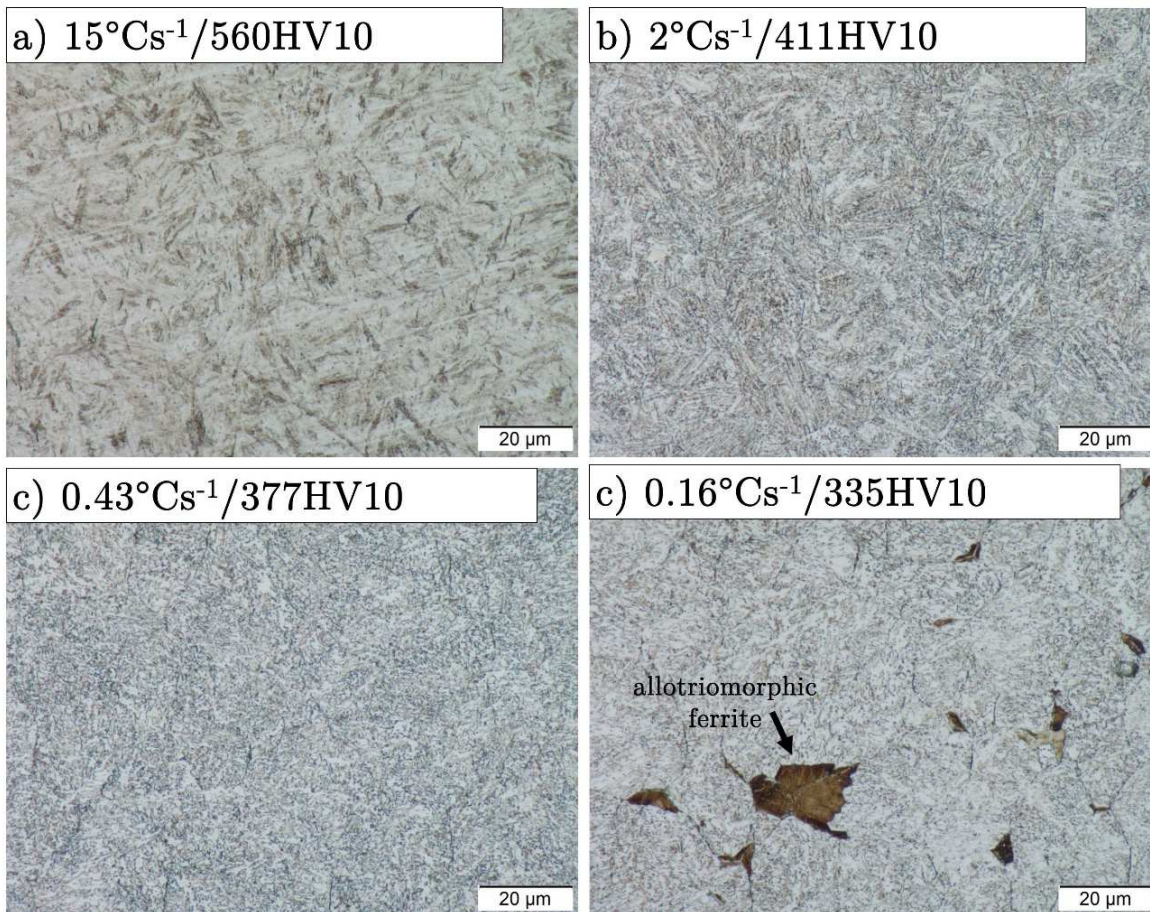


Figure 5.9: Optical micrographs of a) martensite, b) and c) bainite and d) mixed microstructure of allotriomorphic ferrite together with bainite.

Cooling rates less than  $0.43^{\circ}\text{Cs}^{-1}$  lead to the formation of some amount of ferrite and carbides, before the bainitic reaction takes place. **Figure 5.9d** shows a representative mixed microstructure of allotriomorphic ferrite and bainite after cooling with  $0.15^{\circ}\text{Cs}^{-1}$ . Although this mixed microstructure leads to a lower hardness of 335HV, but to many different phases adversely, affect further processability.

The CCT diagram also reveals that the region of austenite decomposition into a mixture of ferrite and carbides is separated from the bainite region. This behaviour can be explained by the high Mo content in the alloy. Mo decreases the activity coefficient of carbon in austenite [145] and ferrite [146] which retards the phase transformation [147,148]. Furthermore, an increase in the Mo content decreases the bainite start temperature, which leads to the splitting of both transformation regions [149].

## 5.5 Summary

The initial microstructure after the hot-rolling and soft annealing process was investigated by a comprehensive set of characterization methods. The microstructure investigations revealed a ferritic matrix with an average grain diameter of  $12\mu\text{m}$ . Within this ferritic matrix, three different carbide types were identified. It was shown that the most common carbide type is  $\text{M}_2\text{C}$  (2.9 vol.-%), followed by  $\text{M}_3\text{C}$  (1 vol.-%) and  $\text{M}_6\text{C}$  (0.5 vol.-%). Further APT measurements showed that the residual ferritic matrix is depleted in Mo, V and C, which also supports the findings regarding the amount of carbides.

Finally, a thermodynamic simulation of the alloy under investigation also approves these carbide fractions. Subsequent reheating of the soft annealed microstructure to  $1020^{\circ}\text{C}$  leads to the dissolution of the  $\text{M}_3\text{C}$  and  $\text{M}_2\text{C}$  carbides. Conversely, the amount of  $\text{M}_6\text{C}$  remains constant during austenitization. Measurements regarding the prior austenite grain size delivered a value of  $23\pm 8\ \mu\text{m}$ . In the end of the chapter, the CCT diagram for constant austenitization conditions of  $1020^{\circ}\text{C}/30\text{min}$  is presented. The diagram reveals that the decomposition of austenite to bainite occurs between cooling rates higher than  $0.3^{\circ}\text{Cs}^{-1}$  and lower than  $6^{\circ}\text{Cs}^{-1}$ .

## 6 Bainitic reaction during continuous cooling

The purpose of the present chapter is twofold: to clarify the continuous transformation kinetics of austenite to bainitic ferrite and the partitioning of carbon during the phase transformation. Therefore, the decomposition of austenite into bainitic ferrite has been studied by two *in-situ* techniques: dilatometry and high-energy X-ray diffraction (HEXRD).

Electron backscatter diffraction (EBSD), scanning electron microscopy (SEM) and transmission electron microscopy (TEM) was used to examine the microstructure after phase transformation.

The global distribution of carbon as obtained from HEXRD data will be compared with local measurements by means of 3D atom probe tomography (3D-APT).

### 6.1 Bainite phase evolution during continuous cooling

#### 6.1.1. Dilatometry

The dilatometer signal obtained for cooling rates between 2 and 0.43°Cs<sup>-1</sup> are shown in **Figure 6.1**. Accordingly, the change in length, which corresponds to the degree of phase transformation from austenite to bainite, progresses from a continuous behaviour at higher cooling (2 to 1°Cs<sup>-1</sup>) rates to a two-stage behaviour with a transformation stasis at lower cooling rates (0.75 to 0.43°Cs<sup>-1</sup>). The transformation stasis becomes more pronounced with decreasing cooling rate. The onsets for the two-stage transformation (2<sup>nd</sup> Onset) are marked with red arrows.

Furthermore, the bainite start temperature ( $B_s$ ) increases from 475°C at 2°Cs<sup>-1</sup> to 520°C at 0.43°Cs<sup>-1</sup>. The dilatometer signal also reveals that no measurable martensitic phase transformation occurs in these ranges of cooling rates.

There are several studies in literature [22,150,151] regarding the evolution of bainitic phase fraction during continuous cooling. The most convenient method to visualize the evolution of the bainitic phase fraction ( $V_{\alpha_b}$ ) during continuous cooling conditions is to apply a lever rule on the dilatometer signal as follows:

$$\frac{V_{\alpha_b}(T)}{V_{\alpha_b \max}} = \frac{L(T) - L_{\gamma}(T)}{L_{\gamma}(T) - L_m(T)} \quad (12)$$

where  $L(T)$  is the actual length of the specimen during transformation,  $L_{\gamma}(T)$  is the calculated length assuming that the specimen has a fully austenitic structure at a certain temperature and  $L_m(T)$  is the calculated length of the specimen after the transformation at a certain temperature  $T$ . The bainitic phase fraction is normalized



according the final volume fraction of bainite  $V_{\alpha_b, max}$  that is measured by image analysis on optical micrographs. However, the differentiation of bainite and retained austenite on such metallographic images is difficult. Therefore, the amount of retained austenite  $V_{\gamma, retained}$  at room temperature was measured by means of X-ray diffraction on a lab scale diffractometer according **Chapter 4.4**. Instead of normalizing equation (14), the amount of retained austenite is subtracted from the bainite fraction, which leads to:

$$V_{\alpha_b}(T) = \frac{L(T) - L_{\gamma}(T)}{L_{\gamma}(T) - L_m(T)} - V_{\gamma, retained} \quad (13)$$

The evolution of bainitic phase fraction by using this method is shown for cooling rates 2, 0.75 and  $0.43^{\circ}\text{C}\text{s}^{-1}$  in **Figure 6.2**, respectively. This illustration clarifies the change in the transformation kinetics from fast ( $2^{\circ}\text{C}\text{s}^{-1}$ ) to slow ( $0.43^{\circ}\text{C}\text{s}^{-1}$ ) cooling rates.

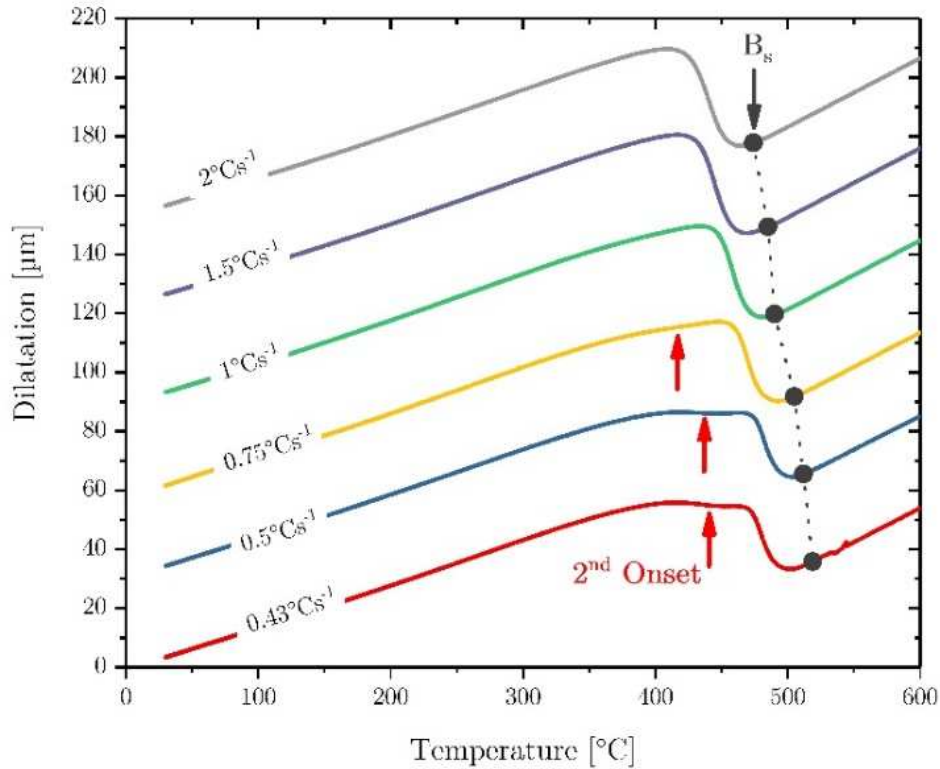


**Figure 6.1:** Plot of the dilatation as a function of temperature obtained from the dilatometer experiments carried out at cooling rates varying from 2 to  $0.43^{\circ}\text{C}\text{s}^{-1}$ .

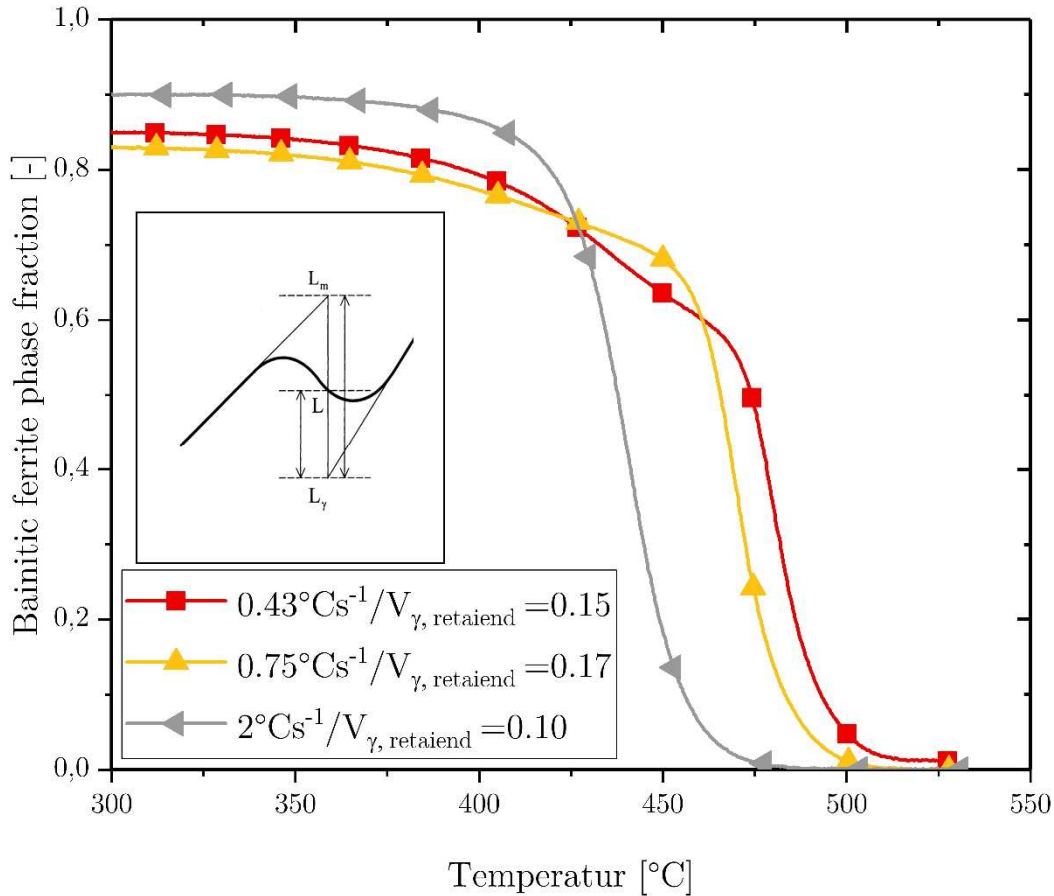


Figure 6.2: Bainite transformation kinetics during continuous cooling with 2, 0.75 and  $0.43^{\circ}\text{C s}^{-1}$  observed from dilatometry by applying a lever rule.

### 6.1.2. High energy X-ray diffraction

The kinetics of bainite formation for cooling rates 2, 0.75 and  $0.43^{\circ}\text{C s}^{-1}$  observed by means of *in-situ* HEXRD measurements is shown in **Figure 6.3**. The same trend for the progress of phase transformation is observed as previously indicated by the dilatometer curves. In the HEXRD measurements, the transformation again shows a change from a continuous to a two-stage behaviour, when decreasing the cooling rate below  $0.75^{\circ}\text{C s}^{-1}$ . The onsets of the bainitic as well as for the two-stage transformation are marked with arrows. The bainite transformation remains incomplete and seems to terminate at approximately  $300^{\circ}\text{C}$  for all cooling rates. The amount of retained austenite increases from 10 vol.% at  $2^{\circ}\text{C s}^{-1}$  to a maximum of 17 vol.% at  $0.75^{\circ}\text{C s}^{-1}$ . For a further decrease of the cooling rate to  $0.43^{\circ}\text{C s}^{-1}$ , the amount of retained austenite seems to slightly decrease again and approaches a value of about 15 vol.%. Analysis of the diffraction pattern revealed no evidence of the formation of carbide phases

during cooling, which would otherwise influence the observed transformation behaviour. But due to the detection limit of about 1 vol.%, carbide precipitation below this limit cannot be totally excluded.

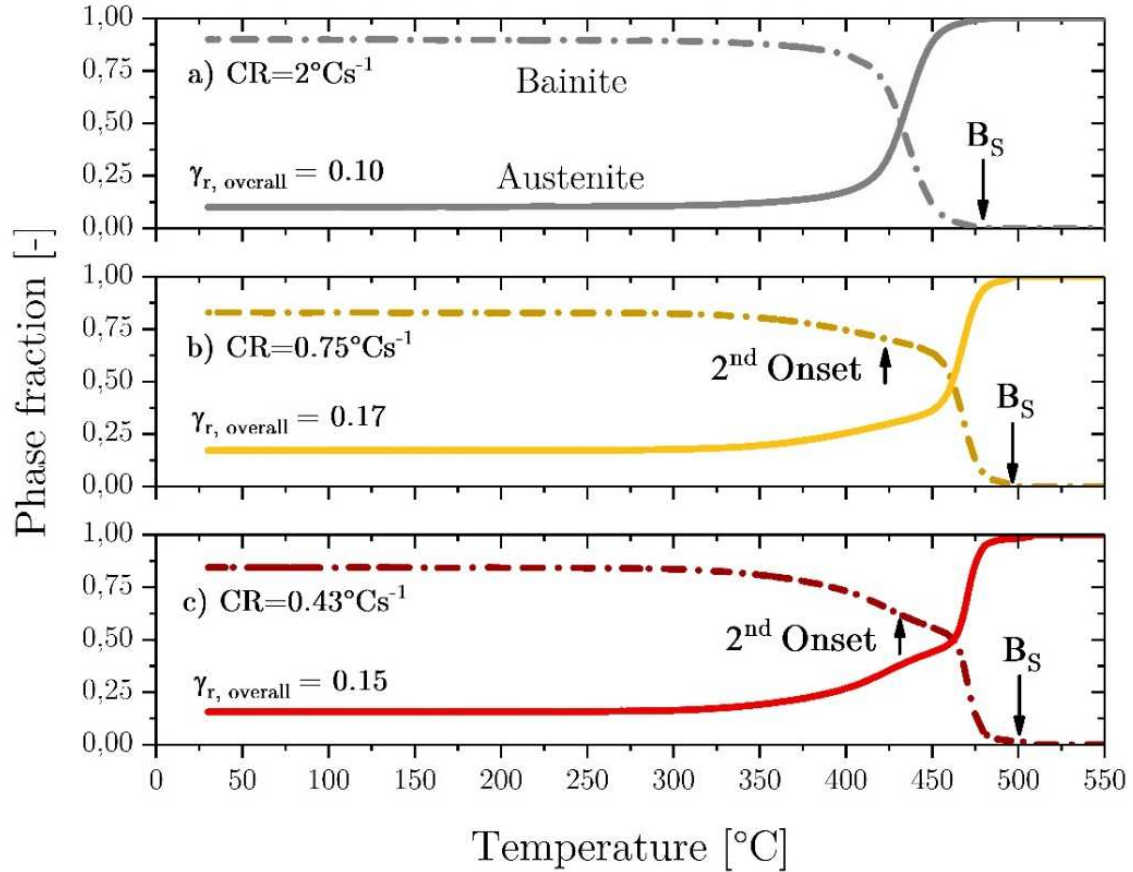


Figure 6.3: Transformation kinetics of austenite (solid lines) to bainitic ferrite (dot dashed lines) for cooling rates a)  $2^{\circ}\text{Cs}^{-1}$ , b)  $0.75^{\circ}\text{Cs}^{-1}$  and  $0.43^{\circ}\text{Cs}^{-1}$  observed by means of HEXRD.

### 6.1.3. Comparison of transformation kinetics obtained by dilatometry and high energy X-ray diffraction

Figure 6.4 compares the evolution of bainitic ferrite volume fraction for cooling rates 2, 0.75 and  $0.43^{\circ}\text{Cs}^{-1}$  obtained from dilatometer curves using the lever rule and HEXRD. The overall kinetics as obtained from both methods are in a good agreement for all cooling rates. However, a general shift of approximately  $5\text{-}20^{\circ}\text{C}$  can be observed between data obtained by these two methods.

A possible origin of this shift may be found in temperature heterogeneities of the specimen. Indeed, HEXRD is a localized analysis carried out in a limited volume

( $\sim 2\text{mm}^3$ ) around the temperature measurement point. In contrast, the information provided by dilatometry corresponds to changes occurring in the full length of the sample. Thus, any thermal (and/or chemical) heterogeneity in the sample will lead to a difference of results obtained by HEXRD and dilatometry.

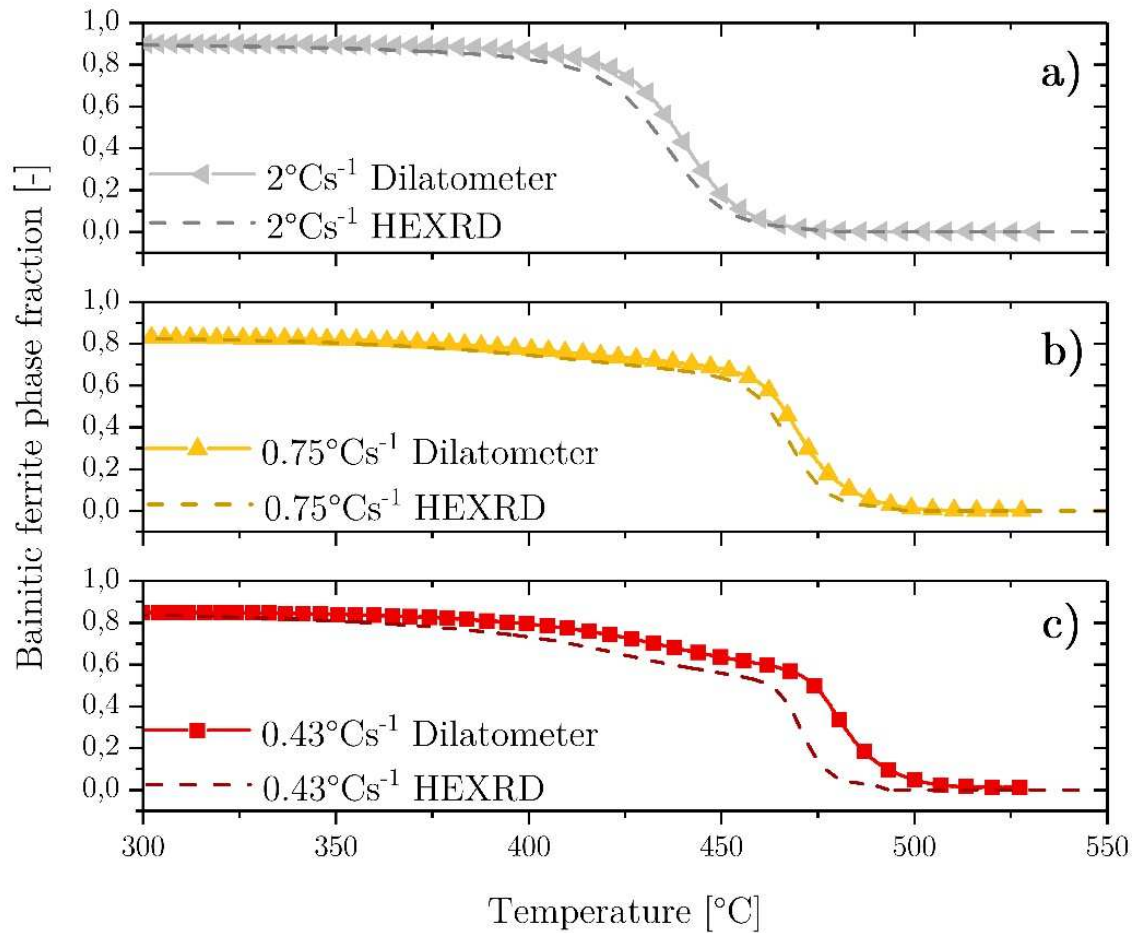


Figure 6.4: Comparison of the bainitic ferrite volume fraction obtained from dilatometer curves using the lever rule and HEXRD for cooling rates of a) 2, b) 0.75, and 0.43 °C s<sup>-1</sup>.

## 6.2 Characterization of the bainitic microstructure

### 6.2.1. Early stages of bainitic transformation during continuous cooling

To get an impression about the initial stages on the bainitic transformation interrupted quenching experiments with time-temperature profiles shown in **Figure 4.4a** were performed in the dilatometer. In order to provide information about the individual microstructure constituents, imaging was carried out on Nital etched samples using the secondary electron contrast by means of SEM. Since bainitic ferrite ( $\alpha_b$ ) is somewhat stronger attacked by the etchant, martensite ( $\alpha'$ ), partially decomposed martensite/austenite islands (M/A), retained austenite as well as undissolved carbides appear to be elevated in these images. It is important to note that retained austenite can exist in two distinct morphologies: films and blocks. As reported in literature [152] austenite films ( $\gamma_f$ ) are entrapped between neighbouring subunits of bainitic ferrite and blocks of retained austenite ( $\gamma_b$ ) are located between the sheaves of bainite.

**Figure 6.5a-b** shows representative SEM micrographs of the microstructures obtained after cooling with a rate of  $2^\circ\text{C s}^{-1}$  and  $0.43^\circ\text{C s}^{-1}$  to  $480^\circ\text{C}$  and subsequent quenching to room temperature. As might be expected, the microstructure is predominantly martensitic, but the stronger etched areas can be recognized as bainitic ferrite. From this presentation, it can be suspected that the formation of bainite begins with the nucleation of bainitic sub-units at prior austenite grain boundaries (PAG - red dashed line). Afterwards a new sub-unit nucleates at the former one and builds up the characteristic wedge-shaped sheave structure (black dashed line), which is consistent with literature [39–41]. Furthermore, the individual sub-units are partially separated by thin films of retained austenite. However, it cannot exclude that these films partially transform into martensite during the interrupted quenching to room temperature.

As already observed by dilatometry or HEXRD, the phase transformation from austenite to bainite, progresses from a continuous behaviour at higher cooling rates ( $>0.75^\circ\text{C s}^{-1}$ ) to a two-stage behaviour with a transformation stasis at lower cooling rates ( $<0.75^\circ\text{C s}^{-1}$ ). **Figure 6.6a-b** compares microstructures obtained after cooling with  $0.43^\circ\text{C s}^{-1}$  to quenching temperatures of  $455^\circ\text{C}$  (begin of stasis) and  $430^\circ\text{C}$  (end of stasis) respectively and subsequent quenching to room temperature. In both cases, the microstructure approximately consists of equal fractions of bainitic ferrite together with films of retained austenite and martensite. This fact clearly verifies the observed behaviour by dilatometry and HEXRD.



Figure 6.6c shows the microstructure obtained after cooling with  $0.43^{\circ}\text{C}\text{s}^{-1}$  to quenching temperature of  $390^{\circ}\text{C}$  respectively and subsequent quenching to room temperature. As can be seen from this micrograph, the degree of phase transformation progresses. The microstructure consists almost entirely of bainitic ferrite together with films and blocks of retained austenite. However, M/A constituents are slightly attacked by the etchant whereas the surface of blocky retained austenite appears smooth.

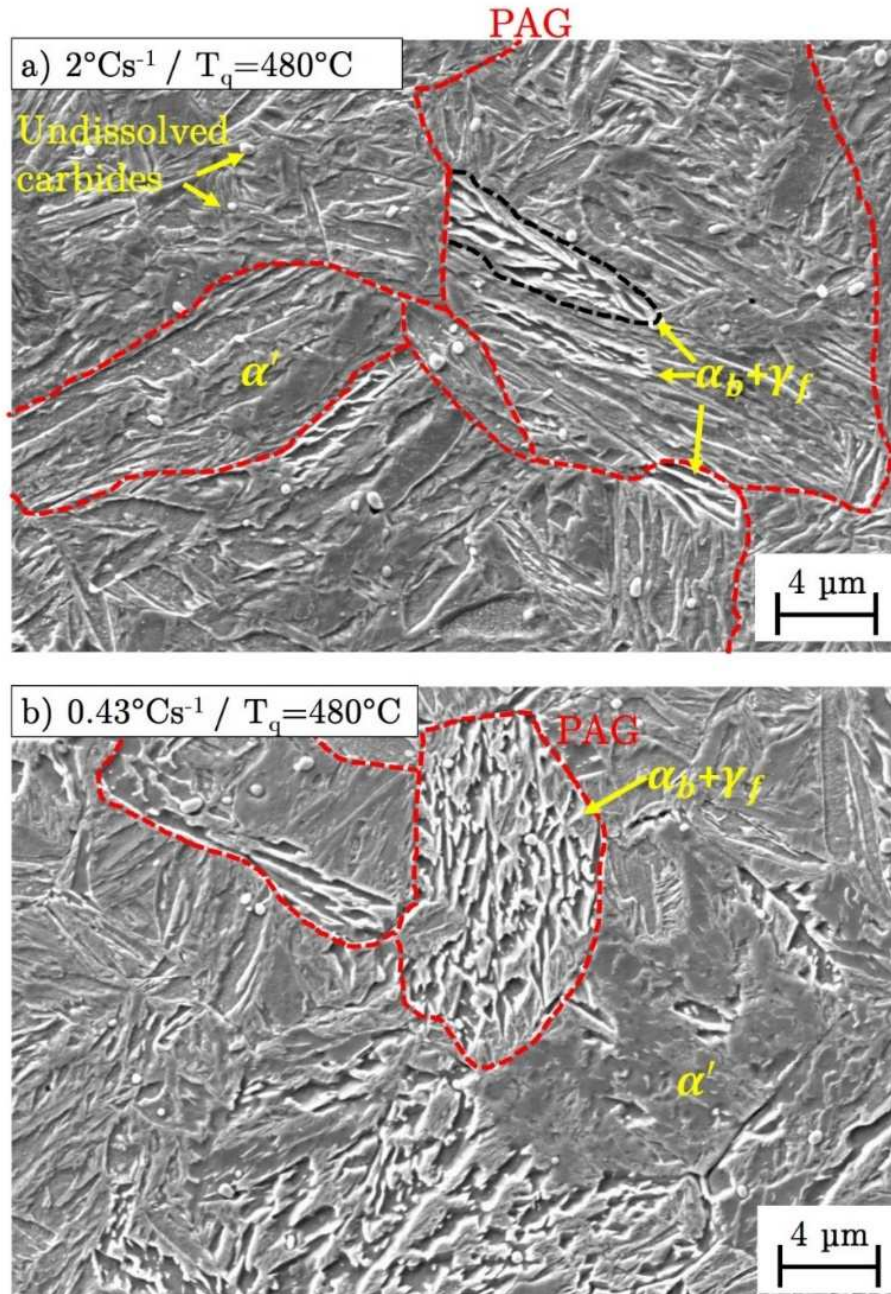


Figure 6.5: SEM micrograph after continuous cooling with a cooling rate of a)  $2^{\circ}\text{C}\text{s}^{-1}$  and b)  $0.43^{\circ}\text{C}\text{s}^{-1}$  to quenching temperature of  $480^{\circ}\text{C}$ , showing the early stages of the bainitic transformation.

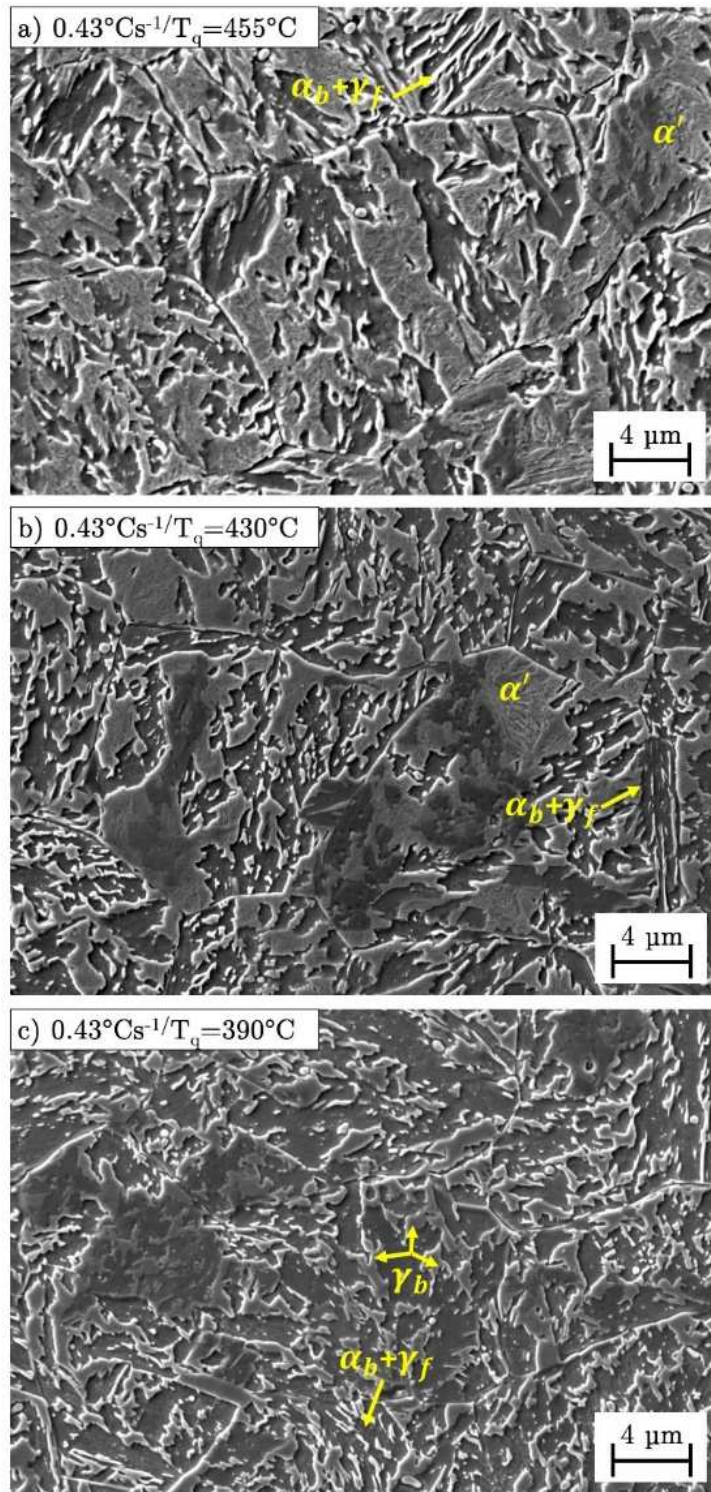


Figure 6.6: SEM micrograph after continuous cooling with a cooling rate of  $0.43^{\circ}\text{C s}^{-1}$  to quenching temperature of a)  $455^{\circ}\text{C}$  (begin of transformation stasis), b)  $430^{\circ}\text{C}$  (end of transformation stasis) and c)  $390^{\circ}\text{C}$ .

### 6.2.2. Microstructure after phase transformation

**Figure 6.7a-c** shows typical microstructures obtained by means of SEM after continuous cooling with 2, 0.75 and  $0.43^{\circ}\text{C}\text{s}^{-1}$  to room temperature. Independent on the cooling rate, the final microstructure consists of bainitic ferrite together with films and blocks of retained austenite. **The only difference is that the microstructure gets coarser with decreasing cooling rate.** This change in the bainitic microstructure has been investigated only to a very limited extent in literature [31,153,154]. A possible origin for this behaviour is recovery or recrystallization of individual sub-units during slow cooling conditions. In the case of recovery, it is the excess surface energy that creates the driving force, whereas during recrystallization, it is the stored energy due to defects such as dislocations or due to elastic strains in the lattice which provides the major component of the driving force for the reaction .

A detailed information regarding the characterization of the retained austenite morphology is given within **Paper A.2** in **Appendix A**. The findings are summarized in **Figure 6.7**. The amount of blocky retained austenite was identified using the EBSD technique.

**Figure 6.8a-c** shows an overlay of EBSD image quality maps with phase maps of ferrite (red) and austenite (green) for the cooling rates 2, 0.75 and  $0.43^{\circ}\text{C}\text{s}^{-1}$ , respectively. Analysing these images with respect to the amount of retained austenite delivered an increase from  $2\pm 0.5$  vol.% to  $10\pm 0.5$  vol.% with decreasing the cooling rate from  $2^{\circ}\text{C}\text{s}^{-1}$  to  $0.43^{\circ}\text{C}\text{s}^{-1}$ . The remaining black areas can be attributed to M/A constituents, due to their higher dislocation density and, therefore, lower image quality parameter [154,155]. The amount of M/A constituents remains approximately constant at about  $1.5\pm 0.5$  vol.%.

To characterize the film-like retained austenite, the microstructure was examined by means of TEM. **Figure 6.8d-f** shows TEM bright field images of specimens cooled with rates of 2, 0.75 and  $0.43^{\circ}\text{C}\text{s}^{-1}$  together with the corresponding dark field images and the selected area diffraction (SAD) pattern of retained austenite films between individual bainitic subunits. The investigations indicate that the thickness of such a retained austenite film is in the magnitude of 20 to 100 nm, which is consistent with literature [156].



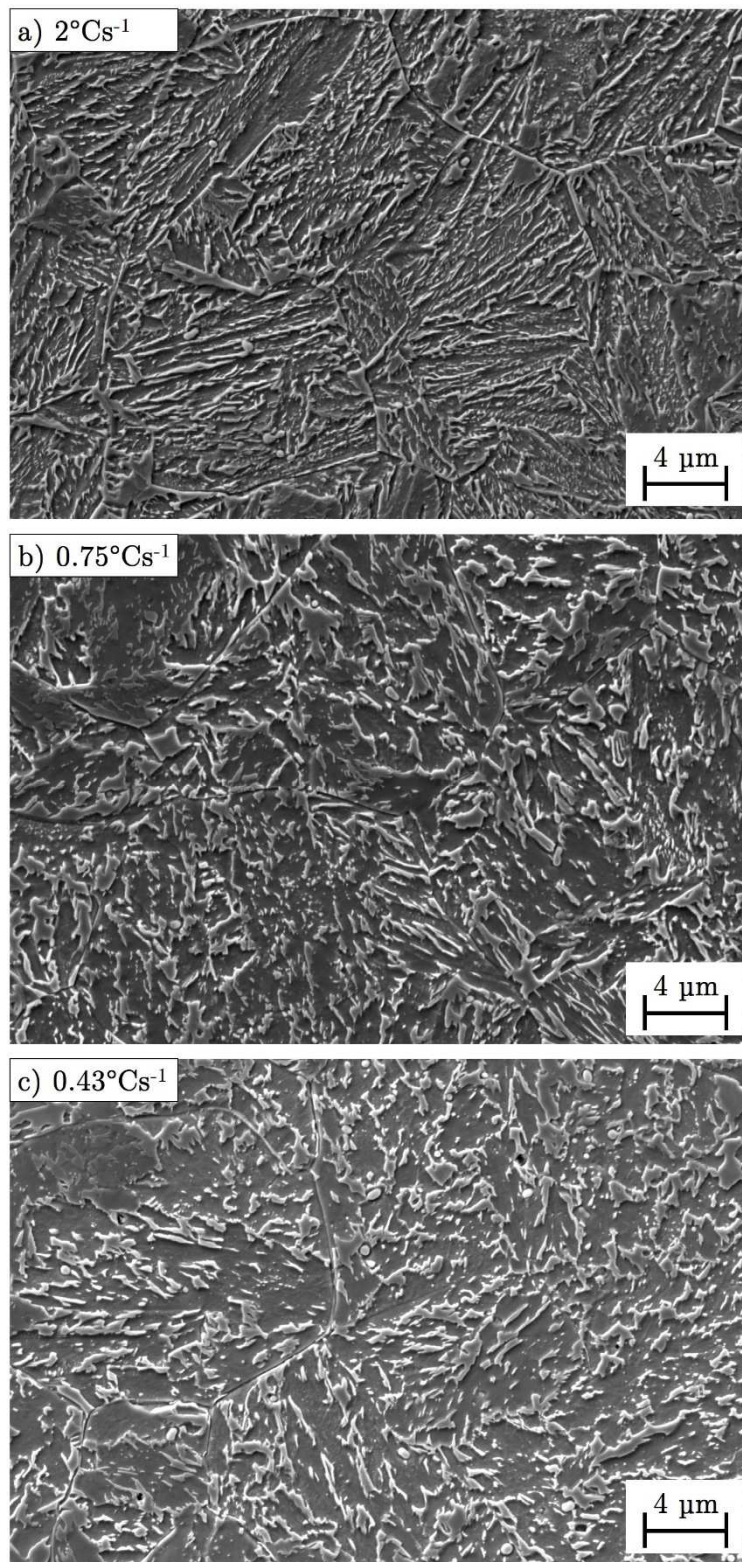


Figure 6.7: Representative SEM micrographs of microstructures obtained after continuous cooling with a cooling rate of a) 2°Cs<sup>-1</sup>, b) 0.75°Cs<sup>-1</sup> and c) 0.43°Cs<sup>-1</sup> to room temperature.

TEM was also used for carbide characterization. The investigations reveal that carbides of type  $M_6C$  are present in the microstructure after all applied cooling rates. **Figure 6.9a** shows a TEM bright field image of the bainitic microstructure including a  $M_6C$ -type carbide with the corresponding SAD pattern after continuous cooling with  $0.75^\circ\text{Cs}^{-1}$ , respectively. These findings are consistent with results obtained by means of HEXRD, where an austenitization temperature of  $1020^\circ\text{C}$  leads to an incomplete dissolution of  $M_6C$  carbides.

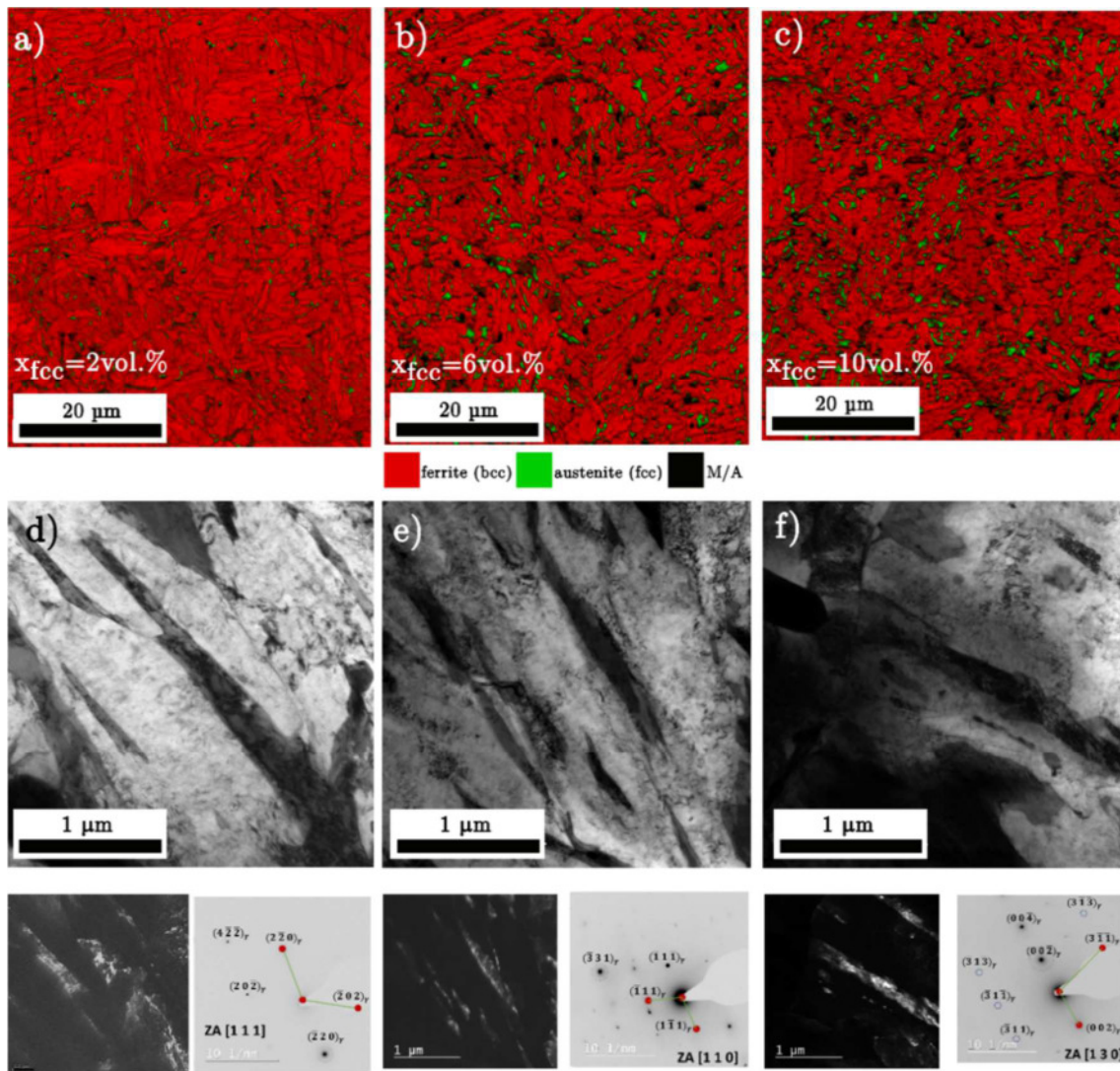


Figure 6.8: Phase map of blocky retained austenite after continuous cooling with a)  $2^\circ\text{Cs}^{-1}$ , b)  $0.75^\circ\text{Cs}^{-1}$  and c)  $0.43^\circ\text{Cs}^{-1}$ ; TEM bright field images with the corresponding SAD pattern and dark field image of film austenite after continuous cooling with d)  $2^\circ\text{Cs}^{-1}$ , e)  $0.75^\circ\text{Cs}^{-1}$  and f)  $0.43^\circ\text{Cs}^{-1}$  after Paper A.2 in Appendix A.

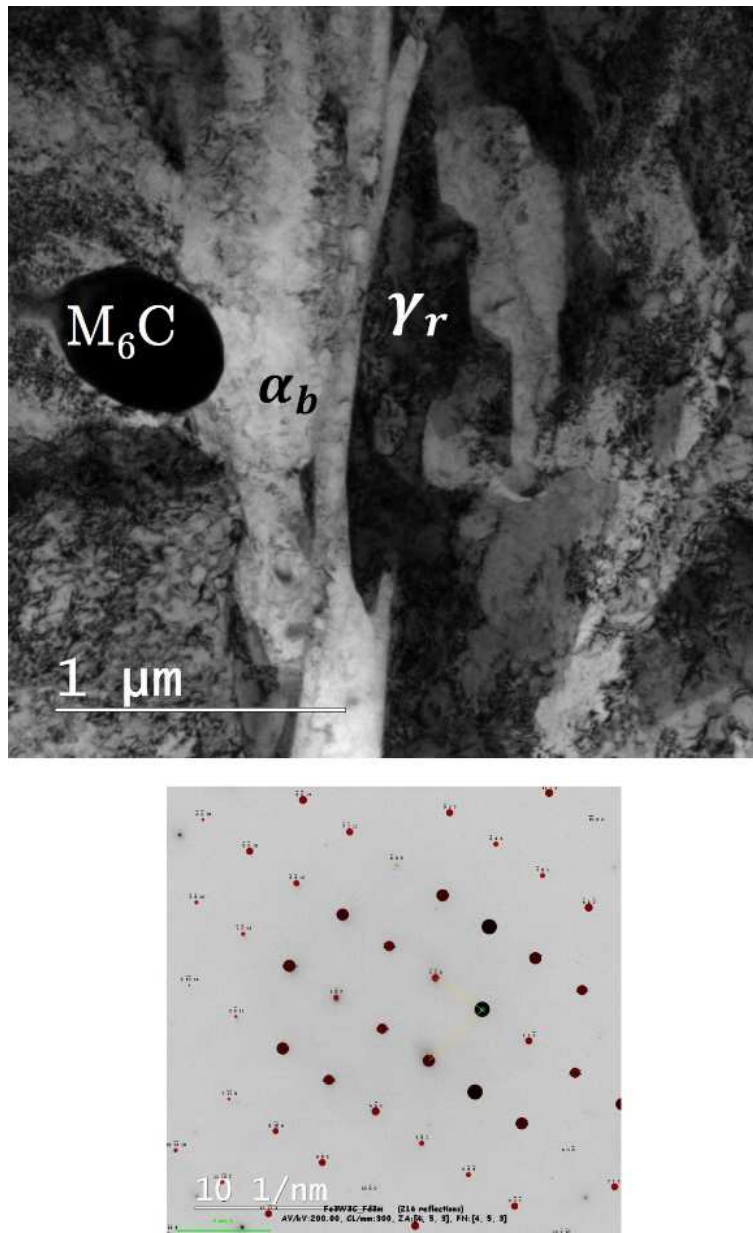


Figure 6.9: TEM bright field image showing a  $M_6C$  carbide with their corresponding SAD pattern on the bottom.



## 6.3 Carbon in bainitic ferrite and retained austenite

### 6.3.1. Overall carbon distribution during transformation

The overall carbon content in bainitic ferrite and austenite during phase transformation was measured using their lattice parameters. Therefore, **Figure 6.10a-c** shows the evolution of austenite and bainitic ferrite lattice parameter during the bainitic reaction ( $\gamma \rightarrow \alpha_b$ ) and subsequent cooling to room temperature for cooling rates 2, 0.75 and  $0.43^\circ\text{C s}^{-1}$ . The beginning of the phase transformation is indicated by the bainite start temperature ( $B_s$ ).

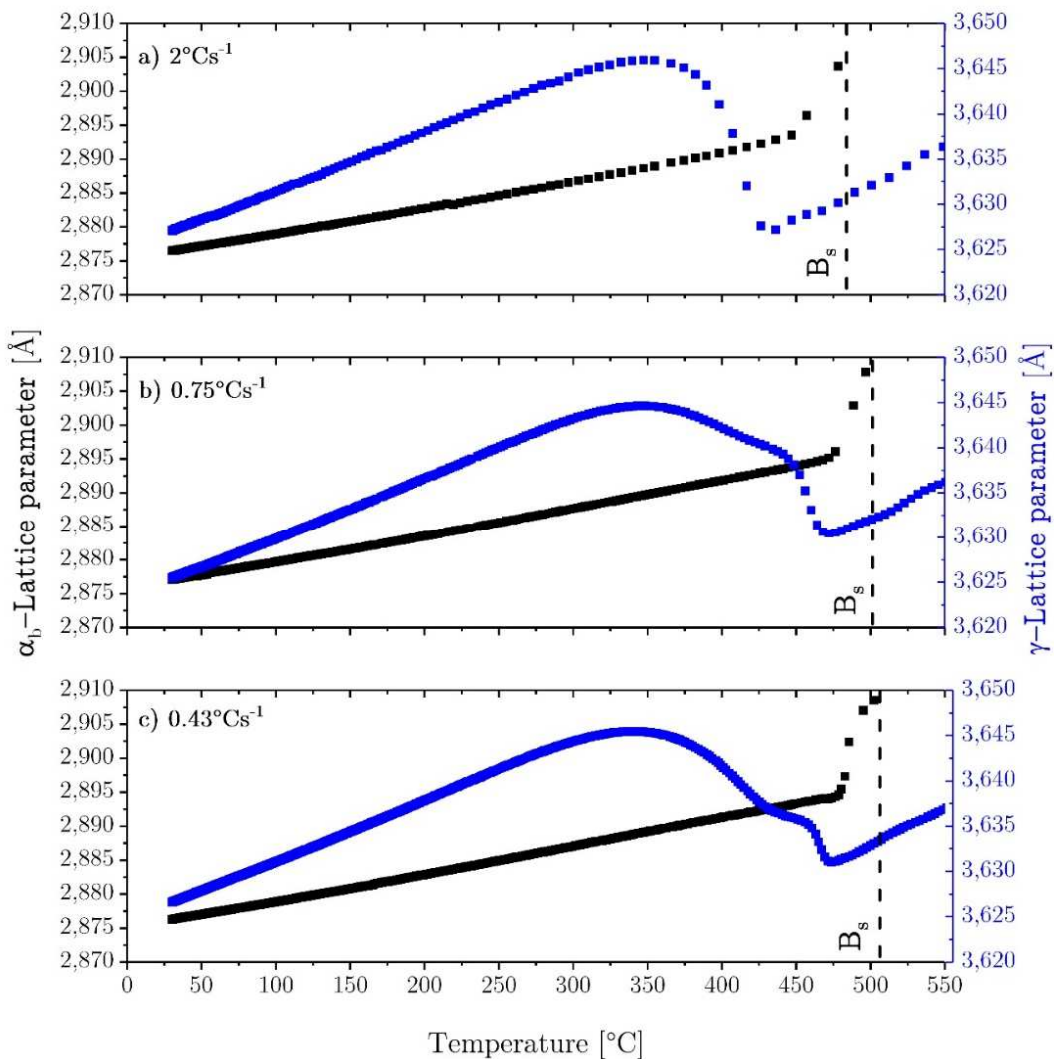


**Figure 6.10:** Evolution of bainitic ferrite and austenite lattice parameter during phase transformation and subsequent cooling to room temperature for cooling rates a) 2, b) 0.75 and c)  $0.43^\circ\text{C s}^{-1}$ .

During the early stages of transformation, the bainitic ferrite lattice parameter is observed to decrease from  $2.905\text{\AA}$  to approximately  $2.8944\text{\AA}$  and follows afterwards a straight trend over all cooling rates, which corresponds, to a constant carbon content in bainitic ferrite. According equation (9), the carbon content of bainitic ferrite can be determined to 0.14, 0.136 and  $0.132\pm 0.01$  wt.-% for cooling rates 2, 0.75 and  $0.43^\circ\text{Cs}^{-1}$ , respectively.

The austenite lattice parameter shows a strong increase during the phase transformation. The corresponding enrichment of carbon in austenite according the calculation scheme outlined in equation (8) is separately shown in **Figure 6.11**. Therefore, the final carbon content in austenite can be determined to 1.55, 0.95 and  $1.1\pm 0.01$  wt.-% for cooling rates 2, 0.75 and  $0.43^\circ\text{Cs}^{-1}$ , respectively.

It should be noted that the evolution of the austenite lattice parameter as well as the corresponding carbon content also shows a stepped behaviour for cooling rates lower than  $0.75^\circ\text{Cs}^{-1}$  during the phase transformation as compared with the observed transformation kinetics by means of dilatometry and HEXRD.

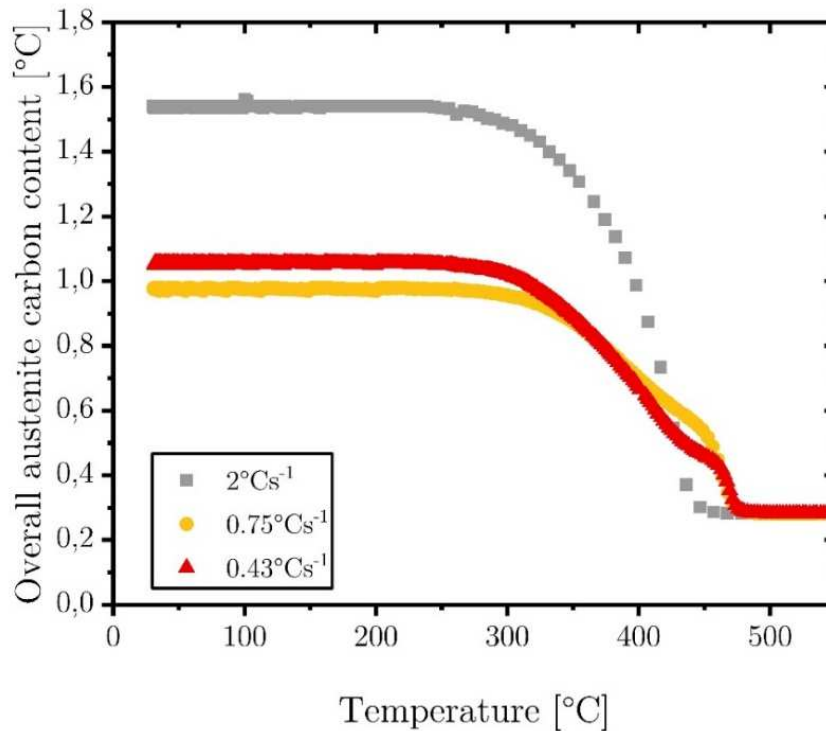


Figure 6.11: Carbon enrichment of austenite versus temperature during phase transformation for cooling rates 2, 0.75 and  $0.43^\circ\text{Cs}^{-1}$  as determined from HEXRD data.

In general, the observed behaviour coincides with the theory of diffusionless growth of bainitic ferrite, whereas the nucleation of individual sub-units occurs under

paraequilibrium conditions and the growth proceeds totally diffusionless [33]. Therefore, the sub-unit inherits the chemical composition of the former austenite during growth, thus the bainitic ferrite is supersaturated with carbon. As a consequence of the high transformation temperatures (350-510°C), much of the excess carbon partitions in the remaining austenite after the phase transformation [37], but some carbon still remains within the bainitic ferrite, either in solid solution or trapped at defects.

### 6.3.2. Local carbon distribution on bainitic ferrite/austenite interface

**Figure 6.12a-c** shows 3D-carbon atom maps of samples cooled down with 2, 0.75 and 0.43°Cs<sup>-1</sup>. It can be seen that the distribution of carbon atoms in the analysed volume is not uniform and carbon-rich and carbon-depleted regions are distinguishable. As no crystallographic information is available by means of APT, the carbon-enriched regions (5-9 at.-%) of the atom maps are assumed to represent austenite and the carbon-depleted regions (0.2-0.55 at.-%) represent bainitic ferrite. Additionally, concentration profiles of C, Mo, Cr and V across these interfaces (designated by an arrow) are shown in **Figure 6.12**. The concentration profiles indicate that no significant segregation of substitutional elements occur to the austenite–ferrite interface. These results are fully consistent with the diffusionless phase transformation of austenite to bainite [1]. A comparison of the carbon content in bainitic ferrite and austenite obtained by means of APT and HEXRD are presented in **Table 6.1**. For a better comparability all values are given in at.-% and wt.-%.

**Table 6.1:** Comparison of carbon content in bainitic ferrite and austenite observed by means of HEXRD and APT.

Cooling rate	HEXRD analysis				APT			
	Austenite		Bainitic ferrite		Austenite		Bainitic ferrite	
	[at.-%]	[wt.-%]	[at.-%]	[wt.-%]	[at.-%]	[wt.-%]	[at.-%]	[wt.-%]
2°Cs <sup>-1</sup>	7.21	1.55	0.65	0.140	8.20	1.76	0.35	0.075
	±0.05	±0.01	±0.05	±0.01	±0.90	±0.20	±0.20	±0.04
0.75°Cs <sup>-1</sup>	4.56	0.98	0.63	0.136	7.35	1.58	0.35	0.075
	±0.05	±0.01	±0.05	±0.01	±1.52	±0.33	±0.20	±0.04
0.43°Cs <sup>-1</sup>	5.12	1.10	0.62	0.132	5.79	1.25	0.32	0.069
	±0.05	±0.01	±0.05	±0.01	±0.7	±0.15	±0.10	±0.02

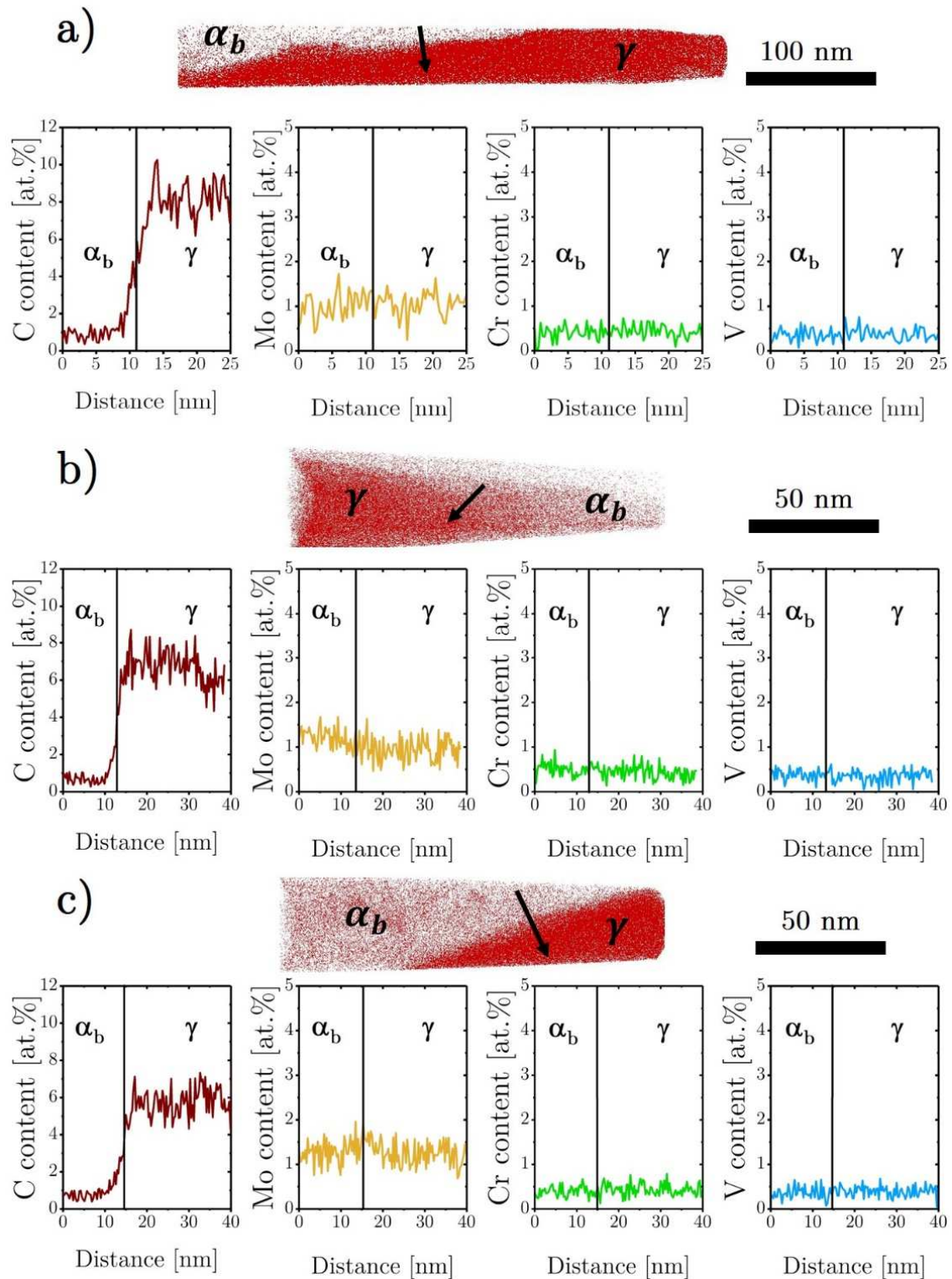


Figure 6.12: 3D carbon atom maps of austenite/bainitic ferrite interface with corresponding concentration profiles of C, Mo, Cr and V for cooling rates a) 2, b) 0.75 and c) 0.43°Cs<sup>-1</sup>.

Additionally, it should be noted that the presented carbon values are determined from selected volumes of each phase that did not contain any carbon enriched regions, such as dislocations or phase boundaries. The APT carbon contents of austenite reveal higher values than those measured by HEXRD analysis. As reported in literature [32, 36, 37] and also shown in this thesis, retained austenite typically exhibits film or block morphologies. Both morphologies are enriched in carbon, but films are stronger enriched due to their geometrical isolation between bainitic sub-units [72]. Since the analysed volume by HEXRD is approximately  $2\text{mm}^3$ , the provided information stems from both morphologies and hence explain the observed difference. Furthermore, it can be assumed that the presented austenite regions by APT corresponds to austenite films, because all values exceed the HEXRD results.

Conversely, the APT carbon contents of bainitic ferrite reveal lower values than those measured by HEXRD analysis. A possible origin of this difference can be explained by the presence of M/A constituents. Mazancova and Mazanec [84] pointed out that the formation of M/A constituents is typical for slow continuous cooling conditions and high transformation temperatures. Under these circumstances, carbon gradients in austenite can be reduced relatively quickly, carbon diffusion can occur over wider distances and the final mean carbon content of the retained austenite blocks ends up above the critical concentration given by the  $T_0'$ -line [33]. Consequently, these blocks do not transform into bainite but they do decompose partially into carbon rich martensite during further cooling at lower temperature. **Figure 6.13** shows a 3D carbon atom map of a supposed M/A constituent together with a carbon concentration profile along the marked arrow. It can be clearly seen from the concentration profile that the carbon varies between 3.5 and 2.5 at.-%.

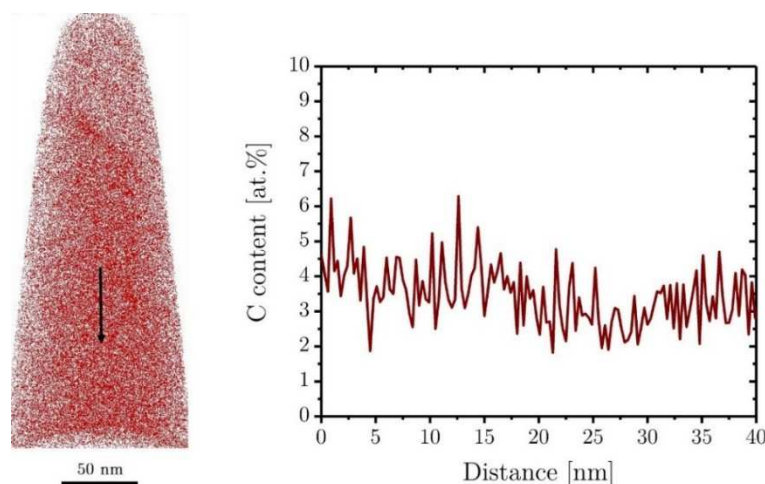


Figure 6.13: 3D carbon atom map of an M/A constituent with corresponding concentration profile of C along the carbon enriched region, designated by the arrow.



### 6.3.3. Carbon trapped at defects

The growth of bainite in steels is accompanied by a shape change of the transformed austenite, a change which is known as an invariant-plane strain with a large shear component. When the transformation occurs at temperatures where the shape change cannot be accommodated elastically, the plastic deformation that is driven by the shape change causes the accumulation of relatively high dislocation densities of approximately  $5 \times 10^{15} \text{m}^{-2}$  in both, the parent and product phase [44]. As auto-tempering accompanies the transformation, some excess carbon in bainitic ferrite may segregate to defects e.g. dislocations or carbon forms clusters [73].

Segregation of carbon to dislocations can be classified as Cottrell atmospheres, where the carbon concentration is typically around 6–8 at.-% [94,157], whereas clusters are considered to represent Fe-C nano-agglomerates that appear randomly distributed within the polycrystalline microstructure and inherit a carbon concentration in the order of 12-14 at.-% [94].

A 3D carbon atom map obtained from a sample continuous cooled with  $2^\circ\text{C s}^{-1}$  is shown in **Figure 6.14a**. The carbon enriched regions at the left and right side of the tip represent austenite and the low carbon regions indicate the bainitic ferrite. **Figure 6.14b** shows a magnified carbon 2D contour plot of the bainitic ferrite region marked in **Figure 6.14a**. A 2D carbon contour plot represents a projection of all carbon atoms onto an arbitrary projection plane. The shown 2D contour plot reveals an inhomogeneous carbon distribution within the bainitic ferrite region. Furthermore, some linear features with higher carbon content (marked with black arrows) can be observed. It can be suspected that these features represent dislocations in bainitic ferrite. Evaluation of such a carbon hot spot reveals carbon contents around 6–10 at.-%, which would coincide with the segregation of carbon to dislocations [94], **Figure 6.14c**.

The segregation of carbon to dislocations would also explain the lack of carbides in the bainitic microstructure. Kalish and Cohen [158] investigated the tempering behaviour of steels containing 0.2-0.45 wt.-% carbon and found that carbon which is segregated to dislocations is stabilised and retards carbide precipitation, because the segregation itself leads to a reduction in free energy.

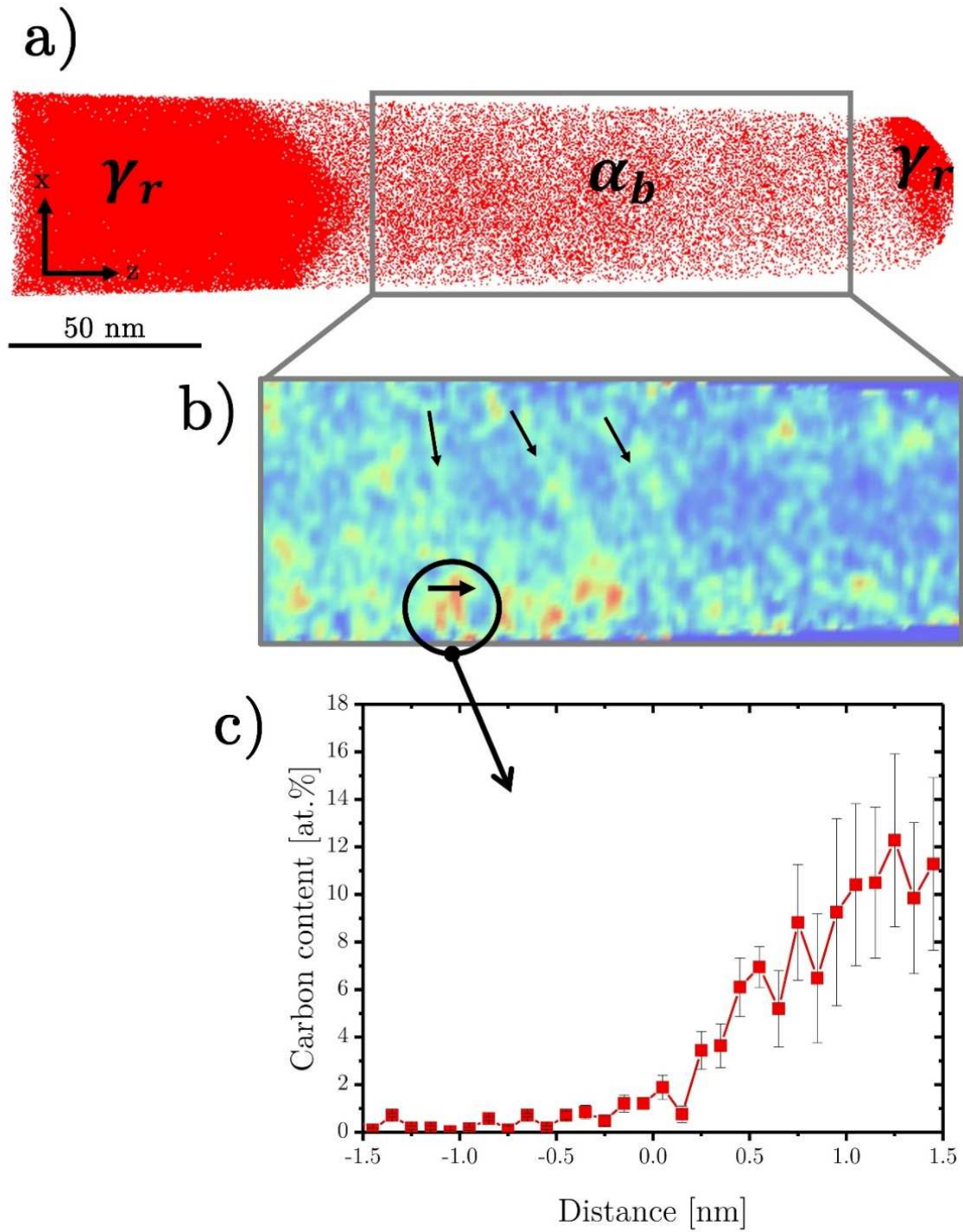


Figure 6.14: a) 3D carbon atom map of a sample cooled with  $2^\circ\text{C/s}^{-1}$  shows a bainitic subunit between retained austenite, b) corresponding 2D-contour plot of the marked bainitic ferrite region indication carbon enriched linear features (black arrows), and c) carbon profile across a highly enriched carbon region.

## 6.4 Discussion of the bainitic reaction during continuous cooling

### 6.4.1. The incomplete transformation phenomenon

The analysis of dilatometer and HEXRD experiments clearly shows that the continuously cooled bainite transformation characteristics change from a continuous single-stage behaviour at fast cooling rates ( $2^{\circ}\text{Cs}^{-1}$ ) to a distinct two-stage behaviour at lower cooling rates ( $0.43^{\circ}\text{Cs}^{-1}$ ), **Figures 6.1 and 6.2**. The observed change in the transformation behaviour at lower cooling rates can be attributed to the incomplete transformation phenomenon (ICT). The nature of the ICT can be explained by the T<sub>0</sub>-temperature theory. The T<sub>0</sub>-temperature is defined as the temperature, where austenite and ferrite of the same composition have the same Gibbs free energy. According [55], austenite with a carbon concentration in excess of that defined by the T<sub>0</sub> curve, cannot transform without an adequate change in composition between the parent and product phase. Thus, any diffusionless transformation involving a supersaturation of carbon can only occur below the appropriate T<sub>0</sub> temperature. The T<sub>0</sub> concept also accounts for the fact that during the growth of bainite, untransformed austenite continuously absorbs carbon rejected from supersaturated bainitic ferrite [60]. As a consequence, the actual T<sub>0</sub> temperature is decreasing, thus eventually a certain point would be reached where diffusionless formation of bainite is thermodynamically impossible.

Bhadeshia [33] estimated that there is an elastic strain energy of  $400\text{Jmol}^{-1}$  related with the diffusionless growth of bainitic ferrite, thus he proposed a new T<sub>0</sub>'-limit that is in core similar to the T<sub>0</sub>-limit but also takes into account the stored strain energy. As reported in **Paper A.2** in **Appendix A** the observed transformation behaviour can be explained by an adopted T<sub>0</sub>'-limit concept taking an additionally required strain energy between  $950$  and  $1100\text{Jmol}^{-1}$  in the energy balance into account. Therefore, the observed transformation kinetics at lower cooling rates ( $>0.75^{\circ}\text{Cs}^{-1}$ ) can be consistently described as a four-stage process, **Figure 6.15**:

- Stage I. Fast grain boundary nucleation of bainitic subunits and stabilization of film-like retained austenite due to carbon enrichment,
- Stage II. further carbon enrichment in austenite leads to a stasis in the transformation, according the T<sub>0</sub>'-concept,
- Stage III. further transformation of the remaining austenite as well as long range diffusion of carbon in austenite leads to a stabilization of blocky retained austenite, and

Stage IV. end of transformation and formation of M/A-constituents.

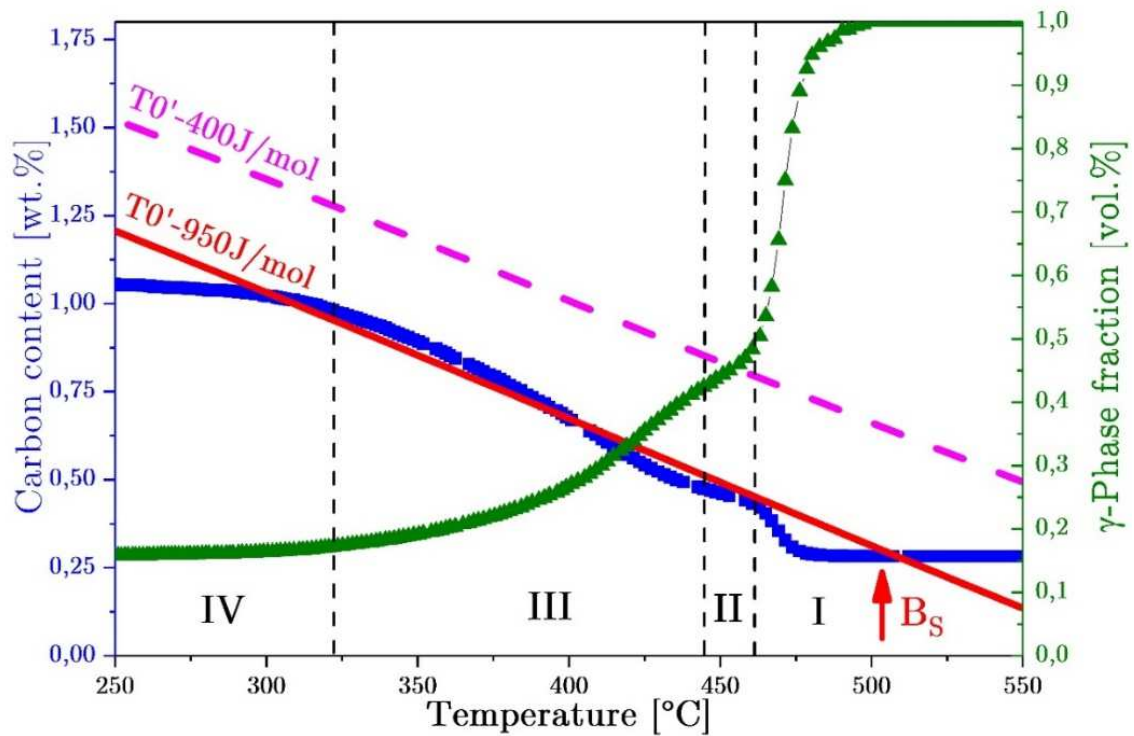


Figure 6.15: The transformation processes which occur in the investigated steel during continuous cooling with cooling rates lower than 0.75K/s can be separated into four main stages: I) Beginning of transformation and stabilization of film-like retained austenite, II) transformation stasis, III) further transformation of the remaining austenite and stabilization of blocky retained austenite, and IV) end of transformation and formation of M/A-constituents after Paper A.2 in Appendix A.

The T0 theory competes with two other theory's, the solute-drag and WBs theory. Both theories will be short explained in the following paragraphs.

### **The solute drag theory:**

Bradley and Aaronson [17] relate the ICT to a solute-drag-like effect (SDLE), which states that the concentration of substitutional alloying elements that have a strong interaction with carbon increases at a migrating ferrite/austenite interface. This may lead to a decrease of the activity of carbon in the austenite in immediate contact with the interfaces, which in turn decrease the activity gradient of carbon in front of the interface and cause sluggish transformation kinetics. This SDLE theory was adopted by Reynolds et al. [62] and Goldenstein and Aaronson [63] to explain the ICT phenomena observed in several high-purity ternary alloys, e.g. Fe-C-Mo, Fe-C-Mn and

Fe–C–Cr. The APT results in **chapter 6.3.2** clearly indicate that there is no significant segregation of substitutional atoms on the bainitic ferrite/austenite interfaces, which would sluggish the transformation kinetics. Therefore, a purely solute drag effect cannot explain the observed transformation kinetics in the present study.

**The  $WB_s$  theory:**

Hillert [159] studied the lengthening rates of acicular ferrite in Fe–C binary alloys and found that the extrapolation of measured growth rates to zero velocity did not yield the equilibrium carbon concentration of austenite. He directly related this effect to what was later described as the ICT phenomenon and proposed that there is a thermodynamic barrier to the growth of acicular ferrite. The results did not indicate any differences between Widmanstätten ferrite at higher temperatures and bainitic ferrite at lower temperatures. He postulated that the growth mechanism of both is essentially the same and defined a critical carbon content of austenite, above acicular ferrite cannot growth, the so-called  **$WB_s$  limit**.

Hillert validated the  $WB_s$  theory by examining published data in some alloy steels showing a transformation stasis and found that these data could be fitted equally well with the  $WB_s$  limit as well as the and T0' concept. In most alloys investigated, the shift of  $WB_s$  by addition of substitutional elements can be well explained purely by thermodynamic effect; in Mo or Cr added alloys, however, an additional amount of energy needs to be added to the growth barrier obtained in Fe–C systems, which is suggested to originate from solute drag effect. Following the findings by Hillert and considering additional energy efforts for Mo and Cr due to a solute drag effect, the  $WB_s$  limit in  $Jmol^{-1}$  as a function of transformation temperature can expressed as follows [159]:

$$WB_s = 3919T - 5.85 + 0.8(T - 573)w_{Mo} + 0.35(T - 573)w_{Cr} \quad (14)$$

In this formula T represents the absolute temperature in Kelvin and  $w_{Mo}$  and  $w_{Cr}$  represents the mole fraction of Mo and Cr in the alloy. After calculating the  $WB_s$  limit in this way, the determined values can be taken as undercooling's from paraequilibrium using MatCalc, thus the  $WB_s$  limit can represented as a function of the carbon content [60].

A comparison of the calculated  $WB_s$  limit (with and without solute drag effort) as a function of carbon content in austenite and the T0' line is shown in **Figure 6.16**, As can be seen, both calculated  $WB_s$  lines do not fit very well with the experimental data. The  $WB_s$  limit with solute drag effort undergoes the experimental data in the

range where the phase transformation occurs. According to this theory the phase transformation would start at approximately 300°C. In contrast, the shown  $WB_s$  limit without any solute drag effects would lead to a bainite start temperature wide above the observed one.

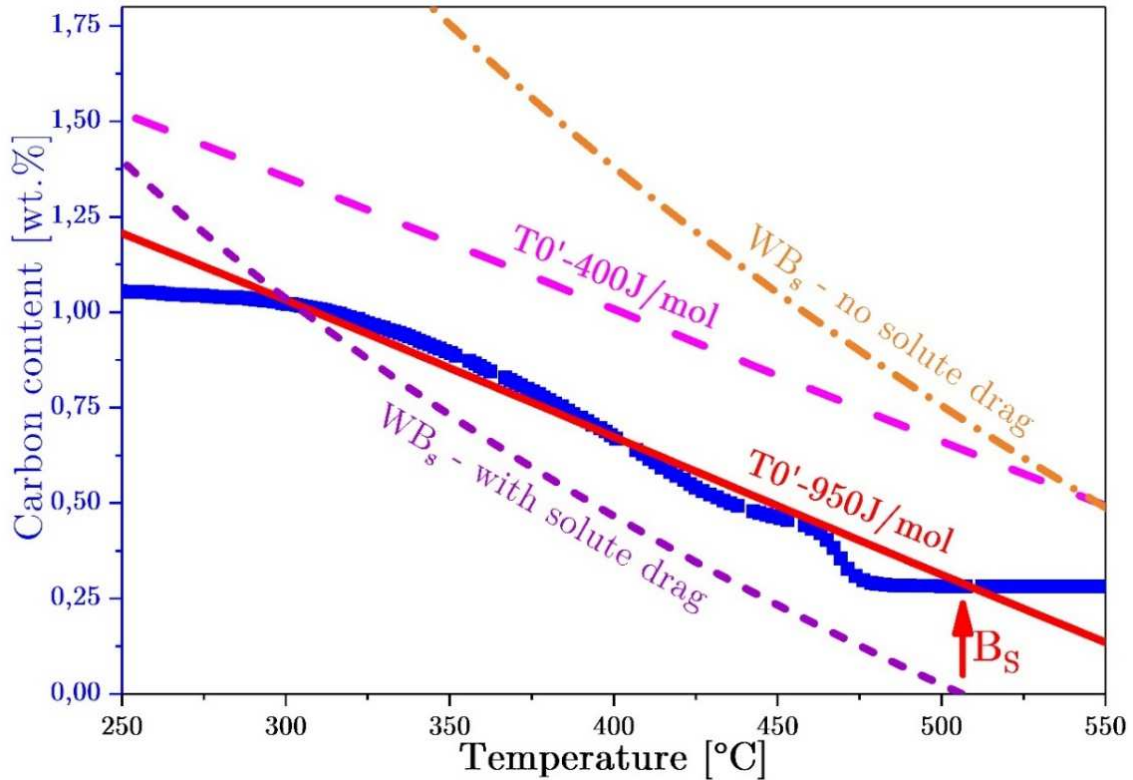


Figure 6.16: Comparison of carbon concentration in austenite during the phase transformation measured by HEXRD with  $T0'$  and  $WB_s$  lines.

#### 6.4.2. Excess carbon in bainitic ferrite

In this discussion part, the adjective excess implies a greater carbon concentration in bainitic ferrite than the solubility of carbon in  $\alpha$ -ferrite that is in equilibrium with  $\gamma$ -austenite. The maximum carbon solubility in  $\alpha$ -ferrite at 723°C in equilibrium equals to 0.02 wt.-% and decreases with decreasing temperature. Considering usual bainite transformation temperatures of 350-550°C the carbon solubility in equilibrium ranges between 0.005 wt.-% at 350°C to 0.012 wt.-% at 550°C.

The results by means of HEXRD in chapter 6.3.1 regarding the carbon content in bainitic ferrite revealed carbon concentrations of 0.14 wt.-% which are on average 16 times higher than expected from equilibrium at usual bainite start temperatures (350°-550°C). However, as already stated earlier, the provided information by

HEXRD stems from an analysed volume of approximately  $2\text{mm}^3$ . The carbon content of 0.14 wt.-% obtained in this manner contains carbon fractions from bainitic ferrite, highly enriched martensite and also from trapped carbon at defects, which is consistent with literature [51,53]. Hence, the carbon concentrations determined by HEXRD should be considered as a maximum value of carbon in all ferritic phases.

Nevertheless, APT also reveal high levels of excess carbon in solid solution (0.075 wt.-%) in the bainitic ferrite compared to equilibrium values at usual bainite start temperatures of 350-550°C. Recent APT studies by Caballero et al. [61] and Pereloma et al. [52] on nano-bainitic steels containing high amounts of carbon (>0.8 wt.-%) and silicon (>1.5 wt.-%) revealed substantial quantities of carbon in solid solution up to 0.3 wt.-%. The fact that carbon remains in solid solution in spite of prolonged isothermal heat treatment at temperatures around 200-400°C where it can easily partition into the residual austenite suggests that the bainitic ferrite is also tetragonal disordered. Jang et al. [54] assumed that there may exist an equilibrium state between tetragonal ferrite (BCT) and austenite. Therefore, they performed first thermodynamic principle calculations using a BCT structure for ferrite instead of the body centered cubic (BCC). These calculations show that the solubility of carbon in BCT ferrite dramatically increases relative to the cubic form of ferrite, **Figure 6.17a**.

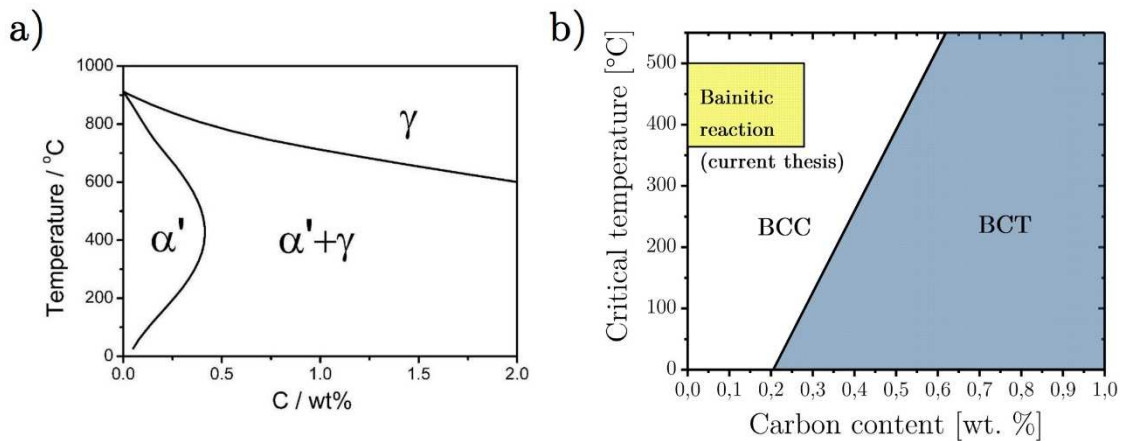


Figure 6.17: a) Increase of carbon solubility, allowing the body centred tetragonal ferrite phase (BCT) instead of the body centered cubic ferrite phase (BCC) to be in equilibrium with austenite in a binary Fe-C system after Jang et al. [54]; b) Critical temperature for the change of the BCC structure to BCT structure as a function of the carbon content according to Zener [36].

However, to preserve this tetragonality, it is suspected that the carbon must remain ordered in form of the BCT structure. According Zener [36], at each carbon concentration a critical temperature exists below which the ordered structure (BCT) is thermodynamically more advantageous than the disordered one (BCC). **Figure 6.17b** shows the trend of that critical temperature as a function of the carbon content which separates the BCC from the BCT structure according Zener [36]. As observed from dilatometry and HEXRD the bainitic reaction for the present steel takes place in the BCC region. This is also reflected by the diffractograms, where no evidence of tetragonality was observed.

However, the bainitic reaction occurs under paraequilibrium conditions, where the bainitic sub-unit inherits the chemical composition of the former austenite during growth, thus the bainitic ferrite is supersaturated with carbon. As a consequence of the high transformation temperatures (200-550°C), much of the excess carbon partitions in the remaining austenite after the phase transformation [37]. Nevertheless, some carbon remains within the bainitic ferrite. The remaining carbon in bainitic ferrite should be in the extent, which is given by the paraequilibrium (PE) between bainitic ferrite and austenite.

Caballero et al. [50], investigated the carbon supersaturation of bainitic ferrite using APT in a medium carbon (0.3 wt.-%) and low silicon steel (0.25 wt.-%) under isothermal conditions in a range between 380-525°C. The investigations showed that the supersaturation of carbon in solid solution in bainitic ferrite increases with decreasing transformation temperature. **Figure 6.18** shows the APT results regarding the carbon content in solid solution in bainitic ferrite from [50] together with the values obtained in this thesis and their corresponding paraequilibrium phase boundary between bainitic ferrite and austenite. Please note that the APT values from the current thesis are set to temperatures, which correspond to 50% of phase transformation according the individual cooling rate. It can be seen that the carbon concentrations from [50] exceeds their paraequilibrium phase boundary at transformation temperatures below 475°C, whereas the carbon concentrations found in this thesis are slightly higher than the paraequilibrium phase boundary. Nevertheless, the experimental APT data also shows an increase of carbon supersaturation in solid solution in bainitic ferrite with decreasing transformation temperature compared to literature [50]. The obtained values are in good agreement with the PE growth theory of bainite. These results assists the displacive view of the bainitic reaction, where the bainitic ferrite grows supersaturated with carbon independent of the transformation temperature.

Furthermore, can be seen that the PE phase boundary for the steel under investigation is approximately 2.5 times higher, compared to literature [50]. This can be



related to the higher Mo content in the present steel, which results to an expansion of the lattice and a higher solubility for interstitial alloying elements.

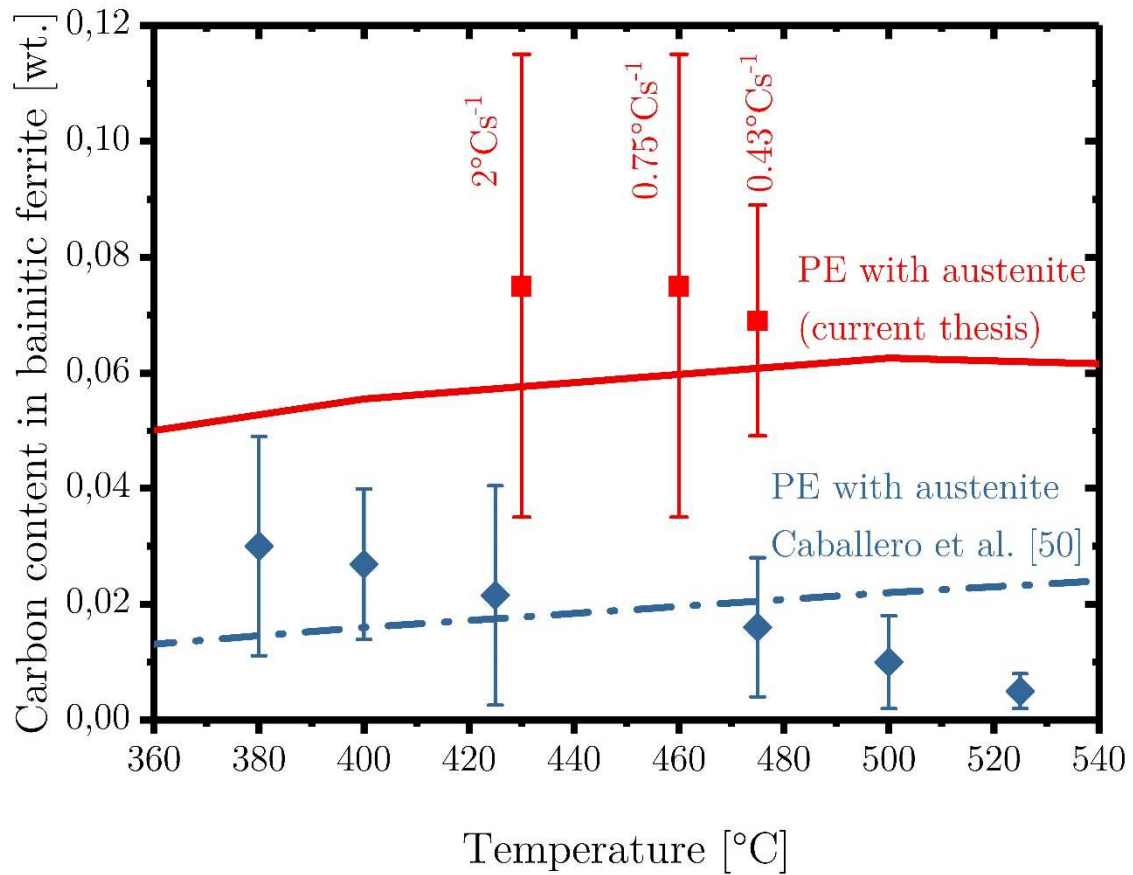


Figure 6.18: Carbon content in solid solution in bainitic ferrite as a function of transformation temperature for experimental APT values in the current thesis (red) and the investigations after Caballero et al. [50] (blue). The paraequilibrium (PE) phase boundary between bainitic ferrite and austenite were calculated for the steels using MatCalc (solid red line: material of the present investigation, dashed dotted line: material investigated by Caballero et al.

## 7 Tempering of continuously cooled bainite

The tempering behaviour of bainitic microstructures and the associated effects, especially during continuous reheating are poorly described in literature [31,67,97,160]. Thus, for example, the internal microstructure consisting of bainitic ferrite and retained austenite substantially determines the evolution of hardness during a tempering treatment.

Therefore, Vickers hardness measurements were determined from the as-hardened bainitic microstructure after continuous cooling with 2, 0.75 and 0.43°Cs<sup>-1</sup> as well as during the tempering process, the time-temperature cycle outlined in **Figure 4.4b**. The initial bainitic microstructures are in the following referred as BM2, BM0.75 and BM0.43 according their cooling rate. The evolution of hardness for the different bainitic microstructures during continuous reheating as well as isothermal tempering at 620°C is shown in **Figure 7.1**.

In general, all microstructures show the same trend for the hardness evolution. During reheating, hardness decreases in a temperature range between 300-510°C and rises again at 620°C, see **Figure 7.1a**. Whereas, isothermal tempering at 620°C leads to a significant increase in hardness up to 100HV for all microstructure, see **Figure 7.1b**.

The aim of this chapter 7 is to clarify the mechanisms controlling the observed hardness evolution during continuous reheating and isothermal tempering. Therefore, dilatometry is first used to get an overview about the tempering kinetics. To investigate the evolution of phase fractions as well as the redistribution of carbon during tempering in detail, *in-situ* high energy X-ray diffraction (HEXRD) is used. To get an insight about the microstructural changes and local processes occurring during tempering, transmission electron microscopy (TEM) and three-dimensional atom probe tomography (3D-APT) is used.

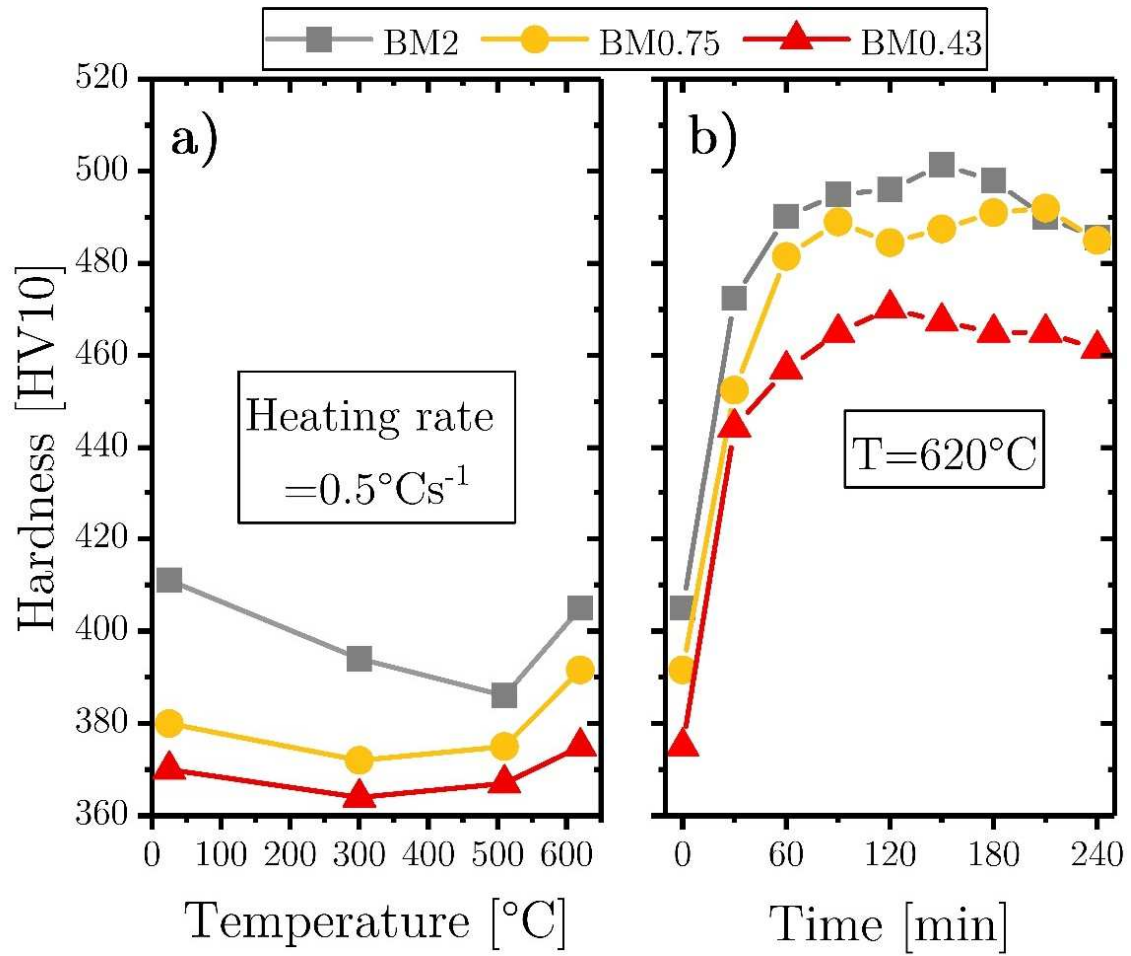


Figure 7.1: Evolution of hardness during a) continuous reheating with  $0.5^{\circ}\text{C s}^{-1}$  to tempering temperature of  $620^{\circ}\text{C}$  followed by immediate quenching, and b) isothermal tempering at  $620^{\circ}\text{C}$  after heating to tempering temperature with  $0.5^{\circ}\text{C s}^{-1}$ . BM2, BM0.75 and BM0.43 designates the initial bainitic microstructure after continuous cooling with cooling rates of 2, 0.75 and  $0.43^{\circ}\text{C s}^{-1}$ .

## 7.1 Tempering effects during continuous reheating

### 7.1.1. Phase evolution during continuous reheating

Figure 7.2 presents the dilatometer signal together with the corresponding differential curve during reheating for the initial bainitic microstructures BM2, BM0.75, and BM0.43. Due to the poorly recognisably length change in the dilatometer signal, arrows mark possible transitions points in the differential curve.

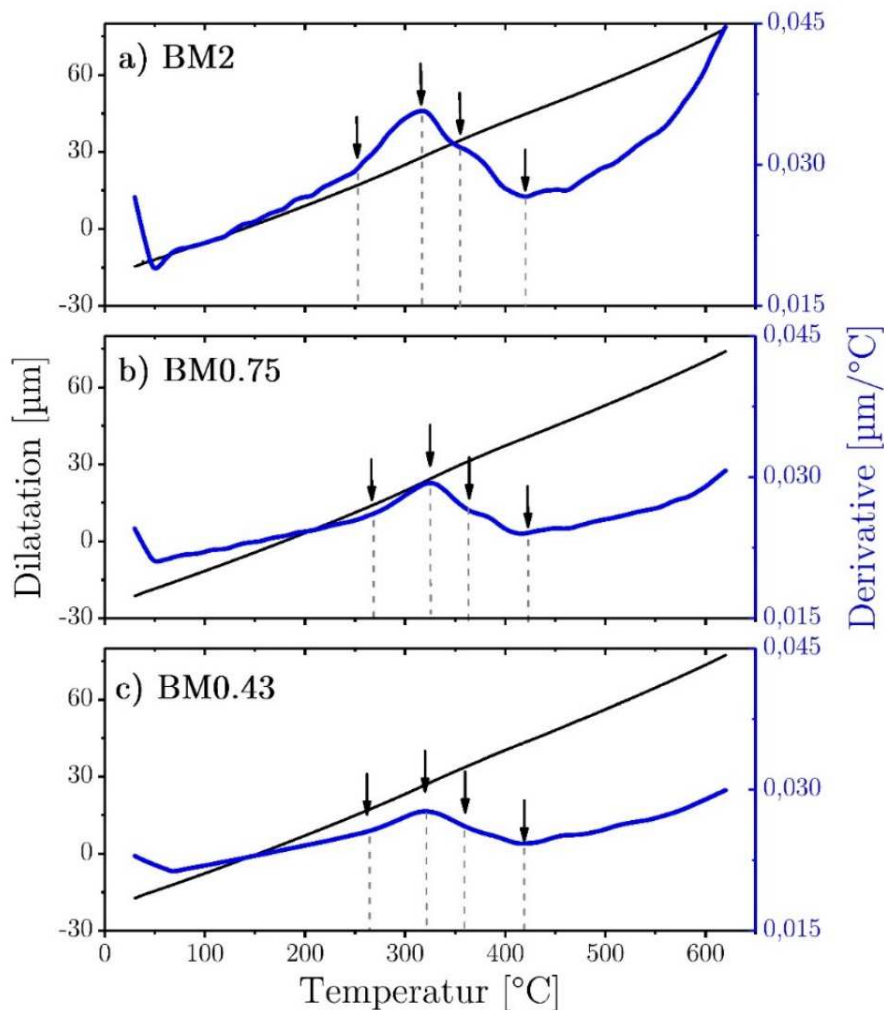


Figure 7.2: Recorded dilatation signal and their corresponding derivative as a function of temperature during reheating of microstructures BM2, BM0.75, and BM0.43 with a heating rate of  $0.5^{\circ}\text{Cs}^{-1}$  to tempering temperature of  $620^{\circ}\text{C}$ . BM2, BM0.75 and BM0.43 designates the initial bainitic microstructure after continuous cooling with cooling rates of 2, 0.75 and  $0.43^{\circ}\text{Cs}^{-1}$ .

Generally, all signals in **Figure 7.2** show the same trend during heating independent from the initial microstructure, whereby the changes in the differential signal are less pronounced for BM0.75 and BM0.43. This fact coincidences with literature [31],

whereas the extent of microstructural changes during tempering depend on how far the initial microstructure deviates from an equilibrium condition. Additionally, a similar trend suggests that the same microstructural changes occur during heating for all initial bainitic microstructures.

In the early stages of tempering, the differential signal shows a linear trend until 260°C. This tendency reflects the thermal expansion of the initial microstructure consisting of bainitic ferrite and retained austenite films or blocks. Subsequently, the differential signal shows a slight increase until a temperature of 320°C is reached followed by a pronounced decrease up to 360°C and a further but minor decrease until 430°C. Literature suggests that in the temperature range between 250-430°C, diffusion of carbon from the matrix into austenite as well as the decomposition of austenite takes place followed by the precipitation of cementite ( $\theta$ ) [92–98]. The former effects lead to a slight expansion whereas the latter one leads to a strong contraction of the sample. These opposite effects would explain the observed change in the differential signals. Afterwards, the differential signals show an almost linear trend up to 580°C comparable to the early stages of tempering followed by a slight increase up to 620°C, which may stem from dissolution of cementite.

To analyse and separate the prevalent tempering reactions in detail, *in-situ* HEXRD was carried out during the heating process. The evolution of austenite and cementite phase fraction as a function of temperature for the three initial bainitic microstructures are shown on **Figure 7.3**. For better orientation, the differential signal is displayed through the blue line on the right y-axis.

Whatever the initial microstructure, the decomposition of retained austenite is accompanied by the precipitation of cementite and appears to start at 320°C and continuous until 430°C. Therefore, the decrease in the differential signal in this temperature range belongs to the decomposition of retained austenite to cementite and ferrite. However, the dissolution of retained austenite is incomplete and significant amounts from 4 to 11 vol.% are still stable until the tempering temperature of 620°C.

The thermal stability of retained austenite is mainly related to the steel composition, especially to the carbon content [73,74]. In the present case, retained austenite exists as thin films and as blocks. Both morphologies are highly enriched in carbon, but retained austenite films are enriched more because of their isolation between the bainitic sub-units. Therefore, the driving force for cementite precipitation increases with the carbon content, which can result in a higher instability of retained austenite films during reheating [67,69]. This suggests that retained austenite blocks are thermally more stable than films and tend to decompose at higher temperatures, which would also explain the change in the differential signal between 360 to 430°C.

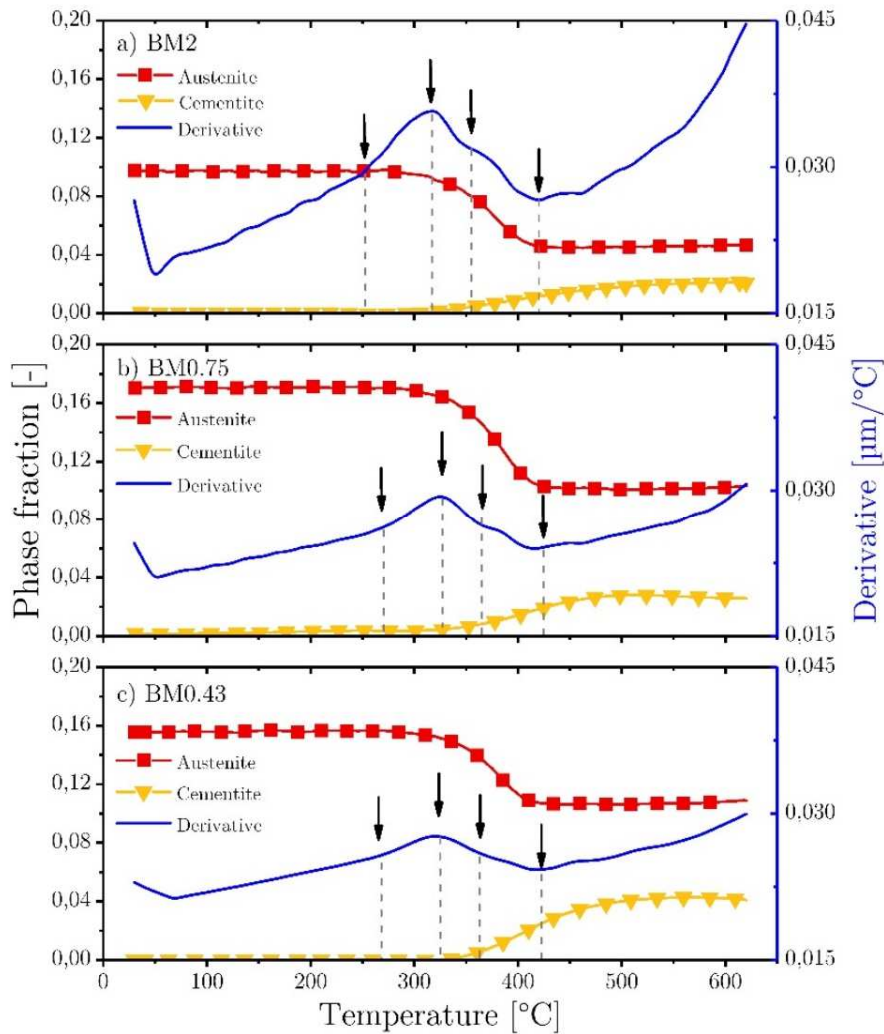


Figure 7.3: Phase evolution of austenite and cementite during reheating for microstructures BM2, BM0.75, and BM0.43 with a heating rate of  $0.5^{\circ}\text{C}\cdot\text{s}^{-1}$  to tempering temperature of  $620^{\circ}\text{C}$  determined by means of in-situ HEXRD experiments. For better orientation, the derivative of the dilatation signal is displayed through the blue line on the right y-axis.

Whatever, the shown phase analysis cannot explain the expansion in the early stages of tempering between  $260$  and  $320^{\circ}\text{C}$ . Literature [97,98] relates this phenomenon to the diffusion of carbon from the ferritic matrix into retained austenite.

In order to prove this, the carbon content in retained austenite during the heating process was determined according to the calculation scheme outlined in equation 8. The evolution of the overall carbon content in retained austenite during the heating process as obtained from the lattice parameter changes is illustrated in **Figure 7.4**. The results indicate an increase of the retained austenite carbon content around  $0.1$  wt.-% in a temperature range of  $260$ - $320^{\circ}\text{C}$ . This further enrichment in carbon leads to an expansion of the retained austenite and therefore to the observed increase in

the differential curve. Furthermore, the carbon content sharply decreases in the temperature range from 320°C to 380°C, which correlates well with the precipitation of cementite. Afterwards, the carbon content decreases continuously with increasing temperature. The observed trend in the development of the carbon content also encourages the statement that the thin retained austenite films decompose at lower temperatures than the thicker austenite blocks.

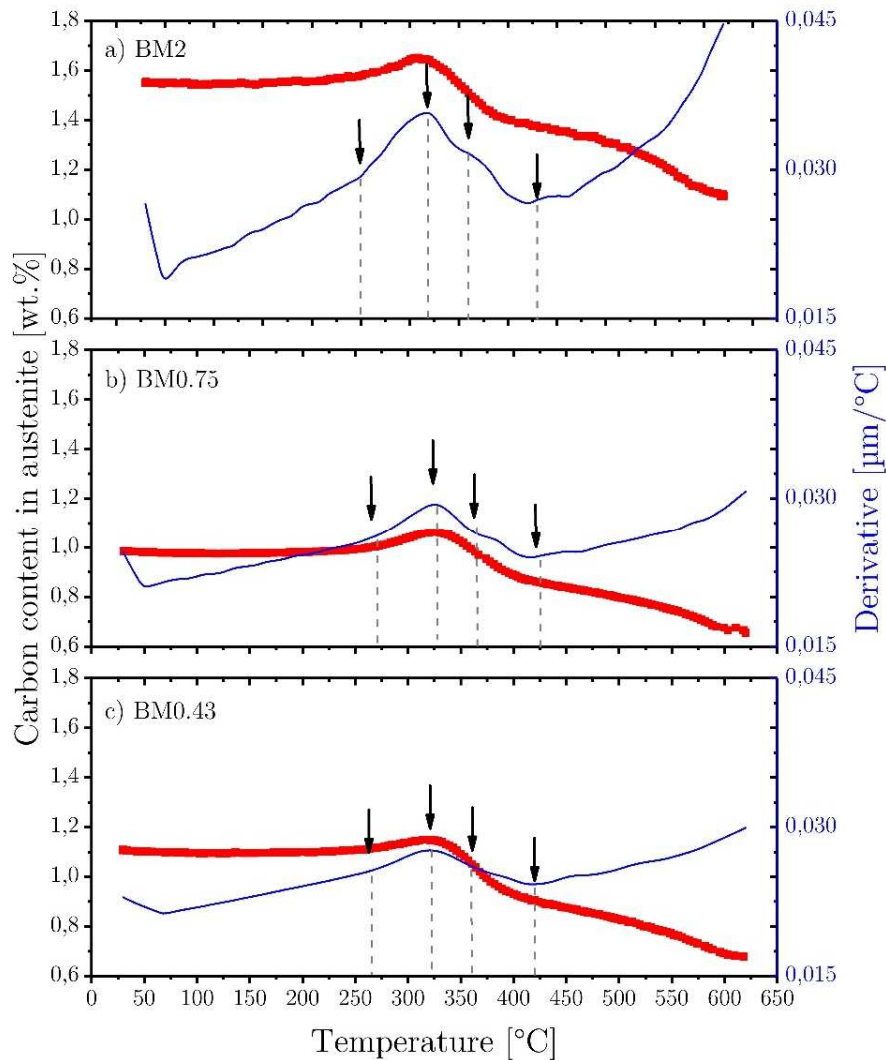


Figure 7.4: Evolution of carbon content obtained from the lattice parameters of austenite during reheating as determined from in-situ HEXRD experiments for microstructures a) BM2, b) BM0.75 and c) BM0.43 with a heating rate of  $0.5^\circ\text{C}\text{s}^{-1}$  to tempering temperature of  $620^\circ\text{C}$ . For better orientation, the derivative of the dilatation signal is displayed through the black line on the right y-axis.



### 7.1.2. Microstructural development during continuous reheating

The results in the previous section indicate that independent from the initial microstructure the same mechanisms seem to occur during reheating. This suggests that also the same microstructural changes occur. Therefore, only representative micrographs and 3D-atom maps obtained from heating experiments of microstructures BM2, BM0.75 and BM0.43 will be shown in the following.

As a starting point, **Figure 7.5** shows representative micrographs of the initial microstructure after continuous cooling with  $2^{\circ}\text{C}\text{s}^{-1}$  before heating. The microstructure consists of bainitic ferrite and carbon enriched retained austenite films or blocks.

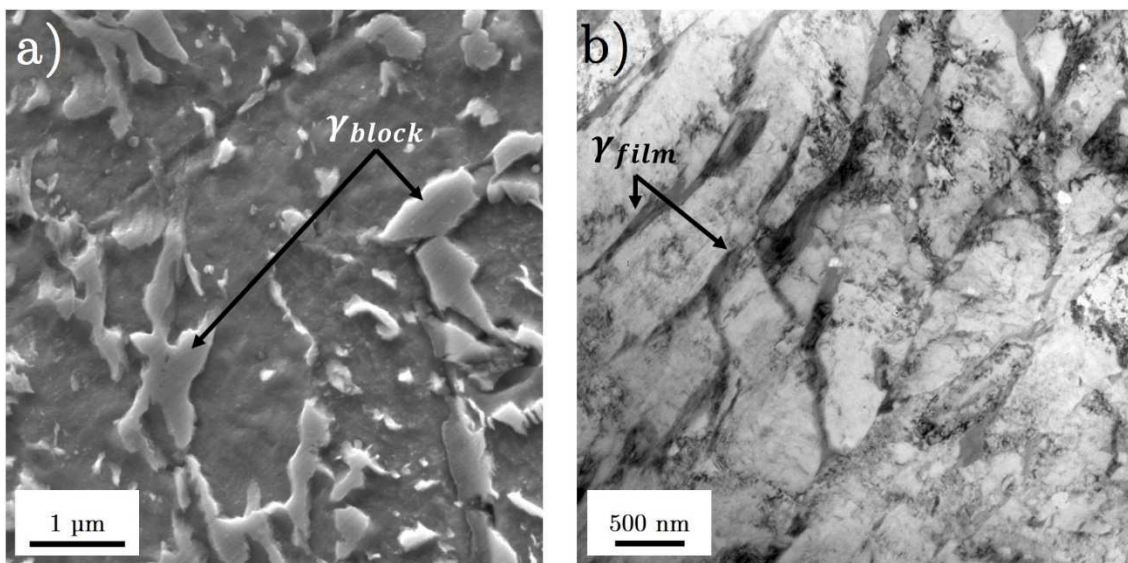


**Figure 7.5:** Representative micrographs of the initial bainitic microstructure after continuous cooling with  $2^{\circ}\text{C}\text{s}^{-1}$  from  $1020^{\circ}\text{C}$ . a) SEM micrograph illustrating blocky retained austenite. b) TEM micrographs showing films of retained austenite between bainitic ferrite sub-units.

The findings based on dilatometry and HEXRD data show that the diffusion of carbon from bainitic ferrite into the retained austenite represent the first microstructural change in a temperature range of  $260$  to  $320^{\circ}\text{C}$ . **Figure 7.6** illustrates an austenite/ferrite interface after heating to  $300^{\circ}\text{C}$  and subsequent quenching to room temperature of BM2, respectively. Element concentration profiles across the interface (designated with a black arrow) of C, Mo, V and Cr are shown on the right side. The carbon content in austenite ( $9.1\pm 0.8\ \text{at.}\%$ ) is marginally higher than that measured from the initial microstructure ( $8.2\pm 0.9\ \text{at.}\%$ ). In contrast, the carbon increase determined from HEXRD data amounts to  $0.1\ \text{wt.}\%$  ( $0.47\ \text{at.}\%$ ) and thus lies within



the error limits of the APT data. Moreover, the element concentration profiles suggest that no partitioning of substitutional elements occurs during this tempering stage.

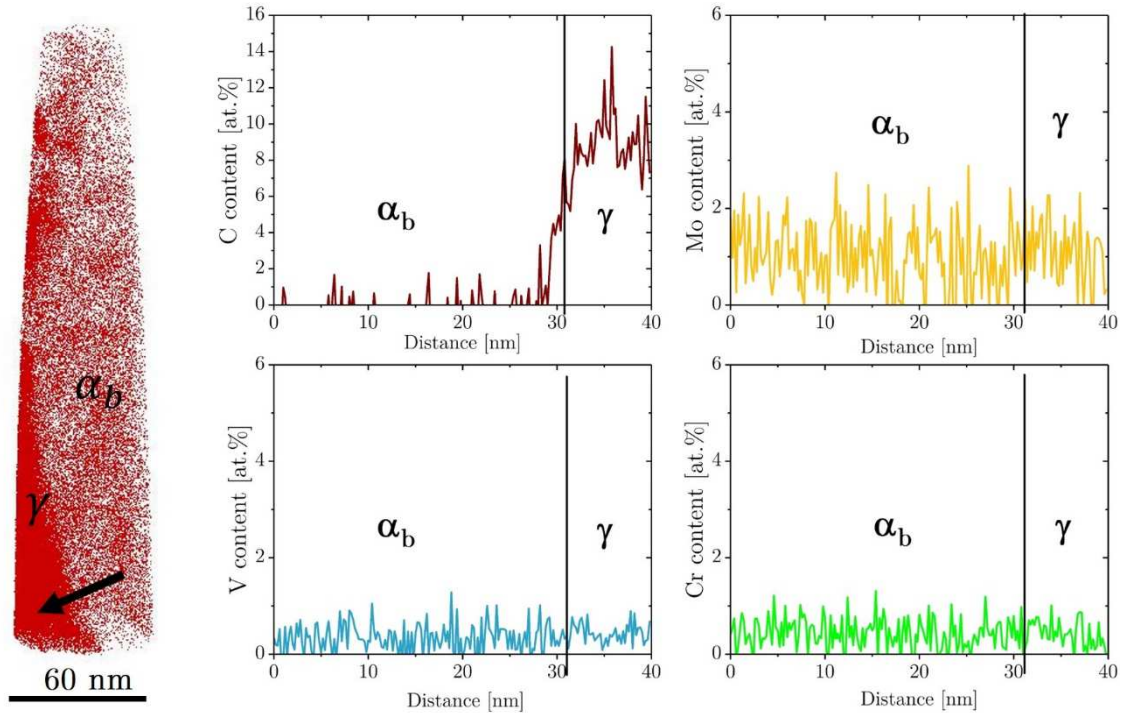


**Figure 7.6:** 3D carbon atom map of austenite/bainitic ferrite interface with corresponding concentration profiles of C, Mo, Cr and V obtained after heating BM2 to 300°C and subsequent quenching. **1** condition: Continuous cooling with 2°Cs<sup>-1</sup> from 1020°C.

As declared in the previous section, retained austenite partially decomposes in a temperature range of 320-430°C into cementite and ferrite. Several studies have shown that retained austenite blocks tend to form colonies of pearlite with a thin inter-lamellar spacing, whereas the films of austenite decompose into discrete particles of cementite which share the same orientation as the adjacent bainitic ferrite [31,67,69]. Similar decomposition products were found in the present thesis. **Figure 7.7** shows typical TEM micrographs of microstructures obtained after heating to 510°C and subsequent quenching to room temperature. **Figure 7.7a** establishes the presence of cementite colonies instead of retained austenite blocks, whereas **Figure 7.7b** shows discrete cementite particles between adjacent bainitic sub-units instead of retained austenite films. However, retained austenite is still present in the microstructure as can be seen on the right side of **Figure 7.7b**. This fact coincides well with the results obtained by HEXRD, which indicates that retained austenite amounts in the range of 4 to 11 vol.% are stable up to 620°C. Accompanying APT examinations also

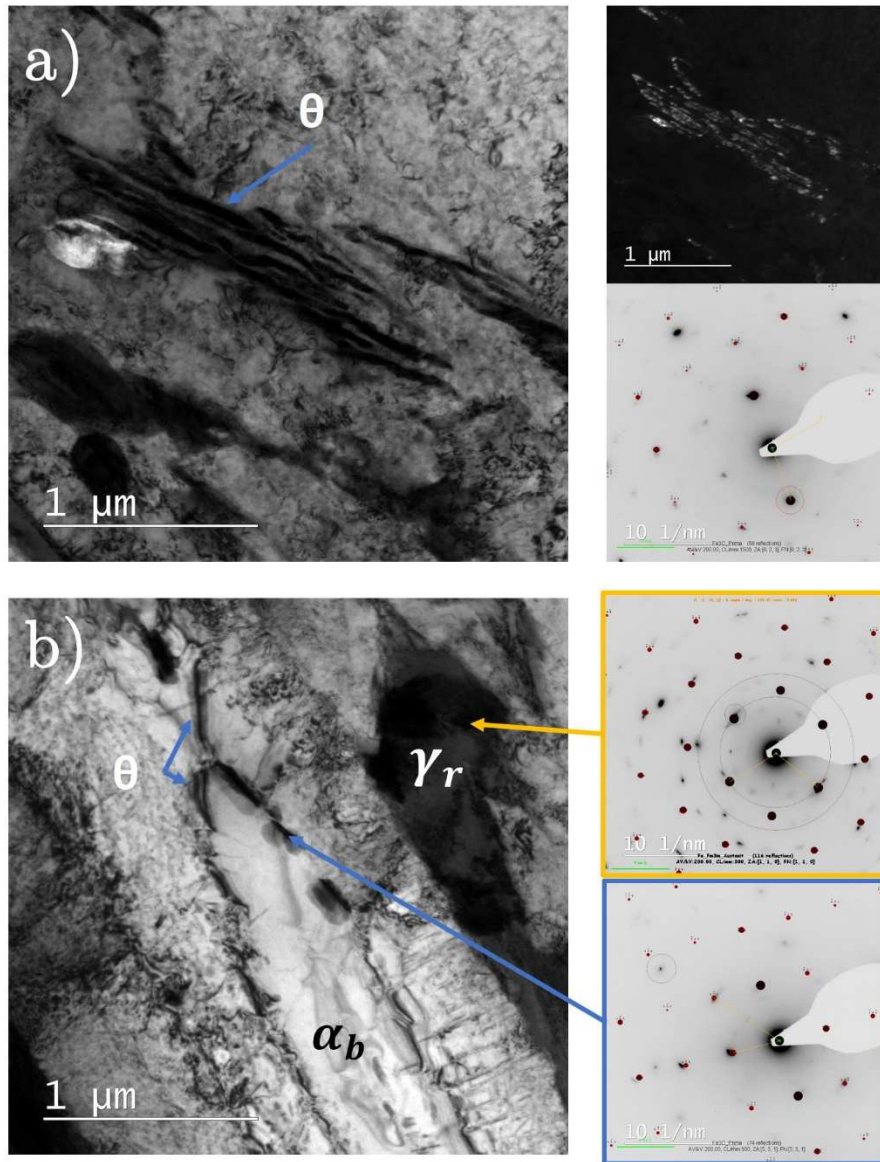


Figure 7.7: Representative TEM micrographs of microstructures obtained after heating to 510°C and subsequent quenching to room temperature showing a) fine colonies of cementite with a thin interlamellar spacing, and b) discrete cementite ( $\theta$ ) precipitates sharing the same orientation as the adjacent bainitic ferrite. The corresponding diffraction pattern and dark field images of cementite and retained austenite are shown on the right side.

reveals cementite precipitates besides retained austenite in the microstructure, as can be seen from the carbon atom map in **Figure 7.8**.

Furthermore, element concentration profiles across the bainitic ferrite/cementite interface reveal that silicon is slightly depleted within the cementite. By contrast, partitioning of chromium and manganese is not clear. Both slight enrichments on the interface could be considered as normal scatter of the composition data. Chromium

or manganese concentration spikes at the interface suggest that cementite grows at a state that is known as “*negligible partitioning local equilibrium*” (NPLE). This means that at the interface the equilibrium composition of the precipitate is reached, whereas the concentration far away from the interface inherits the parent composition [31].

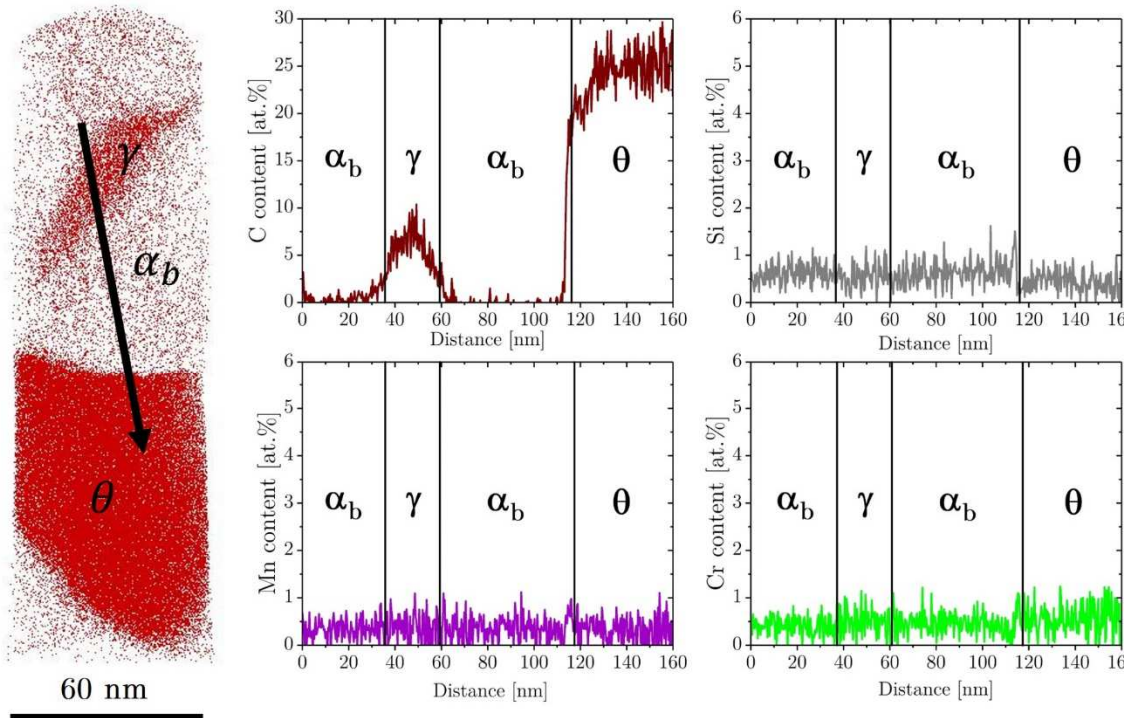
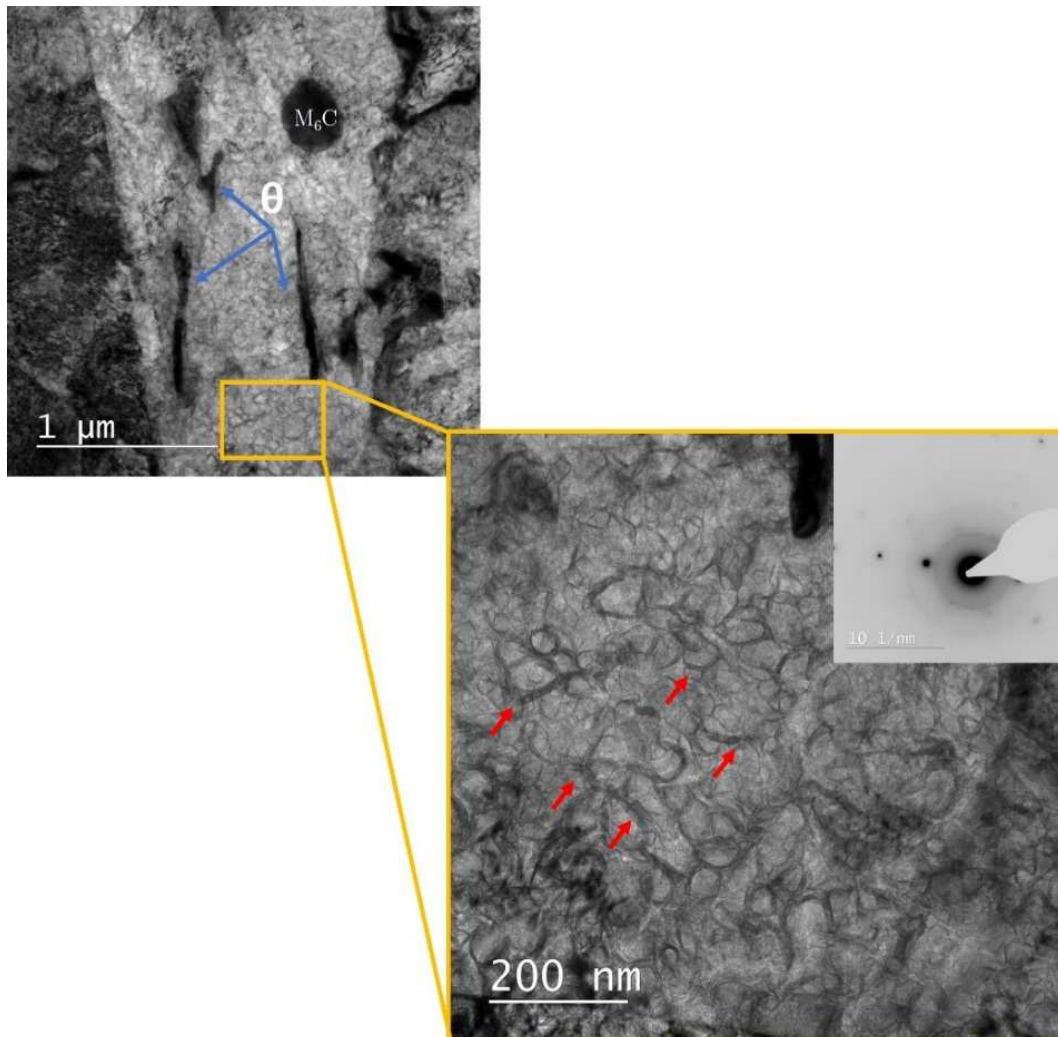


Figure 7.8: Representative carbon atom map after heating to 510°C and subsequent quenching to room temperature. Concentration profiles are shown along the marked arrow.  $\alpha_b$  denotes bainitic ferrite,  $\gamma$  is austenite and  $\theta$  is cementite.

However, the precipitation of cementite starts at 320°C, whereas the presented APT data stem from a sample heated up to 510°C. During this tempering period, it is possible for substitutional elements to diffuse over short distances. Caballero et al. [161] studied the isothermal tempering behaviour at 400°C of bainitic microstructures obtained in a Fe-0.9C-1.3 Cr-1.5Si-2Mn steel. Due to the high silicon content, the initial microstructure consists of bainitic ferrite and carbon enriched austenite comparable to the present thesis. TEM observations and APT showed that the precipitation of cementite occurred after tempering at 400°C for 1h. During the early stages of cementite precipitation neither elemental spikes nor segregation of silicon, chromium or manganese were observed at the cementite interface. Only further tempering leads to partitioning of substitutional elements. Therefore, they claimed that in the

early stages of austenite decomposition cementite nucleates under paraequilibrium conditions and further tempering leads to a transition from paraequilibrium to the equilibrium composition. So, it is concluded that the cementite precipitation in the present thesis also occur under paraequilibrium conditions.

A representative TEM micrograph of the microstructure after heating to 620°C and subsequent quenching to room temperature is shown in **Figure 7.9**. In this state, the microstructure also consists of bainitic ferrite, cementite and the remaining austenite. However, within the bainitic ferrite dark features arranged along lines can be recognised (marked with red arrows). Identification of these features by means of selected area diffraction (SAD) in TEM failed and only ferrite spots were observed, which is indicated by the diffraction pattern in **Figure 7.9**.



**Figure 7.9:** Representative TEM micrographs of microstructures obtained after heating to 620°C followed by subsequent quenching to room temperature. Within the bainitic matrix dark features (marked with red arrows) appear, which deliver no diffraction signal.



The size and distance between these features can be related to the segregation of carbon and substitutional elements to dislocations as can be seen from APT measurements in **Figure 7.10**. These segregations may act as pre-stage to the precipitation of secondary hardening carbides.

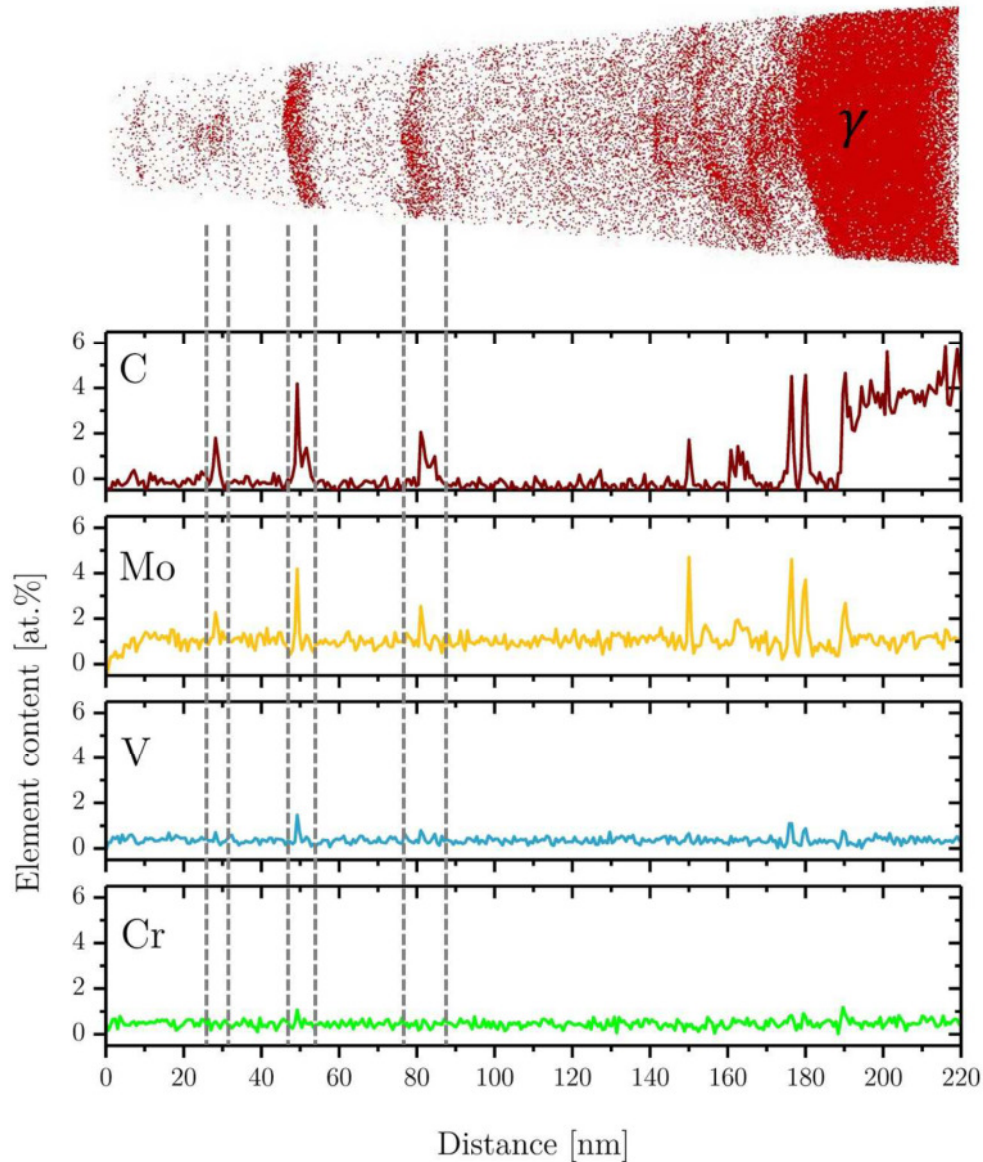


Figure 7.10: Representative carbon atom map after heating to 620°C and subsequent quenching to room temperature. Concentration profiles reveal segregation of C together with Mo and V.

## 7.2 Tempering effects during isothermal tempering

### 7.2.1. Phase evolution during isothermal tempering

The dilatation signal for the three bainitic microstructures during isothermal tempering at 620°C for 4 hours and subsequent cooling with 0.5°Cs<sup>-1</sup> to room temperature is shown in **Figure 7.11**. The dilatation signal slightly increases during the whole tempering process, which corresponds to further decomposition of retained austenite into cementite and ferrite. Furthermore, cooling after tempering leads to a pronounced deviation from linear contraction, which can attribute to a martensitic transformation of the austenite.

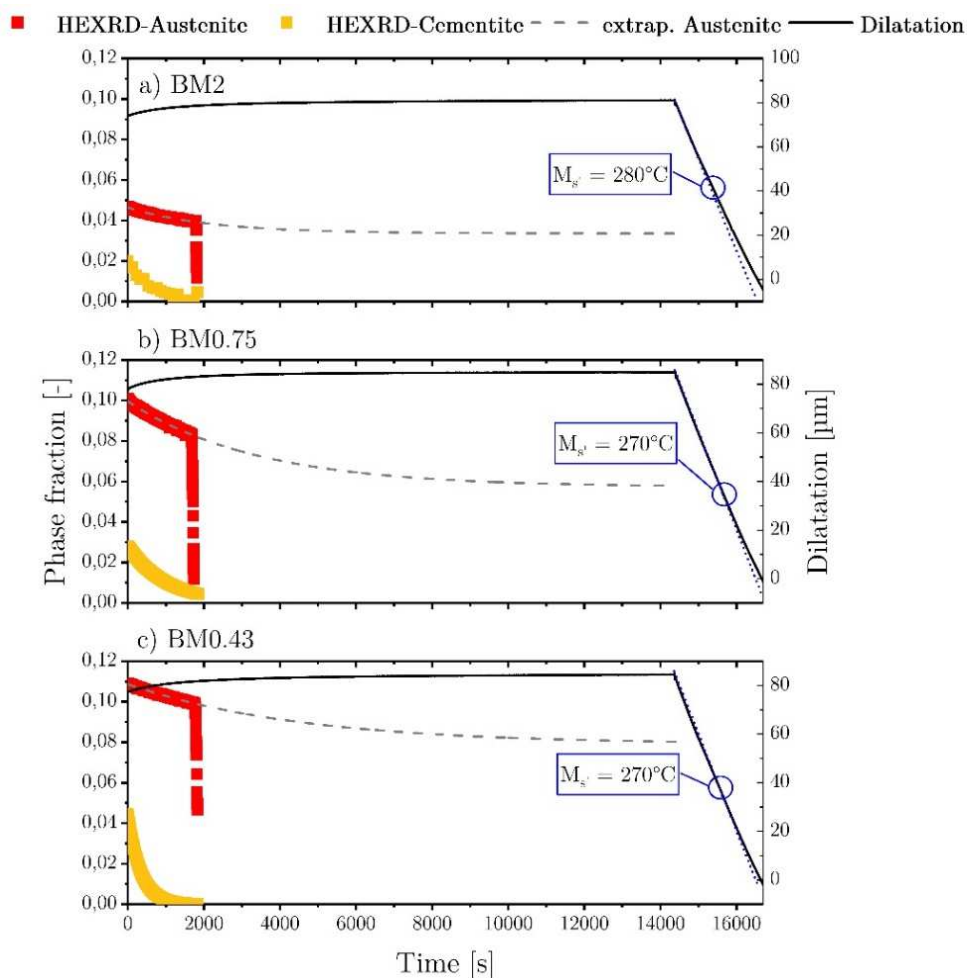


Figure 7.11: Evolution of the dilatation signal (black line) as well as phase fractions of retained austenite determined from in-situ HEXRD measurements during isothermal tempering at 620°C for initial microstructures a) BM2, b) BM0.75 and c) BM0.43. The austenite phase fraction is extrapolated to longer times from HEXRD measurements during the first 0.5h of tempering.

The evolution of austenite and cementite phase fraction determined by means of HEXRD during the first 0.5 hours of isothermal tempering are also shown in **Figure 7.11**. The cementite phase fraction decreases during this time period under the detection limit of 1 vol.%, which is consistent with literature [92–98]. Extended isothermal tempering at temperatures above 500°C leads to coarsening and dissolution of metastable carbides such as cementite. Stable alloy carbides in the following replaces these carbides. The isothermal tempering treatment also leads to a further reduction in the austenite phase fraction. Extrapolation of the austenite fraction to longer times suspects that quantities between 4 to 7 vol.% are stable until the end of the isothermal tempering process. It is evident that prolonged isothermal tempering destabilises the austenite due to the local reduction in carbon following the precipitation of cementite. Therefore, subsequent cooling leads to the transformation of austenite to un-tempered martensite. An example of un-tempered martensite after tempering for 4 hours and subsequent cooling of the initial microstructure BM0.75 is shown in **Figure 7.12**. The twinned martensite is typical for the transformation of carbon enriched austenite [67,69].

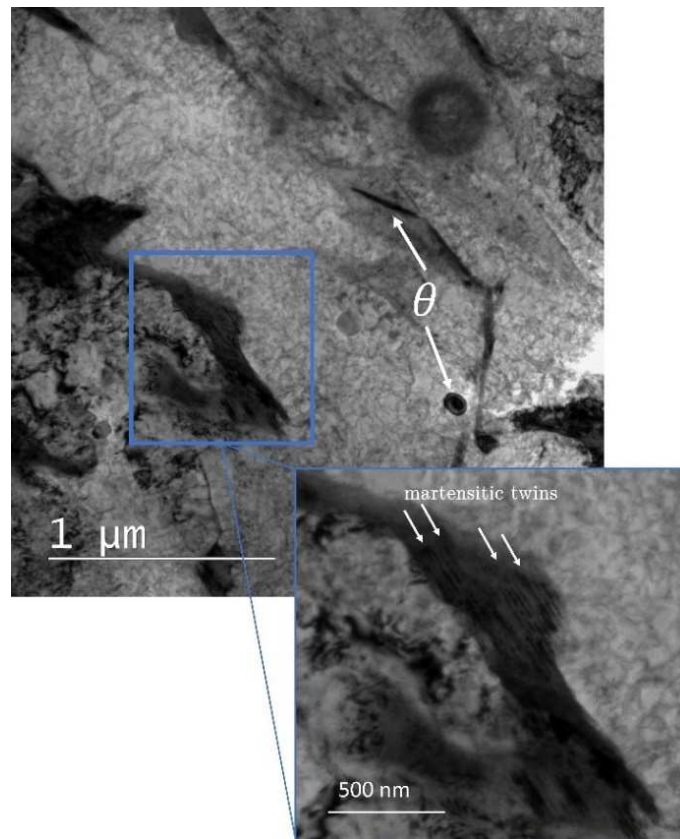


Figure 7.12: Representative TEM micrograph of a microstructure obtained after tempering for 4 hours at 620°C and subsequent cooling to ambient temperature. The residual austenite transforms into martensite, which is indicated by martensitic twins.

### 7.2.2. Precipitation of secondary hardening carbides

In order to characterize secondary hardening carbides TEM investigations are complemented by 3D APT. **Figure 7.13a-c** shows representative TEM micrographs of BM0.75 samples tempered at 620°C for 0.5, 2 and 4 hours, respectively. The rod-like precipitates within the bainitic matrix are identified as  $M_2C$  carbides, according their corresponding diffraction pattern. The mean length( $\bar{l}$ ), width ( $\bar{b}$ ) and aspect ratio ( $A_R = l/b$ ) of the identified carbide types were measured for each tempering condition from at least three positions. The following **Table 7.1** summarizes the obtained results.

**Table 7.1:** Summary of the average carbide dimensions observed via TEM in tempered samples of BM0.75 at 620°C;  $\bar{l}$ ...length,  $\bar{b}$ ...width  $A_R$ ...aspect ratio ( $l/b$ ).

Time [h]	$\bar{l}$ [nm]	$\bar{b}$ [nm]	$A_R$ [-]
0.5	10±2	3±0.5	3.5±1
2	22±4	3±1	8.0±4
4	30±10	4±1	7.5±5

**Figure 7.14a-c** depicts carbon atom maps of BM0.75 tempered for 0.5, 2 and 4 hours at 620°C, respectively. For better visibility of the precipitates, green iso-concentration surfaces at a carbon concentration of 10 at.-% are overlaid with the carbon map. The chemical composition of the precipitates was analysed through proximity histograms of these 10 at.-% carbon iso-concentration surfaces. Proximity histograms measure the element concentration in discrete shells at fixed distances from the iso-concentration surface. Representative element distribution maps obtained in this way are presented on the right side in **Figure 7.14**. The analysis reveals carbon concentrations of approximately 33 at.-% which coincidences with the identified  $M_2C$  carbide structure by means of TEM.

Comparative TEM and APT examinations of the initial bainitic microstructures BM2 and BM0.43 tempered at 620°C for 0.5, 2 and 4 hours reveals the same carbide type and no significant deviations of the above presented results.



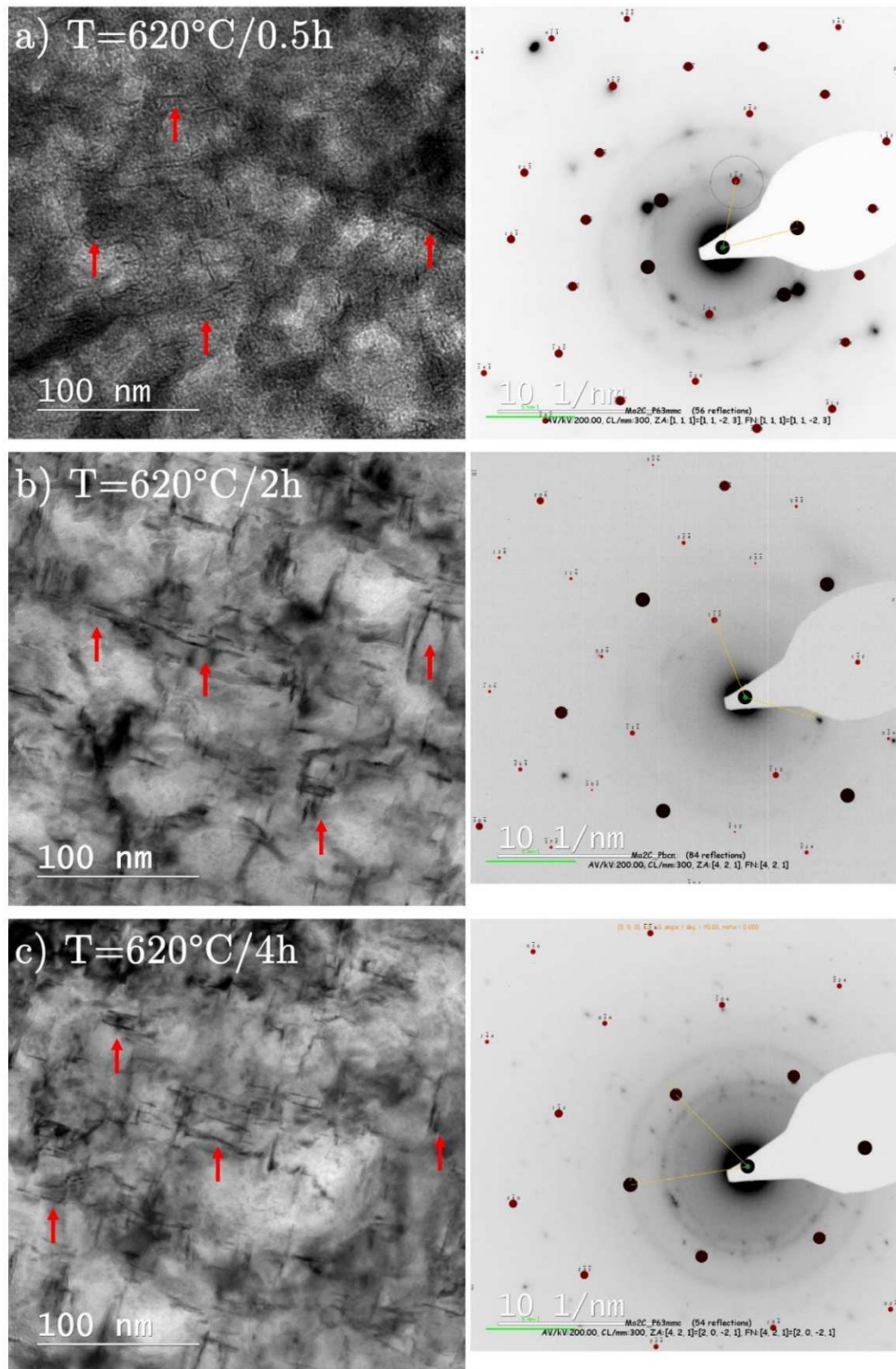


Figure 7.13: TEM micrographs from BM0.75 tempered for a) 0.5, b) 2 and c) 4h at 620°C. The corresponding diffraction pattern indicates the presence of  $M_2C$  carbides in the microstructure.

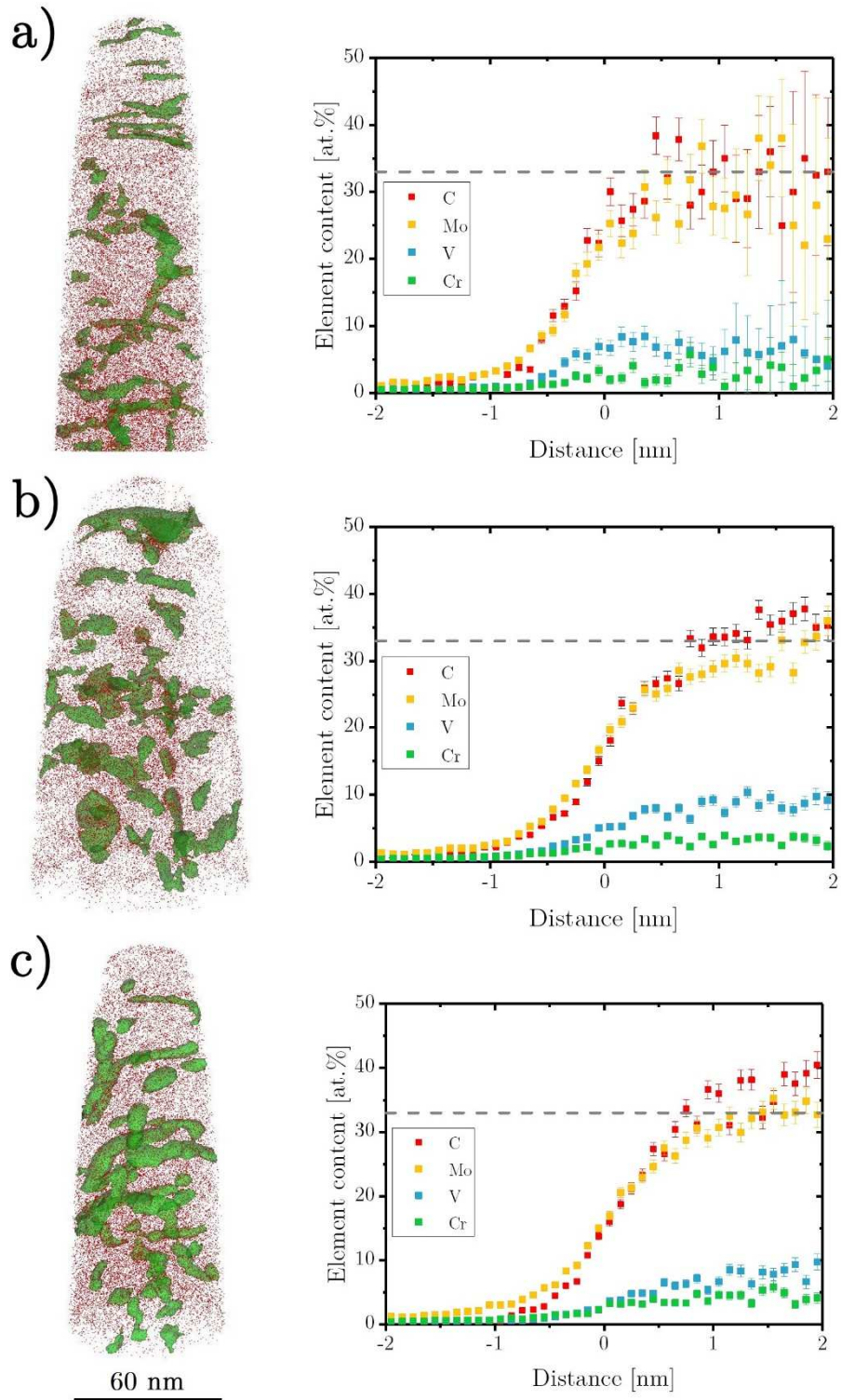


Figure 7.14: Carbon atom maps and a representative proximity histogram of a carbon isosurfaces at 10 at% (green) observed after tempering at 620°C for a) 0.5h, b) 2h and c) 4h. The element content within the isosurfaces indicate  $M_2C$  precipitates after all tempering times.

### 7.3 Discussion on the observed tempering effects

The first mechanisms associated with the structural changes produced by tempering a martensitic microstructure is the redistribution of carbon to lattice defects followed by the precipitation on non-stoichiometric  $\epsilon$  transition carbides. Both effects lead to a decrease in the hardness. The hardness evolution outlined in **Figure 7.1a** depicts also a decrease in the hardness until 300°C for the bainitic microstructure. However, the previously mentioned effects are not observed during heating. This is because, the redistribution of carbon from bainitic ferrite into austenite already takes place to a large extent during the bainitic reaction. As a consequence, too little excess carbon is available for  $\epsilon$ -carbide precipitation during heating. However, the APT results in chapter 6.3.2 also indicate that carbon amounts of 0.075 wt.-% are still in solid solution within the bainitic ferrite after the phase transformation. Therefore, it is concluded that during reheating in a temperature range from 260 to 320°C a further carbon partitioning from bainitic ferrite into retained austenite takes place. This is also confirmed by dilatometry and HEXRD experiments shown in this chapter. This further reduction in the matrix carbon content would also explain the hardness decrease.

At 320°C retained austenite begins to decompose into cementite and ferrite. The results suggest that retained austenite blocks are thermally more stable than films and tend to decompose at higher temperatures. To support this statement, two simple thermo-kinetic calculations are carried out using MatCalc. The MatCalc code for these calculations can be found within **Appendix B**.

#### **Thermo-kinetic calculation 1 (varying carbon content in austenite):**

In a first case, it is assumed in the simulation that cementite precipitates on dislocations in the retained austenite during reheating, whereby the carbon content in austenite is varied and the dislocation density is set to the default value of  $1 \times 10^{11} \text{ m}^{-2}$ . As can be seen in **Figure 7.14a**, cementite precipitation begins earlier with increasing austenite carbon content.

#### **Thermo-kinetic calculation 2 (varying dislocation density in austenite):**

As known from literature [44] the growth of bainitic ferrite in steels is accompanied by a shape change of the transformed austenite, a change that is known as an invariant-plane strain with a large shear component. When the transformation occurs at temperatures where the shape change cannot be accommodated elastically, the plastic deformation that is driven by the shape change causes the accumulation of relatively

high dislocation densities of approximately  $5 \times 10^{15} \text{ m/m}^3$  in both, the parent and product phase [162]. Therefore, in a second simulation the carbon content is held constant at 1 wt.-% and the dislocation density is varied. As can be seen in **Figure 7.14b**, cementite precipitation begins earlier with increasing dislocation density.

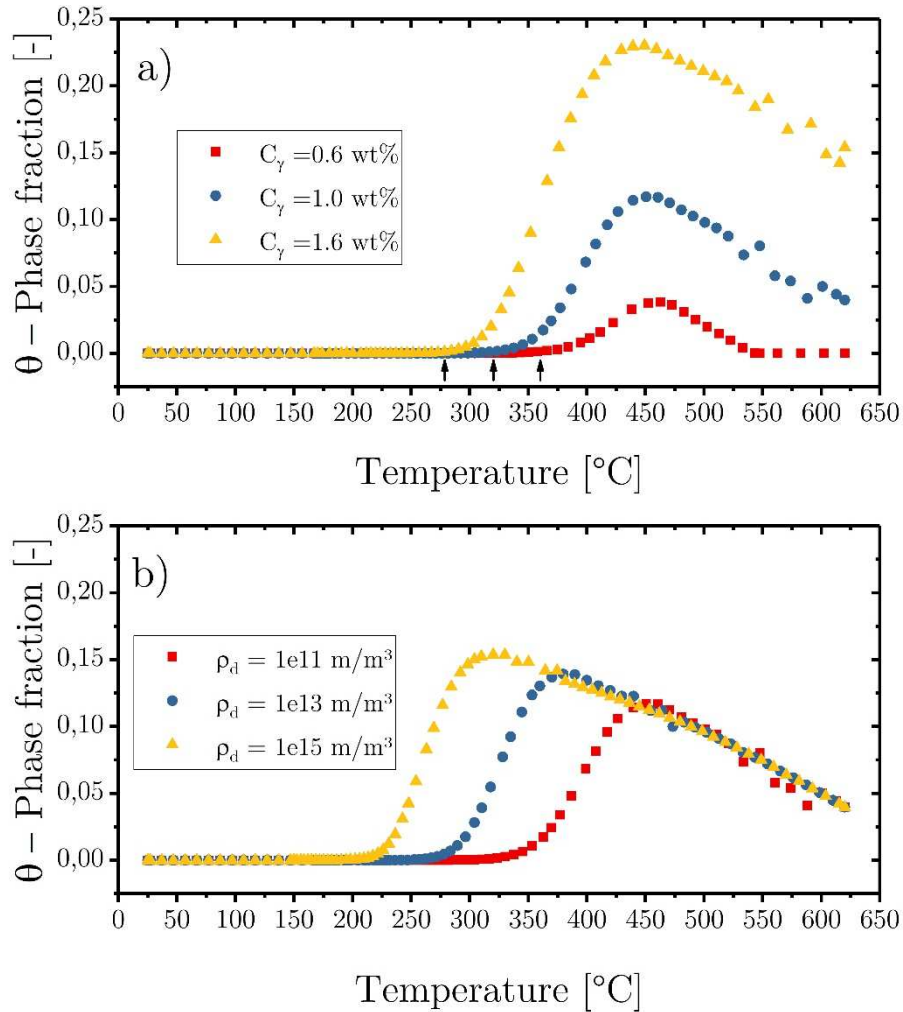


**Figure 7.14:** Thermo-kinetic simulation regarding the influence of a) varying carbon content (dislocation density constant at  $1 \times 10^{11} \text{ m/m}^3$ ) and b) varying dislocation density (carbon content constant at 1 wt.-%) of cementite precipitation in austenite

Both simulations indicate that retained austenite with a higher dislocation density and/or with a higher carbon content tend to decompose at lower temperatures. In fact, this is the case for retained austenite films, because they are located between bainitic sub-units and are therefore highly dislocated and also more enriched in carbon.

Another indication for the different stability of retained austenite can be found by the dilatometer experiments shown in **Figure 7.2**. The differential signal shows a pronounced decrease of the specimen length from 320°C to 360°C and a further minor decrease until 430°C. This behaviour suggests that multiple processes overlap in this temperature range. Literature proposes that between 250 and 420°C the decomposition of austenite into cementite and ferrite takes place [92–98]. Caballero et al. [96], studied the decomposition of retained austenite during reheating in high silicon steels by dilatometry and found a sample contraction for the reaction  $\gamma_r \rightarrow \alpha + \theta$ . By contrast, Yang and Bhadeshia [163] observed an expansion due to the decomposition of austenite into ferrite and cementite on a similar steel grade. To explain these apparently contradictory results a theoretical consideration will be shown in the following.

Assuming that phase changes in polycrystalline samples cause isotropic strains on a macroscopic scale, the linear and volume strains are related as follows [67]:

$$\frac{\Delta l}{l_0} = \frac{\Delta V}{3V_0} \quad (15)$$

Then the relative length change of the sample  $\frac{\Delta l}{l_0}$ , for the reaction  $\gamma_r \rightarrow \alpha + \theta$  can be calculated from the volume of the unit cells and the volume fractions of the different phases present in the microstructure at a given temperature as follows [96,164]:

$$\frac{\Delta l}{l_0} = \frac{1}{3} \left[ \frac{(V_\gamma a_\gamma^3) - \left(2V_\alpha a_\alpha^3 + \frac{1}{3}V_\theta a_\theta b_\theta c_\theta\right)}{(V_\gamma a_\gamma^3)} \right] \quad (16)$$

where  $V_\alpha$ ,  $V_\gamma$ ,  $V_\theta$  are the volume fractions and  $a_\alpha$ ,  $a_\gamma$ ,  $a_\theta$ ,  $b_\theta$ ,  $c_\theta$  are the lattice parameters of ferrite, austenite and cementite, respectively. The numerical factors take into account the different numbers of atoms per unit cell. The volume fractions of ferrite, austenite and cementite at a certain temperature and austenite carbon content can be determined by thermodynamic equilibrium calculations using MatCalc. The lattice parameters at a certain temperature  $T$  are calculated as follows:

$$a_\alpha = a_{\alpha_0} [1 + \beta_\alpha (T - 25)] \quad (17)$$

$$a_\theta = a_{\theta_0} [1 + \beta_\theta (T - 25)] \quad (18)$$

$$b_\theta = b_{\theta_0} [1 + \beta_\theta (T - 25)] \quad (19)$$

$$c_{\theta} = c_{\theta_0}[1 + \beta_{\theta}(T - 25)] \quad (20)$$

where the subscript “o” in each case represents the lattice parameter at room temperature. For ferrite it is  $a_{\alpha_0}=0.28664$  nm and for cementite it equals to 0.45246, 0.50885 and 0.67423 nm according [67,96]. The linear thermal expansion coefficient of ferrite  $\beta_{\alpha}$  is  $1.224e-5^{\circ}\text{C}^{-1}$  and that of cementite  $\beta_{\theta}$  is given in [165] as:

$$\beta_{\theta} = 6 * 10^{-6} + 3 * 10^{-9}(T - 25) + 1 * 10^{-11}(T - 25)^2 \quad (21)$$

To determine the influence of the carbon content in retained austenite ( $w_c^{\gamma}$  in wt.-%) on the relative length change, the austenite lattice parameter is calculated as follows:

$$a_{\gamma} = (a_{\gamma_0} + 0.33w_c^{\gamma})[1 + \beta_{\gamma}(T - 25)] \quad (22)$$

where  $a_{\gamma_0}$  equals to 0.3587 nm and  $\beta_{\gamma}$  is  $2.065 \cdot 10^{-5}^{\circ}\text{C}^{-1}$  [67,96].

**Figure 7.15** shows qualitatively the calculated relative change in length for the reaction  $\gamma_r \rightarrow \alpha + \theta$  at  $360^{\circ}\text{C}$  as a function of the carbon content in retained austenite.

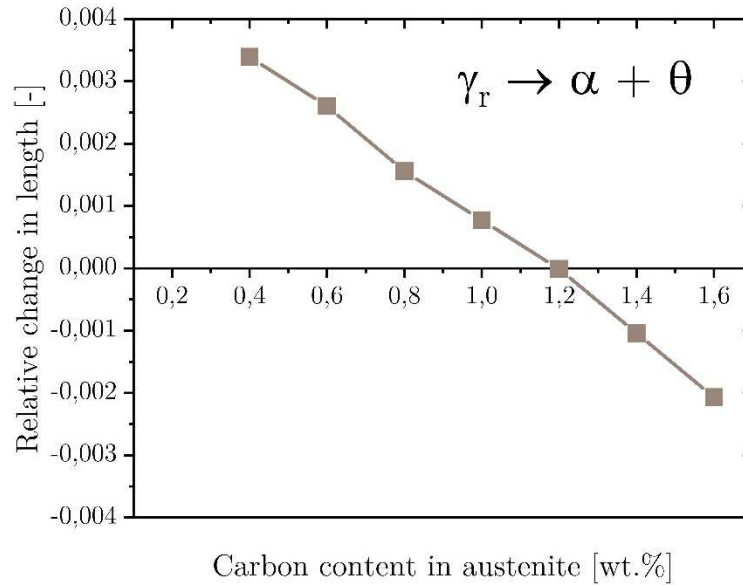


**Figure 7.15:** Calculated relative change in length due to isothermal decomposition of retained austenite into ferrite and cementite at  $360^{\circ}\text{C}$ .

These qualitative calculations indicate that a higher carbon content in austenite leads to an increase in  $a_\gamma$  and hence to a reduction in the density of austenite. Thus, when high-carbon austenite decomposes to ferrite and cementite, there is a net contraction, whereas the decomposition of low-carbon austenite leads to a net expansion of the sample. By comparing these results to the experimental observations, it can be stated that the decomposition of highly enriched austenite films dominates at lower temperatures. In contrast, during isothermal holding the sample shows a continuous expansion, which can be directly related to the decomposition of low-carbon austenite blocks. Furthermore, cooling after tempering leads to a pronounced deviation from linear contraction, which can be attributed to a martensitic transformation of the austenite. According to Andrews [166] the martensite start temperature ( $M_s$ ) for steels containing less than 0.6 wt.-% C, 5.0 wt.-% Cr and 5.4 wt.-% Mo can be calculated as follows:

$$M_s = 539 - 423C - 30.4Mn - 17.7Ni - 12.1Cr - 11Si - 7Mo \quad (23)$$

where the alloy contents are in wt.-%. A calculation of  $M_s$  for the nominal steel composition leads to 381°C which agrees well with the experimentally determined temperature of 380°C. Conversely, the observed deflection points during cooling from 620°C correlate to temperatures of 270 and 280°C. Based on these temperatures the overall carbon content in the austenite at the end of tempering can be estimated to 0.54-0.52 wt.-%. This also indicates that retained austenite blocks are thermally more stable than films and tend to decompose at higher temperatures.

Nevertheless, the presented results by HEXRD and dilatometry indicate that cementite precipitation accompanies the decomposition of the retained austenite. It is remarkable that the precipitation of cementite does not lead to a further decrease in the hardness. This fact reflects that the majority of the former trapped carbon in retained austenite contributes to the precipitation of cementite. On the contrary, the hardness evolution actually shows an increase from 510°C to 620°C. At such elevated temperatures long-range diffusion of substitutional elements is possible. Microstructure observations by means of APT, **Figure 7.10**, revealed segregation of Mo, V, Cr and also carbon along dislocations in this temperature range. The segregation itself cannot be considered to be a carbide phase having a lattice different from that of the matrix, as indicated by the diffraction mode in TEM, **Figure 7.9**. However, the local enrichment of carbon and substitutional elements leads to the observed slight increase in the hardness. Furthermore, the segregation itself acts as a pre-stage to the precipitation of secondary hardening carbides which is consistent with literature [99].

Further isothermal tempering at 620°C leads to the dissolution of metastable cementite and a release of carbon. Subsequently, the precipitation of secondary hardening alloys occurs, as shown in **Figure 7.12** and **Figure 7.13**. The precipitation of secondary hardening carbides leads to the observed hardness increase of 100HV. At long tempering times coarsening of alloy carbides may lead to a hardness decrease.



## 8 General summary

The present thesis deals with the bainitic reaction under continuous cooling conditions and the further tempering behaviour of a bainitic microstructure in a Fe-0.3C-2.8Mo-0.4V-0.4Cr steel. As a starting point for all investigations presented in this thesis, samples were taken from soft annealed rods with dimensions  $\text{Ø}28 \times 4000 \text{ mm}$ . The further time-temperature cycles incorporated austenitizing at  $1020^\circ\text{C}/30 \text{ min}$  followed by continuous cooling with rates of 100 to  $0.15^\circ\text{C s}^{-1}$ . Afterwards, samples were reheated with  $0.5^\circ\text{C s}^{-1}$  to a tempering temperature of  $620^\circ\text{C}$  and held there for 4 hours.

To investigate predominant phase transformations during individual time-temperature cycles, *in-situ* techniques such as HEXRD coupled with dilatometry are used. To characterize microstructural changes over all length scales a couple of *ex-situ* microstructure analysis techniques, such as optical microscopy, SEM, TEM and 3D-APT were carried out. To further support experimental findings, the thermo-kinetic software package MatCalc is used.

The initial microstructure after the soft annealing process consist of a ferritic matrix with embedded carbides, such as  $\text{M}_2\text{C}$  (2.9 vol.-%),  $\text{M}_3\text{C}$  (1 vol.-%) and  $\text{M}_6\text{C}$  (0.5 vol.-%). Subsequent reheating of the soft annealed microstructure to  $1020^\circ\text{C}$  leads to the dissolution of the  $\text{M}_3\text{C}$  and  $\text{M}_2\text{C}$  carbides. Conversely, the amount of  $\text{M}_6\text{C}$  remains constant during austenitization. Measurements regarding the prior austenite grain size after quenching with  $100^\circ\text{C s}^{-1}$  delivered a value of  $23 \pm 8 \text{ }\mu\text{m}$ . The continuous cooling transformation diagram for the constant austenitization conditions of  $1020^\circ\text{C}/30 \text{ min}$  reveals that the decomposition of austenite to bainite occurs between cooling rates higher than  $0.3^\circ\text{C s}^{-1}$  and lower than  $6^\circ\text{C s}^{-1}$ .

The mechanisms behind the bainitic reaction are still in dispute. Nonetheless, several typical features associated with the bainitic phase transformation became well-known. These features include the differentiation of bainite morphologies into upper, lower and granular bainite as well as the incomplete transformation phenomenon. Accordingly, two competing theories have evolved. The first theory invokes a reconstructive transformation, describing the growth of bainite via a propagation of growth ledges on the interface between bainite and austenite. The second interpretation favours a displacive transformation, where bainite growth occurs via the autocatalytic nucleation of sub-units. The findings in the present thesis strongly supports the displacive transformation theory of bainite and the main conclusions are given in the following. Analysis of the transformation kinetics by means of dilatometry an HEXRD show a change from a continuous transformation behaviour (cooling rate  $>1^\circ\text{C s}^{-1}$ ) to

a distinct two-stage behaviour (cooling rate  $<0.75^{\circ}\text{C}\text{s}^{-1}$ ). This change in the transformation behaviour can consistently explained on basis of an adapted T0' concept, taking into account strain energy values between 950 and  $1100\text{Jmol}^{-1}$ .

Microstructure investigations reveal that the formation of bainite begins with the nucleation of bainitic sub-units at prior austenite grain boundaries. Afterwards a new sub-unit nucleates at the former one and builds up the characteristic wedge-shaped sheave structure. The individual sub-units are partially separated by thin films of retained austenite, whereas sheaves are separated by blocks of retained austenite. The bainitic sub-unit inherits the chemical composition of the former austenite during growth, thus the bainitic ferrite is supersaturated with carbon. As a consequence of the high transformation temperatures ( $350\text{-}510^{\circ}\text{C}$ ), much of the excess carbon partitions in the remaining austenite after the phase transformation, but some carbon still remains within the bainitic ferrite, either in solid solution or trapped at defects. Concentration profiles across the austenite/ferrite interface indicate that no significant segregation of substitutional elements occurs during transformation. These results are fully consistent with the diffusionless phase transformation theory of austenite to bainite. The investigations further showed that the supersaturation of carbon in bainitic ferrite increases with increasing cooling rate and that the carbon concentration exceeds the paraequilibrium phase boundary between bainitic ferrite and austenite. Furthermore, the bainite transformation remains incomplete and seems to terminate at approximately  $300^{\circ}\text{C}$  for all cooling rates. The amount of retained austenite increases from 10 vol.-% at  $2^{\circ}\text{C}\text{s}^{-1}$  to a maximum of 17 vol.-% at  $0.75^{\circ}\text{C}\text{s}^{-1}$ . For a further decrease of the cooling rate to  $0.43^{\circ}\text{C}\text{s}^{-1}$ , the amount of retained austenite seems to slightly decrease again and approaches a value of about 15 vol.-%. However, an amount of  $1.5\pm 0.5$  vol.-% of metastable austenite transforms partially to martensite and forms so called M/A-constituents. Analysis of the diffraction pattern revealed no evidence of the formation of carbide phases during cooling, which would otherwise influence the observed transformation behaviour. But due to the detection limit of about 1 vol.-% in X-ray diffraction-based phase analysis, carbide precipitation below this limit cannot be totally excluded. Thus, the final microstructure after continuous cooling consists of bainitic ferrite, retained austenite films/blocks and a small portion of M/A constituents. Comparative hardness measurements reveal an increase from 370HV1 at a cooling rate of  $0.43^{\circ}\text{C}\text{s}^{-1}$  to 410HV1 at a cooling rate of  $2^{\circ}\text{C}\text{s}^{-1}$ .

A further reheating leads to a slight decrease in the hardness, which is related to a further carbon diffusion from bainite into the retained austenite. At approximately  $320^{\circ}\text{C}$  the retained austenite tends to decompose into a mixture of cementite and ferrite. Microstructure observations by TEM show that films of retained austenite

decompose into discrete cementite precipitates between bainitic ferrite sub-units. In contrast, blocks of retained austenite form colonies of cementite and ferrite similar to pearlite. However, cementite precipitation occurs under paraequilibrium conditions and only further tempering leads to a transition from paraequilibrium to the equilibrium composition. Comparative analysis by means of dilatometry and HEXRD reveal that the decomposition of austenite films with a high carbon content transform at lower temperature, whereas austenite blocks are thermally more stable. A thermo-kinetic simulation using MatCalc also supports these results.

In the temperature range of 510 to 620°C the diffusion of substitutional elements become possible. Microstructure observations by means of APT, reveal segregation of Mo, V, Cr and also carbon along dislocations in this temperature range. The local enrichment of carbon and substitutional elements leads to a slight increase in the hardness. Subsequent isothermal tempering at 620°C leads to a significant hardness increase up to 100HV. This drastic hardness increase is caused by the dissolution of the metastable cementite and precipitation of  $M_2C$  carbides.

## 9 References

- [1] H.K.D.H. Bhadeshia, D. V. Edmonds, The bainite transformation in a silicon steel, *Metall. Trans. A.* 10 (1979) 895–907. doi:10.1007/BF02658309.
- [2] H.K.D.H. Bhadeshia, D. V. Edmonds, Bainite in silicon steels: new composition–property approach Part 1, *Met. Sci.* 17 (1983) 411–419. doi:10.1179/030634583790420646.
- [3] H.K.D.H. Bhadeshia, D. V. Edmonds, Bainite in silicon steels: new composition–property approach Part 2, *Met. Sci.* 17 (1983) 420–425.
- [4] S. Zamberger, Through process modeling of microalloyed steel production, Vienna University of Technology, 2015.
- [5] E. Kozeschnik, MatCalc - The materials calculator, (2018). [www.matcalc.at](http://www.matcalc.at).
- [6] E. V. Pereloma, D. V. Edmonds, Phase Transformations in Steels : Diffusionless transformations, high strength steels, modelling and advanced analytical techniques, 2nd ed., 2012.
- [7] H.K.D.H. Bhadeshia, R. Honeycombe, Steels: Microstructure and Properties, 3rd ed., 2006. doi:<https://doi.org/10.1016/B978-0-7506-8084-4.X5000-6>.
- [8] H.K.D.H. Bhadeshia, Some phase transformations in steels, *Mater. Sci. Technol.* 15 (1999) 22–29.
- [9] Y. Ohmori, Isothermal decomposition of an Fe- C- B austenite, *Trans. ISIJ.* 11 (1971) 339–348.
- [10] H.K.D.H. Bhadeshia, Lower Bainite Transformation and the Significance of Carbide Precipitation., *Acta Metall.* 28 (1980) 1103–1114. doi:10.1016/0001-6160(80)90093-0.
- [11] B.P.J. Sandvik, The Bainite Reaction in Fe-Si-C Alloys: The Primary Stage, *Metall. Trans. A.* 13 (1982) 777–787. doi:10.1007/BF02642392.
- [12] J.W. Christian, Accommodation strains in martensite formation, and the use of a dilatation parameter, *Acta Metall.* 6 (1958) 377–379. doi:10.1016/0001-6160(58)90077-4.
- [13] H.K.D.H. Bhadeshia, R. Honeycombe, Steels: microstructure and properties, Third ed., 1995.
- [14] Z. Nishiyama, M.E. Fine, M. Meshii, C.M. Wayman, Martensitic transformation, 1978.
- [15] Y.Y. Meshkov, E. V. Pereloma, The effect of heating rate on reverse

- transformations in steels and Fe-Ni-based alloys, in: Phase Transform. Steels, Volume 2, 2012: pp. 581–618. doi:10.1533/9780857096104.4.581.
- [16] L. Jikai, Influence of metallurgical phase transformation on crack propagation of 15-5PH stainless steel and 16MND5 low carbon steel, (2012).
- [17] H.I. Aaronson, The mechanism of phase transformations in metals: a symposium organised by the Institute of Metals and held at the Royal Institution, London, on 9 November 1955, (1955) 47.
- [18] H.I. Aaronson, H.A. Domian, Partition of alloying elements between austenite and proeutectoid ferrite or bainite, *Trans. Metall. Soc. AIME.* (1966).
- [19] H.K.D.H. Bhadeshia, P. Street, C. Cb, Diffusional transformation of iron and its alloys, *Prog. Mater. Sci.* 29 (1985) 321–386.
- [20] A. Ali, Widmanstätten ferrite and Bainite in Ultra-high Strength Steels, University of Cambridge, 1991.
- [21] G. Krauss, S.W. Thompson, Ferritic Microstructures in Continuously Cooled Low- and Ultralow-carbon Steels., *ISIJ Int.* 35 (1995) 937–945. doi:10.2355/isijinternational.35.937.
- [22] J.H. Park, Y.K. Lee, Non-isothermal austenite formation behavior in an interstitial free steel with different ferrite microstructures, *Scr. Mater.* 58 (2008) 602–605. doi:10.1016/j.scriptamat.2007.11.021.
- [23] M. V. Kral, Proeutectoid ferrite and cementite transformations in steels, Woodhead Publishing Limited, 2012. doi:10.1533/9780857096104.2.225.
- [24] A. Hultgren, Isothermal transformation of austenite, *Trans. Am. Soc. Met.* 39 (1947) 915–1005.
- [25] J.C. Fisher, Eutectoid Decompositions, *Thermodyn. Phys. Metall. Am. Soc. Met. Clevel.* (1950) 201.
- [26] M.E. Nicholson, the Nucleation of Pearlite, *J. Met.* (1954) 1071–1074.
- [27] R.F. Mehl, D.W. Smith, Orientation of ferrite in pearlite, *Trans. AIME.* 116 (1935) 330–341.
- [28] G. V Smith, R.F. Mehl, Lattice relationships in decomposition of austenite to pearlite, bainite and martensite, *Trans. AIME.* 150 (1942) 14.
- [29] R.J. Dippemaar, R.W.K. Honeycombe, The crystallography and nucleation of pearlite, *Proc. R. Soc. London.* 467 (1973) 455–467. doi:10.1098/rspa.1973.0073.
- [30] J.D. Eshelby, Determination of the elastic field of an ellipsoidal inclusion, and related problems, *Proc. R. Soc. London.* (1957) 376–396. doi:10.1098/rspa.1957.0133.

- [31] H.K.D.H. Bhadeshia, *Bainite in steels*, 3rd ed., Maney publishing, 2015.
- [32] H.K.D.H. Bhadeshia, Widmanstätten Ferrite, (1996) 1–3. <https://www.phase-trans.msm.cam.ac.uk/2000/C9/lecture7.pdf> (accessed September 9, 2019).
- [33] H.K.D.H. Bhadeshia, A rationalisation of shear transformations in steels, *Acta Metall.* 29 (1981) 1117–1130. [http://dx.doi.org/10.1016/0001-6160\(81\)90063-8](http://dx.doi.org/10.1016/0001-6160(81)90063-8).
- [34] H.K.D.H. Bhadeshia, Interpretation of the Microstructure of Steels, (n.d.). [https://www.phase-trans.msm.cam.ac.uk/2008/Steel\\_Microstructure/SM.html](https://www.phase-trans.msm.cam.ac.uk/2008/Steel_Microstructure/SM.html) (accessed May 30, 2019).
- [35] E.S. Davenport, E.C. Bain, Transformation of austenite at constant subcritical temperature, *Trans. Amer. Inst. Min. Met. Eng.* 90 (1930) 117–154.
- [36] C. Zener, Kinetics of the decomposition of austenite, *Trans. Aime.* 167 (1946) 550–595.
- [37] H.K.D.H. Bhadeshia, D. V. Edmonds, Mechanism of Bainite Formation in Steels., *Acta Metall.* 28 (1980) 1265–1273. doi:10.1016/0001-6160(80)90082-6.
- [38] F.G. Caballero, H.K.D.H. Bhadeshia, Very strong bainite, *Curr. Opin. Solid State Mater. Sci.* 8 (2004) 251–257. doi:10.1016/j.cossms.2004.09.005.
- [39] J.M. Oblak, R.H. Goodenow, R.F. Hehemann, Morphology of bainite in hypoeutectoid steels, *Trans. Metall. Soc. Aime.* 230 (1964) 258.
- [40] G.R. Srinivasan, C.M. Wayman, Transmission electron microscope study of the bainite transformation in iron-chromium-carbon alloys, *Acta Metall.* 16 (1968) 609–620.
- [41] H.I. Aaronson, C. Wells, Sympathetic nucleation of ferrite, *Trans. AIME.* 8 (1956) 1216–1223.
- [42] H.K.D.H. Bhadeshia, Bainite in Steels, in: *Bainite in Steels*, 2001: pp. 63–90.
- [43] S.V. Parker, Modelling of phase transformations in hot-rolled steels, University of Cambridge, 1997. doi:<https://doi.org/10.17863/CAM.14220>.
- [44] C.H. Young, H.K.D.H. Bhadeshia, Strength of mixtures of bainite and martensite, *Mater. Sci. Technol.* 10 (1994) 209–214. doi:10.1179/026708394790163663.
- [45] S.B. Singh, H.K.D.H. Bhadeshia, Estimation of bainite plate-thickness in low-alloy steels, *Mater. Sci. Eng. A.* 245 (1998) 72–79. doi:10.1016/S0921-5093(97)00701-6.
- [46] E. Swallow, H.K.D.H. Bhadeshia, High resolution observations of displacements caused by bainitic transformation, *Mater. Sci. Technol.* 12 (1996) 121–125.

- doi:10.1179/026708396790165614.
- [47] M. Nemoto, Growth of bainite in an iron-nickel-carbon alloy, *High Volt. Electron Microsc.* (1974) 230–234.
- [48] M. Takahashi, H.K.D.H. Bhadeshia, Model for transition from upper to lower bainite, *Mater. Sci. Technol.* 6 (1990) 592–603. doi:10.1179/mst.1990.6.7.592.
- [49] H.-S. Yang, Design of Low-Carbon, Low-Temperature Bainite, 2011. doi:20080961.
- [50] F.G. Caballero, M.K. Miller, C. Garcia-mateo, J. Cornide, M.J. Santofimia, Temperature dependence of carbon supersaturation of ferrite in bainitic steels, *Scr. Mater.* 67 (2012) 846–849. doi:10.1016/j.scriptamat.2012.08.007.
- [51] F.G. Caballero, M.K. Miller, S.S. Babu, C. Garcia-Mateo, Atomic scale observations of bainite transformation in a high carbon high silicon steel, *Acta Mater.* 55 (2007) 381–390. doi:10.1016/j.actamat.2006.08.033.
- [52] E. Pereloma, H. Beladi, L. Zhang, I. Timokhina, Understanding the Behavior of Advanced High-Strength Steels Using Atom Probe Tomography, *Metall. Mater. Trans. A.* 43 (2012) 3958–3971. doi:10.1007/s11661-011-0782-0.
- [53] H. Bhadeshia, Anomalies in carbon concentration determinations from nanostructured bainite, *Mater. Sci. Technol.* 31 (2015) 758–763. doi:10.1179/1743284714y.00000000655.
- [54] J.H. Jang, H.K.D.H. Bhadeshia, D.W. Suh, Solubility of carbon in tetragonal ferrite in equilibrium with austenite, *Scr. Mater.* 68 (2013) 195–198. doi:10.1016/j.scriptamat.2012.10.017.
- [55] A.S. Podder, Tempering of a Mixture of Bainite and Retained Austenite, 2011. [http://www.msm.cam.ac.uk/phase-trans/2011/Arijit\\_thesis.pdf](http://www.msm.cam.ac.uk/phase-trans/2011/Arijit_thesis.pdf).
- [56] H.K.D.H. Bhadeshia, A.R. Waugh, Bainite: An atom-probe study of the incomplete reaction phenomenon, *Acta Metall.* 30 (1982) 775–784. doi:10.1016/0001-6160(82)90075-X.
- [57] H.I. Aaronson, W.T. Reynolds, G.R. Purdy, The incomplete transformation phenomenon in steel, *Metall. Mater. Trans. A.* 37 (2006) 1731–1745. doi:10.1007/s11661-006-0116-9.
- [58] J.R. Bradley, H.I. Aaronson, Growth kinetics of grain boundary ferrite allotriomorphs in Fe-C-X alloys, *Metall. Trans. A.* 12 (1981) 1729–1741. doi:10.1007/BF02643755.
- [59] H.D. Wu, G. Miyamoto, Z.G. Yang, C. Zhang, H. Chen, T. Furuhashi, Incomplete bainite transformation in Fe-Si-C alloys, *Acta Mater.* 133 (2017) 1–



9. doi:10.1016/j.actamat.2017.05.017.
- [60] Y. Xia, G. Miyamoto, Z.G. Yang, C. Zhang, T. Furuhashi, Direct measurement of carbon enrichment in the incomplete bainite transformation in Mo added low carbon steels, *Acta Mater.* 91 (2015) 10–18. doi:10.1016/j.actamat.2015.03.021.
- [61] F.G. Caballero, M.K. Miller, C. Garcia-Mateo, J. Cornide, New experimental evidence of the diffusionless transformation nature of bainite, *J. Alloys Compd.* 577 (2013) S626–S630. doi:10.1016/j.jallcom.2012.02.130.
- [62] W.T. Reynolds, F.Z. Li, C.K. Shui, H.I. Aaronson, The Incomplete transformation phenomenon in Fe-C-Mo alloys, *Metall. Trans. A.* 21 (1990) 1433–1463. doi:10.1007/BF02672561.
- [63] H. Goldenstein, H.I. Aaronson, Overall reaction kinetics and morphology of austenite decomposition between the upper nose and the Ms of a hypoeutectoid Fe-C-Cr alloy, *Metall. Trans. A.* 21 (1990) 1465–1478. doi:10.1007/BF02672562.
- [64] F.G. Caballero, C. Garcia-Mateo, M.J. Santofimia, M.K. Miller, C. García de Andrés, New experimental evidence on the incomplete transformation phenomenon in steel, *Acta Mater.* 57 (2009) 8–17. doi:10.1016/j.actamat.2008.08.041.
- [65] L.C. Chang, H.K.D.H. Bhadeshia, Austenite films in bainitic microstructures, *Mater. Sci. Technol.* 11 (1995) 874–882. doi:10.1179/026708395790165462.
- [66] H.K.D.H. Bhadeshia, High Performance Bainitic Steels, *Mater. Sci. Forum.* 500–501 (2005) 63–74. doi:10.4028/www.scientific.net/MSF.500-501.63.
- [67] A.S. Podder, H.K.D.H. Bhadeshia, Thermal stability of austenite retained in bainitic steels, *Mater. Sci. Eng. A.* 527 (2010) 2121–2128. doi:10.1016/j.msea.2009.11.063.
- [68] Z.C. Li, H. Ding, R.D.K. Misra, Z.H. Cai, Microstructure-mechanical property relationship and austenite stability in medium-Mn TRIP steels: The effect of austenite-reverted transformation and quenching-tempering treatments, *Mater. Sci. Eng. A.* 682 (2017) 211–219. doi:10.1016/j.msea.2016.11.048.
- [69] A.S. Podder, I. Lonardelli, A. Molinari, H.K.D.H. Bhadeshia, Thermal stability of retained austenite in bainitic steel: An in situ study, *Proc. R. Soc. A Math. Phys. Eng. Sci.* 467 (2011) 3141–3156. doi:10.1098/rspa.2011.0212.
- [70] J. Min, L.G. Hector, L. Zhang, J. Lin, J.E. Carsley, L. Sun, Elevated-temperature mechanical stability and transformation behavior of retained austenite in a quenching and partitioning steel, *Mater. Sci. Eng. A.* 673 (2016)

- 423–429. doi:10.1016/j.msea.2016.07.090.
- [71] D. De Knijf, C. Föjer, L.A.I. Kestens, R. Petrov, Factors influencing the austenite stability during tensile testing of Quenching and Partitioning steel determined via in-situ Electron Backscatter Diffraction, *Mater. Sci. Eng. A.* 638 (2015) 219–227. doi:10.1016/j.msea.2015.04.075.
- [72] F.G. Caballero, C. García-Mateo, J. Chao, M.J. Santofimia, C. Capdevila, C.G. de Andrés, Effects of Morphology and Stability of Retained Austenite on the Ductility of TRIP-aided Bainitic Steels, *ISIJ Int.* 48 (2008) 1256–1262. doi:10.2355/isijinternational.48.1256.
- [73] H.K.D.H. Bhadeshia, *Bainite in Steels*, 1st edition, (1992) 2–9.
- [74] R.M. Wu, W. Li, C.L. Wang, Y. Xiao, L. Wang, X.J. Jin, Stability of retained austenite through a combined intercritical annealing and quenching and partitioning (IAQP) treatment, *Acta Metall. Sin. (English Lett.)* 28 (2015) 386–393. doi:10.1007/s40195-015-0217-9.
- [75] G.R. Speich, W.C. Leslie, Tempering of Steel, *Metall. Trans.* 3 (1972) 1043–1054. doi:10.1361/spsap2005p327.
- [76] C.S. Roberts, B.L. Averbach, M. Cohen, The mechanism and kinetics of the 1st stage of tempering, *Trans. Am. Soc. Met.* 45 (1953) 576–604.
- [77] C. Wells, W. Batz, R.F. Mehl, Diffusion of carbon in austenite, *Trans. AIME.* 188 (1950) 533–560. doi:10.1179/030634581790426525.
- [78] S.J. Matas, R.F. Hehemann, The structure of bainite in hypoeutectoid steels, *Trans. Metall. Soc. AIME.* 221 (1961) 179–185.
- [79] L.J. Habraken, Bainitic transformation of steels, *Rev. Metall.* 53 (1956) 930.
- [80] L.J. Habraken, M. Economopoulos, Bainitic microstructures in low-carbon alloy steels and their mechanical properties, *Transform. Hardenability Steels.* (1967) 69–108.
- [81] B.A. Leont'yev, G.V. Kovalevskaya, On the bainitic transformation mechanism of austenite, *Phys. Met. Metallogr.* 38 (1974) 139–143.
- [82] B. Josefsson, H.O. Andren, Microstructure and Thermodynamic Behaviour of a CrMo SA Weld Metal in the As-Welded State, in: *Proc. Int. Conf. Recent Trends Weld. Sci. Technol.* Gatlinburg, Tennessee, 1989: p. 243.
- [83] F.G. Caballero, H. Roelofs, S. Hasler, C. Capdevila, J. Chao, J. Cornide, C. Garcia-Mateo, Influence of bainite morphology on impact toughness of continuously cooled cementite free bainitic steels, *Mater. Sci. Technol.* 28 (2012) 95–102. doi:10.1179/1743284710Y.0000000047.

- [84] E. Mazancová, K. Mazanec, Physical metallurgy characteristics of the M/A constituent formation in granular bainite, *J. Mater. Process. Technol.* 64 (1997) 287–292. doi:10.1016/S0924-0136(96)02578-2.
- [85] D.P. Koistinen, R.E. Marburger, A general equation prescribing the extent of the austenite-martensite transformation in pure iron-carbon alloys and plain carbon steels, *Acta Metall.* 7 (1959) 59–60. doi:10.1016/0001-6160(59)90170-1.
- [86] G.B. Olson, M. Cohen, A general mechanism of martensitic nucleation: Part I. General concepts and the FCC→ HCP transformation., *Metall. Trans. A.* 7 (1976) 1897–1904.
- [87] G.B. Olson, M. Cohen, A general mechanism of martensitic nucleation: Part II. FCC - BCC and other martensitic transformations. *Metallurgical Transactions A*, 7(12), 1905–1914. <https://doi.org/10.1007/BF02659823> of martensitic, *Metall. Trans. A.* 7 (1976) 1905–1914. doi:10.1007/BF02659823.
- [88] G.B. Olson, M. Cohen, A general mechanism of martensitic nucleation: Part III. Kinetics of martensitic nucleation., *Metall. Trans. A.* 7 (1976) 1915–1923. doi:10.1007/BF02659822.
- [89] S.A. Khan, H.K.D. Bhadeshia, Kinetics of Martensitic transformation in partially bainitic 300M steel, *Mater. Sci. Eng. A.* 129 (1990) 257–272. doi:10.1016/0921-5093(90)90273-6.
- [90] G.B. Olson, M. Cohen, Theory of martensitic nucleation: a current assessment, *Solid to Solid Phase Transform.* (1981) 1145–1164.
- [91] A. Stormvinter, G. Miyamoto, T. Furuhashi, P. Hedström, A. Borgenstam, Effect of carbon content on variant pairing of martensite in Fe-C alloys, *Acta Mater.* 60 (2012) 7265–7274. doi:10.1016/j.actamat.2012.09.046.
- [92] M. Jung, S.J. Lee, Y.K. Lee, Microstructural and dilatational changes during tempering and tempering kinetics in martensitic medium-carbon steel, *Metall. Mater. Trans. A Phys. Metall. Mater. Sci.* 40 (2009) 551–559. doi:10.1007/s11661-008-9756-2.
- [93] M.J. Genderen, M. Isac, a. Böttger, E.J. Mittemeijer, Aging and tempering behavior of iron-nickel-carbon and iron-carbon martensite, *Metall. Mater. Trans. A.* 28 (1997) 545–561. doi:10.1007/s11661-997-0042-5.
- [94] A. Vieweg, E. Povoden-Karadeniz, G. Ressel, P. Prevedel, T. Wojcik, F. Mendez-Martin, A. Stark, J. Keckes, E. Kozeschnik, Phase evolution and carbon redistribution during continuous tempering of martensite studied with high resolution techniques, *Mater. Des.* 136 (2017) 214–222.

- doi:10.1016/j.matdes.2017.09.065.
- [95] L.I.U. Cheng, C.M. Brakman, B.M. Korevaar, E.J. Mittemeijer, The Tempering of Iron-Carbon Martensite ; Dilatometric and Calorimetric Analysis, 19 (1988).
- [96] F.G. Caballero, C. García-Mateo, C. García de Andrés, Dilatometric Study of Reaustenitisation of High Silicon Bainitic Steels: Decomposition of Retained Austenite, Mater. Trans. 46 (2005) 581–586. doi:10.2320/matertrans.46.581.
- [97] T. Klein, M. Lukas, P. Haslberger, B. Friessnegger, M. Galler, G. Ressel, Complementary Thermal Analysis Protocols for the Investigation of the Tempering Reactions of a Carbide-Free Bainitic Steel, Jom. (2019). doi:10.1007/s11837-019-03331-z.
- [98] E. De Moor, C. Föjler, J. Penning, A.J. Clarke, J.G. Speer, Calorimetric study of carbon partitioning from martensite into austenite steel, Phys. Rev. B - Condens. Matter Mater. Phys. 82 (2010) 1–5. doi:10.1103/PhysRevB.82.104210.
- [99] Y.I. Ustinovshchikov, Secondary hardening mechanism of alloy steels, Met. Sci. 18 (1984) 337–344. doi:10.1179/030634584790419917.
- [100] A.A.B. Sugden, H.K.D.H. Bhadeshia, A model for the strength of the As-deposited regions of steel weld metals, Metall. Trans. A. 19 (1988) 1597–1602. doi:10.1007/BF02674034.
- [101] Y. Shingo, Modelling Precipitation of Carbides in Martensitic Steels, n.d.
- [102] T. Gladman, Precipitation Hardening in metals, Mater. Sci. Technol. 15 (1999) 30–36.
- [103] R.C. Thomson, H.K.D.H. Bhadeshia, Changes in chemical composition of carbides in 2-25Cr-1 Mo power plant steel Part 1: bainitic microstructure, 10 (1994) 193–203.
- [104] D. Raynor, J.A. Whiteman, R.W.K. Honeycombe, Precipitation of molybdenum and vanadium carbides in high-purity iron alloys, IRON STEEL INST J. 204 (1966) 349–354.
- [105] M. Tanino, T. Nishida, K. Aoki, The crystallographic orientation relationship between M<sub>2</sub>C and the ferritic matrix, JAP INST Met. J. 30 (1966) 894–895.
- [106] W. Pitsch, A. Schrader, Die Ausscheidungsform des  $\epsilon$ -Karbids im Ferrit und im Martensit beim Anlassen, Steel Res. Int. 29 (1958) 715–721.
- [107] K.G.F. Janssens, D. Raabe, E. Kozeschnik, M.A. Miodownik, B. Nestler, Computational Materials Engineering: An Introduction to Microstructure Evolution, Elsevier Science, 2010.
- [108] J. Svoboda, F.D. Fischer, P. Fratzl, E. Kozeschnik, Modelling of kinetics in

- multi-component multi-phase systems with spherical precipitates I: Theory, *Mater. Sci. Eng. A.* 385 (2004) 166–174. doi:10.1016/j.msea.2004.06.018.
- [109] J. Svoboda, F.D. Fischer, P. Fratzl, E. Kozeschnik, Modelling of kinetics in multi-component multi-phase systems with spherical precipitates: II: Numerical solution and application, *Mater. Sci. Eng. A.* 385 (2004) 157–165. doi:<https://doi.org/10.1016/j.msea.2004.06.016>.
- [110] E. Kozeschnik, J. Svoboda, F.D. Fischer, Modified evolution equations for the precipitation kinetics of complex phases in multi-component systems, *Calphad Comput. Coupling Phase Diagrams Thermochem.* 28 (2004) 379–382. doi:10.1016/j.calphad.2004.11.003.
- [111] R. Radis, Numerical simulation of the precipitation kinetics of nitrides and carbides in microalloyed steel, (2010) 174. <http://scholar.google.com/scholar?hl=en&btnG=Search&q=intitle:Numerical+Simulation+of+the+Precipitation+Kinetics+of+Nitrides+and+Carbides+in+Microalloyed+Steel#2>.
- [112] L. Onsager, Reciprocal relations in irreversible processes. I., *Phys. Rev.* 37 (1931) 405–426. doi:10.1103/PhysRev.37.405.
- [113] H.L. Lukas, S.G. Fries, B. Sundman, others, *Computational thermodynamics: the Calphad method*, Cambridge university press Cambridge, 2007.
- [114] E. Povoden-Karadeniz, Thermodynamic Database mc\_fe.tdb (v.2.059), (2017). <http://matcalc.tuwien.ac.at/index.php/databases/open-databases>.
- [115] and C.S. Higginson, R., *Worked examples in quantitative metallography*, 2003.
- [116] E.E. Underwood, Stereology, or the quantitative evaluation of microstructures, *J. Microsc.* 89 (1969) 161–180. doi:10.1111/j.1365-2818.1969.tb00663.x.
- [117] A. Standard, E112-96, 2004, *Stand. Test Methods Determ. Aver. Grain Size.* (n.d.).
- [118] J. Angeli, E. Füreder, Ätztechniken für die Phasencharakterisierung von niedriglegierten Dual-Phasen- und TRIP-Stählen, *Prakt. Metallogr.* 43 (2006) 489–504. <http://cat.inist.fr/?aModele=afficheN&cpsidt=18219008>.
- [119] S. Reisinger, G. Ressel, S. Eck, S. Marsoner, Differentiation of grain orientation with corrosive and colour etching on a granular bainitic steel, *Micron.* 99 (2017) 67–73. doi:10.1016/j.micron.2017.04.002.
- [120] P.V.C. Hough, *Method and means for recognizing complex patterns*, (1962).
- [121] Dr Paul Edwards., *Nanoscale characterisation of nitride semiconductor thin films using electron backscatter diffraction, electron channelling contrast*

- imaging, cathodoluminescence and electron beam induced current, (n.d.).  
<http://gan-sem.phys.strath.ac.uk/techniques/electron-backscatter-diffraction-ebsd/> (accessed January 29, 2018).
- [122] D.B. Williams, C.B. Carter, *Transmission Electron Microscopy: A Textbook for Materials Science*, 2009. doi:10.1007/978-1-61779-415-5\_23.
- [123] W. Grogger, M. Varela, R. Ristau, B. Schaffer, F. Hofer, K.M. Krishnan, Energy-filtering transmission electron microscopy on the nanometer length scale, *J. Electron Spectros. Relat. Phenomena.* 143 (2005) 139–147. doi:10.1016/j.elspec.2004.09.028.
- [124] M.K. Miller, A. Cerezo, M.G. Hetherington, G.D.W. Smith, *Atom Probe Field Ion Microscopy*, 1996.
- [125] G.B. Thompson, M.K. Miller, H.L. Fraser, Some aspects of atom probe specimen preparation and analysis of thin film materials, 100 (2008) 25–34. doi:10.1016/j.ultramic.2004.01.010.
- [126] M.K. Miller, R.G. Forbes, Atom probe tomography, *Mater. Charact.* 60 (2009) 461–469. doi:10.1016/j.matchar.2009.02.007.
- [127] Astm, Standard Practice for X-Ray Determination of Retained Austenite in Steel with Near Random Crystallographic Orientation 1, *Astm.* 03 (2009) 1–7. doi:10.1520/E0975-13.necessary.
- [128] N. Schell, A. King, F. Beckmann, H.U. Ruhnau, R. Kirchhof, R. Kiehn, M. Miller, A. Schreyer, The High Energy Materials Science Beamline (HEMS) at PETRA III, *AIP Conf. Proc.* 1234 (2010) 391–394. doi:10.1063/1.3463221.
- [129] P. Staron, T. Fischer, T. Lippmann, A. Stark, S. Daneshpour, D. Schnubel, E. Uhlmann, R. Gerstenberger, B. Camin, W. Reimers, E. Eidenberger, H. Clemens, N. Huber, A. Schreyer, In situ experiments with synchrotron high-energy X-rays and neutrons, *Adv. Eng. Mater.* 13 (2011) 658–663. doi:10.1002/adem.201000297.
- [130] A.P. Hammersley, ESRF Internal Report, FIT2D: An Introduction and Overview, 1997.  
[http://www.esrf.eu/computing/scientific/FIT2D/FIT2D\\_REF/node268.html](http://www.esrf.eu/computing/scientific/FIT2D/FIT2D_REF/node268.html).
- [131] G. Faninger, Gezielte Untersuchungen zur quantitativen Röntgen-Phasenanalyse (RPAf), *Heat Treat. Mater.* 30 (1975) 231–244.
- [132] B.D. Cullity, *Elements of X-ray diffraction*, 1956. doi:10.1017/CBO9781107415324.004.
- [133] R.A. Young, The Rietveld Method, *Cryst. Res. Technol.* 30 (1995) 494.

- [134] L. Xiao, Z. Fan, Z. Jinxiu, Z. Mingxing, K. Mokuang, G. Zhenqi, Lattice-parameter variation with carbon content of martensite. I. X-ray-diffraction experimental study, *Phys. Rev. B.* 52 (1995) 9970–9978. doi:10.1103/PhysRevB.52.9970.
- [135] M. Onink, C.M. Brakman, F.D. Tichelaar, E.J. Mittemeijer, S. van der Zwaag, J.H. Root, N.B. Konyer, The lattice parameter of austenite and ferrite in Fe-C alloys as function of carbon concentration and temperature, *Scr. Metall. Mater.* 29 (1993) 1011–1016. doi:10.1017/CBO9781107415324.004.
- [136] E.P. Abrahamson, S.L. Lopata, The Lattice Parameters and Solubility Limits of Alpha Iron as Affected by Some Binary Transition-Elements Additions, *Am. Inst. Mining, Met. Eng.* 236 (1966) 76–87.
- [137] X. Liu, F. Zhong, J. Zhang, M. Zhang, M. Kang, Z. Guo, Lattice parameter variation with carbon content of martensite. I. X-ray diffraction experimental study, *Phys. Rev. B.* 52 (1995) 9970–9978.
- [138] L. Cheng, A. Bouger, T.H. de Keijser, Lattice Parameters of Iron Carbon and Iron Nitrogen Martensites and Austenites, *Scr. Metall. Mater.* 24 (1990) 509–514.
- [139] D.J. DYSON, B. HOLMES, Effect of alloying addition on the lattice parameter of austenite, *J Iron Steel Inst.* 208 (1970) 469–474. <https://www.scopus.com/inward/record.uri?eid=2-s2.0-0014778197&partnerID=40&md5=5b197b267279ed88d140c08a338704d2>.
- [140] H.K.D.H. Bhadeshia, S.A. David, J.M. Vitek, R.W. Reed, Stress induced transformation to bainite in Fe–Cr–Mo–C pressure vessel steel, *Mater. Sci. Technol.* 7 (1991) 686–698. doi:10.1179/mst.1991.7.8.686.
- [141] S.S. Babu, E.D. Specht, S. a. David, E. Karapetrova, P. Zschack, M. Peet, H.K.D.H. Bhadeshia, In-situ observations of lattice parameter fluctuations in austenite and transformation to bainite, *Metall. Mater. Trans. A.* 36 (2005) 3281–3289. doi:10.1007/s11661-005-0002-x.
- [142] M. Werkstoffe, ÖNORM EN ISO 6507-1, 07 (2016).
- [143] V.S. GmbH, Stahl-Eisen-Prüfblätter (SEP) 1680 VDEh, (1998).
- [144] B. Sundman, B. Jansson, J.O. Andersson, The Thermo-Calc databank system, *Calphad.* 9 (1985) 153–190. doi:10.1016/0364-5916(85)90021-5.
- [145] J.C. Greenbank, CARBON SOLUTE INTERACTIONS IN FE-CR-C, FE-MO-C AND FE-W-C ALLOYS, *J Iron Steel Inst.* 209 (1971) 986–990.
- [146] H. Wada, Thermodynamics of the Fe-Mo-C system at 985 K, *Metall. Trans. A.*



- 17 (1986) 391–398. doi:10.1007/BF02643945.
- [147] F.G. Berry, R.W.K. Honeycombe, The isothermal decomposition of austenite in Fe-Mo-C alloys, *Metall. Trans. 1* (1970) 3279–3286. doi:10.1007/BF03037854.
- [148] O. Girina, N. Fonstein, O. Yakubovsky, D. Panahi, D. Bhattacharya, S. Jansto, The Influence of Mo, Cr and B Alloying on Phase Transformation and Mechanical Properties in Nb Added High Strength Dual Phase Steels, *HSLA Steels 2015, Microalloying 2015 Offshore Eng. Steels 2015 Conf. Proc.* (2015) 237–245. doi:10.1002/9781119223399.ch24.
- [149] J. Kong, C. Xie, Effect of molybdenum on continuous cooling bainite transformation of low-carbon microalloyed steel, *Mater. Des.* 27 (2006) 1169–1173. doi:10.1016/j.matdes.2005.02.006.
- [150] D. Quidort, Y.J.M. Brechet, A Model of Isothermal and Non Isothermal Transformation Kinetics of Bainite in 0 . 5 % C Steels, *ISIJ Int.* 42 (2002) 1010–1017. doi:10.2355/isijinternational.42.1010.
- [151] D. Quidort, Y. Bréchet, The role of carbon on the kinetics of bainite transformation in steels, *Scr. Mater.* 47 (2002) 151–156. doi:10.1016/S1359-6462(02)00121-5.
- [152] C. Garcia-Mateo, F.G. Caballero, M.K. Miller, J.A. Jimenez, On measurement of carbon content in retained austenite in a nanostructured bainitic steel, *J. Mater. Sci.* 47 (2012) 1004–1010. doi:10.1007/s10853-011-5880-2.
- [153] M. Ben Haj Slama, N. Gey, L. Germain, J.C. Hell, K. Zhu, S. Allain, Fast Granularization of Lath-Like Bainite in FeNiC Alloys During Isothermal Holding at  $M_s + 20$  K (+20 °C), *Metall. Mater. Trans. A Phys. Metall. Mater. Sci.* 47 (2015) 15–18. doi:10.1007/s11661-015-3209-5.
- [154] C. Hofer, F. Winkelhofer, H. Clemens, S. Primig, Morphology change of retained austenite during austempering of carbide-free bainitic steel, *Mater. Sci. Eng. A.* 664 (2016) 236–246. doi:10.1016/j.msea.2016.04.005.
- [155] C. Hofer, H. Leitner, F. Winkelhofer, H. Clemens, S. Primig, Structural characterization of “carbide-free” bainite in a Fe–0.2C–1.5Si–2.5Mn steel, *Mater. Charact.* 102 (2015) 85–91. doi:10.1016/j.matchar.2015.02.020.
- [156] L.C. Chang, H.K.D.H. Bhadeshia, Austenite films in bainitic microstructures, *Mater. Sci. Technol.* 11 (1995) 874–882. doi:10.1179/026708395790165462.
- [157] L. Chang, S.J. Barnard, G.D.W. Smith, The segregation of carbon atoms to dislocations in low-carbon martensites: studies by field ion microscopy and atom probe microanalysis, in: Gilbert R. Speich Symp. Proc. Fundam. Aging

- Tempering Bainitic Martensitic Steel Prod., 1992: pp. 19–28.
- [158] D. Kalish, M. Cohen, Structural Changes and Strengthening in the Strain Tempering of Martensite \*, *Mater. Sci. Eng.* 6 (1970) 156–166.
- [159] M. Hillert, L. Höglund, J. Ågren, Role of carbon and alloying elements in the formation of bainitic ferrite, *Metall. Mater. Trans. A.* 35 (2004) 3693–3700. doi:10.1007/s11661-004-0275-5.
- [160] B.M. Huang, J.R. Yang, H.W. Yen, C.H. Hsu, C.Y. Huang, H. Mohrbacher, Secondary hardened bainite, *Mater. Sci. Technol.* 30 (2014) 1014–1023. doi:10.1179/1743284714Y.0000000536.
- [161] M.K. Miller, C. Garcia-Mateo, S.S. Babu, C. Capdevila, F.G. Caballero, Redistribution of alloying elements during tempering of a nanocrystalline steel, *Acta Mater.* 56 (2007) 188–199. doi:10.1016/j.actamat.2007.09.018.
- [162] C. Garcia-Mateo, F.G. Caballero, C. Capdevila, C.G. de Andres, Estimation of dislocation density in bainitic microstructures using high-resolution dilatometry, *Scr. Mater.* 61 (2009) 855–858. doi:10.1016/j.scriptamat.2009.07.013.
- [163] J.R. Yang, H.K.D.H. Bhadeshia, Continuous heating transformation of bainite to austenite, *Mater. Sci. Eng. A.* 131 (1991) 99–113. doi:10.1016/0921-5093(91)90349-R.
- [164] C. García De Andrés, F.G. Caballero, C. Capdevila, L.F. Álvarez, Application of dilatometric analysis to the study of solid-solid phase transformations in steels, *Mater. Charact.* 48 (2002) 101–111. doi:10.1016/S1044-5803(02)00259-0.
- [165] M. Takahashi, Reaustenitization from bainite in steels, Ph. D. Thesis,(University Cambridge). (1992).
- [166] K. Andrews, Empirical formulae for the calculation of some transformation temperatures, *J. Iron Steel Inst.* 2030 (1965) 721–727.

## 10 Appendix

### A. Publications

The author of this PhD thesis was also author of several papers, published during his time as a PhD student. The following list shows the references of these papers, which cover investigations on the characterization of bainitic microstructures as well as on the bainitic phase transformation during continuous cooling conditions.

***“Differentiation of grain orientation with corrosive and colour etching on a granular bainitic steel”***

Authors: S. Reisinger, G. Ressel, S. Eck, S. Marsoner

Published in Micron (Vol. 99) p.67-73, 2017

DOI: 10.1016/j.micron.2017.04.002

Numbers of citations as of August 2019: 6

***”Strain energy contributions on the bainitic phase transformation in a CrMoV steel during continuous cooling”***

Authors: S. Reisinger, E. Kozeschnik, G. Ressel, J. Keckes, A. Stark, S. Marsoner, R. Ebner

Published in Materials & Design (Vol. 155) Pages 475-484, 2018,

DOI: 10.1016/j.matdes.2018.06.014

Numbers of citations as of August 2019: 2

*A.1. Differentiation of grain orientation with corrosive and colour etching on a granular bainitic steel*



## Tutorial

# Differentiation of grain orientation with corrosive and colour etching on a granular bainitic steel



S. Reisinger\*, G. Ressel, S. Eck, S. Marsoner

Materials Center Leoben Forschung GmbH, Austria

## A B S T R A C T

This study presents a detailed verification of the etching methods with Nital and Klemm on a granular bainitic steel. It is shown that both methods allow the identification of the crystal orientation, whereas Klemm etching enables also a quantification of the apparent phases, as also retained austenite can be distinguished from the other bainitic microstructures. A combination of atom probe tomography with electron-back-scattered-diffraction showed that both etching methods emphasize the bainitic {100} crystal orientation. However, a cross-section produced by focused ion beam evidenced that Klemm etching leads to the formation of a topography of the different oriented bainitic crystals that directly affects the thickness and therefore the apparent colour of the deposited layer formed during etching.

## 1. Introduction

It is a well-known fact that the mechanical properties of steels are influenced by the solid-solid phase transitions during heat treatment and the corresponding evolution of the microstructure (Eck et al., 2014a, 2014b; Eisenhüttenleute, 1984). Bainitic steels have grown in importance because of their material properties close the gap between conventional martensitic steels and ferritic-perlitic steel grades (Raedt et al., 2017; Bhadeshia, 2001). Due to the related higher costs it is often not possible to accomplish a fully bainitic microstructure by an isothermal heat treatment in steel producing industries. A more favourable variant to achieve a bainitic microstructure is a continuous cooling heat treatment. For this heat treatment variant, the final microstructures strongly depend on the cooling rate (Mazancova and Mazanek, 1997; Wang and Yang, 1992). If the cooling rate is in a certain range, a granular bainitic microstructure is formed. A special feature of this microstructure is often the lack of carbides (e.g. cementite), because the carbon is partitioned from bainitic ferrite to the remaining austenite and stabilizes the austenite (Bhadeshia 2001; Mazancova and Mazanek, 1997). Thus, the final microstructure consists of bainitic ferrite sheaves/platelets which are separated by thin films of retained austenite and blocky islands of retained austenite or high carbon enriched martensite, which influences strongly the mechanical properties. To predict the macroscopic material properties the global and local quantification of the different apparent phases is important (Schemmel et al., 2015). X-ray diffraction (XRD) techniques offer a possibility to determine macroscopic quantities of the apparent phases

via the crystal orientation (Wiessner et al., 2014). However, due to the geometric extension of the excitation (i.e. excitation both on the surface and in the bulk of the material) this technique does not easily allow the determination of the local phase distribution; local investigations are possible, but difficult and expensive.

Etching is one of the most powerful metallographic techniques to identify phases. In most cases corrosive or colour etchants only allow to distinguish between the phases but they do not reveal grain orientation (Angeli et al., 2004). For the determination of grain orientations electron-backscatter-diffraction (EBSD) is commonly used (Pereloma et al., 2014). However, EBSD investigations are on the one hand time consuming (cost intensive) and on the other hand have to be tuned to the expected size of the microstructural effects. With the currently available equipment either a large region of several  $\sim 100 \mu\text{m}^2$  is scanned with a low resolution ( $> 300 \text{ nm}$  pixel size) or a small region ( $\sim 1 \mu\text{m}^2$ ) is scanned with a high resolution ( $< 20 \text{ nm}$  pixel size). Here, etching techniques have an advantage because it is a cheap and simple characterization method and with the optical light microscope (OLM) both large regions ( $\sim 1 \text{ mm}^2$ ) and small regions ( $\sim 1 \mu\text{m}^2$ ) can be investigated in short time on the same sample. Furthermore, correlative microscopy offers the possibility to investigate an etched surface with even higher resolution, e.g. by combining OLM and scanning electron microscopy (SEM).

Therefore, in this paper we present a technique to determine the grain orientation of a granular bainitic microstructure by means of corrosive and colour etching in OLM and evidence that no local chemical differences are responsible for the different etching attack,

\* Corresponding author.

E-mail addresses: [Stephan.reisinger@mcl.at](mailto:Stephan.reisinger@mcl.at) (S. Reisinger), [gerald.ressel@mcl.at](mailto:gerald.ressel@mcl.at) (G. Ressel), [sven.eck@mcl.at](mailto:sven.eck@mcl.at) (S. Eck), [stefan.marsoner@mcl.at](mailto:stefan.marsoner@mcl.at) (S. Marsoner).

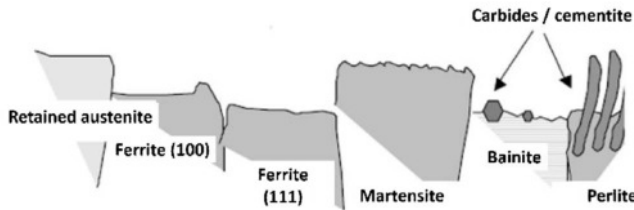


Fig. 1. Model of corrosive etching in multiphase steel taken from Angeli et al. (2004).

by means of EBSD and atom probe tomography (APT). Furthermore, the layer thickness after colour etching was determined to explain the different colours appearing on each grain orientation in the OLM.

## 2. Fundamentals of etching

### 2.1. Corrosive etching

The classical corrosive etching strongly depends on chemical composition, crystal orientation and lattice defects. In Angeli et al. (2004), they developed a model for corrosive etching in multiphase steels. They concluded that carbon rich phases (e.g. austenite) act as anodes in the electrolyte and that the carbon poor phases (e.g. ferrite) represent the cathode. Subsequently, the higher the carbon content of a phase, the higher is its resistance to the removal by etching, as sketched in Fig. 1. The influence of the crystal orientation on the chemical removal is particularly strong in carbon poor phases. In Engell (1958), the author showed in his experiments with dilute sulfuric and nitric acid on  $\alpha$ -iron, that a crystal surface with a {111} orientation is removed two times faster than a surface with a {100} orientation. The reason for this behaviour lies in the different anodic parts of the current density potential curves of both crystal surfaces, which is more positive at a {100} surface.

### 2.2. Colour etching

In addition to the traditional corrosive etching methods, colour etching methods are increasingly used in metallographic laboratories because the colour contrast offers a fast and easy way to distinguish different phases in the microstructure. In the case of colour etching methods, a chemical reaction of the etchant with the substrate forms a deposit layer on the surface. Analogous to the corrosive etching methods, the different phases act as anode or cathode and different etchants form either a cathodic (e.g. molybdenum-acid) or an anodic (e.g. Klemm1-etchant) layer on the surface (Angeli et al., 2004), as shown in Fig. 2. Another analogy to the corrosive etching is that the etchant reaction with the substrate scales with the local carbon content of the phase. This time it is not the material removal that leads to a different contrast in the OLM, but the different thicknesses of the surface layer formed by the aforementioned chemical reaction, henceforth called “deposit”.

The apparent colour of the deposit in an OLM image is generated via an interference effect between metal surface and the surface of the deposit. To keep the illustration simple, we consider only a simple reflection, as schematically shown in Fig. 3. This interference effect depends on the deposit thickness  $d$ , the reflection index  $n$  of the deposit, the wavelength  $\lambda$  and angle of incidence of the light source. When the incident light hits the deposit, a part of the light is reflected at the surface, another part penetrates into the deposit. The penetrating light reaches the metal surface after passing through the deposit and is reflected on the deposit-metal interface. The re-passing of the deposit-air interface results in a path difference between the two reflected light rays. This path difference is proportional to the double of the deposit thickness  $d$  and constructive interference occurs when the path difference is equivalent to an integral multiple of half the wavelength

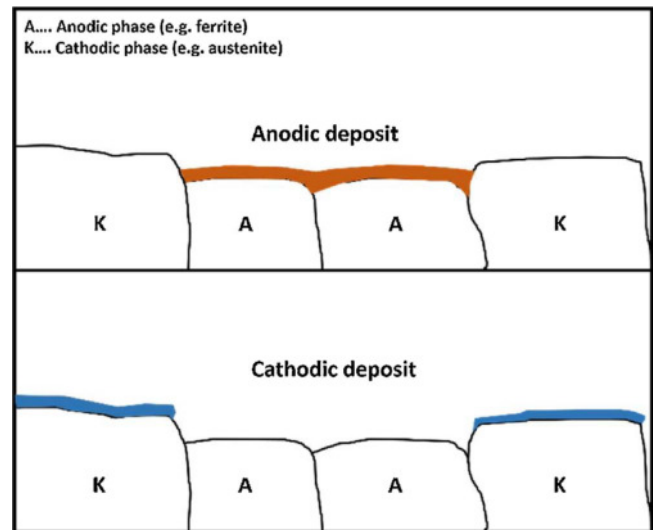


Fig. 2. Model of colour etching with anodic and cathodic deposit.

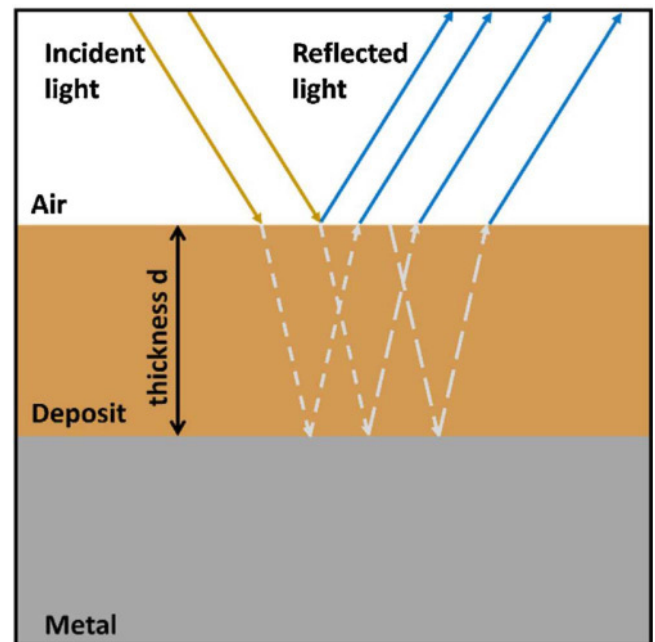


Fig. 3. Schematic diagram for light interference after colour etching.

$\lambda$  (Meschede, 2015). Destructive interference occurs when the deposit thickness corresponds to an integral multiple of the quarter of the wavelength. In this case a part of the light which corresponds to the deposit thickness is removed from the incident light and the observer sees the complementary colour (Szabo and Kardos, 2010; Szabo and Bonyar, 2012). According to constructive/destructive interference, also the order of interference is important for the observed colour. In Britz et al. (2016) they presented an in situ experiment with a Beraha etchant on a dual-phase steel, which shows the colour evolution as a function of the exposure time. The authors pointed out, that during the experiment the colour passes different orders of interference. In the first order the colour changes from yellow, red, purple to a blue staining. However, in the second-order of interference the colour spectrum ranges from yellow to green. The authors also observed third-order colours, from yellow to slight red. They also concluded that higher-order colours appear brighter and more intense. This is contradictory to the findings by Gahn and Jeglitsch (1981), they demonstrated that first-order colours are the most brilliant and intense colours.

**Table 1**

Chemical composition of the investigated bainitic steel in wt.%.

C	Si	Mn	Cr	Ni	Mo	V	Fe
0,28	0,27	0,32	0,43	0,11	2,82	0,39	bal.

### 3. Experimental procedure

Measurements were performed on a low alloyed hot-work-steel, with a chemical composition as shown in Table 1. To produce a bainitic microstructure the steel was austenitized for 30 min at 1020 °C and then cooled to room temperature with a cooling rate of 0.75 K/s in a SYSTERMS™ vacuum chamber VWC 446-15VC. After this heat treatment the following workflow was applied to produce the images shown in this publication:

- Cutting, grinding and polishing.
- XRD measurements of the austenite content.
- Nital etching or Klemm1 etching.
- APT measurements of different areas.
- EBSD measurements of local crystal orientations.

To investigate the microstructure by OLM, a traditional preparation technique of grinding and polishing was applied, followed by corrosive etching for 5 s with Nital (3 ml HNO<sub>3</sub> in 97 ml Ethanol). The corresponding microstructure showed clearly distinguishable areas with a different contrast.

APT was applied to investigate the differences in the local chemical composition. The APT measurements have been carried out using laser mode on a LEAP 3000 × HR from Cameca™, at a temperature of 40 K and with laser pulse energy of 0.2 nJ. The sample preparation was done by applying a lift-out method followed by annular milling as described in (Stevie et al., 2001; Miller and Russel 2007). The reconstruction of the investigated volumes and the analysis of the data sets have been carried out with the software package IVAS 3.4.3 from Cameca™.

To separate individual phases the specimen was colour etched for 20, 40, 80, 120 and 160 s with a Klemm1 etchant (2 g K<sub>2</sub>S<sub>2</sub>O<sub>5</sub> in 100 ml stock solution of 1000 g Na<sub>2</sub>S<sub>2</sub>O<sub>3</sub>·5H<sub>2</sub>O). OLM micrographs were recorded after each preparation step using an Olympus BX51 optical light microscope with 500- and 1000 fold magnification. Phase quantification was performed via the thresholding and area counting method on the Olympus™ Stream Motion Software. XRD measurements were performed according to ASTM E975-03 to quantify the global amount of retained austenite using an Xstress™ G2 diffractometer with Cr-Kα radiation source (exposed area d = 3 mm, exposure time 40 s ferrite/180 s austenite).

Subsequently, the sample was transferred into a ZEISS™ AURIGA-CrossBeam-Workstation SEM to characterize the region of interest. To improve the EBSD quality, the surface was treated with a Hitachi™ IM4000 Plus ion milling system for 10 min. EBSD measurements were then performed using 20 kV accelerating voltage and 70 nm pixel size on one position and 10 nm pixel size on a second position.

## 4. Results and discussion

### 4.1. Investigation of the bainitic microstructure via nital etching

In order to get an overview of the microstructure, in the most cases steel samples are at first investigated by means of OLM. Fig. 4 shows the microstructure of the investigated steel after etching with Nital. The etching revealed a typical bainitic microstructure after continuous cooling that can be attributed to granular bainite. Similar microstructure images can be found by Mazancova and Mazanek, (1997). The microstructure depicted in Fig. 4 shows bright areas (A1) with a size of ~50 μm<sup>2</sup>, which are attributed to a different reaction to the etchant

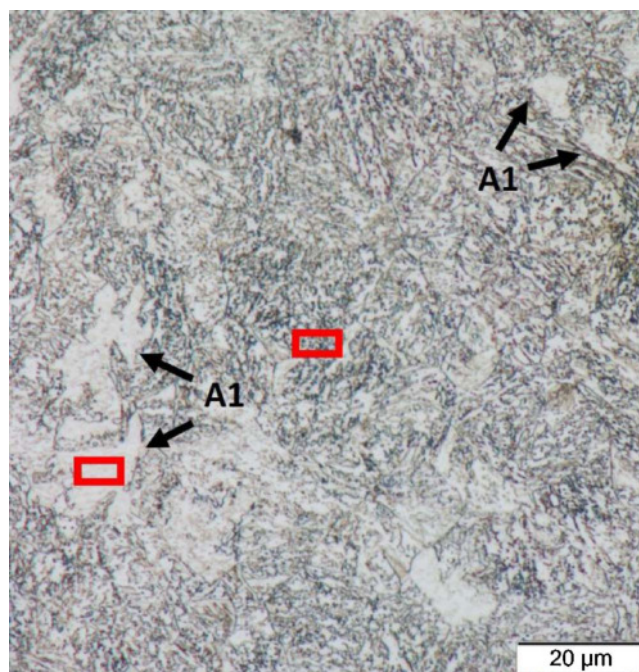


Fig. 4. Sample after etching with Nital. Areas (A1) which are less affected by the electrolyte can be identified; the rectangles indicate the positions of the APT investigations.

Nital. Angeli et al., (2004) proposed that the varying carbon content controls the etching attack and therefore the contrast of the microstructure in OLM images. According to this one is tempted to identify these regions in Fig. 4 as blocky retained austenite or carbon enriched martensite. Consequently, to compare the local chemical composition (especially the carbon content), APT investigations were carried out in the bright areas and the matrix marked with red rectangles in Fig. 4. The corresponding APT results are summarized in Table 2. According to the APT results, in both regions carbon atoms are distributed homogeneously and there is no significant difference in the chemical composition that would explain a different removal during corrosive etching. Furthermore, the low carbon content measured at both positions refutes the assumption, that the bright areas are blocky regions comprising retained austenite and martensite and that the etching attack is controlled only by the chemical composition of the phase.

Therefore, further investigations were performed in order to get a detailed information, which kind of microstructural components are present in the investigated granular bainite.

### 4.2. Investigation of the bainitic microstructure via colour etching

Fig. 5a–d shows the sample after Klemm1 etching for 20, 40, 80, and 160 s, respectively. It can be seen that the regions which are slightly etched by Nital, discolour during each step differently than the matrix. After 160 s the sample appeared blue or purple and the areas A1 and the matrix could not be clearly distinguished. However, a green staining was never observed during the first 160 s, which indicates that the colouring takes place in the first order of interference (Britz et al.,

**Table 2**

Chemical composition in wt.%, measured with APT from A1 and matrix, marked with two red rectangles in Fig. 4.

Pos.	C	Si	Mn	Cr	Ni	Mo	V	Fe
A1	0,1	0,13	0,31	0,43	0,13	2,2	0,36	bal.
Matrix	0,1	0,13	0,26	0,43	0,12	2,32	0,16	bal.



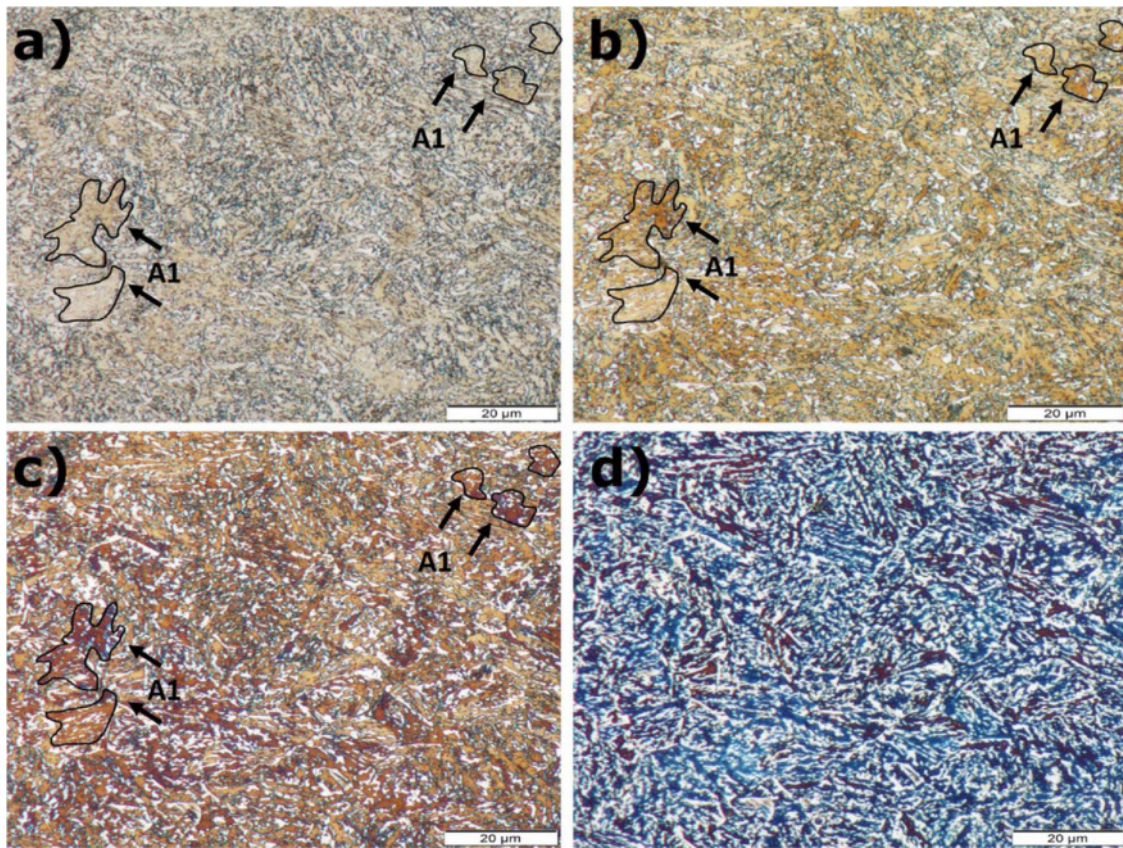


Fig. 5. OLM images showing the microstructure after Klemm1 etching for a) 20, b) 40, c) 80 and d) 160 s. The percentage of white area in c coincides with the XRD measurement of 17% retained austenite in this specimen.

2016). During this etching process, carbon rich phases remain white, because no deposit is formed (Angeli et al., 2004; Beckert and Klemm, 1962). Therefore, it can be excluded, that all areas indexed with “A1” are blocky retained austenite. A corresponding area counting of the white regions lead to an area percentage of  $5 \pm 5\%$ ,  $7 \pm 3\%$  and  $15 \pm 2\%$  for 20, 40 and 80 s of etching, i.e. for the images shown in Fig. 5a, b and c, respectively. An XRD analysis on the same sample revealed a retained austenite content of  $17 \pm 1\%$ . That coincidence suggests that for this particular microstructure, it is possible to estimate the amount of retained austenite by the colour etching quantification method provided that care is taken with respect to a comparable etching time of around 80 s and image contrast (e.g. via an image histogram analysis). A potential error can arise from carbides, which also appear white during colour etching, because of their high carbon content. In our case of a granular bainitic microstructure, carbides can be neglected due to their low phase fraction (Bhadeshia 2001; Mazancova and Mazanek, 1997).

#### 4.3. Investigation of the local crystal orientation

In Engell (1958), the author proposed that the removal of iron atoms by an electrolyte or the formation of a deposit on a metal surface depends also on the crystal orientation of the material. In contrast to pure  $\alpha$ -iron, bainitic microstructures consist of individual packages of sheaves with the same orientation (Bhadeshia, 2001). If this is the case, the bright areas in Fig. 4 after Nital etching should have the same orientation. To confirm this statement an EBSD measurement was performed on the same position. An inverse pole figure map superimposed with the image quality (IPF + IQ) map of this measurement is shown in Fig. 6.

A direct comparison of the OLM image (Fig. 4) with the EBSD measurement (Fig. 6), reveals that the bright areas after Nital etching

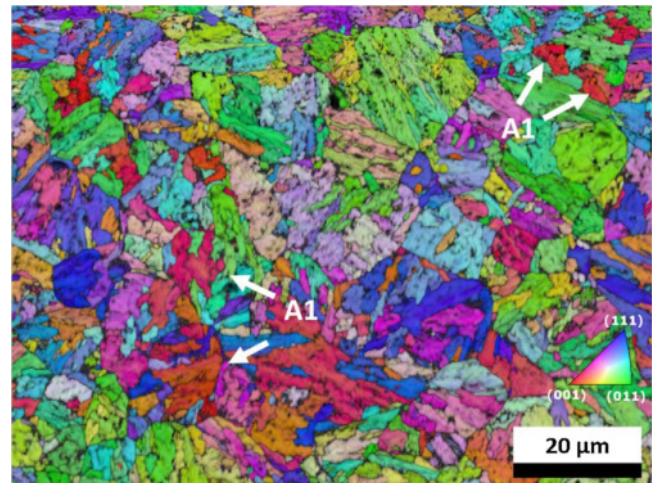


Fig. 6. IPF+IQ map of the position showed in Fig. 1. White arrows point towards the regions appearing bright in Fig. 4.

show a  $\{100\}$  or a close  $\{100\}$  crystal orientation (red in Fig. 6). Therefore, it can be proposed that Nital etching of the investigated steel highlights the  $\{100\}$  orientation. In the case of colour etching, imaging is influenced by the angle of the incident light, multiple reflections, refractive index and the thickness of the deposit. In Petzow (2006), Beckert and Klemm (1962) they pointed out, that a Klemm1 etchant should form a brown to blue layer on ferrite/bainite depending on the crystal orientation. Due to the constant re-preparation of the sample, a second position was selected for further investigations. Based on the Klemm1 etching procedure in Fig. 5 an ideal contrast between the bright areas and the matrix was found at 120 s of etching time with



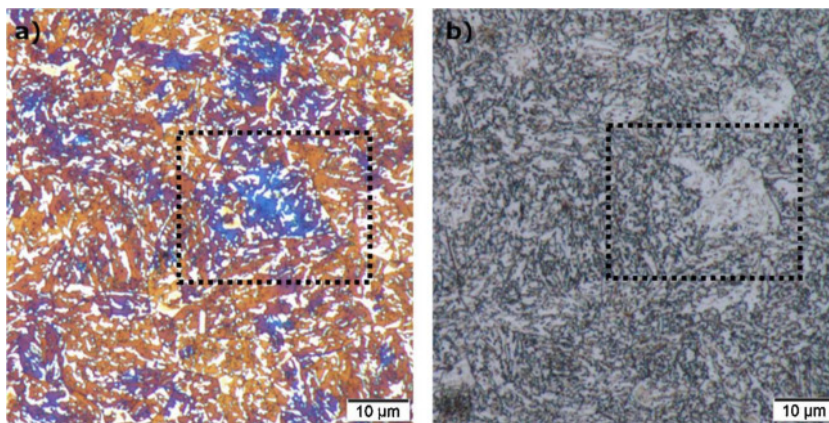


Fig. 7. Sample after a) colour etching with Klemm1 for 120 s and b) after etching with Nital.

Klemm1, which is illustrated in Fig. 7a,b. shows the corresponding Nital image. For better understanding and to confirm a {100} crystal orientation a detailed EBSD map was taken from the position marked with a rectangle in Fig. 7a.

corresponding phase map of austenite in Fig. 8b,c shows a magnified image of the position which is marked in Fig. 7a with a rectangle. The comparison of Fig. 8a,c clearly shows a {100} orientation for the blue area in Fig. 8c. Taking the fact into account, that there is another polishing step between EBSD measurement and colour etching, wherein

The IPF map of ferrite and austenite is shown in Fig. 8a with the

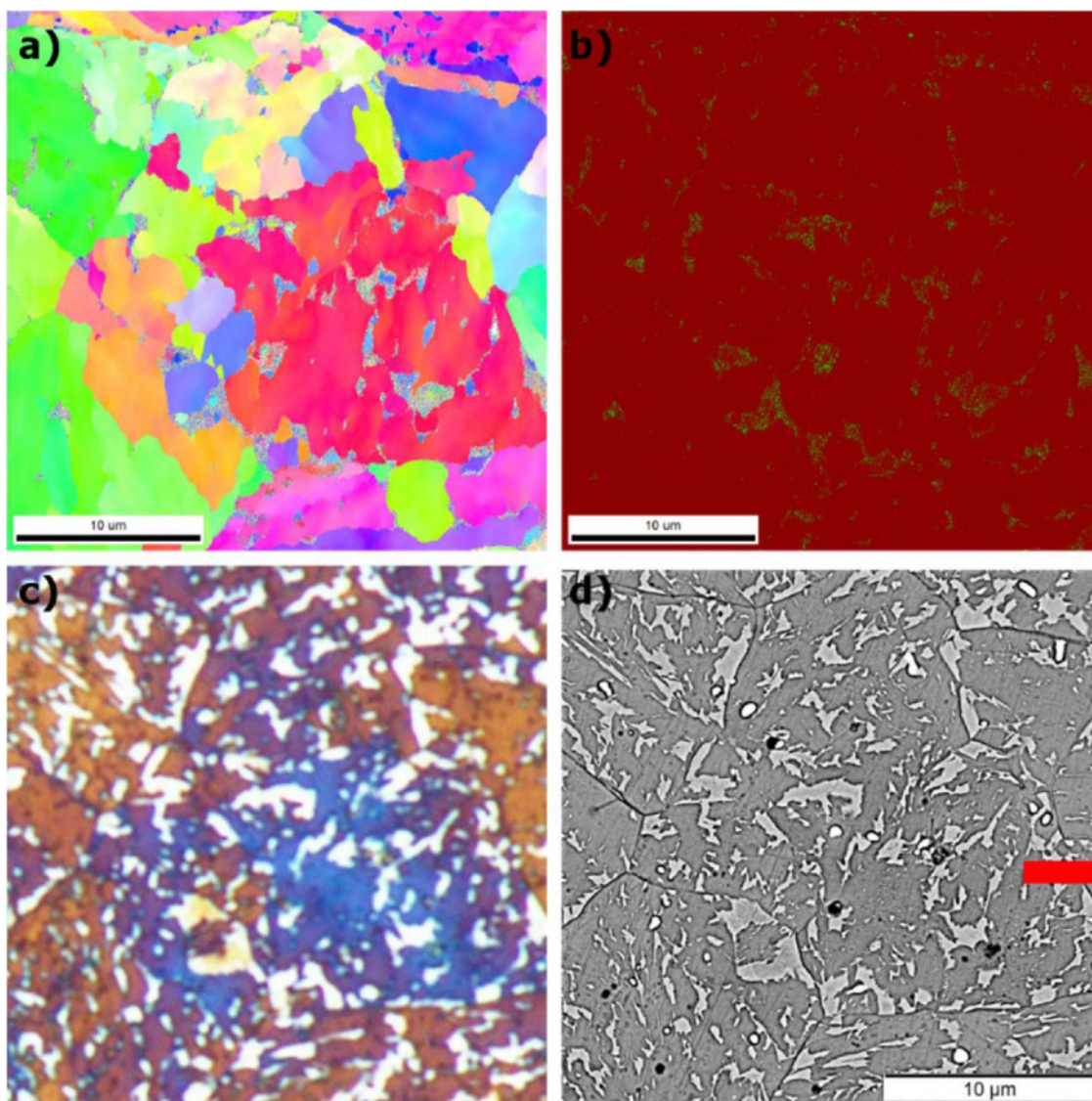


Fig. 8. a) IPF map of ferrite and austenite, b) corresponding austenite phase map green areas correspond to austenite, c) magnified OLM image and d) SEM image after colour etching. (For interpretation of the references to colour in this figure legend, the reader is referred to the web version of this article.)

a portion of retained austenite may be transformed into martensite, the comparison of retained austenite between Fig. 8b,c is also possible by means of Klemm1 colour etching. Therefore, it can be stated that colour etching with a Klemm1 etchant on this steel highlights the {100} crystal orientation and in addition it is also possible to determine the retained austenite content. However, in Szabo and Kardos (2010) the authors showed a combined process of corrosive pre-etching followed by colour etching on grey cast iron. They found a strong correlation of shading and colour parameters (R, G and B components and the Luminescence Y) after colour etching and the deviation of the surface normal from the <100> direction determined by means of EBSD. They assumed that grains with surface normal close to the <100> direction were etched more after corrosive pre-etching, so that on this grains a thicker layer is formed during colour etching. In a further work Bonyar and Szabo (2012) disconfirm this statement. They pointed out that the removal by Nital etching is slowest on a grain with a near <100> direction, which agrees well with the findings in Engell (1958). On the other hand, they showed that the formation of a deposit is fastest on a grain with a near <100> direction by Beraha colour etching.

#### 4.4. Measurement of the local deposit thicknesses after colour etching

In order to correlate the staining and luminescence of different areas after colour etching with deposit thickness, it was necessary to measure the thickness. Therefore, a focused ion beam (FIB) cross section was performed after colour etching at the position marked with a red bar in the SEM micrograph, Fig. 8d.

Fig. 9 shows the cross section after colour etching. The dark sulphide deposit, which is indicated by a white arrow, can be seen between the metal surface and the Pt-layer. Unexpectedly there was a slight removal of the metal surface during colour etching on the bainitic microstructure, which is inconsistent with literature (Angeli et al., 2004; Petzow, 2006; Weck and Leistner, 1995; Beckert and Klemm, 1962). It also can be seen, that on carbon rich phases, i.e. retained austenite or carbon enriched martensite, no or only a minor deposit is formed, which agrees well with Angeli et al. (2004), Beckert and Klemm (1962).

It can be seen, that the deposit thickness on a grain with an {110} crystal orientation was approximately  $30 \pm 2$  nm and on a grain with an {100} crystal orientation it was  $39 \pm 2$  nm. This results are in

strong correlation with the findings by Bonyar and Szabo (2012). In the work Angeli et al. (2004), they suspected a deposit thickness of 70 nm for a blue staining and a thickness over 70 nm for a brown. The measurements shown in Fig. 9 indicate that for this sample and 120 s Klemm etching the thickness was only half of the thickness that Angeli predicted in Angeli et al. (2004). Furthermore, the thickness is zero on carbon rich phases. It is also possible to measure the RGB components from every pixel in Fig. 8c. According to these values the luminescence (Y) can be calculated for each position according to Eq. (1) (Cheng et al., 2001):

$$Y = 0.299 \times R + 0.587 \times G + 0.114 \times B \quad (1)$$

However, the observed colour depends on the deposit thickness and so do the RGB and luminescence values. Analogous to the layer thickness, calculations of the luminescence on a grain with an {110} or {111} crystal orientation showed a value of approximately 125–150 [–] and on a grain with an {100} crystal orientation approximately 100. The colour white corresponds to a luminescence value of 255, which is observed by a deposit thickness near zero. According to the resolution of Fig. 5c one pixel corresponds to 90 nm. It follows that on small retained austenite areas (< 90 nm) the luminescence does not reach the maximum value, as is seen in Fig. 9. Since the resolution is limited by the pixel size, a mixed value for RGB colour components is determined on boundaries between bainitic ferrite and austenite. As a result of this fact, small areas of retained austenite cannot correctly be detected by an area counting. On the other hand, (large) blocky retained austenite regions do not form a sharp edge on the phase boundary, due to the cathodic long term protection. This may result in an over-estimated amount of retained austenite by the area counting method on over etched samples. This fact could explain the difference between the previously presented XRD results and the results of the area counting.

## 5. Conclusion

This work deals with the verification of the effect of the Nital and Klemm etching method on the microstructure of a granular bainitic steel. Investigations in this work showed:

- It is possible to identify the {100} crystal orientation in the investigated steel, by means of both, Nital or Klemm etching. In

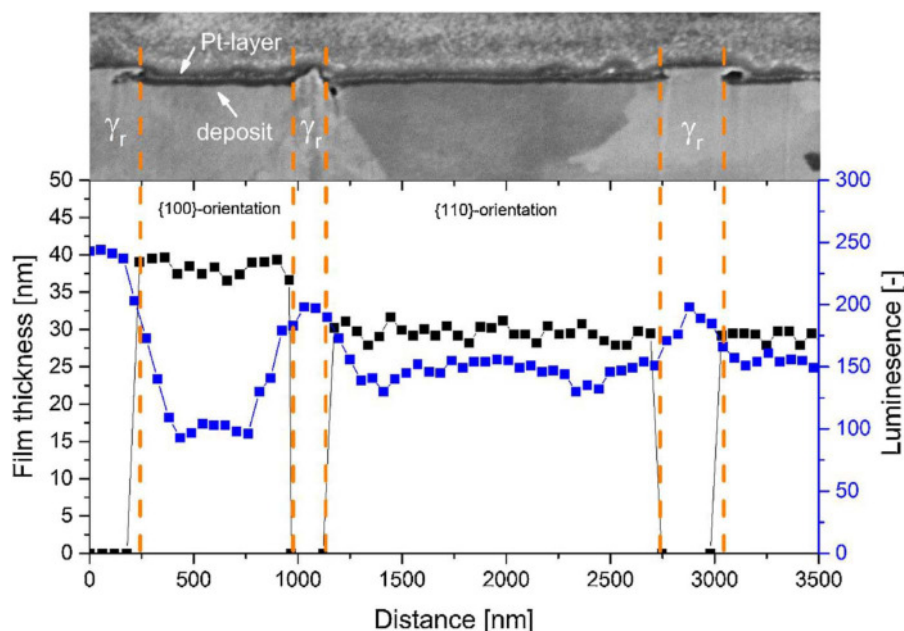


Fig. 9. Cross section after colour etching at a grain boundary between a {100} and a near {110} orientation. The deposit thickness is zero on retained austenite ( $\gamma_r$ ).



the case of Nital etching, bainitic sheaves near to an {100} crystal orientation are different affected by the etchant, which leads to a different contrast in the OLM. In the case of colour etching with a Klemm1 etchant for 120 s, bainitic sheaves near to an {100} crystal orientation are discoloured faster, which leads to a purple/blue colour.

- A cross section after Klemm etching showed, that bainitic ferrite (carbon poor phase) is also removed during colour etching and there is no removal on retained austenite (carbon rich phase).
- The cross section also showed that on a {100} crystal orientation the deposit thickness is approximately 39 nm and on a {110}/{111} crystal orientation 29 nm.
- The luminescence, which is directly affected by the deposit thickness, is around 100 for a {100} crystal orientation and approximately 120–150 for a {110}/{111} crystal orientation.
- It can be confirmed that Klemm etching for 80 s also allows the determination of the retained austenite content via an area counting, which agrees well with XRD measurements.

### Acknowledgements

Financial support by the Austrian Federal Government (in particular from Bundesministerium für Verkehr, Innovation und Technologie and Bundesministerium für Wissenschaft, Forschung und Wirtschaft) represented by Österreichische Forschungsförderungsgesellschaft mbH and the Styrian and the Tyrolean Provincial Government, represented by Steirische Wirtschaftsförderungsgesellschaft mbH and Standortagentur Tirol, within the framework of the COMET Funding Programme is gratefully acknowledged.

### References

- Angeli, J., Kneissel, A.C., Füreder, E., 2004. Ätztechniken für die Phasencharakterisierung von niedriglegierten, hochfesten Mehrphasenstählen. In: Paper Presented at the Fortschritte in Der Metallographie. (38. Metallographietagung, Bochum), 29.09.2004. pp. 1–11.
- Beckert, M., Klemm, H., 1962. Handbuch der metallographischen Ätzverfahren. VEB Verlag für Grundstoffindustrie, Leipzig.
- Bhadeshia, Harshad Kumar Dharamshi Hansraj, 2001. Bainite in Steels. OM Communications Ltd.
- Bonyar, Attila, Szabo, Peter, 2012. Correlation between the grain orientation dependence of color etching and chemical etching. *Microsc. Microanal.* (June (17)), 1389–1392.
- 18 Ausg.
- Britz, D., Hegetschweiler, A., Roberts, M., Mücklich, F., et al., 2016. “Reproducible Surface Contrasting and Orientation Correlation of Low-Carbon Steels by Time-Resolved Beraha Color Etching”. *Mater. Perform. Character.* 5 (5), 553–563. <http://dx.doi.org/10.1520/MPC20160067>. ISSN 2165-3992.
- Cheng, H.D., Jiang, X.H., Sun, Y., Wang, Jingli, 2001. Color image segmentation: advances and prospects. *Pattern Recogn.* 34, 2259–2281.
- Eck, Sven, Oßberger, H., Oßberger, Uwe, Marsoner, Stefan, Ebner, Reinhold, 2014a. Comparison of the fatigue behaviour of 5 different steel grades used in the frog of turnout. *Int. J. Rail Rapid Transit* 208, 603–610.
- Eck, Sven, Prevedel, Petri, Marsoner, Stefan, Ecker, Werner, Illmeier, M., 2014b. Using finite element simulation to optimize the heat treatment of tire protection chains. *J. Mater. Eng. Perform.* 1288–1295.
- Eisenhüttenleute, Verein deutscher, 1984. *Werkstoffkunde Stahl, Band 1: Grundlagen.* Verein deutscher Eisenhüttenleute, Verlag Stahleisen, Düsseldorf.
- Engell, Hans Jürgen, 1958. *Elektrochemische Betrachtung über Das Metallographische Ätzen.* Archiv für das Eisenhüttenwesen, Düsseldorf.
- Gahn, Harald, Jeglitsch, Franz, 1981. Color Methods and their application in metallography. *Met. Prog.* 120 (3), 48–53.
- Wiessner, Manfred, Angere, Paul, Prevedel, Petri, Skalnik, Katharina, Marsoner, Stefan, Ebner, Reinhold, 2014. Advanced X-ray diffraction techniques for quantitative phase content and or quantitative phase content and lattice defect characterization during heat treatment of high speed steels. *Ger-und Hüttenmännische Monatshefte* 9 (July (30)), 390–393.
- Mazancova, E., Mazanek, K., 1997. Physical metallurgy characteristics of the M/A-constituent formation in granular bainite. *J. Mater. Process. Technol.* 64, 287–292.
- Meschede, Dieter, 2015. *Gerthsen Physik*, bd. 25 auflage. Springer Verlag, Bonn.
- Miller, M., Russel, K., 2007. Atom probe specimen preparation with a dual beam SEM/FIB. *Ultramicroscopy* 107, 761–766.
- Pereloma, Elena V., Al-Harbi, Fayez, Azidar Gazder, A., 2014. The crystallography of carbide-free bainites in thermo-mechanically processed low Si transformation-induced plasticity steels. *J. Alloys Compd.* 615, 96–110.
- Petzow, Günther, 2006. *Metallographisches. Keramographisches Und Plastographisches Ätzen*, 6 auflage. Borntraeger, Stuttgart.
- Raedt Hans-Willi, Ulrich Speckenhauer, Klaus Vollrath. [www.massivumformung.de](http://www.massivumformung.de). 03 2012. [http://www.massivumformung.de/uploads/tx\\_news/12-03-02\\_Fachaufsatz\\_Neue\\_Staehle\\_deutsch.pdf](http://www.massivumformung.de/uploads/tx_news/12-03-02_Fachaufsatz_Neue_Staehle_deutsch.pdf) (Zugriff am 07. 03.2017).
- Schemmel, Manuel, Prevedel, Petri, Schöngrundner, Ronald, Ecker, Werner, Antretter, Thomas, 2015. Size effects in residual stress formation during quenching of cylinders made of hot-work tool steel. *Adv. Mater. Sci. Eng.* 15 (Article ID 678056).
- Stevie, F., Vartuli, C., Giannuzzi, L., 2001. Application of focused ion beam lift-out specimen preparation to TEM, SEM, STEM, AES and SIMS analysis. *Surf. Interface Anal.* 345–351 Ausg 31.
- Szabo, Peter J., Bonyar, Attila, 2012. Effect of grain orientation on chemical etching. *Micron* 349–351.
- Szabo, P.J., Kardos, I., 2010. Correlation between orientation and the shade of color etching. *Sci. Direct* 814–817.
- Wang, Shyi Chin, Yang, Jer-Ren, 1992. Effects of chemical composition, rolling and cooling conditions on the amount of martensite/austenite (M/A) constituent formation in low carbon bainitic steels. *Mater. Sci. Eng.* A154, 43–49.
- Weck, Erika, Leistner, Elisabeth, 1995. *Deutscher Verlag für Schweißtechnik*, Düsseldorf.

*A.2. Strain energy contributions on the bainitic phase transformation in a CrMoV steel during continuous cooling*



# Strain energy contributions on the bainitic phase transformation in a CrMoV steel during continuous cooling

S. Reisinger<sup>a,\*</sup>, E. Kozeschnik<sup>b</sup>, G. Ressel<sup>a</sup>, J. Keckes<sup>c</sup>, A. Stark<sup>d</sup>, S. Marsoner<sup>a</sup>, R. Ebner<sup>a</sup>

<sup>a</sup> Materials Center Leoben Forschung GmbH, Austria

<sup>b</sup> TU Wien, Institute of Materials Science and Technology, Austria

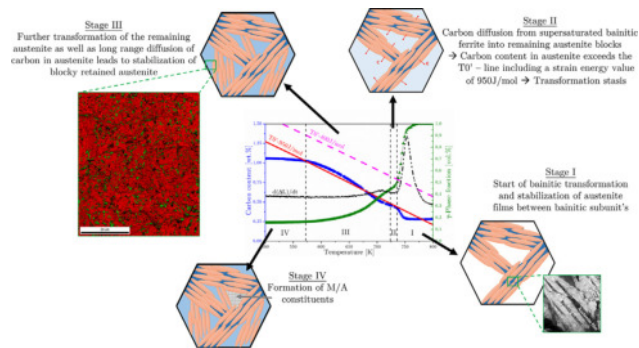
<sup>c</sup> Erich Schmid Institute, Montanuniversität Leoben, Austria

<sup>d</sup> Helmholtz Zentrum Geesthacht, Institute of Materials Research, Germany

## HIGHLIGHTS

- The transformation characteristics from austenite to bainite during continuous cooling changes with decreasing cooling rate
- High amounts of retained austenite are present in the final microstructure in two distinct morphologies: films and blocks
- This high amounts of retained austenite cannot be explained by a  $T_0'$ -line with a strain energy contribution of 400 J/mol
- Simulations and calculations of the strain energy depending on the bainitic microstructure yield values of 950 to 1100 J/mol

## GRAPHICAL ABSTRACT



## ARTICLE INFO

### Article history:

Received 9 April 2018

Received in revised form 17 May 2018

Accepted 7 June 2018

Available online 15 June 2018

### Keywords:

Bainite

Continuous cooling

Strain energy

## ABSTRACT

The bainitic phase transformation during continuous cooling in low alloyed steels is a complex process since many different reactions are taking place simultaneously. Since all of them are rather sensitive to the applied cooling rates, the present study investigates the mechanisms taking place during the bainitic phase transformation by using a comprehensive set of methods including in-situ high energy X-ray diffraction combined with dilatometry, ex-situ microstructure characterization by means of scanning and transmission electron microscopy including electron back scatter diffraction. The results demonstrate that the phase transformation characteristics changes from a continuous to a two-stage behaviour with decreasing cooling rate. The reason for this change is discussed and explained on basis of an adapted  $T_0'$ -limit concept taking an additionally required strain energy between about 950 and 1100 J/mol in the energy balance into account. Apart from the observed transformation characteristics, it is also shown that the amount of blocky instead of film like retained austenite increases with decreasing cooling rate.

© 2018 Elsevier Ltd. All rights reserved.

## 1. Introduction

Since 1930, when bainite was first mentioned in literature by Davenport and Bain [1], several studies were performed in order to investigate the formation of this microstructure. However, in literature, there still exists some dispute with respect to the formation mechanisms of

\* Corresponding author.

E-mail address: [reisinger21@gmx.at](mailto:reisinger21@gmx.at) (S. Reisinger).

bainite in steel and, therefore, it is difficult to find an exact definition of this “unique phase” [2–4]. A rather accurate definition follows the theory by Swallow and Bhadeshia [5], where a surface relief is formed during transformation according to an invariant plane strain. In their work, these authors demonstrated that austenite is plastically deformed on the adjacent interfaces to bainitic subunits. This plastic deformation is facilitated by the low yield strength of austenite at typical bainite start temperatures ( $B_s$ ). Their fundamental statement is that the plastic deformation of austenite stops the growth of a single subunit longitudinal as well as perpendicular to the growth direction. As a result, a new carbon supersaturated bainitic subunit must nucleate for further transformation, thus forming the characteristic sheaf morphology [3, 6, 7].

Under certain conditions, the bainitic phase transformation remains incomplete and significant amounts of retained austenite can be observed at room temperature [8–10]. This behaviour is called incomplete transformation (ICT) phenomenon. The nature of the ICT phenomenon is still discussed in literature [10, 11]. Zener [12] used the idea of free energy change to explain the growth of bainite by calculating a  $T_0$  temperature. The  $T_0$  temperature represents that temperature at which austenite and ferrite of the same composition have the same Gibbs free energy. Zener expressed the change in free energy of the system as a sum of three factors [12]:

$$\Delta G = -\Delta G_{Fe^{a\gamma}} + C\Delta G_{C^{f\gamma}} - CT\Delta S_{C^{a\gamma}} \quad (1)$$

where  $-\Delta G_{Fe^{a\gamma}}$  is the change in free energy of 1 mol of pure iron in the austenite phase compared to that of ferrite,  $C\Delta G_{C^{f\gamma}}$  is the change in free energy of 1 mol of carbon in the ferrite compared to that of austenite and  $-CT\Delta S_{C^{a\gamma}}$  is the excess of entropy of 1 mol of carbon dissolved in austenite (which is negligible for displacive transformations, where the transformation proceeds faster compared to the rate of carbon diffusion). By setting  $\Delta G$  equal to zero, it is possible to solve Eq. (1) for the carbon concentration in austenite in terms of the critical temperature ( $T_0$  temperature). A plot of temperature versus carbon concentration, where austenite and ferrite of the same chemical composition also have identical free energies, represents the  $T_0$  line. According to this concept, only austenite with a carbon concentration lower than that given by the  $T_0$  line can transform into bainitic ferrite.

The ICT phenomenon is commonly explained on the basis that untransformed austenite close to bainite packets can absorb carbon atoms from the supersaturated bainitic ferrite subunits. As a consequence, the remaining austenite enriches in carbon, the  $T_0$  temperature decreases and further diffusionless transformation of bainite becomes thermodynamically impossible.

Bhadeshia and Edmonds [7] adopted the diffusionless mechanism of bainite formation and applied Zener's theory in an Fe–C–Mn–Si alloy, showing that the carbon concentration limits in austenite measured by X-ray diffraction were in good agreement with the  $T_0$  line, although some data exceeded the carbon concentration in austenite at  $T_0$  by 0.2–0.4 m.% below 623 K. In a subsequent article, after a detailed examination of the experimental data in an Fe–C–Ni–Si alloy, Bhadeshia [13] estimated that there is a strain energy contribution of ~400 J/mol associated with the diffusionless growth of bainite. Thus, he proposed a new  $T_0'$  limit on top of  $T_0$ , which takes into account the impact of strain energy. It must be noted that the strain energy can be reduced by plastic relaxation of the adjacent austenite, which is the case during the bainitic transformation [5]. Therefore, the strain energy effort calculated for an elastically accommodated shape change should be interpreted as an upper limit of the strain energy contribution on the phase transformation [14].

The present study is in line with this assumption of diffusionless growth mechanism of bainitic ferrite but the results indicate that the strain energy contribution for the present steel exceeds the 400 J/mol limit suggested by Bhadeshia [21]. On basis of results obtained with in-situ high energy X-ray diffraction (HEXRD) combined with dilatometry as well as scanning electron microscopy (SEM) to study the

transformation kinetics during continuous cooling, a strain energy value contribution between 950 and 1100 J/mol is derived. With these values, the transformation characteristics from austenite to bainite in the present steel can be consistently described.

## 2. Experimental procedure

### 2.1. Investigated material

Measurements were performed on a CrMoV steel, with a chemical composition as shown in Table 1. The initial microstructure was adjusted by means of soft annealing of a rolled steel rod and consisted of a ferritic matrix with coarse carbides.

### 2.2. Dilatometry

#### 2.2.1. Time-temperature cycles for in-situ HEXRD

Time-temperature cycles for the in-situ HEXRD experiments were carried out on a DIL805A/D dilatometer (TA-Instruments). Samples with 4 mm diameter and 10 mm length and co-planar ends were used. During dilatometry measurements, the samples were held between two quartz push-rods, one of the rods being fixed and the other connected to a linear voltage differential transducer. Samples were heated by means of an induction coil and temperature was measured with a type S thermocouple. To achieve a homogenous microstructure prior bainitic phase transformation, the samples were austenitized for 30 min at 1293 K. To study the bainitic transformation kinetics, continuous cooling to room temperature with various cooling rates between 2 K/s and 0.43 K/s were applied, as schematically shown in Fig. 1a.

#### 2.2.2. Time-temperature cycles for ex-situ microstructure observations

To investigate different stages in the bainitic phase transformation, time-temperature cycles as schematically shown in Fig. 1b were carried out on a TA-instruments DIL805L dilatometer. To this end, the samples were also austenitized for 30 min at 1293 K followed by cooling with rates of 2 K/s, 0.75 K/s and 0.43 K/s to different quenching temperatures  $T_q$  (753, 743, 728, 703, 663 and 298 K). After reaching  $T_q$ , the samples were quenched to room temperature with a maximum achievable quenching rate of ~100 K/s.

### 2.3. In-situ HEXRD

For in-situ phase analysis, HEXRD measurements for each cooling rate were conducted at the Deutsches Elektronen-Synchrotron (DESY, Hamburg-Germany) on the beamline P07 at Petra III [15], where the above described dilatometer is placed within the beamline [16]. In order to penetrate the 4 mm thick samples, high energy X-rays were used with a photon energy of 87.1 keV, corresponding to a wavelength of 0.14235 Å. The beam size was  $0.7 \times 0.7$  mm, which corresponds to an examined volume of ~2 mm<sup>3</sup>. The resulting diffraction rings were recorded with a Perkin Elmer XRD1621 flat panel detector with “slow” mode acquisition. In this acquisition mode, 10 diffraction patterns at an exposure time of 0.2 s per diffraction pattern were accumulated. The total recording time for one measurement, which includes shutter opening, data acquisition, subtracting the dark current image (that represents a thermal background of the detector), shutter closure and finally data erasing from the 2-D detector, requires 5 s per pattern. Due to this time lag between two measurements, the average temperature between two measurements was used for further analysis. The temperature difference between two measurements is accordingly 10 K for

**Table 1**  
Chemical composition of the investigated bainitic steel in wt%.

C	Si	Mn	Cr	Ni	Mo	V	Fe
0.28	0.27	0.32	0.43	0.11	2.82	0.39	bal.

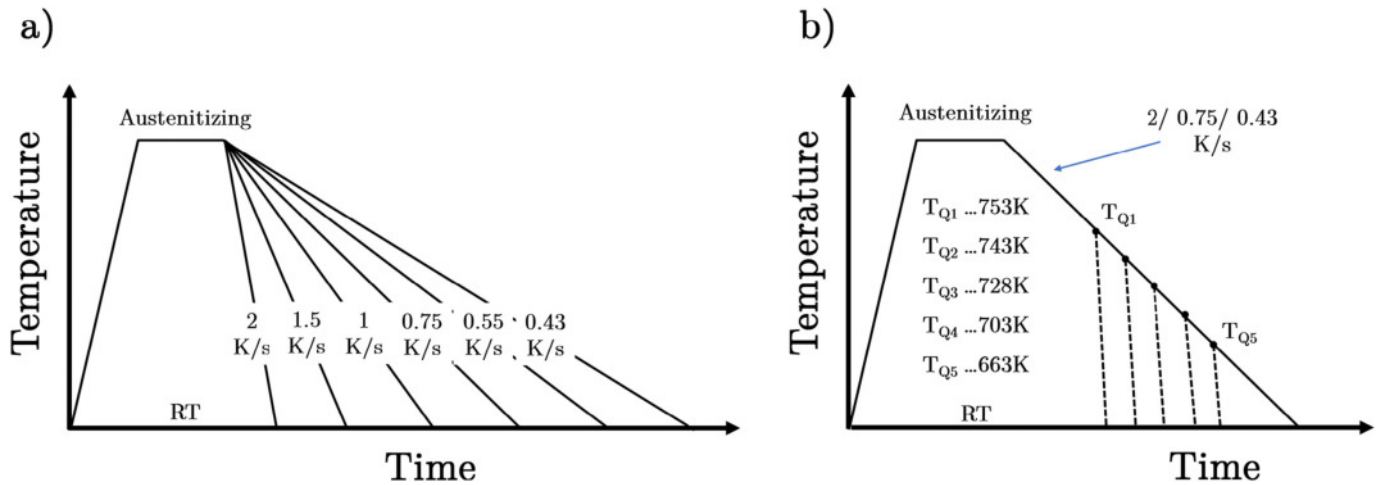


Fig. 1. Schematic illustration of heat treatments for a) high energy X-ray diffraction (HEXRD) experiments, and b) quenching experiments during the bainitic reaction.

2 K/s and 2 K for 0.43 K/s. In order to obtain sufficient diffraction peaks for quantitative phase analysis of ferrite and austenite, the distance between sample and detector was set to 1536 mm.

The raw data in form of Debye-Scherrer rings were integrated using the software package Fit2D from ESRF [17]. The distance and tilt of the detector as well as the wavelength were calibrated with patterns obtained by a LaB<sub>6</sub> standard powder. The resulting corrected X-ray diagrams spanned  $2\theta$ -angles from 1 to 10.8° with a step size of 0.0073076°. For peak analysis, a Pseudo-Voigt fit function was used.

### 2.3.1. Calculation of phase fractions and lattice parameter

Phase fractions of bainitic ferrite and retained austenite were calculated from the integrated intensities of the (200), (220) and (311) austenite peaks and the ferrite (200), (211) and (220) reflections, according to ASTM-E975-13 [18].

For each measured diffraction pattern, also the lattice parameters for ferrite ( $a_\alpha$ ) and austenite ( $a_\gamma$ ) were calculated with Cohen's method [19, 20]. The calculated lattice parameters from individual ferrite or austenite peaks were plotted against  $\cos^2\{\theta\}/\sin\{\theta\}$  and the lattice parameters were obtained by extrapolating the diffraction angle to 90°. This method results in an average error of  $\pm 0.0002$  Å for the lattice parameters of both, bainitic ferrite and austenite. According to this small error, it is possible to calculate the carbon content in bainitic ferrite as well as retained austenite on the basis of the lattice parameter.

### 2.3.2. Determination of overall carbon content in austenite and bainitic ferrite

It is well known that the lattice parameter is influenced by alloying elements [21–25]. In the case of a bainitic transformation, the lattice parameter of retained austenite should predominantly be affected by the carbon content, which is controlled by relatively rapid diffusion of carbon atoms from the supersaturated bainitic ferrite into the remaining austenite. In [26], Dyson and Holmes pointed out that the lattice parameter of austenite at room temperature varies by 0.033 Å per weight percent carbon. In the present case, the lattice parameters of austenite and ferrite during phase transformation are also influenced by thermal expansion. If the final microstructure consists only of bainitic ferrite and carbon enriched retained austenite, it is possible to determine the carbon content of retained austenite ( $w_c^\gamma$ ) in weight percent at any temperature by a mass balance using the following equation [27]:

$$w_c^\gamma = \frac{f_\alpha \cdot a_{\alpha,T}^3}{(1-f_\alpha) \cdot a_{\gamma,T}^3} (\bar{w} - w_c^\alpha) + \bar{w} \quad (2)$$

where  $f_\alpha$  represents the volume fraction of bainitic ferrite,  $a_{\alpha,T}$  denotes

the lattice parameter of bainitic ferrite at given temperature,  $a_{\gamma,T}$  that of austenite,  $w_c^\alpha$  is the carbon content in bainitic ferrite at room temperature and  $\bar{w}$  stands for the overall carbon content in mass percent in the alloy. To estimate the carbon enrichment of austenite during transformation at any temperature, Eq. (1) must be solved iteratively. As a convergence criterion, a fractional change of  $1 \times 10^{-4}$  wt% C in austenite was defined. The error in the austenite carbon content was determined to 0.06 wt%.

The residual carbon content in bainitic ferrite ( $x_{\alpha,C}$ ) in mole fraction was calculated from the bainitic ferrite lattice parameter at room temperature ( $a_\alpha$ ) using the following equation [27, 28]:

$$a_\alpha = a_{Fe} + \frac{(a_{Fe} - 0.279x_{\alpha,C})^2 (a_{Fe} + 2.496x_{\alpha,C}) - a_{Fe}^3}{3a_{Fe}^2} - 0.03x_{\alpha,Si} + 0.06x_{\alpha,Mn} + 0.07x_{\alpha,Ni} + 0.31x_{\alpha,Mo} + 0.05x_{\alpha,Cr} + 0.096x_{\alpha,V} \quad (3)$$

where  $x_i$  represents the mole fraction of element "i" in bainitic ferrite in mole fraction. Based on the assumption of low mobility of substitutional elements at transformation temperature and a homogenous distribution of alloying elements due to austenitization, their nominal concentration in the alloy is used. The lattice parameter of pure iron ( $a_{Fe}$ ) at room temperature is 2.8664 Å [27]. According Eq. (3), the carbon content of bainitic ferrite for all cooling rates is determined to  $0.65 \pm 0.04$  at.% or for a better comparability  $0.14 \pm 0.009$  wt%. Furthermore, no evidence of tetragonality was observed from the diffractograms. This is in good agreement with literature [21], whereas tetragonality is observed at carbon contents higher than 0.18 wt%.

### 2.4. Microstructure investigations

The microstructure after the bainitic phase transformation was characterized by means of a ZEISS™ AURIGA scanning electron microscope (SEM) equipped with a field emission gun. All investigated samples were conventionally prepared by grinding and polishing, followed by etching with Nital (3 ml HNO<sub>3</sub> in 97 ml Ethanol) for 3 s. To differentiate between bainitic ferrite and retained austenite, EBSD measurements were carried out using 20 kV accelerating voltage and 50 nm pixel size. The data were analysed using the Orientation Imaging Microscopy (OIM) data analysis software from EDAX and subsequently cleaned using the grain dilatation fit, where an angle of 10.5° was chosen (as seen to be the best fit in literature [29]). After the clean-up, 99.5% of the measured data points were successfully indexed.

For identification of carbides and film-like retained austenite, transmission electron microscopy (TEM) analysis was carried out on a FEI Tecnai F20, equipped with a field emission gun at an accelerating voltage of 200 kV. Thin foils were mechanically sliced from the tested



dilatometer samples followed by mechanical polishing to a thickness of around 70  $\mu\text{m}$ . Finally, the polished thin foils were electrochemically etched on a Struers Tenupol 5, using a 7% solution of perchloric acid at temperatures around  $-14^\circ\text{C}$ .

### 3. Results

#### 3.1. Bainitic phase transformation during continuous cooling

In order to investigate the transformation characteristics of the present bainitic steel, various dilatometer measurements with the time-temperature profiles shown in Fig. 1a were conducted. A comparison of the change in length (filled symbols) and the time derivative (open symbols) as a function of time are shown in Fig. 2 for the different cooling rates. Accordingly, the change in length, which corresponds to the degree of phase transformation from austenite to bainite, progresses from a continuous behaviour at higher cooling rates (Fig. 2a–c) to a two-stage behaviour with a transformation stasis at lower cooling rates (Fig. 2d–f). At cooling rates smaller than 0.75 K/s, a second peak in the time derivative curve and, additionally, a second onset temperature ( $2^{\text{nd}}$  Onset) depending on the cooling rate, is observed. The transformation stasis becomes more pronounced with decreasing cooling rate.

#### 3.2. Study of the transformation kinetics by means of HEXRD

##### 3.2.1. Evolution of bainitic ferrite and austenite phase fraction

The kinetics of bainite formation for the chosen cooling rate observed by means of in-situ HEXRD measurements are shown in Fig. 3. The same trend for the progress of phase transformation is observed

as previously indicated by the dilatometer curves. In the HEXRD measurements, the transformation again shows a change from a continuous to a two-stage behaviour, when decreasing the cooling rate below 0.75 K/s.

The onsets of the bainitic as well as for the two-stage transformation are marked with arrows. The bainite transformation remains incomplete and seems to terminate at approximately 575 K for all cooling rates. The amount of retained austenite increases from 10 vol% at 2 K/s to a maximum of 17 vol% at 0.75 K/s. For a further decrease of the cooling rate to 0.5 K/s and 0.43 K/s the amount of retained austenite seems to slightly decrease again and approaches a value of about 15 vol%. Analysis of the diffraction pattern revealed no evidence of the formation of carbide phases during cooling, which would otherwise influence the observed transformation behaviour. But due to the detection limit of about 1 vol%, carbide precipitation below this limit cannot be excluded.

##### 3.2.2. Carbon enrichment of austenite during phase transformation

Fig. 4 shows the overall enrichment of carbon in austenite ( $w_{\text{C}}$ ) for the applied cooling rates as determined from the HEXRD experiments and the calculation scheme outlined in Eq. (2). The dashed pink line represents the  $T_0'$  line, which was calculated with the software package MatCalc (<http://matcalc.at>) and the thermodynamic database 'mc\_fe' [30] for the present steel taking a strain energy value of 400 J/mol according to the findings of Bhadeshia [13] into account. As already mentioned earlier, only austenite with a carbon concentration higher than that given by the  $T_0'$  line is stable and will be retained at room temperature. In turn, austenite with a carbon content below the  $T_0'$  line can transform into bainitic ferrite subunits. The experimental results clearly

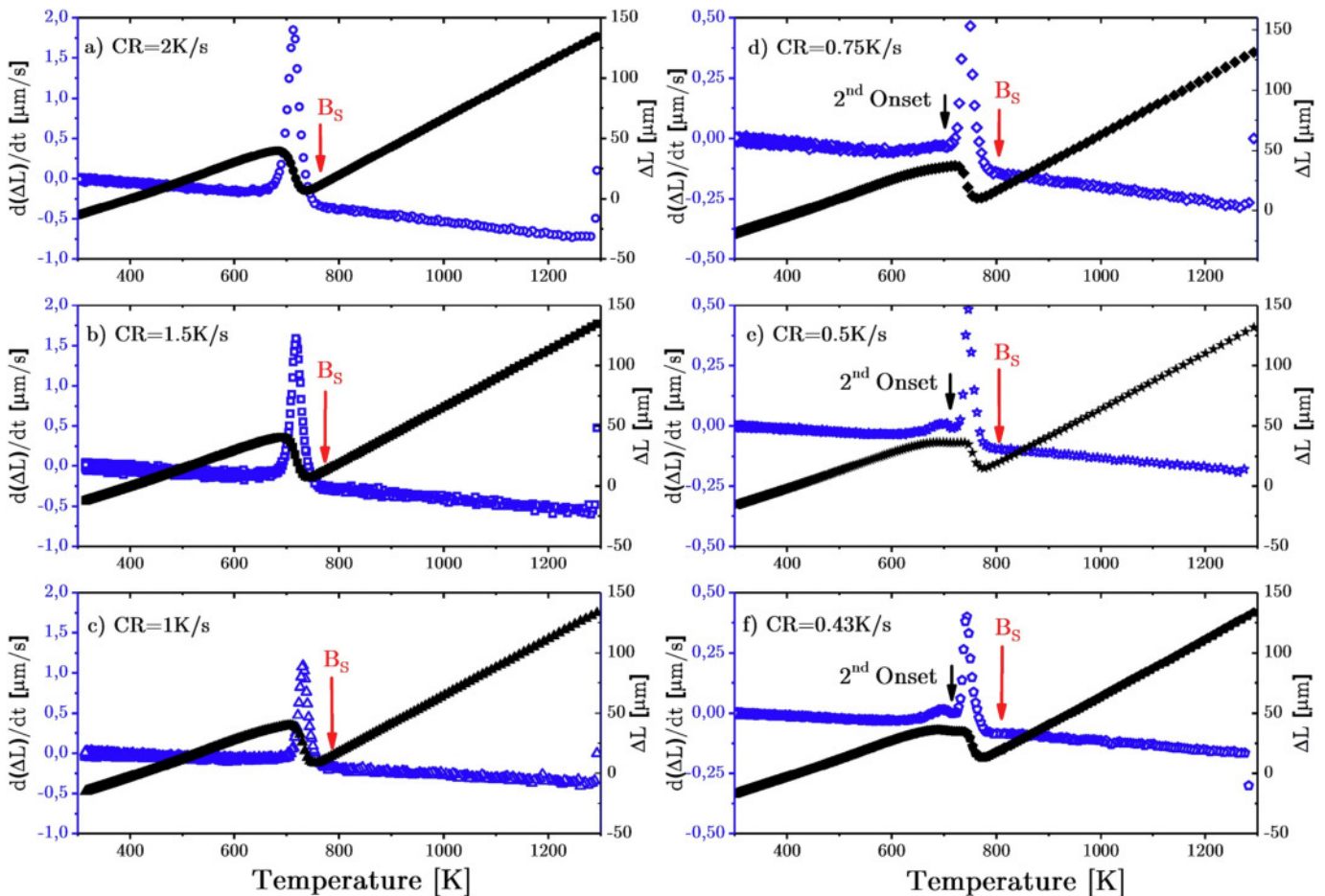


Fig. 2. Illustration of the change in length,  $\Delta L$  (filled symbols), and the time derivative,  $d(\Delta L)/dt$  (open symbols), as a function of temperature for cooling rates between 2 and 0.43 K/s. For cooling rates of 0.75 K/s, 0.5 K/s and 0.43 K/s, a second peak arises during the phase transformation from austenite to bainite.

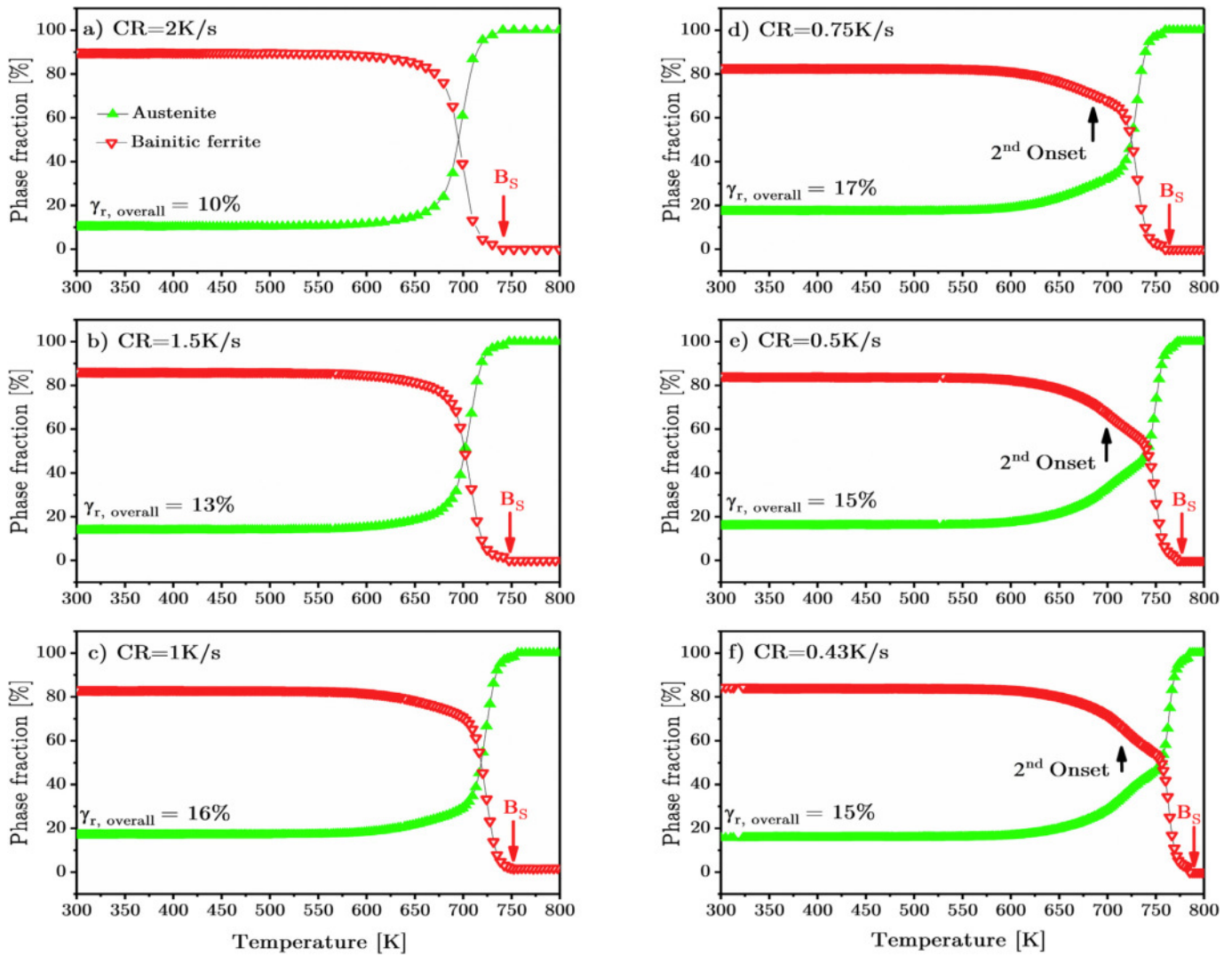


Fig. 3. Transformation kinetics of austenite (solid triangles up) to bainitic ferrite (triangle down) for cooling rates between 2 and 0.43 K/s.

indicate that bainitic phase transformation occurs at much lower temperatures than it would be expected from the  $T_0'$  line, which indicates that additional driving forces are needed. Thus, in addition to the 400 J/mol line, an adapted  $T_0'$  line (solid red line) is plotted for strain energy values which are adjusted in a way that the onset of bainitic phase transformation is possible.

The experimentally determined bainite start temperatures fit well when choosing 1150 J/mol (2 K/s) to 950 J/mol (0.43 K/s) as additional energy effort and there seem to be a trend that the additional energy effort decreases with decreasing cooling rate. With these values, the bainite start temperatures (corresponding to the intersection of the nominal C content with the critical C content given by  $T_0'$ ) can be closely reproduced in the present alloy.

In addition to the overall austenite C content, Fig. 4 also shows the full width at half maximum (FWHM) for the austenite {220} reflection as a function of temperature. In the present measurements, each austenite reflection consists of two contributions, one from the retained (blocky) austenite with a low degree of C-enrichment, and one from the film-like austenite in between the ferritic subunits with strong C-enrichment. Since the enrichment of film-like austenite is stronger at higher cooling rates, the absolute value of the FWHM is also higher at higher cooling rates. The FWHM decreases with decreasing cooling

rate suggesting that the fraction of film-like and blocky austenite also changes. This is confirmed in the EBSD analysis of the following section.

### 3.2.3. Characterization of retained austenite morphology after phase transformation

In order to determine the amount of blocky and film-like retained austenite, EBSD and TEM investigations were carried out. Fig. 5a–c shows an overlay of EBSD image quality maps with phase maps of ferrite (red) and austenite (green) for the cooling rates 2, 0.75 and 0.43 K/s, respectively. Evaluation of these images with respect to the amount of retained austenite delivered an increase from  $2 \pm 0.5$  vol% to  $10 \pm 0.5$  vol% with decreasing the cooling rate from 2 K/s to 0.43 K/s. The remaining black areas can be attributed to M/A constituents, due to their higher dislocation density and, therefore, lower image quality parameter [9, 31].

The amount of M/A constituents remains approximately constant at about  $1.5 \pm 0.5$  vol%.

To characterize the film-like retained austenite, the microstructure was examined by means of TEM. Fig. 5d–f shows TEM bright field images of specimens cooled with rates of 2, 0.75 and 0.43 K/s together with the corresponding dark field images and the selected area diffraction (SAD) pattern of retained austenite films between individual

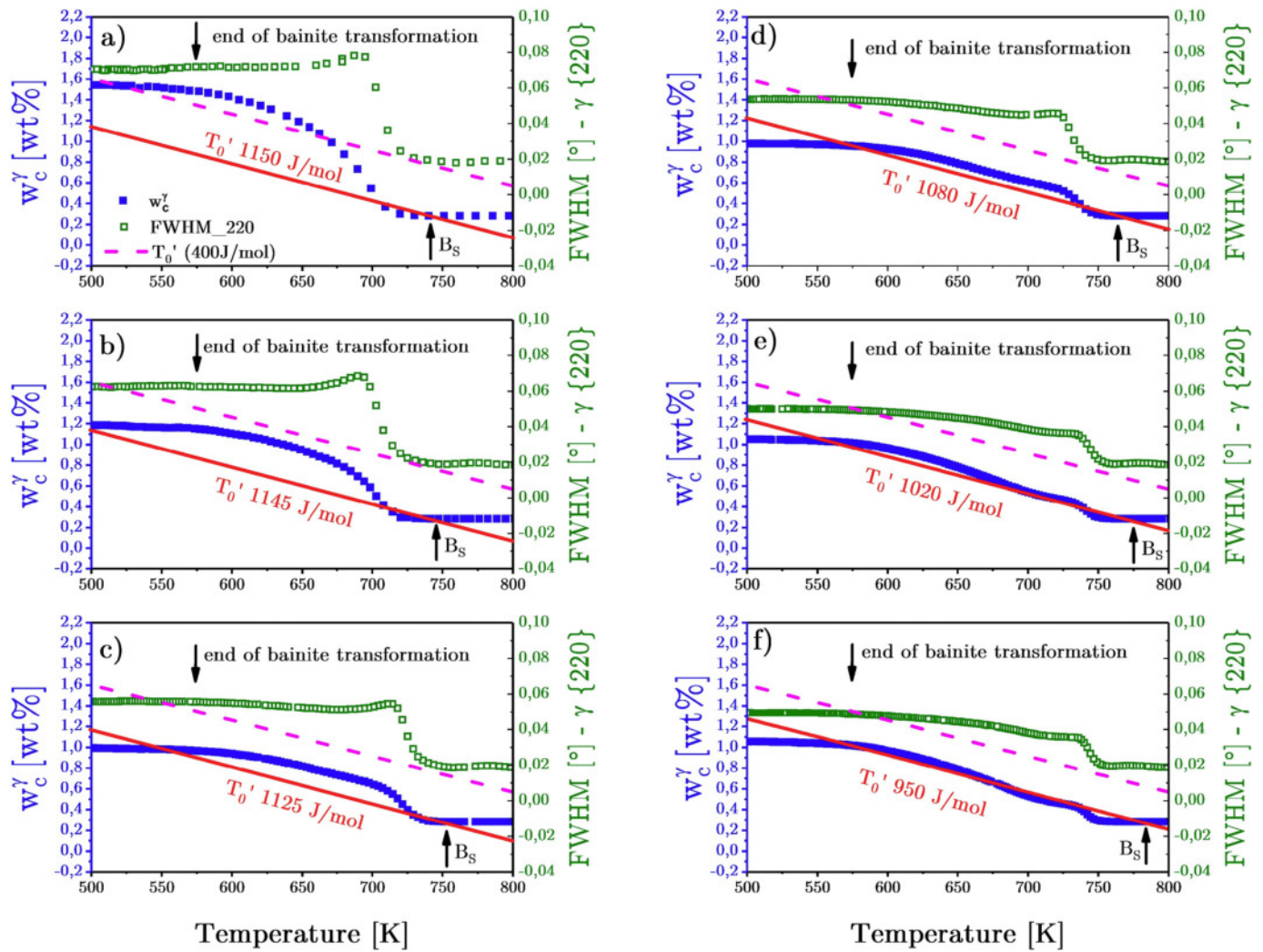


**Fig. 4.** Carbon enrichment of austenite (filled blue squares), FWHM of austenite {220} peak (open green squares) versus temperature during phase transformation for cooling rates a) 2 K/s, b) 1.5 K/s, c) 1 K/s, d) 0.75 K/s, e) 0.5 K/s and f) 0.43 K/s. The dotted line represents the  $T_0'$  line with a strain energy contribution of 400 J/mol and the solid red line represents simulated  $T_0'$  lines with different strain energy contributions varying from 1150 J/mol (2 K/s) to 950 J/mol (0.43 K/s), according the individual  $B_s$ .

bainitic subunits. The investigations indicate that the thickness of such a retained austenite film is in the magnitude of 20 to 100 nm. Since the retained austenite films are small ( $\leq 100$  nm), they can hardly be detected by EBSD, considering a step size of 50 nm during the measurements. Hence, the austenite regions identified by means of EBSD can be interpreted as blocky austenite.

### 3.3. Early stages of bainitic transformation during continuous cooling

In order to investigate different stages in the bainitic transformation, interrupted quenching experiments with time-temperature profiles shown in Fig. 1b were performed in the dilatometer. Fig. 6a shows the dilatometer signals during continuous cooling from austenitization temperature with a cooling rate of 0.43 K/s to different temperatures ( $T_Q$ ) inside the transformation region followed by subsequent quenching to room temperature (RT) with a cooling rate of  $\sim 100$  K/s. The dotted grey line corresponds to a dilatometer signal observed during continuous cooling with 100 K/s from austenitization temperature to room temperature without stopping and maintaining the sample at an intermediate temperature.

This experiment reveals increasing fraction of transformed bainite when decreasing  $T_Q$  as indicated by the dilatation since the untransformed austenite transforms into martensite during quenching.

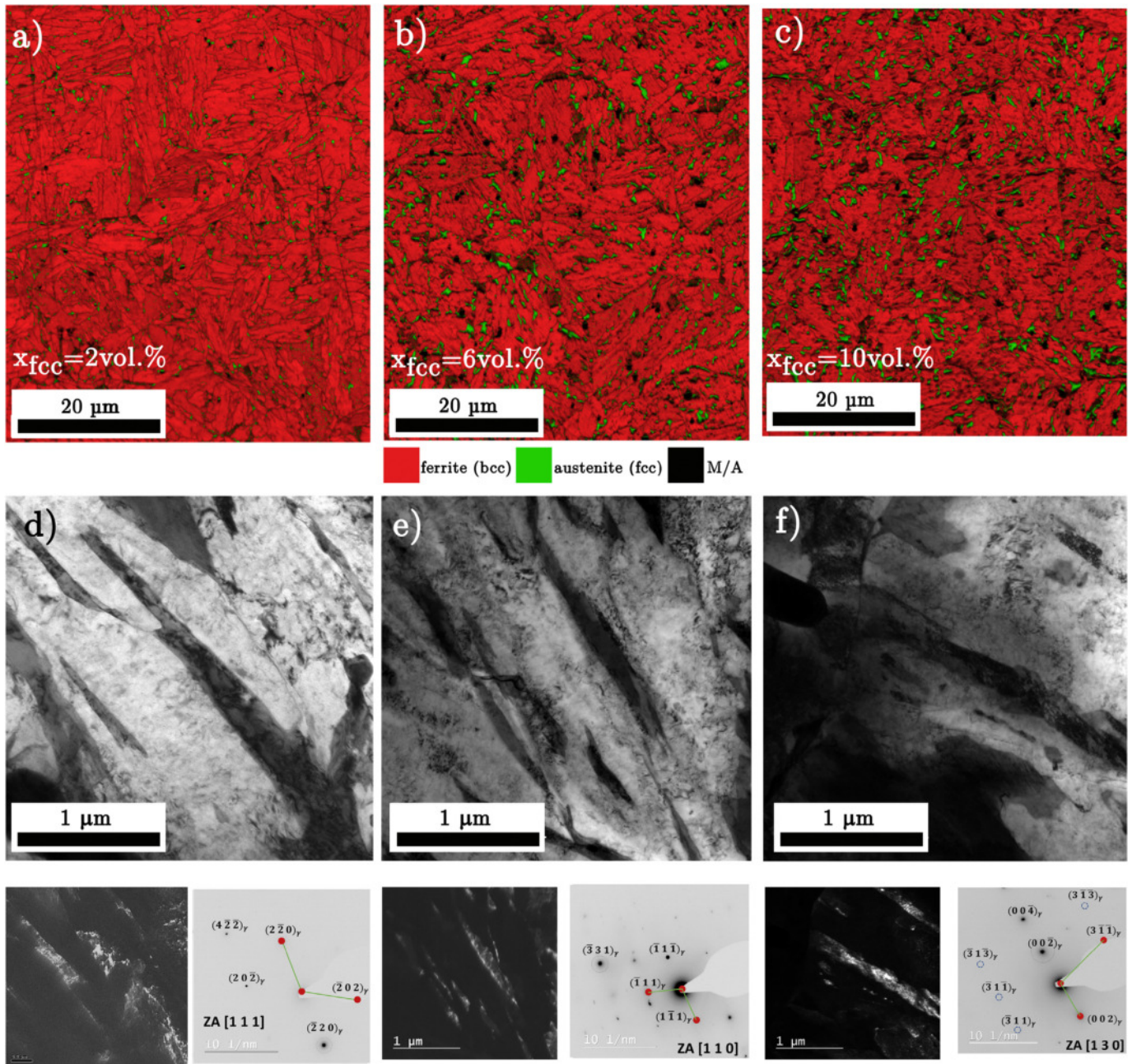
Moreover, with decreasing  $T_Q$ , corresponding to a higher degree of bainite transformation, the remaining austenite becomes more enriched in carbon and the martensite start temperature ( $M_s$ ) seem to decrease with decreasing  $T_Q$ . Additionally, a small change in length in the temperature range between  $T_Q$  and  $M_s$  can be observed. But, the origin of this was not analysed in detail and will be neglected in all further considerations.

Fig. 6b summarizes the measured  $M_s$  as a function of  $T_Q$  for the investigated cooling rates. The results indicate that the  $M_s$  temperature tends to decrease with decreasing quenching temperature. This trend can be related to less carbon enrichment of the remaining austenite blocks in specimens with higher cooling rates.

Fig. 7a–c shows representative SEM micrographs of microstructure obtained after cooling with a rate of 2 K/s to quenching temperatures of 728 K, 663 K and continuous cooling to room temperature, respectively. Since bainitic ferrite ( $\alpha_b$ ) is somewhat stronger attacked by the etchant, martensite and film-like and blocky austenite appear to be elevated in the images. In the absence of carbide precipitation, which applies to the present case, these structures are, therefore, identified as blocky and film-like retained austenite or M/A constituents, which is in accordance with literature [32, 33].

At an intermediate cooling rate of 0.75 K/s, the amount of blocky austenite (austenite is marked with white arrows) increases compared





**Fig. 5.** Phase map of blocky retained austenite after continuous cooling with a) 2 K/s, b) 0.75 K/s and c) 0.43 K/s; TEM bright field images with the corresponding SAD pattern and dark field image of film austenite after continuous cooling with d) 2 K/s, e) 0.75 K/s and f) 0.43 K/s.

to the highest cooling rate (Fig. 7d–f). This trend is continued at the lowest cooling rate of 0.43 K/s (Fig. 7g–i), which is in accordance with the previously discussed findings from EBSD.

#### 4. Discussion

In order to get a better understanding of the mechanisms taking place during the bainitic phase transformation in the framework of this study, a comprehensive set of experimental techniques were combined. The analysis of dilatometer and HEXRD experiments clearly shows that the continuously cooled bainite transformation characteristics change from a continuous single-stage behaviour at fast cooling rates (2 K/s) to a distinct two-stage behaviour at lower cooling rates (0.43 K/s), Figs. 2–3. Gupta et al. [34] observed a similar behaviour in their investigation on a CrMoV steel. They pointed out that the first peak can be attributed to the (fast) growth of bainitic ferrite subunits

nucleated at grain boundaries, whereas the second peak in the time derivative stems from the precipitation of carbides or the formation of M/A constituents. In the present investigation, high resolution SEM and TEM images as well as selected area diffraction provide no evidence of precipitates. These can, consequently, not be responsible for the second transformation peak as suggested by Gupta et al. in their work.

EBSD analysis indicates that M/A constituents are present in the microstructure after all applied cooling rates. Mazancova and Mazanec [35] pointed out that the formation of M/A constituents is typical for slow continuous cooling conditions and high transformation temperatures. Under these circumstances, carbon gradients in austenite can be reduced relatively quickly, carbon diffusion can occur over wider distances and the final mean carbon content of the retained austenite blocks ends up above the critical concentration given by the  $T_0'$ -line [13]. Consequently, these blocks do not transform into bainite but they do decompose partially into martensite during further cooling at

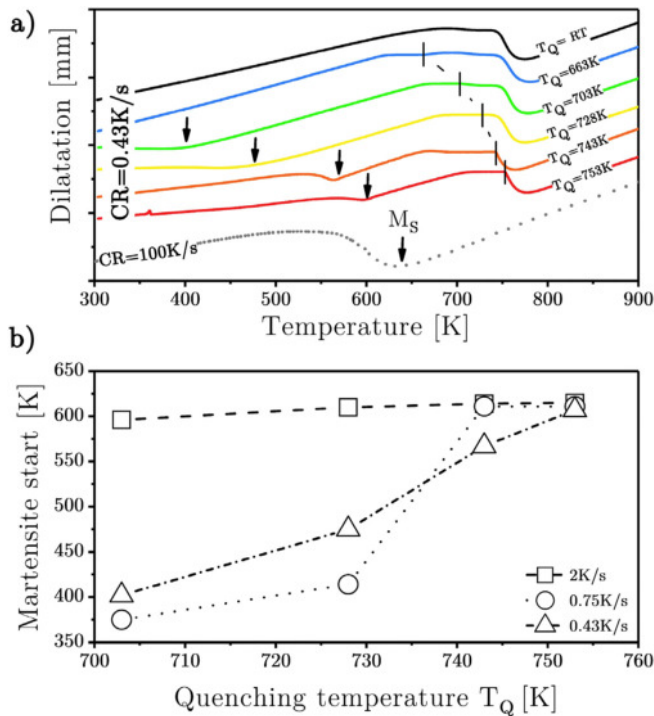


**Fig. 6.** a) Dilatometer signal for cooling rate 0.43 K/s to quenching temperatures ( $T_q$ ) and a dilatometer signal for cooling rate 100 K/s to room temperature, which corresponds to a fully martensitic transformation; b) shift of the martensite start temperature ( $M_s$ ) as a function of the interrupted quenching temperature ( $T_q$ ) for cooling rates 2, 0.75 and 0.43 K/s.

lower temperature. The quenching experiments shown in Fig. 6 indicate that the transformation of carbon-enriched austenite to martensite occurs at temperatures below the region of bainite transformation. Therefore, the formation of M/A constituents did not influence the observed bainite transformation characteristics which takes place at higher temperatures.

The SEM micrographs in Fig. 7 as well EBSD measurements in Fig. 5 show that the microstructure after continuous cooling consists of bainitic ferrite and retained austenite. In literature [32, 36, 37], retained austenite is described in two distinct morphologies, i.e., as blocky retained austenite and film-like retained austenite. Furthermore, it is reported that blocky retained austenite occurs between different sheaves of bainite, whereas film-like retained austenite is located between individual bainitic subunits within a sheave of bainite [37]. In the present work, both, film-like and block-like structures are observed by SEM and TEM and they are recognized as blocky (Fig. 5a–c) and film-like (Fig. 5d–f) retained austenite at the expected location as described in literature. The presence of both morphologies is also indicated by the FWHM of the {220}-austenite reflection in Fig. 4. Scherrer [38] showed in his pioneering work on X-ray diffraction in polycrystalline materials that a smaller crystal size leads to peak broadening. It is thus expected that the retained austenite films with thicknesses in the range of 20 to 100 nm lead to a higher FWHM than blocky retained austenite. This is in good accordance with the observed FWHM behaviour. Additionally, carbon inhomogeneities in retained austenite would also influence the peak broadening. It is reported in literature that the carbon content in blocks of retained austenite is lower (especially at higher cooling rates) than that in film-like retained austenite [9, 32]. As a consequence, spatially different lattice parameters are present which contributes to the observed peak broadening.

Fig. 4 also shows the carbon enrichment in austenite during the bainitic reaction, for the applied cooling rates. By comparing the measured carbon content evolution in austenite and the  $T_0'$  line including an offset of 400 J/mol for cooling rates lower than 2 K/s, no retained

austenite should be present in the microstructure. According to the  $T_0'$ -concept, only austenite with a carbon concentration higher than that given by the  $T_0'$ -line is stable and will be retained at room temperature, which is in contrast to the findings of the present study. A similar behaviour was observed by Xia et al. [11] in their investigations on Mo-added low carbon steels. These authors showed that the addition of Mo leads to a stasis in the bainitic phase transformation at a given temperature. Furthermore, they measured the carbon content in austenite in the stasis stage by means of electron probe microanalysis (EPMA) and found out that the carbon concentration in austenite also lies below the  $T_0'$  line with a strain energy offset of 400 J/mol, for alloys with a Mo content higher than 0.3 wt%. This phenomenon can thus be also expected in the present steel, which has an overall content of 2.82 wt% Mo. When Bhadeshia and Edmonds [39] first analysed strain energy effects on the formation of bainite, they assumed the bainitic subunits as oblate spheroids with thickness  $c$  and radius  $r$ , where  $r \gg c$ . The elastic strain energy  $E$  per unit volume can be calculated to be:

$$E = A \times \frac{c}{r} \quad (4)$$

$A$  is constant, which scales linearly with the shear modulus of austenite. The constant  $A$  is in the order of 2090 J/cm<sup>3</sup> at room temperature and decreases with about 9 J/cm<sup>3</sup> per K [39]. Therefore,  $A$  can be estimated for any temperature. By following the proposed equation, Bhadeshia and Edmonds calculated a strain energy contribution of 260 J/mol, considering a subunit thickness of 0.1  $\mu$ m and a radius of 5  $\mu$ m at a transformation temperature of 743 K. Additionally, the strain energy for the present steel can be calculated similarly. In order to determine the length and width of the individual subunits, a minimum of 100 measurements for both microstructure parameters were carried out on the SEM micrographs presented in Fig. 7. Following the procedure in [40], the subunit width and length can be determined to  $0.27 \pm 0.02 \mu$ m and  $3.5 \pm 0.5 \mu$ m.

Applying these microstructure parameters and considering an average transformation temperature of 728 K, the strain energy offset for the present steel can be calculated to  $981 \pm 185$  J/mol. This calculated offset range for the strain energy is in good accordance with the values used for the calculation of the  $T_0'$ -line which were found to be between 1150 J/mol and 950 J/mol, see Fig. 4. Considering these strain energy values, the observed bainitic transformation characteristics can be consistently described as a four-stage process at cooling rates lower than 0.75 K/s, Fig. 8:

- Stage I. fast grain boundary nucleation of bainitic subunits and stabilization of film-like retained austenite due to carbon enrichment
- Stage II. further carbon enrichment in austenite leads to a stasis in the transformation, according to the  $T_0'$ -concept.
- Stage III. further transformation of the remaining austenite as well as long range diffusion of carbon in austenite leads to a stabilization of blocky retained austenite
- Stage IV. end of transformation and formation of M/A-constituents

## 5. Summary

In the present study, the phase transformation from austenite to bainitic ferrite in a CrMoV steel during continuous cooling was investigated by means of in-situ HEXRD coupled with dilatometry and ex-situ microstructure analysis after heat treatment by means of SEM, EBSD and TEM. The results lead to following conclusions:

- The transformation kinetics during continuous cooling changes from a continuous transformation behaviour (cooling rate > 1 K/s) to a distinct two-stage transformation behaviour (cooling rate < 0.75 K/s).
- Phase and crystallographic analysis by means of HEXRD suggest that the observed high amounts of retained austenite (up to 17 vol%)



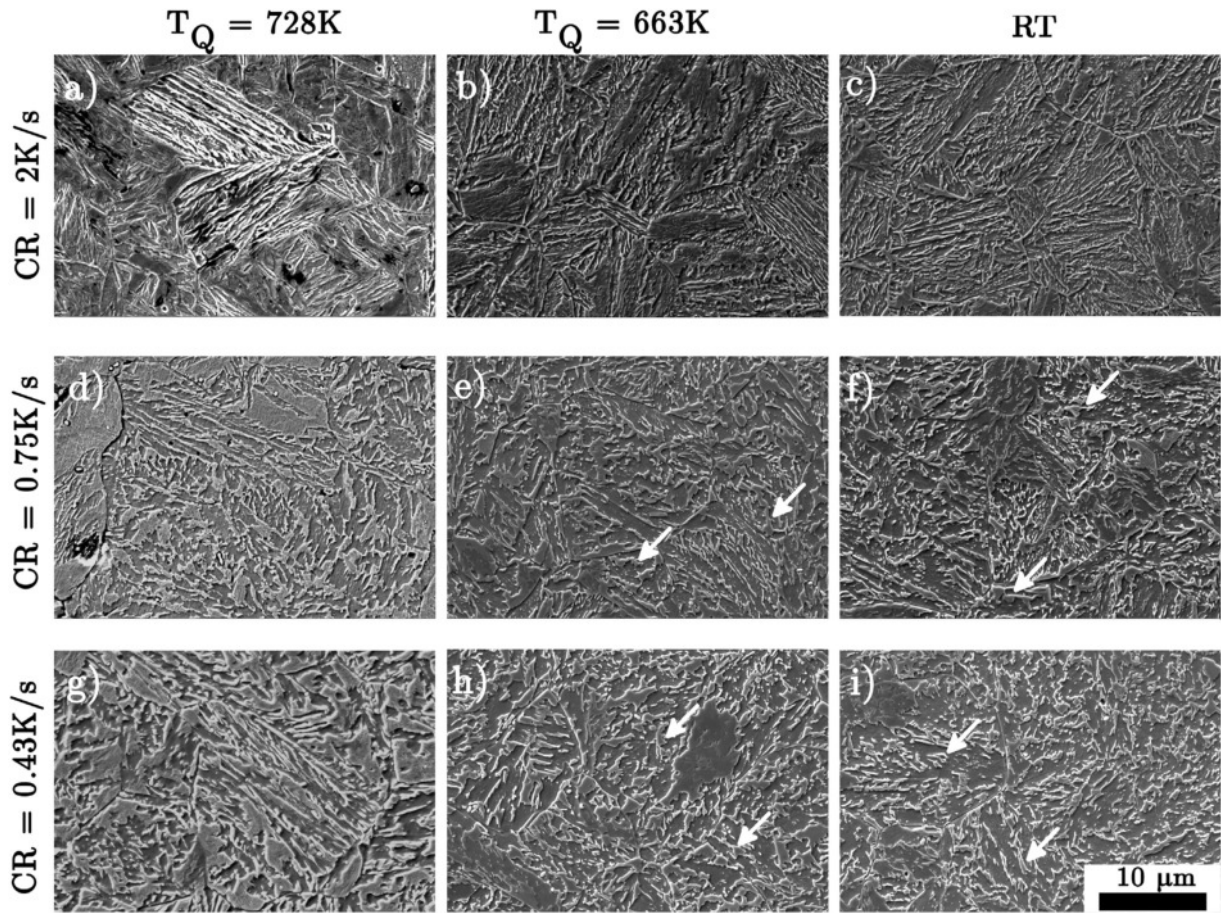


Fig. 7. SEM micrographs after continuous cooling with cooling rates varying from 2 K/s to 0.43 K/s and interrupted quenching at different  $T_Q$  (728, 663 K and RT).

cannot be explained on basis of the  $T_0'$ -line with a strain energy contribution of 400 J/mol.

- Taking strain energy values between 950 and 1100 J/mol into account the observed transformation characteristics can be consistently described.
- A calculated strain energy value of  $981 \pm 185$  J/mol energy offset according the investigated bainitic microstructure are in good

agreement with the simulated strain energy values between 950 and 1100 J/mol.

#### Acknowledgement

Financial support by the Austrian Federal Government (in particular from Bundesministerium für Verkehr, Innovation und Technologie and Bundesministerium für Wissenschaft, Forschung und Wirtschaft) represented by Österreichische Forschungsförderungsgesellschaft mbH and the Styrian and the Tyrolean Provincial Government, represented by Steirische Wirtschaftsförderungsgesellschaft mbH and Standortagentur Tirol, within the framework of the COMET Funding Programme is gratefully acknowledged.

#### References

- [1] E.S. Davenport, E.C. Bain, Transformation of austenite at constant subcritical temperature, *Trans. Am. Inst. Min. Met. Eng.* 90 (1930) 117–154, <https://doi.org/10.1179/1743284712Y.0000000157>.
- [2] R.F.H.F. Hemann, K.R. Kinsman, H.I. Aaronson, A debate on the bainite reaction, *Metall. Trans.* 3 (1972) 1077–1094.
- [3] L.C.D. Fielding, The bainite controversy, *Mater. Sci. Technol.* 29 (2013) 383–399, <https://doi.org/10.1179/1743284712Y.0000000157>.
- [4] M. Hillert, The nature of bainite, *ISIJ Int.* 35 (1995) 1134–1140.
- [5] E. Swallow, H.K.D.H. Bhadeshia, High resolution observations of displacements caused by bainitic transformation, *Mater. Sci. Technol.* 12 (1996) 121–125, <https://doi.org/10.1179/026708396790165614>.
- [6] H. Matsuda, H.K.D.H. Bhadeshia, Kinetics of the bainite transformation, *Proc. R. Soc. A Math. Phys. Eng. Sci.* 460 (2004) 1707–1722, <https://doi.org/10.1098/rspa.2003.1225>.
- [7] H.K.D.H. Bhadeshia, D.V. Edmonds, The bainite transformation in a silicon steel, *Metall. Trans. A.* 10 (1979) 895–907, <https://doi.org/10.1007/BF02658309>.
- [8] H.K.D.H. Bhadeshia, D.V. Edmonds, Bainite in silicon steels: new composition-property approach part 1, *Met. Sci.* 17 (1983) 411–419, <https://doi.org/10.1179/030634583790420646>.

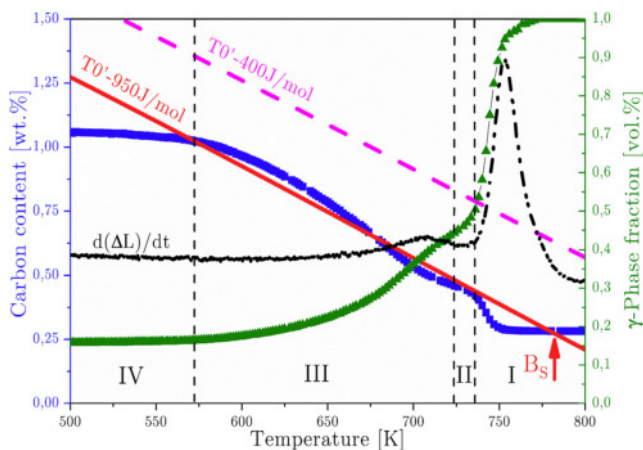


Fig. 8. The transformation processes which occur in the investigated steel during continuous cooling with cooling rates lower than 0.75 K/s can be separated into four main stages: I) beginning of transformation and stabilization of film-like retained austenite, II) transformation stasis, III) further transformation of the remaining austenite and stabilization of blocky retained austenite and IV) end of transformation and formation of M/A-constituents.

- [9] C. Hofer, F. Winkelhofer, H. Clemens, S. Primig, Morphology change of retained austenite during austempering of carbide-free bainitic steel, *Mater. Sci. Eng. A* 664 (2016) 236–246, <https://doi.org/10.1016/j.msea.2016.04.005>.
- [10] H.D. Wu, G. Miyamoto, Z.G. Yang, C. Zhang, H. Chen, T. Furuhashi, Incomplete bainite transformation in Fe-Si-C alloys, *Acta Mater.* 133 (2017) 1–9, <https://doi.org/10.1016/j.actamat.2017.05.017>.
- [11] Y. Xia, G. Miyamoto, Z.G. Yang, C. Zhang, T. Furuhashi, Direct measurement of carbon enrichment in the incomplete bainite transformation in Mo added low carbon steels, *Acta Mater.* 91 (2015) 10–18, <https://doi.org/10.1016/j.actamat.2015.03.021>.
- [12] C. Zener, Kinetics of the decomposition of austenite, *Trans. AIME* 167 (1946) 550–595.
- [13] H.K.D.H. Bhadeshia, A rationalisation of shear transformations in steels, *Acta Metall.* 29 (1981) 1117–1130, [https://doi.org/10.1016/0001-6160\(81\)90063-8](https://doi.org/10.1016/0001-6160(81)90063-8).
- [14] H.K.D.H. Bhadeshia, *Bainite in Steels*, 1st edition, 1992 2–9.
- [15] N. Schell, A. King, F. Beckmann, H.U. Ruhnau, R. Kirchhof, R. Kiehn, M. Möller, A. Schreyer, The High Energy Materials Science Beamline (HEMS) at PETRA III, *AIP Conf. Proc.* 1234, 2010 391–394, <https://doi.org/10.1063/1.3463221>.
- [16] P. Staron, T. Fischer, T. Lippmann, A. Stark, S. Daneshpour, D. Schnubel, E. Uhlmann, R. Gerstenberger, B. Camin, W. Reimers, E. Eidenberger, H. Clemens, N. Huber, A. Schreyer, In situ experiments with synchrotron high-energy X-rays and neutrons, *Adv. Eng. Mater.* 13 (2011) 658–663, <https://doi.org/10.1002/adem.201000297>.
- [17] A.P. Hammersley, ESRF internal report, ESRF97HA02T, "FIT2D: an introduction and overview", (1997), n.d. [http://www.esrf.eu/computing/scientific/FIT2D/FIT2D\\_REF/node268.html](http://www.esrf.eu/computing/scientific/FIT2D/FIT2D_REF/node268.html).
- [18] ASTM, Standard Practice for X-ray Determination of Retained Austenite in Steel With Near Random Crystallographic Orientation 1, ASTM, 03, 2009 1–7, <https://doi.org/10.1520/E0975-13.necessary>.
- [19] B.D. Cullity, Elements of X-ray Diffraction, 1956 <https://doi.org/10.1017/CBO9781107415324.004>.
- [20] R.A. Young, The Rietveld method, *Cryst. Res. Technol.* 30 (1995) 494.
- [21] L. Xiao, Z. Fan, Z. Jinxiu, Z. Mingxing, K. Mokuang, G. Zhenqi, Lattice-parameter variation with carbon content of martensite. I. X-ray-diffraction experimental study, *Phys. Rev. B* 52 (1995) 9970–9978, <https://doi.org/10.1103/PhysRevB.52.9970>.
- [22] M. Onink, C.M. Brakman, F.D. Tichelaar, E.J. Mittemeijer, S. van der Zwaag, J.H. Root, N.B. Konyer, The lattice parameter of austenite and ferrite in Fe-C alloys as function of carbon concentration and temperature, *Scr. Metall. Mater.* 29 (1993) 1011–1016, <https://doi.org/10.1017/CBO9781107415324.004>.
- [23] E.P. Abrahamson, S.L. Lopata, The lattice parameters and solubility limits of alpha iron as affected by some binary transition-elements additions, *Am. Inst. Min. Met. Eng.* 236 (1966) 76–87.
- [24] X. Liu, F. Zhong, J. Zhang, M. Zhang, M. Kang, Z. Guo, Lattice parameter variation with carbon content of martensite. I. X-ray diffraction experimental study, *Phys. Rev. B* 52 (1995) 9970–9978.
- [25] L. Cheng, A. Bouger, T.H. de Keijser, Lattice parameters of iron carbon and Iron nitro-gen martensites and austenites, *Scr. Metall. Mater.* 24 (1990) 509–514.
- [26] DDJ, HB, Effect of alloying additions on the lattice parameter of austenite, *J. Iron Steel Inst.* 208 (1970) 469–474 <https://www.scopus.com/inward/record.uri?eid=2-s2.0-0014778197&partnerID=40&md5=5b197b267279ed88d140c08a338704d2>.
- [27] H.K.D.H. Bhadeshia, S.A. David, J.M. Vitek, R.W. Reed, Stress induced transformation to bainite in pressure vessel steel, *Metall. Mater. Trans. A* 7 (1991) 686–698.
- [28] S.S. Babu, E.D. Specht, S.a. David, E. Karapetrova, P. Zschack, M. Peet, H.K.D.H. Bhadeshia, In-situ observations of lattice parameter fluctuations in austenite and transformation to bainite, *Metall. Mater. Trans. A* 36 (2005) 3281–3289, <https://doi.org/10.1007/s11661-005-0002-x>.
- [29] S. Morito, H. Yoshida, T. Maki, X. Huang, Effect of block size on the strength of lath martensite in low carbon steels, *Mater. Sci. Eng. A* 438–440 (2006) 237–240, <https://doi.org/10.1016/j.msea.2005.12.048>.
- [30] E. Povoden-Karadeniz, Thermodynamic database mc\_fe.tdb (v.2.059), <http://matcalc.tuwien.ac.at/index.php/databases/open-databases> 2017.
- [31] C. Hofer, H. Leitner, F. Winkelhofer, H. Clemens, S. Primig, Structural characterization of "carbide-free" bainite in a Fe-0.2C-1.5Si-2.5Mn steel, *Mater. Charact.* 102 (2015) 85–91, <https://doi.org/10.1016/j.matchar.2015.02.020>.
- [32] F.G. Caballero, C. Garcia-Mateo, M.J. Santofimia, M.K. Miller, C. García de Andrés, New experimental evidence on the incomplete transformation phenomenon in steel, *Acta Mater.* 57 (2009) 8–17, <https://doi.org/10.1016/j.actamat.2008.08.041>.
- [33] S. Reisinger, G. Ressel, S. Eck, S. Marsoner, Differentiation of grain orientation with corrosive and colour etching on a granular bainitic steel, *Micron* 99 (2017) 67–73, <https://doi.org/10.1016/j.micron.2017.04.002>.
- [34] C. Gupta, G.K. Dey, J.K. Chakravarty, D. Srivastav, S. Banerjee, A study of bainite transformation in a new CrMoV steel under continuous cooling conditions, *Scr. Metall. Mater.* 53 (2005) 559–564, <https://doi.org/10.1016/j.scriptamat.2005.04.031>.
- [35] E. Mazancová, K. Mazanec, Physical metallurgy characteristics of the M/A constituent formation in granular bainite, *J. Mater. Process. Technol.* 64 (1997) 287–292, [https://doi.org/10.1016/S0924-0136\(96\)02578-2](https://doi.org/10.1016/S0924-0136(96)02578-2).
- [36] L. Morales-Rivas, H.W. Yen, B.M. Huang, M. Kuntz, F.G. Caballero, J.R. Yang, C. Garcia-Mateo, Tensile response of two nanoscale bainite composite-like structures, *JOM* 67 (2015) 2223–2235, <https://doi.org/10.1007/s11837-015-1562-x>.
- [37] A.S. Podder, H.K.D.H. Bhadeshia, Thermal stability of austenite retained in bainitic steels, *Mater. Sci. Eng. A* 527 (2010) 2121–2128, <https://doi.org/10.1016/j.msea.2009.11.063>.
- [38] P. Scherrer, Bestimmung der Größe und der inneren Struktur von Kolloidteilchen mittels Röntgenstrahlen, *Nachrichten von Der Gesellschaft Der Wissenschaften Zu Göttingen, Math. Klasse*, 1918, 1918 98–100, <https://doi.org/10.1007/978-3-662-33915-2>.
- [39] H.K.D.H. Bhadeshia, D.V. Edmonds, Mechanism of bainite formation in steels, *Acta Metall.* 28 (1980) 1265–1273, [https://doi.org/10.1016/0001-6160\(80\)90082-6](https://doi.org/10.1016/0001-6160(80)90082-6).
- [40] C. Garcia-Mateo, J.A. Jimenez, B. Lopez-Ezquerria, R. Rementeria, L. Morales-Rivas, M. Kuntz, F.G. Caballero, Analyzing the scale of the bainitic ferrite plates by XRD, SEM and TEM, *Mater. Charact.* 122 (2016) 83–89, <https://doi.org/10.1016/j.matchar.2016.10.023>.



## B. MatCalc scripts

### B.1. Thermodynamic equilibrium calculation

```

$$*****
*****          GENERAL INFORMATION          *****
*****$
$
Last update: 01.03.2019
$$*****
*****          SETUP INFORMATION          *****
*****$
$
use-module core          $ Use "core" module (MatCalc uses "core" module by default
                          anyway)
new-workspace           $ creates a new workspace

$$*****
*****          SYSTEM SETUP          *****
*****$
$
$ verify correct MatCalc version (is accessible as internal variable)
if (matcalc_version<6000000)
send-dialog-string "MatCalc version must be 6.00.0000 or higher to run this script. Stop-
ping."
stop_run_script $ stop script
endif
open-thermodynamic-database mc_fe.tdb
select-elements Fe C Mn Cr Mo Si V Va Ni
select-phases FCC_a1 Bcc_a2 M6C Cementite HCP_A3 Liquid
read-thermodynamic-database
read-mobility-database mc_fe.ddb
set-reference-element FE
enter-composition wp c=0.28 Mo=2.82 Cr=0.43 V=0.39 Mn=0.32 Si=0.27 Cu=0.2 Ni=0.11
change-phase-status FCC_A1#01 set-flag=suspended
change-phase-status HCP_A3 set-flag=suspended
change-phase-status HCP_A3#02 set-flag=suspended
set-temperature-celsius 1025

```

```
set-automatic-startvalues
calculate-equilibrium
step-equilibrium
set-step-option range 1600 400 lin 10

$$*****
*****          SETUP      GUI          *****
*****$

$
new-gui-window p1          $ create XY-data plot window
move-gui-window displace . 150 100 600 500    $ move and resize plot window

$ define default x-axis properties
set-gui-window-property window-id=. default-x-axis-for-all-plots=yes
set-gui-window-property window-id=. default-x-axis-title="temperature / C"
set-gui-window-property window-id=. default-x-axis-data=T$c

$ define plot properties: phase fraction
set-plot-option . axis y-axis-title="phase fraction"
set-plot-option . series new buffer f$*
set-plot-option . y-axis-type=log

$$*****
*****          DATA      EXCHANGE      *****
*****$

$

set-plot-option . series convert-to-table * no
export-global-table f$LIQUID Liquidus
export-global-table f$FCC_A1 FCC_Austenite
export-global-table f$BCC_A2 BCC_Ferrite
export-global-table f$HCP_A3#01 M2C
export-global-table f$CEMENTITE Cementite
export-global-table f$M6C M6C
```

## B.2. Decomposition of retained austenite during reheating

```

$$*****
***** GENERAL INFORMATION *****
*****$
$
Last update: 01.03.2019
$$*****
***** SETUP INFORMATION *****
*****$
$
use-module core          $ Use "core" module (MatCalc uses "core" module by default
anyway)
new-workspace            $ creates a new workspace

$$*****
***** SYSTEM SETUP *****
*****$
$
$ verify correct MatCalc version (is accessible as internal variable)
if (matcalc_version<6000000)
send-dialog-string "MatCalc version must be 6.00.0000 or higher to run this script. Stop-
ping."
stop_run_script $ stop script
endif
open-thermodynamic-database mc_fe.tdb
select-elements Fe C Mn Cr Mo Si V Va Ni
select-phases FCC_a1 Cementite
read-thermodynamic-database
read-mobility-database mc_fe.ddb

set-reference-element FE
enter-composition wp c=1.6 Mo=2.82 Cr=0.43 V=0.39 Mn=0.32 Si=0.27 Ni=0.11

change-phase-status FCC_A1#01 set-flag=suspended

set-temperature-celsius 1025
set-automatic-startvalues
calculate-equilibrium

```

```

$$*****
***** Precipitates and Precipitation domain *****
*****$

```

\$

```

create-precipitation-domain Retained_austenite
set-precipitation-parameter Retained_austenite thermodynamic-matrix-phase= FCC_A1
set-precipitation-parameter Retained_austenite equilibrium-dislocation-density= 1e15

```

```

create-new-phase CEMENTITE precipitate Cementite
set-precipitation-parameter CEMENTITE_P0 nucleus-composition-model=para-composi-
tion
set-precipitation-parameter CEMENTITE_P0 nucleation sites dislocations

```

```

$$*****
***** Heat treatment *****
*****$

```

\$

```

create-tm-treatment Reheating
append-tmt-segment Reheating
edit-tmt-segment Reheating . segment-start-temperature=25
edit-tmt-segment Reheating . T_end+T_dot 620 0.5
edit-tmt-segment Reheating . precipitation-domain=Retained_austenite

```

```

$$*****
***** SETUP GUI *****
*****$

```

\$

```

new-gui-window p1 $ create plot window
move-gui-window displace . 75 15 880 790 $ move and resize plot window

```

```

$ define default x-axis properties
set-gui-window-property window-id=. default-x-axis-for-all-plots=yes
set-gui-window-property window-id=. default-x-axis-title="time / s"
set-gui-window-property window-id=. default-x-axis-type=lin

```

```

$set-gui-window-property . number-of-plot-columns=auto

```

```
$ define plot properties: temperature profile
set-plot-option . y-axis-title="temperature / C"
set-plot-option . series new buffer T$C
```

```
$ define plot properties: phase fraction
create-new-plot xy-plot .
set-plot-option . use-alias-names-in-legend=yes
set-plot-option . series new buffer f_prec$*
set-plot-option . y-axis-title="phase fraction"
```

```
$ define plot properties: number density
create-new-plot xy-plot .
set-plot-option . use-alias-names-in-legend=yes
set-plot-option . series new buffer num_prec$*
set-plot-option . y-axis-title="number density / m<sup>-3</sup>"
set-plot-option . y-axis-type=log
set-plot-option . y-axis-scaling=1e10..
```

```
$ define plot properties: mean radius
create-new-plot xy-plot .
set-plot-option . use-alias-names-in-legend=yes
set-plot-option . series new buffer r_mean$*
set-plot-option . y-axis-title="mean radius / nm"
set-plot-option . y-axis-type=log
set-plot-option . y-axis-scaling=1e-1..
set-plot-option . y-axis-factor=1e9
```

```
$$*****
***** Simulation Setup *****
*****$
```

```
$
set-simulation-parameter temperature-control tm-treatment-name=Reheating
start-precipitate-simulation
```